

# Dissertation

submitted to the

Combined Faculty of Mathematics, Engineering and Natural Sciences

of Heidelberg University, Germany

for the degree of

Doctor of Natural Sciences

Put forward by

Daniel Heuchel

born in: Giessen

Oral examination: June 15, 2022

# Particle Flow Studies with Highly Granular Calorimeter Data

Particle Flow Studien mit Hoch-Granularen Kalorimeter Daten

Referee 1:  
Referee 2:

Priv.-Doz. Dr. Felix Sefkow  
Prof. Dr. Norbert Herrmann

# Abstract

The particle flow reconstruction concept is based on a set of pattern recognition algorithms promising to deliver unprecedented jet energy resolution in a future lepton collider experiment. One of the key requirements for this concept is highly granular calorimetry, capable of revealing the substructure of particle showers. The CALICE collaboration has developed the highly granular Analog Hadron Calorimeter (AHCAL) prototype, a steel sampling calorimeter featuring  $\sim 22\,000$  readout channels of scintillating tiles coupled to silicon photomultipliers (SiPMs). During extensive beam test campaigns at the SPS CERN in 2018, the prototype has been successfully operated in muon, electron and pion beams proving feasibility of the technology and scalability to a collider detector.

The first part of this thesis focuses on the characterisation and calibration of the AHCAL prototype. For all channels excellent signal-to-noise ratios, very good uncalibrated response uniformities and stable operation over time and for different operating modes are demonstrated.

In the second part, the Pandora particle flow algorithm (PandoraPFA) framework is applied to AHCAL prototype data and Monte Carlo simulations. On the basis of extensive studies with regard to the limiting effects of particle flow reconstruction in single and two hadron events, the reliability of performance projections for future lepton collider experiments has been further validated with realistic detector data and detailed simulations. In addition, profound understanding of the PandoraPFA sub-algorithm interplay and the impact of counteracting increased noise levels on the particle flow reconstruction performance has been gained by studying modified PandoraPFA settings and increased energy thresholds on calorimeter channel level for AHCAL prototype data and jet simulations in a potential future lepton collider experiment.



# Zusammenfassung

Das Particle Flow Rekonstruktions Konzept basiert auf einer Reihe von Mustererkennungs-Algorithmen, welche eine unerreichte Energieauflösung für Jets in zukünftigen Leptonen-Collider Experimenten in Aussicht stellt. Eine der Schlüsselvoraussetzungen für dieses Konzept ist die hoch-granulare Kalorimetrie, die es ermöglicht die Substruktur von Teilchenschauern aufzudecken. Die CALICE Kollaboration hat den hoch-granularen Analogen Hadronischen Kalorimeter (AHCAL) Prototypen entwickelt, ein Stahl-Sampling Kalorimeter mit  $\sim 22\,000$  Auslesekanälen, welche aus Szintillator Kacheln gekoppelt an Silizium-Photovervielfachern (SiPMs) bestehen. Während umfangreicher Strahlentests am SPS CERN im Jahr 2018 wurde der Prototyp erfolgreich in Myonen, Elektronen und Pionen Strahlen betrieben, was sowohl die Realisierbarkeit der Technologie als auch die Skalierbarkeit zu einem Collider Detektor zeigt.

Der erste Teil dieser Dissertation fokussiert sich auf die Charakterisierung und die Kalibrierung des AHCAL Prototypen. Für alle Auslesekanäle werden dabei ein exzellentes Signal-zu-Rauschen Verhältnis, sehr gute unkalibrierte Uniformitäten der Detektorsignale und ein stabiler Betrieb über die Zeit und in verschiedenen Betriebsmodi demonstriert.

Im zweiten Teil wird das Pandora Particle Flow Algorithmus (PandoraPFA) Framework auf AHCAL Prototyp Daten und Monte Carlo Simulationen angewandt. Auf Basis von ausgiebigen Studien hinsichtlich der limitierenden Effekte der Particle Flow Rekonstruktion in Einzel- und Zwei-Hadronen Events wurde die Zuverlässigkeit der projizierten Leistungen für zukünftige Leptonen-Collider Experimente mit realistischen Detektordaten und detaillierten Simulationen in einem weiteren Schritt bestätigt. Zusätzlich wurde ein tiefgründiges Verständnis über das Wechselspiel der Teil-Algorithmen in PandoraPFA und die Auswirkung eines Entgegenwirkens von erhöhtem Rausch Niveau auf die Particle Flow Rekonstruktions Leistung gewonnen, in dem modifizierte PandoraPFA Einstellungen und erhöhte Energieschranken auf Kalorimeter Kanal Ebene für die AHCAL Prototyp Daten und Jet Simulationen in einem potentiellen zukünftigen Leptonen-Collider Experiment studiert wurden.

# Contents

<b>Abstract</b> . . . . .	i
<b>Zusammenfassung</b> . . . . .	iii
<b>Contents</b> . . . . .	iv
<b>1 Introduction</b> . . . . .	1
<b>2 Theoretical Backgrounds</b> . . . . .	5
2.1 The Standard Model of Particle Physics . . . . .	5
2.1.1 Fermions . . . . .	5
2.1.2 Fundamental Forces and Mediator Gauge Bosons . . . . .	7
2.1.3 Higgs Boson . . . . .	7
2.2 Open Questions and Physics Beyond the Standard Model . . . . .	8
2.3 Experimentally Probing the Standard Model . . . . .	9
<b>3 Prospects for Future <math>e^+e^-</math> Collider Experiments</b> . . . . .	11
3.1 Motivation and Physics Program . . . . .	12
3.1.1 Exploiting the Higgs Sector . . . . .	13
3.1.2 Electroweak Precision Measurements . . . . .	18
3.1.3 Top Quark Measurements . . . . .	18
3.1.4 Direct Beyond SM Searches . . . . .	18
3.2 The International Linear Collider . . . . .	19
3.2.1 Overview and Status . . . . .	19
3.2.2 Detector Systems . . . . .	20
3.2.2.1 International Large Detector . . . . .	21
3.2.2.2 Silicon Detector . . . . .	22
3.3 Compact Linear Collider . . . . .	23
<b>4 Basics of Calorimetry and Particle Flow Reconstruction</b> . . . . .	25
4.1 Interactions of Particles with Matter . . . . .	25
4.1.1 Electromagnetic Cascades . . . . .	26
4.1.2 Heavy Charged Particles . . . . .	28
4.1.3 Hadronic Cascades . . . . .	29
4.2 Modelling of Particle Showers . . . . .	31
4.2.1 Electromagnetic Shower Models . . . . .	31
4.2.2 Hadronic Shower Models . . . . .	32

4.2.3 GEANT4 Physics Lists	34
4.3 Calorimeters	35
4.3.1 Basic Concepts	35
4.3.2 Energy Resolution	36
4.3.3 Hadronic Response Compensation	37
4.4 Particle Flow Reconstruction	38
4.4.1 Basic Concept	38
4.4.2 Limitations	39
4.4.3 PandoraPFA	41
4.4.3.1 Algorithm Overview	41
4.4.3.2 Implementation	44
4.4.4 Requirements for a Particle Flow Detector System	44
4.4.5 PandoraPFA Jet Energy Resolution for ILD Simulations	45
4.5 The CALICE Collaboration and Highly Granular Calorimeters	46
4.5.1 Electromagnetic Calorimeters	46
4.5.2 Hadronic Calorimeters	47
<b>5 The CALICE Analog Hadron Calorimeter Prototype</b>	49
5.1 The SiPM-on-Tile Concept	49
5.1.1 Silicon Photomultipliers	50
5.1.2 Scintillator Tiles	53
5.2 The SPIROC2E Read-Out Chip	54
5.3 The Hadron Calorimeter Base Unit	56
5.4 Prototype Commissioning and Test Beam Campaigns 2018	58
5.5 Prototype Calibration, Uniformity and Stability Studies	62
5.5.1 Pedestal	62
5.5.2 MIP Constants	66
5.5.3 Gain Constants	71
5.5.4 Light Yield	73
5.5.5 High Gain - Low Gain Intercalibration	74
5.5.6 SiPM Saturation	77
5.5.7 Hit Time Calibration	78
5.6 Summary	79
<b>6 AHCAL Prototype Event Simulation and Software Tools</b>	81
6.1 Software Frameworks	81
6.1.1 iLCSoft	81
6.1.2 CALICEsoft	82
6.2 AHCAL Prototype Event Simulation	82
6.2.1 Geometry Implementation and Interaction Simulation	82
6.2.2 Digitisation Chain and Reconstruction	84
6.3 Central Software Tools	85
6.3.1 Hadronic Shower Start Finding Algorithm	86
6.3.1.1 Basic Concept	86
6.3.1.2 Threshold Optimisation	87
6.3.1.3 Validation and Results	90
6.3.2 Pseudo-Neutral Hadron Generation Algorithm	93

6.3.3 Event Overlay Algorithm	95
6.3.4 Particle Identification	98
<b>7 AHCAL Prototype Performance and Simulation Validation</b>	101
7.1 Beam Positions and Profiles	101
7.2 Energy Response	102
7.2.1 Muons	102
7.2.2 Electrons	103
7.2.3 Charged Pions	104
<b>8 PandoraPFA Studies with AHCAL Prototype Data</b>	107
8.1 Event Preparation, Selection and Sample Overview	108
8.1.1 Track Implementation and Quality Validation	108
8.1.2 Basic Event Selection	113
8.1.3 Generation and Classification of Two Particle Event Samples	114
8.1.4 Sample Overview and Quality Validation	114
8.1.4.1 Single Particle Events	114
8.1.4.2 Two Particle Events	115
8.2 Adaptations of PandoraPFA Framework for AHCAL Prototype Study	116
8.2.1 DDMarlinPandora Interface Processor	117
8.2.2 Detector Geometry and Material Description	118
8.2.3 MIP to GeV Calibration	118
8.2.4 Internal PandoraPFA Energy Scale Calibration	119
8.2.5 PandoraPFA Algorithms	120
8.2.5.1 PandoraPFA Visual Monitoring	120
8.2.5.2 Track to Cluster Association Algorithm	121
8.2.5.3 Track Driven Merging Algorithm	122
8.2.5.4 Impact of Outer Sampling Layer Definition on Re-clustering Algorithms	123
8.2.5.5 Isolated Hit Merging Algorithm	124
8.2.6 PFO Analysis Chain	125
8.3 Reconstruction of Single Particle Events	125
8.3.1 Reconstructed Event Classes	126
8.3.2 Confusion for Different Particle Energies	128
8.3.2.1 Neutral PFO Multiplicity and Energy	129
8.3.2.2 Charged Hit Clustering Efficiency	130
8.3.3 Total Energy Reconstruction Performance	131
8.3.4 Impact of Shower Leakage	133
8.4 Reconstruction of Two Particle Events	134
8.4.1 Reconstructed Event Classes	135
8.4.2 Pseudo-Neutral Hadron Energy Recovery for Different Shower Distances and Energies	137
8.4.2.1 Comparison to Previous Studies	140
8.4.3 Confusion for Different Shower Distances and Energies	142
8.4.3.1 Energy Reconstruction Efficiency and Purity	142
8.4.3.2 Confusion Level and Type Balance	144
8.4.4 Total Energy Reconstruction Performance	146
8.4.5 Impact of Longitudinal Shower Separation	148

<b>9 Studies of Different PandoraPFA Settings and Hit Energy Thresholds</b> . . . . .	151
9.1 ILD Di-Jet Samples . . . . .	152
9.1.1 Simulation, Reconstruction and Event Selection . . . . .	152
9.1.2 Performance Validation for Default PandoraPFA Settings . . . . .	153
9.2 Confusion Sensitive Algorithms and Parameters . . . . .	154
9.2.1 Impact on Level of Confusion . . . . .	155
9.2.2 Impact on Jet Energy Linearity and Resolution . . . . .	157
9.2.3 Comparison to AHCAL Prototype Data . . . . .	158
9.2.4 Conclusions . . . . .	159
9.3 Hit Energy Thresholds . . . . .	159
9.3.1 PandoraPFA Re-Calibration . . . . .	161
9.3.2 Impact on Level of Confusion . . . . .	162
9.3.3 Impact on Jet Energy Linearity and Resolution . . . . .	164
9.3.4 Comparison to AHCAL Prototype Data . . . . .	165
9.3.5 Conclusions . . . . .	168
<b>10 Summary, Conclusions and Outlook</b> . . . . .	169
10.1 Summary and Conclusions . . . . .	169
10.2 Outlook . . . . .	171
<b>A Additional Plots: AHCAL Prototype Calibration</b> . . . . .	173
<b>B Additional Plots: Simulation and Algorithm Validation</b> . . . . .	175
<b>C Sample Overview and Quality Validation for PandoraPFA Studies with AHCAL   Prototype Data</b> . . . . .	177
<b>D Additional Plots: Two Particle PandoraPFA Studies with AHCAL Prototype Data</b> . . . . .	197
<b>E Additional Plots and Tables: Studies of Different PandoraPFA Settings and Hit   Energy Thresholds</b> . . . . .	209
<b>Bibliography</b> . . . . .	213
<b>List of Figures</b> . . . . .	225
<b>List of Tables</b> . . . . .	230
<b>Acknowledgements</b> . . . . .	231



# 1 Introduction

The Standard Model of particle physics is widely considered as the most accurate theory, precisely describing the fundamental particles and forces of nature. In the year of 2012, it was completed by the discovery of a Higgs Boson within the independent experiments ATLAS and CMS at the Large Hadron Collider (LHC) at CERN, which collides protons with a center-of-mass energy of up to  $\sqrt{s} = 14 \text{ TeV}$ . This discovery marked a milestone in the research of particle physics and far beyond. However, based on experimental and cosmological observations many unanswered questions remain, which hint towards physics beyond the Standard Model.

Different approaches are pursued by the particle physics community to answer these open questions. At the energy frontier, the collisions and measurements at the LHC are pushed further to higher energies and luminosities with the planned concept of the High-Luminosity LHC (HL-LHC). A complementary approach, with respect to the achievable precision and discovery reach, is a future lepton collider facility like the International Linear Collider (ILC) or the Compact Linear Collider (CLIC). Such experiments would further push the precision frontier by colliding electron and positron beams with energies in the range of 250 GeV up to a few TeV in well controlled and clean environments in contrast to hadron collisions. To achieve the desired precision for testing the Standard Model, stringent requirements are set for the detector systems. One of those requirements is an unprecedented jet energy resolution of 3 – 4% for jet energies 40 – 250 GeV. Due to the intrinsically limited energy resolution of the hadronic calorimeter, this requirement can not be fulfilled with the conventional approach to calorimetry in which all calorimeter energy depositions in an event are simply summed up. Thus, it is planned to be achieved by utilising calorimeters optimised for the concept of particle flow reconstruction. Dedicated pattern recognition particle flow algorithms aim to reconstruct each individual particle in a jet and use the energy measure of the sub-detector providing best resolution. This allows to exploit the preciser momentum measurement of the tracker for all charged particles in a jet, specifically omitting the energy measure of the hadronic calorimeter for all charged hadrons. To facilitate this approach, a tracking system with an excellent momentum resolution and highly granular calorimeter systems instrumented within the magnetic coil of the experiment are required, which provide the environment to sufficiently separate showers initiated by charged and neutral particles. Various simulation studies have shown that the desired jet energy resolution achievable with particle flow reconstruction in such experiments is in reach. However, the projected performance is highly dependent on the accuracy of the simulated shower sub-structure details, which are revealed by the highly granular calorimeters and exploited within the pattern recognition algorithms of the particle flow reconstruction.

This thesis focuses on the commissioning, calibration and performance of one of these highly granular calorimeter systems, which has been developed by the CALICE collaboration: the Analog Hadron Calorimeter (AHCAL) prototype. Based on scintillator tiles coupled to silicon photomultipliers (SiPMs), this  $\sim 22\,000$  channel steel sampling calorimeter was successfully commissioned

and operated in muon, electron and pion beams at the SPS CERN in 2018. The excellent results achieved during the calibration, characterisation and response investigation enable the possibility of higher level analyses based on this prototype data and corresponding simulations.

One goal of this work is to further validate the reliability of the particle flow performance projections for a future lepton collider experiment using AHCAL prototype data and simulations. For this reason, the Pandora particle flow algorithm (PandoraPFA) is applied for the first time to beam test data and simulated events of a standalone calorimeter scenario in the form of the AHCAL prototype. Limiting effects of the particle flow reconstruction and their impact on the total reconstruction performance are investigated in detail for different event scenarios, mimicking typical jet environments, and compared between data and simulation. Furthermore, the goal of this work is to get a profound understanding of the sub-algorithms interplay in PandoraPFA and their connection to specific limiting effects. By modifying internal settings of PandoraPFA, the impact on these limiting effects and the total reconstruction performance is studied for AHCAL prototype data as well as simulated jets in a potential future lepton collider experiment. Lastly, the projected particle flow performance in an experimental environment facing increased noise levels and consequently a loss of effective shower sub-structure information in the calorimeter systems is studied in the scope of this thesis.

## Thesis Outline

In Chapter 2 of this thesis, an overview about the Standard Model of particle physics is provided, open questions are discussed and the concepts of ongoing and future experiments are presented. The motivation and prospects for a future lepton collider experiment are summarised in Chapter 3 with the focus set on two potential experiments in the form of the International Linear Collider (ILC) and the Compact Linear Collider (CLIC). Chapter 4 describes the central concepts on which the studies in this thesis are based on: the physics of the interactions within particle showers, the particle flow concept with PandoraPFA as the state of the art algorithm and the advantages of highly granular calorimetry. The highly granular AHCAL prototype is introduced in detail in Chapter 5 including its individual hardware components, a summary of the commissioning and beam test campaigns and a detailed description of extensive calibration and characterisation studies. The Monte Carlo simulation of AHCAL prototype events and developed central software tools, used for the analyses in this thesis, are presented and evaluated in Chapter 6. The energy response performance of the prototype to muons, electrons and pions is evaluated for recorded beam test data and compared to simulations in Chapter 7. Chapter 8 and 9 represent the central analysis part of this thesis. In the first part, the application of PandoraPFA to AHCAL prototype data and simulation is discussed from a technical point of view and the preparation and selection of dedicated events is explained and evaluated. In the second part, the particle flow reconstruction performance of single and two particle events is studied in detail with respect to the limiting effects for different energy and shower distance scenarios. In the last part, the impact of modified PandoraPFA settings and hit energy thresholds on the particle flow reconstruction performance is studied for simulated ILD jets and AHCAL prototype data. Lastly, Chapter 10 concludes the thesis and provides an outlook.

---

## Contributions from the Author and Thesis Related Publications

The AHCAL prototype has been designed and developed in a collaborative effort by the CALICE collaboration. The author was not involved in the design, development, assembly and quality insurance phase of the individual hardware components. During the mechanical integration, cosmic tests and beam test campaigns of the prototype at DESY and SPS CERN, the author played a significant role in the prototype commissioning, online and offline data quality monitoring and in-situ calibration. The automated calibration routines for the pedestal and MIP constants have been developed by the author and the extracted calibration constants and stability information have been provided for collaboration-wide physics analyses of the prototype data. In addition, various quality checks for the channel-wise light yield and high gain low gain intercalibration constants was performed by the author. The general prototype design, construction and commissioning is summarised in [1], further calibration results can be found in different PhD theses [2-4].

The software frameworks utilised within this thesis have been developed by CALICE and the linear collider community. The author has been part of a task force to implement and optimise the geometrical implementation and the digitisation chain for the latest prototype simulation. Furthermore, the author developed and validated the central software tools required for the particle flow studies and implemented those into the common software framework, except for the multi-variate PID [5]. The development of the hadronic shower start finding algorithm was done in close collaboration with a supervised Bachelor student [6].

With respect to the performance validation of the AHCAL prototype, the author contributed to the evaluation of the MIP response in strong collaboration with a Master student partly publishing the results in [7]. The electron and pion response studies are part of other PhD theses [3, 2].

The calibration and analysis of the delay wire chamber data was not performed by the author, but a colleague whose results are not published but can be found in several talks [8, 9]. In strong collaboration with this colleague, the track implementation in PandoraPFA and the event overlay algorithm were developed. All other algorithms and simulation efforts with respect to the sample generation, preparation and selection were developed and performed by the author. In addition, the author adapted and technically validated the full PandoraPFA interface and analysis framework for the application on AHCAL prototype data and simulations. Regular meetings and discussions with the PandoraPFA developers laid the foundation for these implementations. For the studies of ILD jets, the author has used pre-existing simulation samples and analysis frameworks of the linear collider community.



# 2 Theoretical Backgrounds

Since thousands of years, mankind has tried to reveal the secrets of nature and explain its fundamental processes. Natural science has developed out of this effort covering a broad spectrum of different areas. As the most fundamental one, physics itself covers a vast field of different research areas. Among those, particle physics aims to understand the properties and interactions of the fundamental constituents of our universe: elementary particles. Since the impetus by the discovery of the atomic sub-structure in scattering experiments by Geiger and Marsden in 1909 [10], a common theory has been developed during the 20th century that covers the elementary particles and the fundamental forces of nature and has withstood many experimental tests: the Standard Model of particle physics.

This chapter provides the theoretical background and the motivation for the investigation of the physics processes described in the scope of this thesis. In Section 2.1 a brief overview about the Standard Model of particle physics is given. Subsequently, a selection of shortcomings, which indicate physics beyond Standard Model, are shortly discussed in Section 2.2. Lastly, in Section 2.3 general experimental concepts for probing the Standard Model and searching for physics beyond are introduced.

## 2.1 The Standard Model of Particle Physics

The Standard Model of particle physics (SM) is widely considered the most successful theory of modern particle physics, experimentally tested to a large extent and able to provide precise predictions of physics processes. It classifies all known elementary particles and describes their respective interactions in the framework of a constituent quantum field theory (QFT). The postulation of the SM has its origin in the 1960's during the efforts to unify the electromagnetic and weak interaction [11-14] and evolved in the following decades [15], in which many of its predictions could be verified in various experiments, to its current formulation. With the discovery of a Higgs Boson in 2012, by the ATLAS and CMS experiments at the Large Hadron Collider (LHC) at CERN [16, 17], experiments have observed all elementary particles of the SM. Figure 2.1 presents an overview of the SM content. In total the SM consists of 17 fundamental particles, which can be divided into twelve spin-1/2 fermions, four spin-1 gauge bosons and one spin-0 scalar Higgs Boson. The individual types of particles are further discussed in the next sections.

### 2.1.1 Fermions

The fermions are further sub-classified into further categories (top to bottom in Figure 2.1): up-type quarks, down-type quarks, charged leptons and neutrinos. Each fermion-category contains

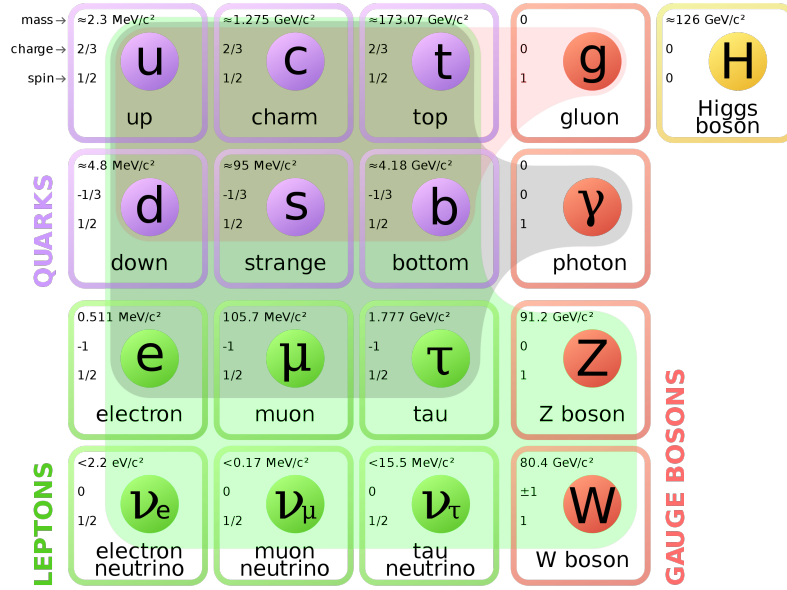


Figure 2.1: The Standard Model elementary particles with denoted mass, charge and spin. Coloured areas are indicating which gauge boson couples to which fermion. The Higgs Boson is necessary to give masses to fermions and gauge bosons. Taken from [18].

three generations (left to right in Figure 2.1). With the potential exception of neutrinos, the mass increases with the generation. Each fermion particle there exists an anti-particle with opposite-sign quantum numbers and otherwise identical properties. The opposite-sign quantum numbers allow a particle to annihilate with its antiparticle when they come into contact.

The quarks are categorised into up-like quarks (up, charm, top) with an electric charge of  $\pm 2/3$  and down-like quarks (down, strange, bottom) with electric charge of  $\mp 1/3$ . Next to the electric charge, quarks feature a so-called colour charge. Up to now, no isolated quarks but only colour-neutral multi-quark bound states have been observed in nature in the form of hadrons. Those states can be further subdivided into mesons, quark-antiquark pairs of opposing colour charge, and baryons, neutral net colour charge bound states of three quarks. All observed mesons and baryons are unstable with the exception of the proton, consisting of two up and one down quarks (uud). The neutron, consisting of one up and two down quarks (udd), can also be stable when it is bound with protons in a nucleus.

Each of the three generations features a charged lepton and a corresponding neutral neutrino. The charged leptons are the electron ( $e$ ), muon ( $\mu$ ), and tau ( $\tau$ ) and have an electric charge of  $\pm 1$ . The neutrinos ( $\nu_e, \nu_\mu, \nu_\tau$ ) are electrically neutral and nearly massless. Out of those, only the electron and the neutrinos are stable particles. Muons and taus have an average lifetime of  $\sim 2.2 \times 10^{-6} \text{ s}$  and  $\sim 290 \times 10^{-15} \text{ s}$ , respectively.

To sum up, the matter around us only consist of protons, neutrons and electrons. Fermions of the two higher generations are only accessible by their generation in high energy particle collisions before they do decay into fermions of the first generation again via different channels and with different lifetimes. Exceptions are the neutrinos constantly traversing us with basically no interaction and cosmic muons, produced in interactions of cosmic rays with nuclei of the earths' atmosphere.

### 2.1.2 Fundamental Forces and Mediator Gauge Bosons

The SM includes three out of the four fundamental forces describing the interactions between particles: electromagnetism, the weak and the strong force. Since no description of gravity in form of a consistent QFT has been achieved yet and gravity is considered as negligible on the sub-atomic particle scales, it is not included in the SM. The remaining forces are described to be mediated by gauge bosons within the SM.

Photons ( $\gamma$ ) are the mediators of the electromagnetic force and are exchanged between all electrically charged particles. Since they are massless and uncharged, the force has an infinite reach with the Coloumb potential decaying with the radius like  $1/r$ .

Massive gauge bosons,  $W^\pm$  ( $\sim 80.4$  GeV) and  $Z^0$  ( $\sim 91.2$  GeV), are mediating the weak nuclear force. All fermions are involved in the weak interaction, with a special emphasis on the neutrinos as the only particles, which can only interact weakly. Due to the high mass of the gauge bosons, the effective range of the weak interaction is limited to  $\sim 10^{-17}$  m, based on the respective Yukawa potential [19, 20].

Lastly, massless gluons are the carriers of the strong force and couple to color charge. Only quarks and the gluons themselves carry color charge. Because they are charged themselves, gluons are self-interacting [21]. The gluon self-interaction leads to a potential between the quarks in a bound quark pair that linearly increases with their distance. This effectively limits the reach of the strong force because if the distance between two bound particles increases too much it exceeds the pair production threshold for a new quark-antiquark pair, at which point the original pair decouples into two new pairs. This process becomes important for the quark pair production in high energy particle collisions. Such quark pairs radiate gluons which decay into new quark pairs, creating a shower of quarks. In accordance with color confinement, these quarks then form a cascade of color-neutral hadrons<sup>1</sup> in the following referred to as a jet [22]. This process is called hadronisation and typically splits up the initial quark momentum in a cascade producing a mix of final state hadrons, which is in the following referred to as jet. Thus, to reconstruct the momentum and energy of the original quark, the reconstruction of the distinctive jet particles is required.

### 2.1.3 Higgs Boson

The Higgs mechanism is introduced to explain the mass of the weak gauge bosons  $W^\pm$  and  $Z$ , and respectively for the electrically charged fermions via Yukawa couplings [23]. It causes spontaneous electroweak symmetry breaking while the local gauge symmetry is conserved, which creates the symmetry-breaking mass terms. This mechanism postulates a self-interacting complex scalar field, the Higgs field, which couples with non-zero vacuum expectation value  $\nu$  [24–26]. In this context, the coupling  $g_{HXX}$  of the Higgs field to a given fermion  $X$  is proportional to the fermions mass  $m_X$ :

$$g_{hXX} = \frac{m_X}{\nu} \quad (2.1)$$

As the basic excitation of the Higgs field, the postulated SM Higgs Boson (H) manifests in form of a scalar particle with spin 0 and a measured mass of around  $m_H = 125.2$  GeV [16, 17]. In the SM, the Higgs Boson couples to all massive particles. It can decay into all massive SM particles, except the top quark, with a fractional decay width proportional to the squared coupling of the Higgs to the respective particle. The Higgs mass, decay width and the individual couplings to different particles are important parameters to be measured with high precision in order to validate the SM.

<sup>1</sup>This process is often referred to as hadronisation.

Slight deviations from the SM predicted values could indicate, that the observed boson is not the postulated SM Higgs Boson and hint towards new physics. Therefore, precision measurements of the Higgs Boson properties are considered as one of the most sensitive windows to physics beyond standard model.

## 2.2 Open Questions and Physics Beyond the Standard Model

Over the last decades, the SM has proven to succeed in describing many physics processes and experimental results. Different experiments have measured the 19 free parameters of the SM with different levels of precision. New physics might hide under the less precisely measured parameters, as a more precise determination could uncover inconsistencies. These investigations are considered crucial, since up to this day there are many open questions, which can not be explained by the SM and might imply that it is only a low energy approximation of a superior theory. A brief overview of selected open questions based on experimental observations is presented in the following.

### Dark Matter

Many astrophysical and cosmological observations, like the rotational velocity curves of galaxies [27] or the anisotropy of the cosmic microwave background (CMB) [28], provide evidence for additional invisible matter next to the visible matter content making up only 4% of our universe. This invisible matter, termed Dark Matter, has not been observed directly in any experiment yet. In many theoretical models it is supposed to interact via the weak force only. Physics beyond the SM is required to explain the indirect observations and the nature of Dark Matter.

### Neutrino Masses

The SM postulates massless neutrinos, since the exclusively existing left-handed neutrinos do not acquire mass through Yukawa coupling. In contrast to this prediction by the SM, different neutrino experiments have observed oscillations between the neutrino flavour eigenstates [29]. This implies, that neutrinos have mass eigenstates resulting in non-zero masses. Currently only upper limits on the neutrino masses in the order of  $10^{-1}$  eV can be set by different experiments. The mechanism behind the neutrino mass generation is still unknown and hints to physics beyond SM.

### Matter-Antimatter Asymmetry

According to the SM, matter and anti-matter should be equally produced at the beginning of the universe and still be equally existent to this date. However, it is widely observed that our universe is composed mostly of matter (baryons). This baryon asymmetry is not explained by the SM. Observed CP violation for weak interactions in the quark sector, which is part of the SM, can only explain a small fractional contribution to this asymmetry [30]. Therefore, other processes not part of the SM are required to explain the full extent of this asymmetry.

Based on these questions, numerous theoretical models have been developed over the last decades trying to address these questions by extending the SM. One of these approaches is Supersymmetry (SUSY), adding an additional symmetry to the system by introducing a boson super-partner to each SM fermion and vice versa.

## 2.3 Experimentally Probing the Standard Model

Without experiments probing theoretical models and predictions, the open questions discussed in the previous section remain unanswered. In general, the modern particle physics community follows two basic experimental concepts: direct and indirect searches for physics beyond the standard model.

For direct searches, the energy of particle collisions is further pushed to its limits. This is done in order to directly probe unexplored phase space, in which the direct production of new particles with high masses could be achieved. Currently, one of the driving forces for direct searches is the LHC and its multi purpose detector systems analysing proton-proton collision data of up to 14 TeV. However, especially with respect to the planned high luminosity upgrade of the LHC (HL-LHC) and the corresponding detector systems [31], data from these experiments are as well utilised for the second approach.

Within indirect searches the main focus lies on extensively and precisely probing the SM parameters and predictions. Small deviations from the predictions, due to higher order loop corrections including contributions by new physics, or the observation of decays forbidden by the SM could indirectly indicate physics beyond the SM. Indirect searches are typically performed with highly specialised detector systems often optimised to find signatures of single new physics processes with very high mass scale reaches or with high precision collider experiments pushing luminosity to its limit and utilising novel reconstruction techniques for the data recorded with multi-purpose detector systems.

A future lepton collider experiment could potentially combine both approaches to an even larger extent. On the one hand, high precision measurements of SM properties like the Higgs coupling constants, Higgs decay width or the electroweak sector could potentially uncover deviations from SM predictions. On the other hand, depending on the exact energy reach of the collider, phase space still unexplored by the LHC, due to the different type of particle collision, could be scanned for direct new particle searches. Physics prospects and potential candidates for such experiments are discussed in the following chapter.



# 3 Prospects for Future $e^+e^-$ Collider Experiments

Despite being the most successful theory to describe physics processes up to the TeV energy scale, the SM is not able to answer all open questions, as discussed in Chapter 2. Therefore, more theoretical and experimental efforts are required to understand all phenomena observed in our universe.

Currently, the Large Hadron Collider (LHC) at CERN is the pioneer machine in experimental particle physics and the only high energy hadron collider in operation. With a circumference of 27 km, it collides protons with a center-of-mass energy of up to  $\sqrt{s} = 14$  TeV [32]. With these unprecedented energies, one of the milestones achieved by the LHC was the discovery of the Higgs Bosons in 2012 as the last missing particle in the SM. Since that, the LHC continues to probe the SM at the energy frontier and searches for physics signatures beyond SM. This effort is reflected in the various upgrade campaigns for the LHC and its employed detector systems, like the luminosity upgrade towards the High Luminosity Large Hadron Collider (HL-LHC) [31] for improved and continuous operation over the next decades.

However, a hadron collider like the LHC suffers from specific limitations given by the nature of the colliding particles and the complexity of the collision environment limiting not only the measurement precision of SM parameters, but also the reach for searches beyond the SM. By colliding leptons instead of hadrons most of these limitations can be overcome, potentially opening up a window to observe new physics beyond the SM. Over the last decades, several concepts for future lepton colliders have been developed, which can be categorised in linear and circular collider options. The proposed physics prospects of such experiments are mostly complementary to the physics program of the LHC (and HL-LHC). While the LHC is still mainly pushing towards the energy frontier, a future lepton collider is mainly designed to perform precision measurements and therefore further pushing the precision frontier.

This chapter summarises the physics prospects of a potential future lepton collider experiment with the focus on the linear option. In Section 3.1 the benefits of a lepton in contrast to a hadron collider are generally discussed and details of the explicit physics program and physics reach are briefly summarised. After that, in Section 3.2 the International Linear Collider (ILC), as the most mature concept for a linear  $e^+e^-$  collider experiment, is introduced in more detail including proposed detector concepts. Lastly, Section 3.3 provides a brief overview about the Compact Linear Collider (CLIC) as an alternative experimental concept.

### 3.1 Motivation and Physics Program

A future lepton collider experiment is motivated by several key aspects mainly based on overcoming the limitations a hadron collider faces. First of all, leptons are elementary and non-composite particles. In contrast to colliding hadrons, which allow only an unknown fraction of their center-of-mass energy to be available in the actual collision process due to their composite nature, the initial states (four-momenta) of the colliding leptons are well defined and known. This allows for equal center-of-mass energies in each individual lepton collision. In addition, the spin orientation of the leptons can be changed and controlled via beam polarisation in order to enhance specific production cross-sections for example. Furthermore, the typically large QCD SM and pile-up background within hadron collisions is reduced within lepton collisions, providing a much cleaner collision environment and therefore allowing highly precise measurements.

In general, there are two main concepts for high energy particle colliders with specific benefits and limitations: circular and linear. Circular particle colliders (synchrotrons) benefit from being able to use the accelerating structures multiple times by many circulations of the particles in the ring and achieve increased collisions rates since non-interacting particles can be recycled again for further collision processes. The largest drawback of a circular collider, however, is the emission of synchrotron radiation arising if the charged particles are bent in the magnetic field to be kept on the circular trajectory. The energy loss per cycle  $\Delta E$  scales with:

$$\Delta E \sim \frac{E^4}{m^4 R} \quad (3.1)$$

where  $E$  is the energy of the charged particle,  $m$  its mass and  $R$  the radius of the synchrotron ring. This shows, that especially circular  $e^+e^-$  colliders are limited in achieving highest energies by synchrotron radiation energy losses due to the low mass of the electrons and positrons. The largest and most powerful  $e^+e^-$  collider built to this day is the Large Electron-Positron Collider (LEP) at CERN operated in the same tunnel as the LHC nowadays [33]. From 1989 to 2000 it collided  $e^+e^-$  beams with a center-of-mass energy up to 209 GeV. Higher beam energies excessively suffered from synchrotron radiation losses due to the limited tunnel radius of roughly 4.25 km. However, proposed future circular lepton colliders are aiming for higher energies by significantly increasing the synchrotron radius like the Future Circular Collider (FCC) [34] or the Circular Electron Positron Collider (CEPC) [35] with radii of  $\sim 15.8$  km,  $\sim 8.6$  km respectively.

In contrast to circular colliders, linear colliders do not suffer from the limitation of synchrotron radiation. However, one limitation of linear colliders is that the non-interacting particles can not be reused. The accelerating mechanism can only be traversed once and after passing the collision region all remaining particles are dumped. Therefore, a long acceleration path, high acceleration gradients and optimised final focusing schemes are required to reach highest particle energies and collision rates. Due to the limitation of synchrotron radiation for electrons in circular option and the well advanced acceleration gradients achieved over the last years, the linear option is widely considered as the most promising candidate for a future lepton collider. Therefore, in the scope of this thesis, the focus is set on two proposed linear lepton collider options: the International Linear Collider (ILC) and the Compact Linear Collider (CLIC).

Extensive physics programs for future lepton colliders have been developed over the last 20 years across the various proposed experiments. These programs mainly focus on high precision measurements of the Higgs Boson properties, the electroweak sector and the top quark properties, but also include direct searches and exclusion studies of signatures beyond the SM. In the following sections a brief overview is provided.

### 3.1.1 Exploiting the Higgs Sector

With the discovery of the Higgs Boson at the LHC in 2012 and the measurement of its mass, the SM of particle physics is considered as completed. However, many questions about the nature of the Higgs Boson remain, like the reason for the electroweak symmetry breaking, if it is a scalar or composite particle or if the coupling to other particles and itself behaves as the SM predicts. Therefore, any measured deviation from the SM Higgs parameters could indicate the existence of physics beyond the SM. Many beyond SM models predict deviations from the SM Higgs parameters to be at the level of 5% or less, making high precision measurements of the Higgs properties the most attractive physics program for many high energy physics experiments. In the hadron environment of the LHC, however, the level of precision is limited and the desired precision goal of  $\sim 1\%$  with respect to the predicted SM Higgs parameters are a difficult challenge. In the clean and well controlled environment of a future lepton collider, unprecedented and model independent precision measurements of Higgs Boson parameters such as its production cross-sections, branching ratios, mass and consequently its couplings to other particles can be performed.

#### Higgs Production

The two dominant production modes of the Higgs Boson at a future lepton collider are Higgsstrahlung and vector boson fusion (VBF). In the Higgsstrahlung process the Higgs Boson is produced in association with a  $Z$  boson ( $e^+e^- \rightarrow HZ$ ). For the VBF production mode either two  $W$  bosons fuse into a Higgs Boson leading to associated production of two electron neutrinos ( $e^+e^- \rightarrow H\nu_e\bar{\nu}_e$ ), or by the fusion of two  $Z$  bosons into a Higgs Boson to a production of an electron and positron ( $e^+e^- \rightarrow He^+e^-$ ). Corresponding Feynman diagrams of these production channels are illustrated in Figure 3.1a.

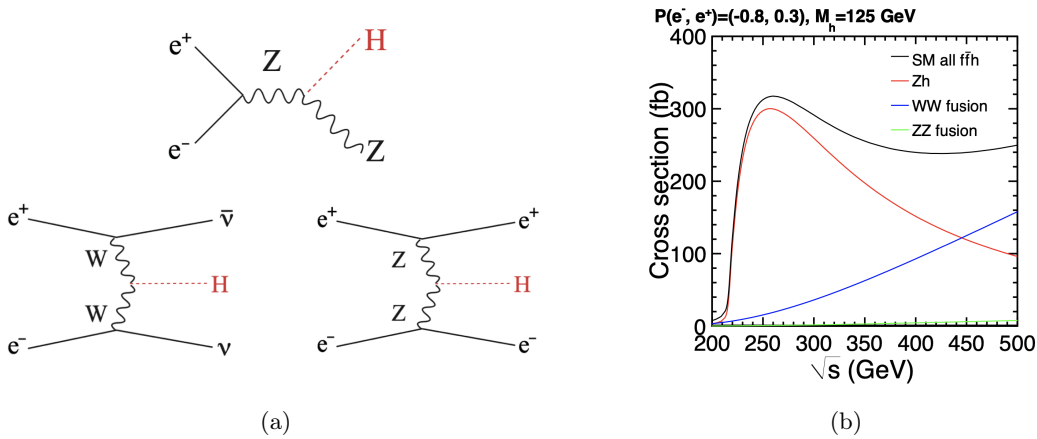


Figure 3.1: Higgs Boson production at a future  $e^+e^-$  collider: (a) Tree-level Feynman diagrams. (b) Corresponding simulated cross-sections for polarised lepton beams at the ILC [36].

With respect to the center-of-mass energy of the colliding electrons and positrons, the Higgs production cross-sections for these processes are depicted in Figure 3.1b. Peaking around 250 GeV, the Higgsstrahlung production cross-section is dominant in the lower energy regime. The production cross-section for  $WW$  fusion slowly increases from 200 GeV onwards and becomes dominant only at center-of-mass energies higher than 450 GeV. The cross-section of  $ZZ$  fusion Higgs production

is a factor  $\sim 30$  smaller than for the  $WW$  fusion. Since  $WW$  fusion only occurs in collisions with left-handed electrons and right-handed positrons, specific beam polarisation configurations can increase the cross-section of this production mode.

### Higgs Branching Ratios

The decay modes of the SM Higgs Boson are depicted in Figure 3.2 by the respective branching ratios (BR) as a function of the Higgs Boson mass  $M_H$ . Primarily it decays into a pair of bottom quarks (BR:  $\sim 60\%$ ). While this channel is difficult to access at a hadron collider like the LHC due to the presence of large QCD backgrounds, a future lepton collider provides better accessibility. With a BR of  $\sim 20\%$ , the next likely decay of the Higgs Boson is into a pair of  $W$  bosons, followed by a pair of gluons, tau leptons and  $c$  quarks. For two of the main discovery channels of the Higgs Bosons at the LHC<sup>1</sup>  $ZZ^*$  and  $\gamma\gamma$ , the BRs are significantly lower with  $\sim 2.6\%$ ,  $\sim 0.2\%$  respectively. For the Higgs Boson decay channels into massless particles ( $gg$  or  $\gamma\gamma$ ), the respective particles are radiated off from virtual heavy quark or charged gauge boson loops, which couple to the Higgs Boson initially.

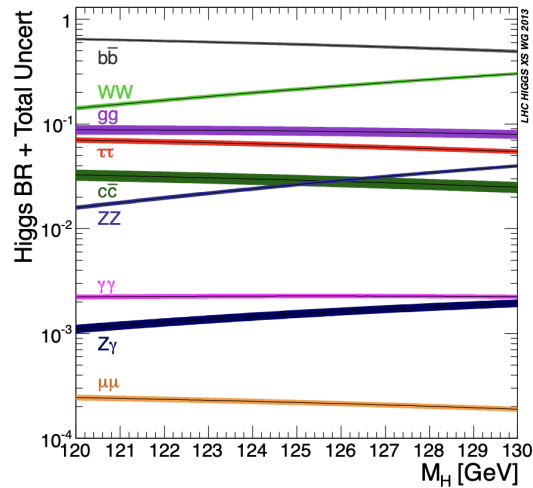


Figure 3.2: Branching ratios of the SM Higgs Boson versus Higgs Boson mass close to  $M_H = 125$  GeV. The bands indicate the total uncertainty [37].

### Higgs Recoil Measurement

The Higgsstrahlung production channel at a future lepton collider offers an unique possibility for precision measurements of the Higgs Boson properties. Since the initial states of the electron and positron (their respective four-momenta) are well defined and precisely known, one can reconstruct the four momentum of the  $Z$  boson and subsequently apply kinematic calculations to draw conclusions on the recoiling Higgs Boson without measuring its decay products. With this method, precise and model independent measurements of the Higgs Boson mass, full decay width, absolute coupling constants and branching ratios to invisible or exotic particles are accessible.

<sup>1</sup>For the  $ZZ^*$ , the Higgs was discovered in the so-called *golden channel*:  $ZZ^* \rightarrow 4l$ .

By exploiting leptonically decaying  $Z$  events<sup>2</sup> ( $Z \rightarrow e^+e^-$  and  $Z \rightarrow \mu^+\mu^-$ ), one can calculate the recoil mass  $M_{rec}$  as:

$$M_{rec}^2 = (\sqrt{s} - E_{l+l-})^2 - |\vec{p}_{l+l-}|^2 \quad (3.2)$$

with  $E_{l+l-} \equiv E_{l+} + E_{l-}$  and  $\vec{p}_{l+l-} \equiv \vec{p}_{l+} + \vec{p}_{l-}$  the measured energies and momenta of the leptonic  $Z$  decay products [38]. By monitoring the number of events in which the invariant mass of the di-lepton system is consistent with the mass of the  $Z$  boson, one can additionally determine the full model independent cross-section of the Higgsstrahlung process. A projected recoil spectrum of the decay channel  $ZH \rightarrow \mu^+\mu^-X$  for an assumed Higgs Boson mass of  $M_H = 125$  GeV based on simulations for a future lepton collider experiment is illustrated in Figure 3.3. Different studies have shown, that an absolute Higgs Boson mass resolution of better than 30 MeV and a total Higgsstrahlung cross-section uncertainty at the sub-percent level is achievable if the muon and electron decay channels of the  $Z$  boson are combined [39].

The introduced measurement technique can be extended to the hadronic decay channel of the  $Z$  boson ( $Z \rightarrow q\bar{q}$ ), resulting in two or more jets in the final state of the Higgsstrahlung channel. By doing that, one can profit from the approximately ten times higher branching ratio at  $\sqrt{s} = 350$  GeV in comparison to the leptonic decay of the  $Z$  bosons, since more processes like top quark production are kinematically accessible. However, since the Higgs Boson decays hadronically as well, one has to avoid misclassifications and ambiguities in the jet reconstruction by sophisticated event classification and fitting of signal and background templates to likelihood distributions of specific variables. Simulation studies have shown, that a measurement precision of 1.8% can be achieved for the reconstructed Higgs Boson mass and total Higgsstrahlung cross-section with  $350 \text{ fb}^{-1}$  at  $\sqrt{s} = 350$  GeV, comparable to the  $250 \text{ fb}^{-1}$  scenario at  $\sqrt{s} = 250$  GeV for the leptonic  $Z$  decay channels [40].

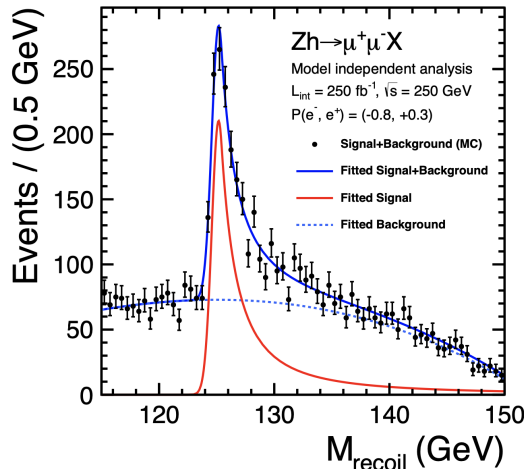


Figure 3.3: Reconstructed recoil mass distribution for the process  $e^+e^- \rightarrow ZH \rightarrow \mu\mu H$  simulated for  $M_H = 125$  GeV at  $\sqrt{s} = 125$  GeV and polarised lepton beams at the ILC [39].

<sup>2</sup>The choice of leptonic decay channels is motivated by the anticipated excellent tracking resolution at a future lepton collider experiment.

### Higgs Coupling Measurements

The measurements of the Higgs Boson coupling  $g_{HX\bar{X}}$  to SM particles  $X$  are of particular interest, since they are highly sensitive to BSM physics. Many generic beyond SM models predict deviations in the order of a few percent with respect to the values predicted by the SM [41]. At a future lepton collider experiment, model independent measurements of the Higgs Boson coupling constants can be performed by exploiting that the branching ratio of a specific decay channel  $BR(H \rightarrow X\bar{X})$  can be described by the specific partial decay width of the Higgs  $\Gamma(H \rightarrow X\bar{X})$  over the total Higgs decay width  $\Gamma_H$  via:

$$BR(H \rightarrow X\bar{X}) = \frac{\Gamma(H \rightarrow X\bar{X})}{\Gamma_H} \quad (3.3)$$

with

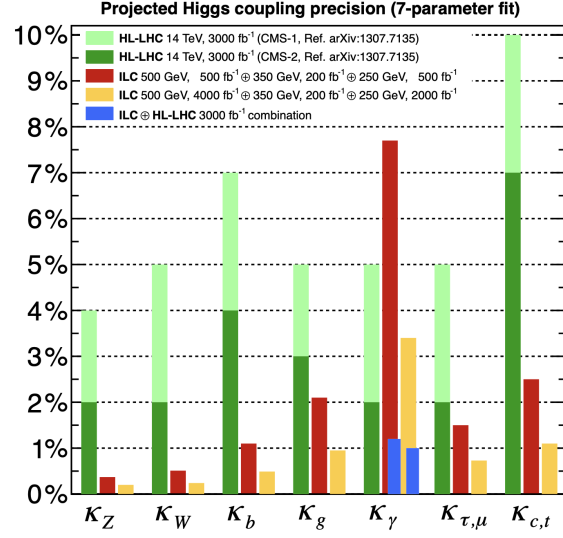
$$\Gamma(H \rightarrow X\bar{X}) \sim g_{HXX}^2 \quad (3.4)$$

Thus, to obtain the coupling constant of any given particle to the Higgs Boson, the partial decay width of the corresponding decay process can be calculated if the branching ratio is measured and the total Higgs Boson decay width is known. In order to determine the total Higgs Boson decay width, the model independent measurement of the inclusive Higgsstrahlung production cross-section  $e^+e^- \rightarrow HZ$ , and therefore  $g_{HZZ}$ , via the recoil mass measurement is utilised. In a collider experiment, one typically measures final state event rates, which correspond to the production cross-section of a process times the branching ratio into the final state. In a first step, the branching ratio  $BR(H \rightarrow b\bar{b})$  is calculated by dividing the corresponding  $b\bar{b}$  final state<sup>3</sup> event rate in Higgsstrahlung processes by the already known  $e^+e^- \rightarrow HZ$  production cross-section. Next, the total  $WW$ -fusion Higgs production cross-section, and therefore  $g_{HWW}$ , can be calculated by dividing the measured event rates of  $b\bar{b}$  final states within  $WW$ -fusion processes ( $e^+e^- \rightarrow H\nu\bar{\nu}$  with  $H \rightarrow b\bar{b}$ ) by the already determined  $BR(H \rightarrow b\bar{b})$ . Since  $g_{HWW}$  is known at this point and according to Equation 3.4 also  $\Gamma(H \rightarrow W\bar{W})$ , only  $BR(H \rightarrow W\bar{W})$  has to be measured according to Equation 3.3 to determine the total Higgs decay width  $\Gamma_H$ . This can either be done via the final state event rates in the Higgsstrahlung or  $WW$  fusion processes, since both total production cross-sections are known.

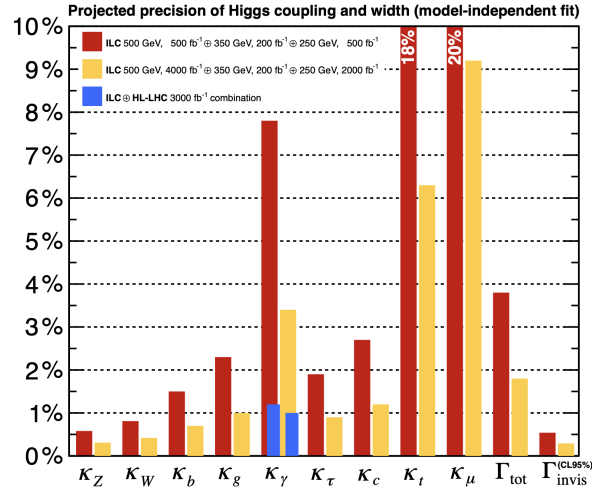
The measurement uncertainty of  $\Gamma_H$  is propagated to the total measurement uncertainty of each coupling constant. In order to improve the precision on  $\Gamma_H$ , a global fit can be applied including all measured production cross-sections times branching ratios of other available channels determined with the method described above. The projected relative precision of the coupling constant measurements with respect to the SM predicted values are presented in Figure 3.4a for a model dependent fit and in Figure 3.4b for a model-independent fit for different data sets of the ILC. One can see, that for most coupling constants the lepton collider measurements are one order of magnitude more precise than the projected precisions with the full HL-LHC data sets. The channel  $H \rightarrow \gamma\gamma$  is exempted, due to the low branching ratio of around 0.2% and background processes creating  $\gamma\gamma$  signatures in a lepton collider.

Lastly, the trilinear Higgs self-coupling measurement is of important interest at a future lepton collider experiment. It does not only provide crucial information on the Higgs potential, but also helps to understand the transition of the symmetric to symmetry-broken state of the electroweak sector. The process is accessible over both Higgs Boson production modes at energies higher than  $\sqrt{s} = \sim 350$  GeV, with a production cross-section peaking at around  $\sqrt{s} = 600$  GeV. Recent studies

<sup>3</sup>For this method  $b\bar{b}$  is often chosen as the final state since it provides the highest statistics and characteristic event topology with two  $b$ -tagged jets.



(a)



(b)

Figure 3.4: Projected relative precisions of the measured Higgs Boson coupling to SM particles with respect to SM predicted values for an initial and a full data set of the ILC: (a) Model dependent analysis. Projected relative precisions for the full data set of the HL-LHC are added for a pessimistic (CMS-1) and an optimistic (CMS-2) scenario of systematic uncertainties. (b) Model independent analysis [39].

have shown, that a relative precision of around 27% for the Higgs self-coupling constant is expected with  $4 \text{ ab}^{-1}$  at  $\sqrt{s} = 500 \text{ GeV}$  combining the  $HH \rightarrow b\bar{b}b\bar{b}$  and  $HH \rightarrow b\bar{b}WW^*$  channels [42].

### 3.1.2 Electroweak Precision Measurements

Precision measurements of the electroweak sector are a challenging task at hadron colliders like the LHC and rely not only on rather complex SM background estimations, but also to a large extent on theoretical assumptions. Despite the employment of novel multivariate analysis techniques to improve rare event tagging and therefore the achievable precision in such an environment, the reach of the LHC in the electroweak sector is limited [43].

At a future lepton collider experiments, unrivaled precision measurements of electroweak parameters could be achieved based on the same reasons as discussed previously. In processes like  $e^+e^- \rightarrow W^+W^-$ ,  $e^+e^- \rightarrow ZZ$ ,  $\gamma\gamma \rightarrow W^+W^-$ ,  $e^+e^- \rightarrow VVV$  (triple boson production) or vector boson scattering processes, the masses, widths and couplings of the heavy gauge bosons  $W$  and  $Z$  could be determined with highest precision. Since many beyond SM models expect additional couplings to these gauge bosons, consequences of radiative correction effects could be uncovered by precision measurements at a future lepton collider experiment hinting towards new physics or at least further constrain the parameters of electroweak sector in the SM.

### 3.1.3 Top Quark Measurements

Being discovered by the Tevatron experiments CDF and DØ, the top quark is the heaviest particle in the SM with  $M_{top} = 173.34 \pm 0.27$  (*stat.*)  $\pm 0.71$  (*syst.*) GeV [44]. Since the coupling to the Higgs Boson is proportional to the mass of a fermion (see Section 2.1.3),  $M_{top}$  is an important parameter of the SM. Precision measurements of  $M_{top}$  provide substantial input to fits of global electroweak parameters constraining Higgs and gauge boson properties, allowing to test the internal consistency of the SM. Additionally, the value of  $M_{top}$  affects the stability of the SM Higgs potential, which consequently has cosmological implications [45, 46].

Up to now, the top quark has only been studied in hadron collisions with limited precision caused by the aspects discussed previously. A future lepton collider would offer the clean and well controlled environment for significant enhancement of the achievable measurement precision of the top quark properties. Additionally, due to the well known initial states of the colliding leptons, a resonance scan in the range of  $\sqrt{s} \sim 2M_{top}$  could be performed to precisely measure the top production cross-section,  $M_{top}$ ,  $\Gamma_{top}$  and the strong coupling constant  $\alpha_s$ . Furthermore, the beam polarisations can be tuned to study and exploit the enhancement of the top production cross-section with a lepton machine. Based on these points, the top quark is expected to offer a promising window to new physics at the TeV scale.

### 3.1.4 Direct Beyond SM Searches

Finally, an important part of the physics program of a future lepton collider is the direct search for physics beyond SM.  $e^+e^-$  collisions offer a clean environment and, therefore, many advantages and new possibilities for the discovery of direct physics beyond SM signatures in contrast to hadron colliders like the LHC. While at a hadron collider only missing transverse momentum can be determined, in  $e^+e^-$  collisions missing four-momentum can be investigated for example. Additionally, due to much lower background levels, events with much less visible energy can be observed and studied in contrast to hadron collisions. Recent studies investigate the discovery and exclusion reaches at a future lepton collider experiment for dark matter WIMPs in mono-photon signatures from initial state radiation [47] or challenging SUSY channels, like higgsinos, winos and charginos, at low mass differences [48] for example.

## 3.2 The International Linear Collider

The International Linear Collider (ILC) is considered as the most mature concept of a future linear  $e^+e^-$  collider experiment. Situated in Japan, it is foreseen to collide polarised electron and positron beams with a center-of-mass energy starting at 250 GeV in order to realise the physics program as discussed above. A schematic drawing of the ILC is provided in Figure 3.5. In the following sections, a brief overview of the proposed accelerator, the detector systems and the status of the project is summarised.

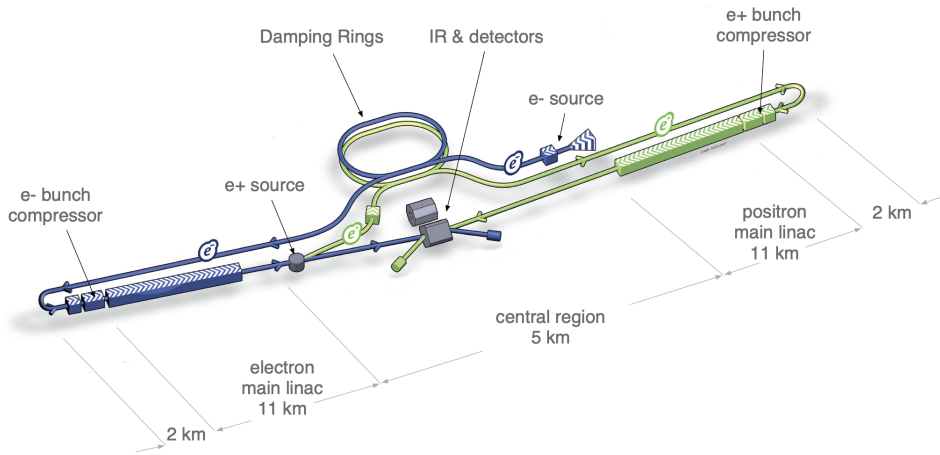


Figure 3.5: Schematic layout of the ILC featuring its main sub-systems (not to scale) [49].

### 3.2.1 Overview and Status

The ILC baseline design has a total length of 31 km mainly comprised by the two main linear accelerators (linacs) for electrons and positrons [49]. Both linacs are based on superconducting radio-frequency (SRF) cavities of niobium operating in cryomodules at 2 K for the acceleration of the respective particles with average gradients of  $\geq 31.5 \text{ MV m}^{-1}$ .

One of the key features of the ILC is the collision of longitudinally polarised electron and positron beams. Polarisation of up to  $P_{e^-} = \pm 0.8$  and  $P_{e^+} = \pm 0.3$  allow for enhancements of specific SM processes and suppression of SM backgrounds depending on the polarisation configuration in order to effectively increase the measurement precision.

By illumination of a GaAs photocathode with a polarised laser beam, polarised electrons are generated. After a bunching and pre-acceleration step to 76 MeV, the electron bunches are accelerated to 5 GeV by a SRF linac and stored in a damping ring of 3.2 km circumference. While circulating in the damping ring, bunch trains are formed and the beam emittance is reduced approximately by 5 orders of magnitude by normal, superconducting and wiggler magnets. Subsequently, the electron beam is accelerated further to 15 GeV by the ring to main linac (RTML) and the bunch length is compressed to a few micrometers. Within the main linac the electron beam is now accelerated to its final collision energy. However, before the collision the electron beam passes through a superconducting 147 m long helical undulator generating photons between  $\sim 10 - 30 \text{ MeV}$ . These

photons are directed on a rotating thin titanium (Ti) alloy<sup>4</sup> target to produce electron-positron pairs 500 m downstream. While the remaining photons and generated electrons are dumped, the positrons are accelerated to 400 MeV with a linac and additionally focused with a solenoid. From this point on the positrons follow a similar procedure as described for the electrons. After the acceleration to their final energy, electron and positron beams propagate through the beam delivery system (BDS). It consists of a sequence of final focusing magnets and collimators to squeeze the beams down to  $x = 474$  mm and  $y = 5.9$  mm (values for the operation at  $\sqrt{s} = 500$  GeV) in order to reach the design goal of an instantaneous luminosity of up to  $2 \times 10^{34} \text{ cm}^{-2}\text{s}^{-1}$ . Finally, both beams enter the interaction region (IR), where the beam collision occurs and dedicated detectors are instrumented.

The final ILC beam structure features bunch trains separated by 200 ms corresponding to a bunch train repetition frequency of 5 Hz. Each of these trains consists of 1312 bunches separated by 554 ns with  $\sim 2 \times 10^{10}$  particles in each bunch.

The initial plan has foreseen the construction of a 500 GeV machine. This was motivated by the accessibility of both Higgs production mechanisms, Higgsstrahlung and VBS, for Higgs Boson coupling measurements, top quark precision measurements and a higher direct discovery potential for new particles. At the moment, a staging concept is under consideration, which features an extended primary operation<sup>5</sup> at a center-of-mass energy of 250 GeV with potential upgrades to 350 GeV, 500 GeV and 1 TeV based on extensions of the two main linac lengths next to other major upgrades [50]. One of the arguments for the staged approach, next to cost reasons, is that the 250 GeV program already provides highly precise and model-independent measurements of Higgs Boson properties based on the sufficiently large number of produced Higgs Bosons via Higgsstrahlung<sup>6</sup> at low background levels [51].

From a technological point of view, all key components of the accelerator have been developed and demonstrated successfully, which is documented in the ILC Accelerator Technical Design Report [52]. Specifically the operation and mass production of the SCRF cavity units have been demonstrated at the linear SCRF-based synchrotron facilities FLASH [53] and XFEL [54] at DESY. Therefore, the ILC could potentially be constructed without any major delays as soon as a positive decision on its realisation would be made. Currently different parts of the Japanese government are debating on hosting the ILC in the northern part of the country. In parallel, intergovernmental discussions of governance and sharing of responsibilities and costs are ongoing with no clear outcome yet. An ILC Preparatory Laboratory (Pre-lab) is planned in order to prepare and execute further technical and engineering work and provide all relevant information to the intergovernmental discussions upon request [55].

### 3.2.2 Detector Systems

Two multi purpose detector systems are being developed for the ILC, the International Large Detector (ILD) and the Silicon Detector (SiD). Both systems share the interaction region by employing a push-pull configuration. While one detector is located within the beam acquiring collision data, the other one is laterally parked in a maintenance position within the detector hall. Every few weeks the configuration is changed in order to allow sufficient data taking for both experiments. The two-detector concept allows not only the investigation of complementary detection approaches, but also the independent confirmation of results.

<sup>4</sup>The thickness corresponds to  $0.4 X_0$ .

<sup>5</sup>Currently an initial operation at the Z-pole ( $\sim 91$  GeV) is under consideration as well.

<sup>6</sup>Up to half a million events depending on the running scenario [51].

Driven by the extensive physics program introduced in Section 3.1, both detector concepts are optimised with respect to particle flow reconstruction (see Section 4.4). One goal of this concept is to achieve a relative jet energy resolution of  $<4\%$  for jet energies of  $40\text{--}250\text{ GeV}$  [56]. This requires highly efficient tracking systems (with momentum resolution:  $\sigma_p/p^2 < 5 \times 10^{-5} \text{ GeV}^{-1}$ ) and highly segmented calorimeters within the magnetic coil of the system. Furthermore, the material budget of the innermost systems and support structures is minimised. This is partly realised by a passive cooling scheme (power pulsing), which exploits the bunch spacing of the ILC, to avoid active cooling elements. The two individual detector concepts are briefly introduced in the following sections.

### 3.2.2.1 International Large Detector

The ILD is foreseen to feature a near to cylindrical shape of  $13\text{ m}$  length and  $7.8\text{ m}$  radius [56]. Surrounded by a superconducting solenoid coil of inner radius  $3.4\text{ m}$ , the tracking as well as the full calorimeter system are located within a magnetic field of  $3.5\text{ T}$  oriented parallel to the beam axis. Figure 3.6 illustrates the schematic layout of the ILD.

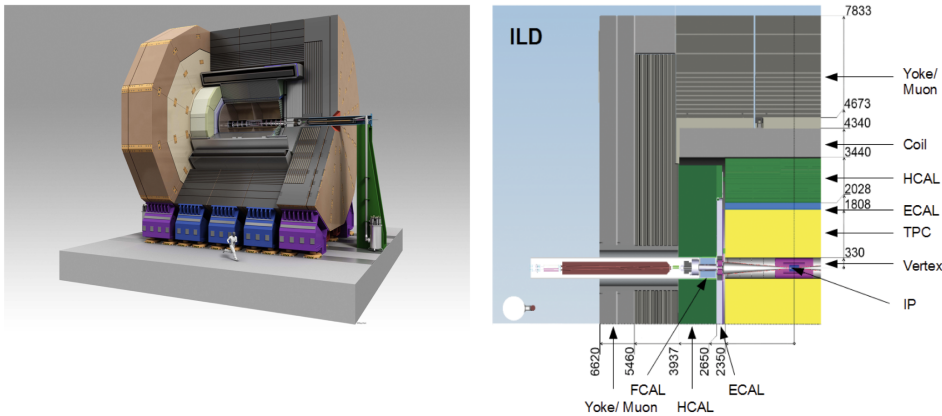


Figure 3.6: Illustration of the ILD concept showing full detector and detector cross section. Dimensions are given in units of millimeter [49].

The tracking system of ILD consist of multiple sub-detectors. The innermost system is a multi-layer vertex detector (VXD) located around  $16\text{ mm}$  from the beam axis. It is optimised for a minimal material budget of less than  $0.0015 X_0$  per layer and a single point resolution of better than  $6\text{ }\mu\text{m}$ . Different proposals are made for the system featuring either three double layers or five single layers of novel silicon pixel sensors, like CMOS [57] or DEPFET [58]. Further outside, located at a radius of  $153\text{ mm}$  and  $300\text{ mm}$ , two layers of silicon strip detectors providing comparable spatial resolution with a material budget of  $0.0065 X_0$  per layer are installed. Furthermore, in the forward regions several silicon pixel and strip disks are implemented to allow for low angle tracking. As the main tracking device of ILD, the time projection chamber (TPC) covers the volume of radius  $330\text{ mm}$  to  $1808\text{ mm}$ . Electrons generated by the ionisation of gas along the trajectory of charged particles are amplified by an electric field oriented parallel with respect to the beam axis. Electrons are planned to be multiplied and read out by either gas electron multiplier (GEM) [59] or micro-mesh gaseous structure (micromegas) [60] technology located in both endcaps. The proposed TPC offers a 3-dimensional spatial point resolution of  $100\text{ }\mu\text{m}$  in the  $r\phi$  plane and

around 1.4 mm in the  $z$  direction. Despite featuring a lower spatial resolution in comparison to silicon sensors, the TPC allows for continuous tracking measuring up to 224 points per track being specifically advantageous for the reconstruction of kinked and non-pointing tracks caused by multiple scattering. At the same time, the TPC benefits from a very low material budget and the ability of performing particle identification via the measurement of the specific energy loss  $dE/dx$ , see Section 4.1. For the complete ILD tracking system, a total momentum resolution  $\sigma_{p_T}/p_T^2$  of  $2 \times 10^{-5} \text{ GeV}^{-1}$  is expected.

Following the tracking system in the radial direction, a finely segmented electromagnetic calorimeter (ECAL) is planned. In the baseline option it consists of 30 active layers of silicon readout pads, with a readout segmentation of  $5 \text{ mm} \times 5 \text{ mm}$ , and passive tungsten absorber plates allowing for a compact design of barrel as well as the endcap region of the system. Other options under discussion are the usage of plastic scintillator strips as the active medium or a combination of both technologies for an optimised cost to performance ratio of the ECAL system. Right after the ECAL, a highly segmented hadronic calorimeter (HCAL) is implemented and separated in barrel and endcap systems as well. The HCAL consists of up to 48 layers with steel as passive absorber material. Two options are currently considered for the active layers: either analog scintillator-based readout with tiles of  $3 \text{ cm} \times 3 \text{ cm}$  dimension or (semi-)digital readout based on resistive plate chambers (RPCs) with an effective segmentation of  $1 \text{ cm} \times 1 \text{ cm}$ . Further details about the various considered calorimeter technologies and the development status are provided in Section 4.5.

Covering the forward region, additional calorimeter systems are instrumented<sup>7</sup> for direct and indirect luminosity and background measurements at very low angles down to 5 mrad. Finally, in order to detect muons and energy leakage of high energy jets, the magnetic field return iron yoke is planned to be instrumented with RPCs or scintillator strips.

### 3.2.2.2 Silicon Detector

Designed as a multi-purpose detector, SiD is a detector concept very similar to the ILD. A schematic view of the detector is illustrated in Figure 3.7. In comparison to ILD it features reduced overall

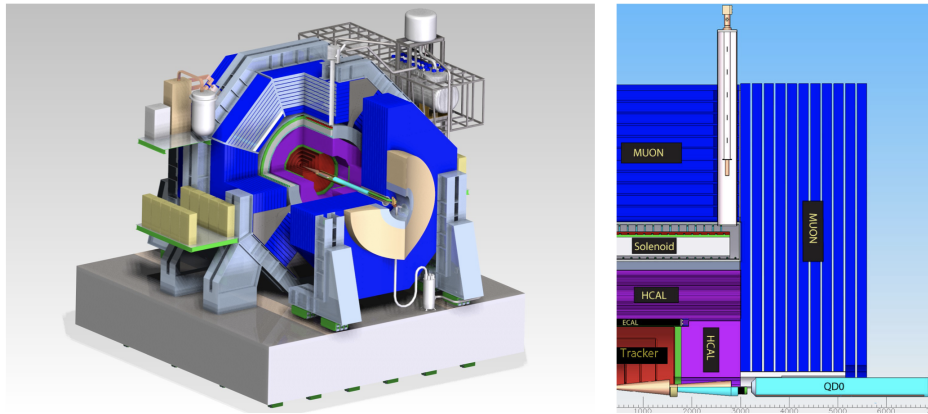


Figure 3.7: Schematic view of the SiD concept showing full detector and detector cross section [49].

dimensions with a length of 11 m and a radius of 6.6 m, but operates a stronger magnetic field

<sup>7</sup>LumiCal, BeamCal and LHCAL summarised as FCAL.

of 5 T [56]. SiD features a completely silicon-based tracking system instead of a TPC. While the electromagnetic calorimeter system is planned to be based on silicon as well, the baseline design of the hadronic calorimeter has recently been changed to a scintillator-based calorimeter instead of digital RPC readout [61]. With respect to physics prospects and overall detector performance, the SiD concept is comparable to ILD.

### 3.3 Compact Linear Collider

An alternative concept for a future linear  $e^+e^-$  collider experiment is the Compact Linear Collider (CLIC), planned to be located at CERN [62, 63]. In comparison to ILC, CLIC features a different acceleration technology and conceptual design. Firstly, normal-conductive RF copper cavities operating at 12 GHz are used allowing for much higher acceleration gradients up to  $100 \text{ MVm}^{-1}$ . Secondly, a two-beam concept is planned to be used in which a driver beam provides the acceleration power for a collision beam. This scheme allows CLIC to be upgradable to a collision center-of-mass energy of 3 TeV without revising its compact design. Figure 3.8 illustrates the proposed CLIC site in the Geneva area with a total length of roughly 48 km for the 3 TeV machine. The resulting beam structure is planned to consist of 20 ms separated bunch trains, each composed of  $\sim 300$  bunches separated by only 0.5 ns. The acceleration technology of CLIC is not yet mature and still requires several years of R&D.

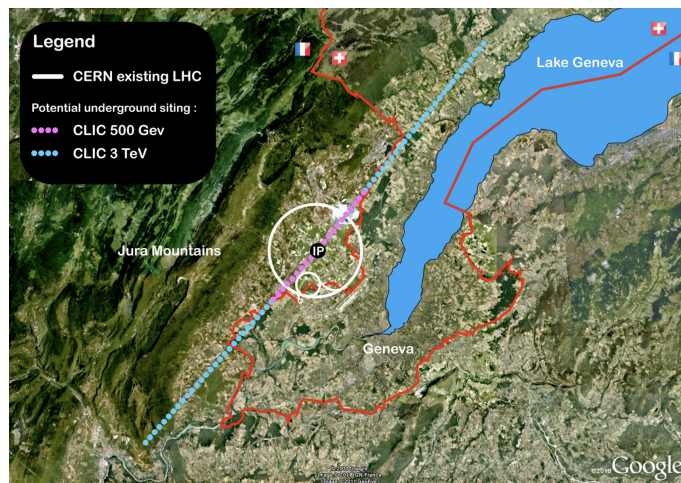


Figure 3.8: Map showing potential CLIC accelerator complex in the Geneva area. Taken from [62].

A potential CLIC detector encounters many different challenges regarding its design in comparison to the introduced detector systems for ILD. In order to cope with the higher collision energies, the 0.5 ns bunch spacing, related pile-up and larger  $\gamma\gamma \rightarrow$  hadron background, different requirements are defined for the individual detector sub-systems to be able to successfully employ particle flow reconstruction techniques. The hadronic calorimeter for example is planned to consist of tungsten as absorber material to allow for more compact and contained hadron showers. Furthermore, a high magnetic field of 4 T is planned to be used to achieve better particle separation. Lastly, all sub-detectors must feature an excellent time resolution for background and pile-up rejection. A sketch of the proposed detector concept is provided in Figure 3.9.

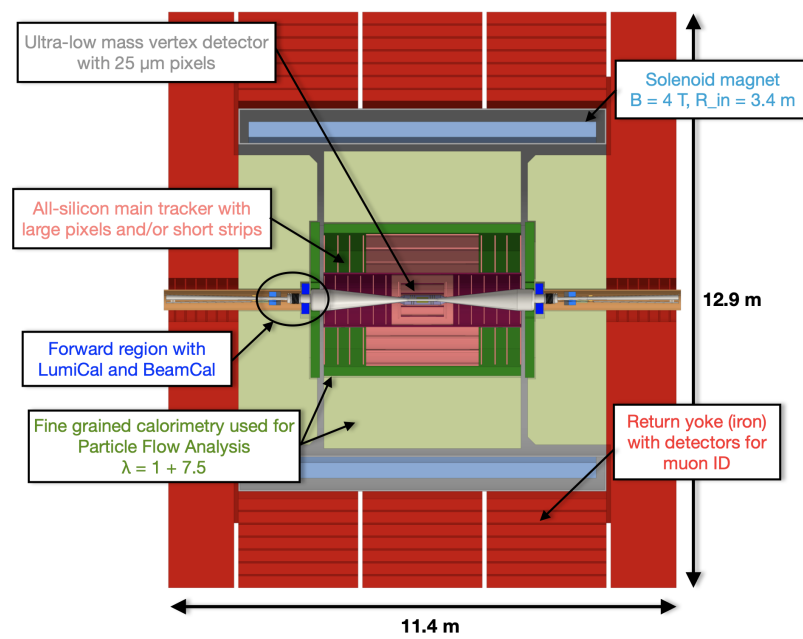


Figure 3.9: Proposed detector concept for CLIC (top view). Taken from [64].

# 4 Basics of Calorimetry and Particle Flow Reconstruction

In the context of particle physics, calorimeters are fundamental detector systems to measure the energy of particles. Typically they consist of a large instrumented volume of a specific material in which traversing particles convert their energy into a measurable signal. If these particles are of high energy, their interaction with matter within the calorimeter can trigger a particle shower. A particle shower is a cascade like process, based on the generation of daughter particles as long as their energy is large enough to self-sustain the process. Depending on the type and energy of the traversing particle and the calorimeters effective thickness, it is often stopped completely by depositing all of its energy during the cascade process. In general, a completely contained particle shower is desired in order to achieve an adequate measure of the particle energy.

In general, the particles within such a shower can interact with the matter of the calorimeter system via various processes. In Section 4.1 these processes are introduced and the physics of the two types of particle showers, electromagnetic and hadronic, are discussed on the basis of that. Different simulation models of these interactions within particle showers, which are employed in the analysis presented within the scope of this thesis, are briefly summarised in Section 4.2. Furthermore, basic principles of calorimetry, classical calorimetric observables and limitations are discussed in Section 4.3.

Section 4.4 introduced the particle flow reconstruction as a key concept for unprecedented precision at a future  $e^+e^-$  collider experiment. After introducing the basic principles and limitations of the concept, the implications for a particle flow designed detector system, specifically the calorimeters, are discussed. Furthermore, the state of the art algorithm for particle flow reconstruction, PandoraPFA, is introduced and a simulation study showing the projected jet energy reconstruction performance at the proposed ILC by using PandoraPFA is presented. Lastly, the efforts of the CALICE collaboration to develop multiple types of highly granular calorimeter systems optimised for particle flow reconstruction are briefly summarised in Section 4.5.

## 4.1 Interactions of Particles with Matter

In the environment of a high energy particle collider, only a bunch of different final state or longer living particles reach the calorimeter systems. Those particles can be categorised by the way they are interacting with the matter of the calorimeter system:

- $e^\pm, \gamma$ : inducing electromagnetic particle showers.
- $\pi^\pm, K^\pm, K^0, p^\pm, n$ : inducing hadronic particle showers.

- $\mu$ : typically not showering and just leaving ionisation tracks.
- $\nu$ : almost never interacting and traversing the calorimeters without any energy depositions.

In this section, a brief overview of the basic interaction processes of particles with matter and the physics of induced particle showers is provided.

### 4.1.1 Electromagnetic Cascades

Depending on their kinetic energy, electrons and positrons lose their energy in different physics processes while traversing matter. The energy loss contributions for electrons and positrons energy traversing lead are depicted in Figure 4.1a. At lower energies, up to the order of 10 MeV, the dominant process is ionisation of the atoms in the traversed material. However, different scattering processes also contribute slightly to the total energy loss in this energy regime, namely Bhabha and Møller scattering. Additionally, low energy positrons can be captured and annihilate with an electron of the traversed material. For energies higher than 10 – 100 MeV Bremsstrahlung takes over as the main contribution to energy losses in the form of radiated photons due to the Coulomb interactions of the electron/positron with the Coulomb field of the nuclei. The energy spectrum of those emitted photons follows a  $1/E$  dependency [65]. The critical energy  $\epsilon_c$  in this context is defined as the energy where energy losses of ionisation and Bremsstrahlung are on the same level. It is material dependent and for solid matter it can be parametrised with the atomic number  $Z$  as follows:

$$\epsilon_c = \frac{610 \text{ MeV}}{(Z + 1.24)} \quad (4.1)$$

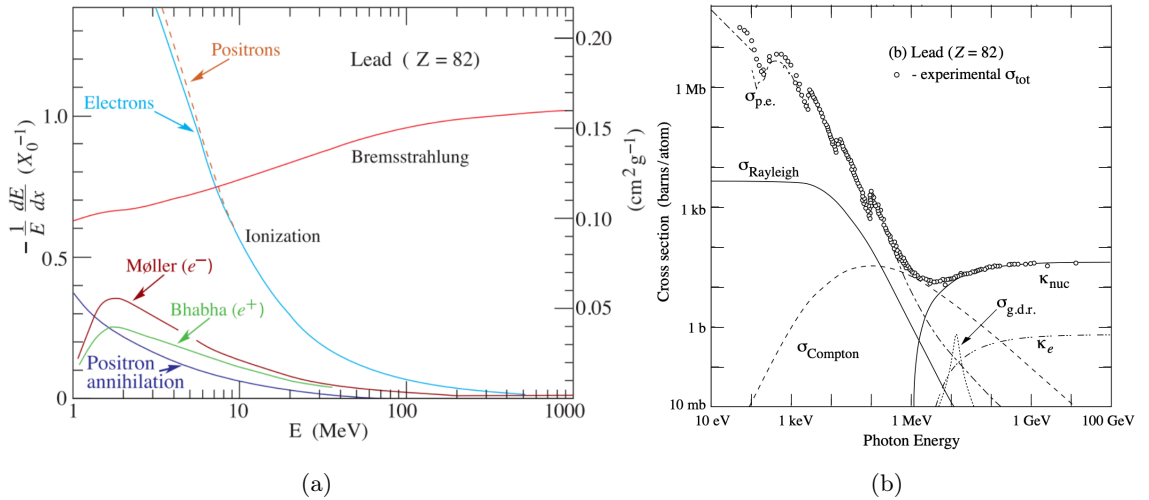


Figure 4.1: **(a)** Electron (positron) energy loss in lead as a function of the particle energy for different energy loss processes. **(b)** Total experimental cross-section of the photon as a function of the photon energy in lead. Contributions from the photo-electric effect ( $\sigma_{p.e.}$ ), Compton scattering ( $\sigma_{\text{Compton}}$ ) and pair production within a Coulomb field of an electron ( $\kappa_e$ ) and a nucleus ( $\kappa_{\text{nuc}}$ ) are illustrated.  $\sigma_{g.d.r.}$  indicates the photo-nuclear cross-section (great dipole resonance) [66, 67].

Photons lose their energy while transversing matter in different processes, depending on their respective energy, as well. The corresponding cross-sections of these processes in lead as a function of the photons energy is given in Figure 4.1b. For energies below  $\sim 1$  MeV, energy losses are dominated by the photoelectric effect, in which electrons of the atom are emitted if the absorbed photon energy overcomes their binding energy. In the same energy regime up to energies of a few 10 MeV, scattering processes contribute to the total energy loss of photons in matter. In Rayleigh and Compton scattering, photons electromagnetically interact with electrons of the traversed matter coherently or incoherently respectively. Lastly, at a threshold of two times the rest mass of the electron/positron ( $E_\gamma = 2 \times 511$  keV), the process of pair production starts and becomes the dominant process at energies in the order of 100 MeV and higher. Within this process, photons traversing the Coulomb field of the nuclei or electrons can create electron-positron pairs.

If a high energy electron, positron or photon penetrates dense matter, a cascade like process is initiated including a mixture of all processes introduced above. In a simplified picture, for a photon, the first interaction could be a pair production creating a secondary electron and positron, which subsequently could irradiate Bremsstrahlung photons potentially generating new electron-positron pairs. A simplified picture for a primary electron is depicted in Figure 4.2. As soon as the electron of energy  $E_0$  enters the matter, Bremsstrahlung photons are emitted. While most of them are of low energy and undergo Compton scattering or are absorbed via the photoelectric effect, a few of them might exceed the threshold for pair production and initiate the next generation of electron-positron pairs. The number of generated particles in this cascade scales roughly with  $E_0/\epsilon_c$  and the cascade starts to get quenched if the average electron energy gets smaller than  $\epsilon_c$ . Electromagnetic cascades, which are in the following referred to as showers, are characterised by the radiation length,  $X_0$ , in terms of the longitudinal and the Moliere radius,  $\rho_M$ , with respect to the transversal development.

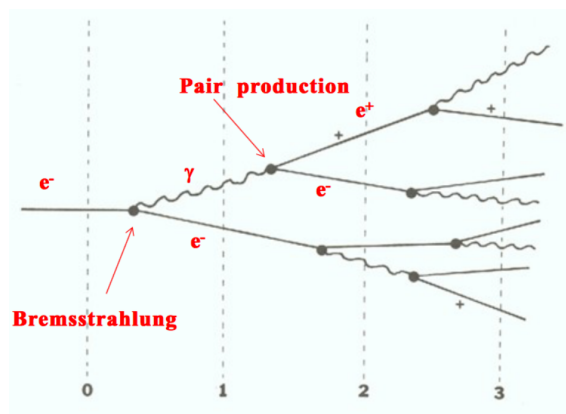


Figure 4.2: Simplified picture of electromagnetic shower development with numbers corresponding to the depth of the shower in units of radiation length  $X_0$  [68].

The radiation length is defined as the characteristic amount of matter a traversing high energy electron (positron) has lost all but  $1/e$  of its initial energy by the Bremsstrahlung process. At the same time it is defined as  $7/9$  of the mean free path,  $\lambda_\gamma$ , a high energy photon can traverse matter before initiating a pair production process. It can be parametrised with the atomic number  $Z$  and

the atomic mass number  $A$  in the following way [65]:

$$X_0 = \frac{716A}{Z(Z+1)\ln(287/\sqrt{Z})} \left[ \frac{\text{g}}{\text{cm}^2} \right] \quad (4.2)$$

The level of shower energy containment in longitudinal direction is proportional to  $\ln(E_0)$ . Therefore,  $14X_0$  of copper to contain on average 95% of the energy induced by a 10 GeV electron shower is needed, while approximately  $22X_0$  of copper would be necessary to achieve the same for an induced 1 TeV electron shower [65].

The Moliere radius is defined by the average transversal containment of 90% of the shower energy in a cylinder of radius  $\rho_M$ . It can be parametrised with the radiation length  $X_0$  and the critical energy  $\epsilon_c$  as [65]:

$$\rho_M = 21.2 \text{ MeV} \frac{X_0}{\epsilon_c} \quad (4.3)$$

### 4.1.2 Heavy Charged Particles

For high energy charged particles, Bremsstrahlung is typically the dominant process for energy losses, as discussed in the previous section. However, this process is suppressed by the particle mass with  $1/m^4$ . Therefore, for heavy charged particles like muons or charged hadrons the dominating processes for energy losses are ionisation and excitation of the electrons bound to the nuclei. The mean energy loss per distance unit  $dE/dx$  of heavy charged particles is provided by the Bethe-Bloch formula [65]:

$$\left\langle \frac{dE}{dx} \right\rangle = Kz^2 \frac{Z}{A} \frac{1}{\beta^2} \left( \frac{1}{2} \ln \frac{2m_e c^2 \beta^2 \gamma^2 W_{max}}{I^2} - \beta^2 - \frac{\delta}{2} \right) \quad (4.4)$$

where  $K$  is a numerical constant,  $z$  the traversing particle charge,  $Z$  ( $A$ ) the atomic (mass) number of the absorber material,  $m_e$  the mass of the electron,  $I$  the mean excitation energy of the absorber material,  $W_{max}$  the maximal kinetic energy transferable in a single collision,  $\delta(\beta\gamma)$  a correction term for density effects,  $\beta$  the particle velocity and  $\gamma$  the Lorentz factor. Figure 4.3 depicts the mass stopping power for positively charged muons in copper as a function of the muons momentum and  $\beta\gamma$ .

Only for  $\beta\gamma > \sim 1000$ , corresponding to muons with energies higher than several 100 GeV, radiative energy losses via Bremsstrahlung become dominant again. For lower energies in the Bethe-Bloch range  $0.1 < \beta\gamma < 1000$ , energy losses due to ionisation and excitation are described by the Bethe-Bloch formula within an accuracy on the percent level [69]. Within this range a broad minimum is situated around  $\beta\gamma = 2 - 4$ , which corresponds to a minimal energy loss of  $\sim 13 \text{ MeV/cm}$  for 450 MeV muons traversing copper. Particles in this regime are called minimum ionising particles (MIPs), often utilised for detector calibration due to their well defined energy deposition spectrum.

Within thin layers the stochastical energy loss of MIPs is well described by a Landau-Vavilov distribution [67, 70], as illustrated in Figure 4.4 for 10 GeV muons penetrating 1.3 mm of silicon. The mean of this distribution is subject to large variations due to the fluctuating high energy tail, caused by only several infrequent high energy loss interactions like high energy Bremsstrahlung photons or interactions with the nuclei. In contrast, the Most Probable Value (MPV) of the distribution is insensitive to the high energy tail. For these reasons, the MPV of MIP energy losses is often used as a standard candle providing a well defined energy deposition scale exploited for detector calibration purposes [70]. In the provided example of the MIP energy loss distribution, the mean is  $\sim 65\%$  larger than the MPV.

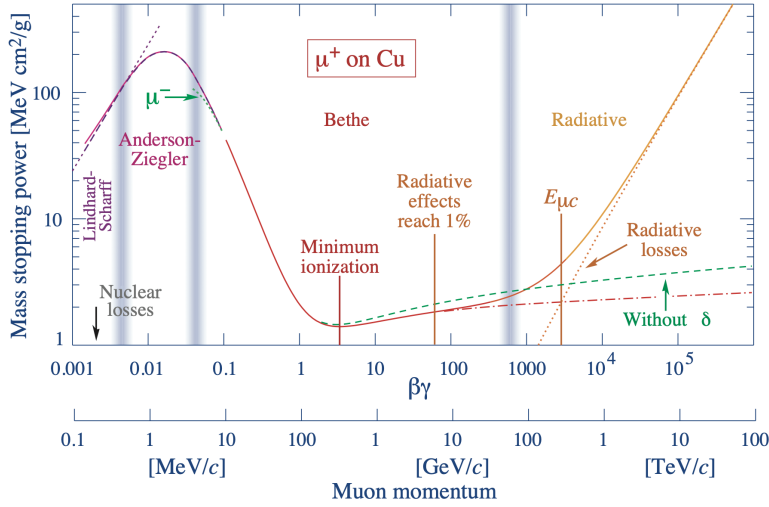


Figure 4.3: Mass stopping power  $\langle -\frac{dE}{dx} \rangle$  versus particle momentum for positive muons in copper. Transitions of different interaction models are indicated by shadowed regions [67].

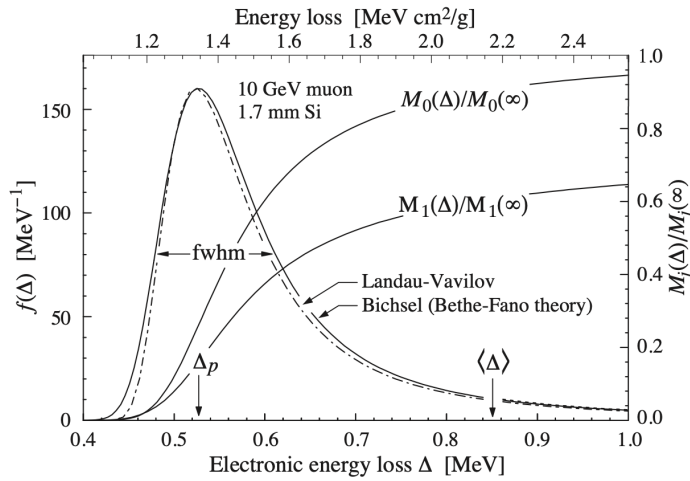


Figure 4.4: Energy loss spectrum of a 10 GeV muon traversing 1.7 mm of silicon (equivalent to  $\sim 3$  mm of PVC scintillator).  $\Delta_p$  corresponds to most probable,  $\langle \Delta \rangle$  to mean energy loss [67].

### 4.1.3 Hadronic Cascades

Besides ionisation processes, charged (and neutral) hadrons can lose energy via inelastic hard scattering with nuclei of traversed matter, in the following referred to as hadronic interaction. This initial hadronic interaction initiates a hadronic cascade or hadronic shower, as schematically shown in Figure 4.5. Interacting with one or several nucleons of the target nucleus, the incident hadron transfers a significant fraction of its momentum. This can lead to a variety of nuclear reactions:

spallation, fission, nuclear breakup and excitations. Within these processes, typically protons and neutrons are ejected, secondary mesons ( $\pi^\pm$ ,  $\pi^0$ ,  $\eta$ ) are generated and excited fragments of the hit nucleus are left behind. Secondary particles with high momenta are able to further traverse the material potentially initiating further interactions. The cascade starts to die out if particles in later generations do not have sufficient momentum to induce further hadronic interactions. Depending on the hardness of the interaction, namely the absolute momentum transfer and the impact parameter, the type, momenta and number of secondary particles can strongly fluctuate event by event. This makes the hadronic shower much more complex and diverse compared to an electromagnetic shower. In the following brief descriptions of the sub-components of a hadronic shower are provided.

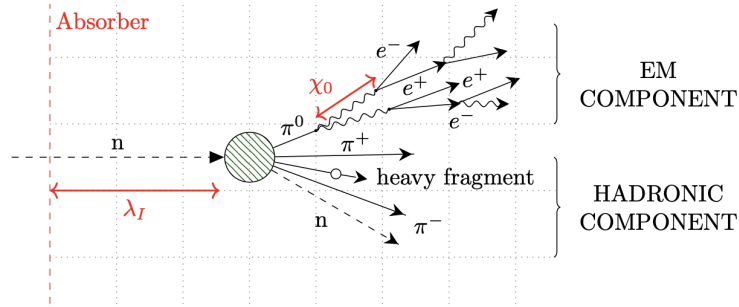


Figure 4.5: Illustration of hadronic shower development. Next to the depicted electromagnetic and hadronic component the shower features an invisible component as well. Taken from [71].

The electromagnetic component is mainly initiated by generated  $\pi^0$  and  $\eta$  mesons, decaying (lifetime  $\sim 10^{-7}$  s) into photons according to

$$\pi^0 \rightarrow 2\gamma \quad (BR : 99\%)$$

$$\eta \rightarrow 2\gamma \quad (BR : 39\%)$$

$$\eta \rightarrow 3\pi^0 \quad (BR : 33\%)$$

Generated photons subsequently induce local electromagnetic sub-showers. The electromagnetic fraction of the total available energy  $f_{EM}$  strongly varies from event to event and scales with the energy of the incident hadron, since the probability of generating additional  $\pi^0$  and  $\eta$  mesons gets higher with every energetically accessible daughter generation of hadrons. The mean electromagnetic fraction is typically  $\langle f_{EM} \rangle = \frac{1}{3}$  for hadronic showers induced by hadrons in the 10 GeV range, while it grows to  $\langle f_{EM} \rangle = 0.73$  for hadrons of 1 TeV [65].

The hadronic component consists of further strongly interacting secondary hadrons or heavy fragments of the nuclei created in the initial hadronic interaction. Again, those particles are subject to energy losses via ionisation and, if their momentum is sufficiently high, further hadronic interactions.

Lastly, each hadronic shower features an invisible energy component, which remains undetected and fluctuates from event to event as well. This can either be energy going into the excitation or recoil of target nuclei or energy from binding secondary particles in nuclei of the material. Furthermore, energy might be carried away by neutrinos generated in the decay of charged hadrons

in the shower. Lastly, in the spallation processes neutrons might be released. Until thermalisation, they elastically scatter through the matter with a mean free path in the order of cm losing most of their kinetic energy undetected. Only the late ( $\mathcal{O}(s)$ ) emittance of  $\gamma$ -rays by an excited nucleus, due to neutron capture, is potentially detectable.

The mean free path between hadronic interactions is defined as the nuclear interaction length  $\lambda_n$ , which is the characteristic length scale of hadronic showers. It is typically much larger than the corresponding value of  $X_0$  for the same material, like e.g. for steel:  $\lambda_n/X_0 \approx 9.5$ .  $\lambda_n$  can be parametrised for materials with  $A > 7$  according to [72]:

$$\lambda_n = (20A^{0.4} + 32) \frac{\text{g}}{\text{cm}^2} \quad (4.5)$$

Based on the ratio of the cross section of protons and pions for hadronic interactions with target protons, the specific pion interaction length,  $\lambda_\pi$ , is approximately 3/2 larger than  $\lambda_n$ . For a  $\sim 95\%$  energy containment of a hadronic shower induced by a 100 GeV pion, matter equal to  $\sim 8\lambda_\pi$  is required longitudinally. For transversal containment of on average  $\sim 90\%$  energy of the same shower, a cylinder with a radius corresponding to  $\sim 1\lambda_\pi$  would be necessary [65].

Due to the fact that  $\lambda_n/X_0 \gg 1$  for most material, the hadronic shower development is in general spatially more extended in comparison to electromagnetic showers. Since a hadronic shower is characterised only by several hadronic interactions featuring more complex processes compared to electromagnetic showers, a highly variable number of secondary particles per interaction is generated. This finally results in a large statistical fluctuation of the energy fractions in the different shower sub-components and therefore in the longitudinal and transversal development of the shower. As a consequence each hadronic shower looks substantially different if visualised, while electromagnetic showers look the same on average. Another crucial difference between electromagnetic and hadronic showers is the corresponding time development. While electromagnetic showers and the respective electromagnetic sub-component in hadronic showers are prompt, parts of the hadronic component can be significantly delayed. Examples are the de-excitation of nuclear states ( $\mathcal{O}(\mu\text{s})$ ) or the release and subsequent thermalisation of neutrons ( $\mathcal{O}(\mu\text{s})$ - $\mathcal{O}(s)$ ) generating late and potentially isolated energy depositions.

## 4.2 Modelling of Particle Showers

The GEANT4 toolkit [73, 74] is a simulation framework to model particle interactions for a wide range of energies, which is the reason why it is commonly used even in non high energy physics applications [75]. In the scope of this thesis, it is utilised to simulate the interactions of MIPs and the interactions within electromagnetic and hadronic showers with different models. Details about the used version and explicit implementation are provided in Chapter 6. In the following, the different interaction models and their combination into specific physics list are briefly discussed.

### 4.2.1 Electromagnetic Shower Models

Since the relatively interaction processes for electrons, positrons and photons can be precisely parametrised, electromagnetic showers are generally well understood. In GEANT4, electromagnetic interactions are simulated with an EM standard package reproducing classical calorimetry observables, see Section 4.3, with an accuracy better than 1% [76]. Depending on the specific type of detector technology and desired precision of individual sub-processes in the electromagnetic interactions, GEANT4 has introduced many extensions of the EM standard package over the last

decade. One example is the `_EMY` option, introduced to improve the description of ionisation processes in thin layers of low density matter, where energy detection methods are dominated by primary ionisation processes. Different studies have shown, that the agreement of simulations with data is greatly improved by using the `_EMY` option for example in gas-based detector systems like Resistive Plate Chambers (RPCs) [77].

### 4.2.2 Hadronic Shower Models

As discussed in Section 4.1.3, hadronic showers are much more complex than their electromagnetic counterpart. Due to the compositeness of incident hadron and target nuclei, possible high energy interactions have a very large final state phase space, mainly governed by the strong force. Due to this, hadronic shower simulations have a high level of complexity and can often not be analytically processed. Hence, models using different parametrisation and approximations of processes within hadronic showers are used for simulation applications. None of the developed hadronic shower models have reached the level of accuracy to describe corresponding shower observables to the same precision as achieved for electromagnetic shower models to this day. However, significant progresses have been achieved over the last decade improving and validating the accuracy of hadronic shower simulation models with respect to acquired experimental data [78].

On the basis of the deBroglie wavelength,  $\lambda_B = h/p$ , the interaction scale of the modeling is defined to steer the level of projectile and target sub-structures to be considered for the interaction. While at low energies, the modelling of individual nucleons in the target nuclei is sufficient, at higher energies the projectile and target's quark sub-structure has to be considered within the modelling. Therefore, GEANT4 features different models aiming to describe interactions in various energy ranges. In general, all implemented interaction models follow a two-step procedure: In a first step, the interactions of the projectile hadron with a target nucleus is simulated, typically resulting in an excited nucleus and a composition of secondary particles. In the subsequent second step, the de-excitation process is simulated resulting in more secondary particles or its fragmentation. In the following, GEANT4 models relevant for the work presented in this thesis are briefly introduced. More details can be found in the GEANT4 physics reference manual [79].

#### Intra-nuclear Cascade Models

For energies up to a few GeV, typically interaction models describing individual nucleons are used, since  $\lambda_B$  is still too large to resolve the quark sub-structure. The baseline model for this energy regime is the intra-nuclear cascade (INC), schematically illustrated in Figure 4.6. The hadron projectile is tracked while entering the target nucleus and interacting with individual nucleons according to a mean free path, which is parametrised from modelled nucleon densities and measured interaction cross-sections. In these intra-nuclear interactions secondary particles are generated and similarly tracked until they interact as well, are absorbed in the nucleus by not exceeding the threshold for further interactions, or leave the nucleus.

The Bertini cascade model is one of the implemented INC models in GEANT4 [81]. It models the nucleus as three concentric spherical shells with respectively constant nucleon densities. Within those shells, the nucleons are treated as a degenerated Fermi gas occupying all energy levels up to the Fermi energy. For each interaction within the INC, the interaction type, interaction products and corresponding four-momenta are calculated as long as the energy of the tracked particle is  $>2$  MeV. Within the implemented de-excitation model, in a first step pre-equilibrium evaporations are computed corresponding to the emission of neutrons and protons from the excited nucleus. In a second step a full de-excitation of the nucleus is modelled including different possible mechanisms

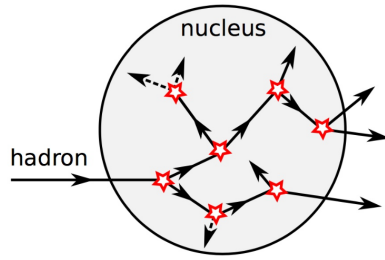


Figure 4.6: Schematic of an intra nuclear cascade. Taken from [80].

like Fermi-breakup into fragments for light nuclei ( $A < 17$ ), simple nucleus explosion releasing all nucleons or fission for heavier nuclei until the excitation energy is below 0.1 MeV.

### Parton String Models

For energies higher  $>5$  GeV, parton string models are typically employed within GEANT4. In this energy domain,  $\lambda_B$  gets to the level in which quark sub-structures of the projectile hadron and target nucleon can be resolved and have to be taken into account. For these models, the initial projectile hadron interacts with a single nucleus in the target nucleon in a first step. A specific interaction is modelled by forming a gluon string between constituent quarks of the projectile and target to generate color-neutral objects. The choice of this interaction is based on the impact parameter, the center-of-mass energy of the projectile-target system and the implemented cross-sections of inelastic and diffractive interactions. Consequently, this leads to a fragmentation of the target nucleon, generating secondary particles and an excitation of the nucleus [82]. Sketches illustrating the string formation and string fragmentation principles are depicted in Figure 4.7a and 4.7b.



Figure 4.7: Main concepts of the parton string models implemented in GEANT4: (a) String formation between constituent quarks of the transversing hadron and a target nucleus. (b) Gluon string fragmentation by creation of quark-antiquark pairs followed by hadronisation processes [80].

In GEANT4, two different parton string models are implemented: the Fritiof and the Quark-Gluon String model. Both models differ in the formation and fragmentation processes of gluon

strings. While the Fritiof model only considers diffractive excitation processes [83] to form a string, the Quark-Gluon String model additionally takes inelastic scattering processes, mediated by pomerons [84], into account during the momentum exchange between projectile hadron and target nucleon. The subsequent interactions of secondary particles traversing through the nucleus are treated with cascade models as described previously. Lastly, the de-excitation of the nucleus is simulated via models of fragmentation, nuclear de-excitation and pre-compound implemented as a standard in GEANT4 [85].

### Parametrisation Models

Next to INC and parton string models, GEANT4 also features much simpler parametrisation models, namely the low energy parametrisation (LEP) and high energy parametrisation (HEP) [79]. Those are generated by fits to experimental data to predict the composition and energies of secondary particles in the hadronic shower development without modelling any explicit sub-interaction. Parametrisation models do not reach the precision as the previously introduced models do for their optimised energy range, but are often used to cover energy regions of model transitions.

### 4.2.3 GEANT4 Physics Lists

A physics list in GEANT4 is a composition of different interaction models covering different energy ranges for interacting particles. Energy transition regions, in which a random selection of one out of two models is performed, allow a smooth transition between two models [86]. Within the scope of this thesis, the QGSP\_BERT\_HP and FTFP\_BERT\_HP physics lists of GEANT4 are used, since they are considered to be the most mature and tuned [87]. The physics lists composition of these models is depicted in Figure 4.8 and described in the following.

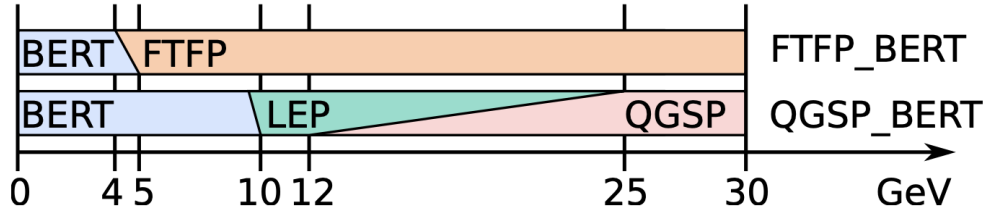


Figure 4.8: Depiction of GEANT4 physics list interaction models for different energy ranges [88].

#### QGSP\_BERT

In the low energy range, up to 10 GeV, the QGSP\_BERT physics list utilises the Bertini cascade model. For energies  $> 12$  GeV it uses the Quark-Gluon String precompound (QGSP) modeling. In the transition region, the LEP model is used covering a range 9 GeV to 25 GeV.

#### FTFP\_BERT

For the FTFP\_BERT physics list, the Bertini cascade model is utilised up to an energy of 5 GeV. The Fritiof precompound (FTFP) model starts to take over at 4 GeV and is fully applied for energies  $> 5$  GeV.

### High Precision Neutron Tracking

The high precision (HP) neutron tracking package can be combined with the QGSP\_BERT and FTFP\_BERT physics list. It provides an increased accuracy for the simulated interactions and timing of low energetic neutrons ( $< 20$  MeV), especially in high  $Z$  absorbers.

## 4.3 Calorimeters

In high energy particle physics and many other fields of application, calorimeters are devices to detect incident particles with the main goal of measuring their energy by initiating respective particle showers fully contained within the instrumented volume. Next to the energy measurement, calorimeters currently employed in running high energy physics experiments, are often used as part of the event trigger or veto logic, for particle identification and for event selection purposes. For precision measurements at future  $e^+e^-$  collider experiments, further exploitation of spatial and time-based shower sub-structure information is investigated on the basis of latest advancements in calorimeter technology.

In the following, the basic concepts and types of calorimeters are summarised, the energy resolution is defined and examples for calorimeters currently in operation are provided. Lastly, the calorimeter response with the focus on hadronic showers is discussed and concepts to overcome potential limitations are presented.

### 4.3.1 Basic Concepts

A calorimeter typically utilises dense absorber material to initiate a particle shower as soon as a particle enters the device. This is done to allow a full energy absorption and avoid shower leakage. Based on that condition, the deposited energy in a calorimeter is proportional to the energy of the projectile particle in general. In order to measure the deposited energy accurately different approaches are used. One approach is the employment of charge-sensitive devices to allow amplification and collection of free charge carriers generated within the energy deposition processes. Another approach is the usage of scintillators coupled to photo-sensitive devices.

Homogeneous calorimeters are systems in which the absorber itself is the sensitive material being able to measure energy depositions by traversing particles. Typically dense scintillating crystals like  $\text{PbWO}_4$  ( $\rho = 8.2 \text{ g/cm}^3$ ) are used to match spatial constraints of such calorimeter implementations. Those materials are coupled to photo-sensitive devices like photo-multiplier tubes or state-of-the-art silicon-based sensors (see Section 5.1.1) in order to detect the emitted photons.

In sampling calorimeters, passive and dense absorber layers alternate with sensitive layers. Therefore, most of the incident particle energy is deposited in the absorber layers without being detected, while only a smaller fraction of the energy is deposited within the sensitive layers. Thus, the measured energy in the sensitive layers is extrapolated to the full particle energy. In contrast to homogeneous calorimeters, the energy resolution (see Section 4.3.2) of sampling calorimeters is degraded, since the fraction of deposited energy in the passive and sensitive layers fluctuates. The fraction of measured energy in the sensitive layers is quantified with the electromagnetic sampling fraction  $f_{\text{sampling}}$ . It is defined as the fraction of energy deposited in the sensitive layers over the total energy deposited by a purely and fully contained electromagnetic shower and can be approximated to:

$$f_{\text{sampling}} \approx \frac{X_0^{\text{sensitive}}}{X_0^{\text{sensitive}} + X_0^{\text{absorber}}} \quad (4.6)$$

with  $X_0^{sensitive}$  the radiation length of one sensitive layer and  $X_0^{absorber}$  the radiation length of one absorber layer. Benefits of sampling calorimeters are the highly flexible choice of absorber material, the sensitive layer technology and the geometrical layout of the full system. Single sensitive layers can easily be replaced and different readout patterns with respect to transversal granularity can be implemented. Additionally, the alternating concept of passive and sensitive layers allows a longitudinal readout granularity. Furthermore, sampling calorimeters are potentially more cost effective and well suited for limited detector volume in comparison to homogeneous calorimeters.

In general, calorimeters are designed and optimised to measure either electromagnetic or hadronic showers. For electromagnetic calorimeters (ECALs), typically both types, homogeneous and sampling calorimeters, are operated and feature high density absorbers (Pb, W) to achieve compact electromagnetic shower development. Typical sampling fractions for sampling ECALs are in the order of at least 5% and is the main driver of the energy resolution [89]. Hadronic calorimeters (HCALs) are commonly designed as sampling calorimeters. Often steel is used as the passive absorber material providing mechanical support at the same time. In comparison to ECALs, the dimension of HCALs have to be significantly larger in order to achieve full hadronic shower containment on average according to  $\lambda_n/X_0 \gg 1$ . Electromagnetic showers can still be measured by HCALs, however, with degraded energy resolution in comparison to ECALs due to a sampling fraction typically in the order of a few percent only. In general, HCALs are not optimised on the sampling fraction since it is not the main driver for the energy resolution, as discussed next.

### 4.3.2 Energy Resolution

The main figure of merit quantifying the performance of a calorimeter is the energy resolution. For most calorimeters the relative energy resolution can be parametrised with three terms added in quadrature as follows:

$$\frac{\sigma_E}{E} = \frac{a}{\sqrt{E}} \oplus \frac{b}{E} \oplus c \quad (4.7)$$

where  $a$  corresponds to the stochastic term, mainly representing intrinsic statistical shower fluctuations [1]. The form of the term can be derived [2] by assuming that the intrinsic shower fluctuations follow Poisson statistics and the calorimeter response is in the first order proportional to the incident particle energy and therefore the number of generated shower particles  $N$ . For sampling calorimeters,  $a$  includes an additional uncertainty by sampling fluctuations scaling proportional to  $1/\sqrt{f_{sampling}}$ . Also included in the term are the fluctuations of the invisible and electromagnetic energy component within the shower, scaling as well with  $1/\sqrt{E}$ ,  $1/E^{\leq 0.5}$  respectively. Those fluctuations are the driving factors for the energy resolution of hadronic showers. The stochastic term is typically in the order of a few  $\%/\sqrt{E}$  for homogenous ECALs,  $\sim 10\%/\sqrt{E}$  for sampling ECALs and in the order of  $60\%/\sqrt{E}$  for sampling HCALs.

The noise term,  $b$ , is energy independent and mostly corresponds to electronic readout noise. Since pedestal level fluctuations of individual readout channels are rather low in comparison to physics signals in modern calorimeter devices, this term dominates at lower energies, if at all. Therefore, it is often omitted when reporting the energy resolution of a calorimeter device.

$c$  represents a constant term. It reflects the maximum achievable relative energy resolution limited only by the quality of the hardware and calibration procedures. The term includes inhomogeneities of the individual readout channels, calibration imperfections, dimensional variations

---

<sup>1</sup>Signal quantum fluctuations like SiPM photo-electron statistics are considered negligible in comparison.

<sup>2</sup>Assuming  $\sigma_E/E = \sqrt{E}/E = 1/\sqrt{E}$ .

in the calorimeter construction, non linearities in the readout electronics, etc. Typically in the order of a few percent, the constant term dominates at highest energies.

For highest particle energies, the calorimeter might not be thick enough to fully contain all hadron showers specifically if the first hadronic interaction happens rather deep inside the calorimeter. Due to shower leakage, the energy resolution might degrade for highest particle energies, which can be parametrised with an additional leakage term scaling with  $E^{-0.25}$ . However, this term can be avoided by selecting events where the first hadronic interaction happens in one of the first layers of the calorimeter.

The currently operating ECAL in the CMS experiment is a homogeneous calorimeter based on lead tungstate ( $\text{PbWO}_4$ ) scintillating crystals achieving an energy resolution of  $2.8\%/\sqrt{E [\text{GeV}]} \oplus 0.3\%$  [90]. Operating as a sampling ECAL, the ATLAS lead liquid argon calorimeter features a sampling fraction of 4 – 6% and reaches an energy resolution of  $10\%/\sqrt{E [\text{GeV}]} \oplus 0.17\%$  [91]. Both experiments use hadronic sampling calorimeters. CMS operates a scintillator-based endcap and barrel calorimeter with brass as absorber material achieving a sampling fraction of about 7% and an energy resolution of  $84\%/\sqrt{E [\text{GeV}]} \oplus 7\%$  for single charged hadrons during beam tests [92]. The ATLAS barrel HCAL is based on scintillating tiles coupled to photo-multiplier tubes via wavelength-shifting fibres and steel absorber achieving a sampling fraction in the order of 3% and an energy resolution of  $52\%/\sqrt{E [\text{GeV}]} \oplus 3\%$  for single charged pions [91, 93].

### 4.3.3 Hadronic Response Compensation

In general, the calorimeter response to the electromagnetic sub-component within hadronic showers,  $e$ , is significantly different compared to the response for the purely hadronic sub-component,  $h$ , due to the different processes during the specific sub-component development and the fraction of invisible energy, as discussed in Section 4.1.3. The ratio of these individual responses,  $e/h$ , defines the level of response compensation a given calorimeter achieves. A calorimeter with  $e/h = 1$  is termed compensating,  $e/h > 1$  undercompensating and  $e/h < 1$  overcompensating. As discussed in Section 4.1.3,  $f_{EM}$  strongly fluctuates from shower to shower and on average increases with the incident particle energy. Therefore, this leads not only to the already discussed degradation of the energy resolution, but also to a non linear energy response for a non-compensating calorimeter. Most calorimeters employed in the past, currently in operation and planned for future experiments are undercompensating devices with a typical  $e/h = 1.5 - 2$ . Different approaches developed to achieve response compensation in a calorimeter are presented briefly in the following.

#### Passive and Sensitive Material Optimisation

To match the electromagnetic sub-component response, the response of the hadronic component can be boosted by the enhancement of the energy depositions by low energy neutrons in the sensitive layers. This can be achieved by using a high  $Z$  material as absorber and a low  $Z$  material within the sensitive layers, since the energy transfer of the neutrons in elastic interactions is maximised if  $\Delta m = |m_{neutron} - m_{target}| = 0$ . By carefully choosing the material and optimising the thickness ratio of the absorber and sensitive layers, the ZEUS sampling calorimeter achieved a near perfect compensation of  $e/h = 1.00 \pm 0.03$  [94] with the combination of U ( $Z = 82$ ) absorbers and plastic scintillator readout. A single charged pion energy resolution of  $35\%/\sqrt{E [\text{GeV}]} \oplus 2\%$  could be reached [94], considered as the best hadronic energy resolution of a hadronic sampling calorimeter achieved to this day.

### High Granularity and Software Compensation

With a high spatial resolution it is possible to identify the electromagnetic sub-component within the hadronic shower by investigating the shower topology or measuring the local hit energy density. This information can be exploited to reweight the whole reconstructed shower energy or individual hit energies within the shower sub-structure. With this method significant improvements for the energy resolution of hadrons were achieved in various experiments and calorimeter prototypes in beam tests [95, 96].

### Dual Readout

Next to an active medium measuring energy depositions by ionisation processes, a second separated active medium, typically non-scintillating quartz fibres, can be used to measure generated Cherenkov radiation. With this second measurement, the approach aims to estimate the energy fraction of the electromagnetic sub-component for each hadronic shower. Based on this information, a shower-by-shower energy reweighting can be introduced to achieve an effective response compensation [97, 98].

## 4.4 Particle Flow Reconstruction

At future lepton collider experiments, important physics processes are often characterised by multi-jet final states, as discussed in Section 3.1.1. Many of these jets originate from  $W$  or  $Z$  bosons decaying into a pairs of quarks. Therefore, one of the goals at such experiments is a sufficient separation of the two heavy gauge bosons within the reconstructed di-jet invariant mass spectrum. In order to achieve this, a challenging requirement for the jet energy resolution of the detector system is set:  $\sigma_E/E < 4\%$  for jet energies of 40-250 GeV at the ILC [56] and  $\sigma_E/E < 5\%$  for jet energies up to 1 TeV at CLIC [99].

With the classical approach to calorimetry, a stochastic term in the order of  $60-100\%/\sqrt{E}$  [GeV] for the jet energy resolution is achieved, which does not fulfil the defined requirement. The particle flow reconstruction is a concept specifically developed to overcome this limitation, which mainly originates from the poor hadronic calorimeter energy resolution. In the following sections, the basic concept and its limitations are summarised and the particle flow algorithm PandoraPFA is introduced. Furthermore, implications for potential detector systems are discussed and the projected jet energy resolution performance based on an ILD simulation study is presented.

### 4.4.1 Basic Concept

The paradigm of the particle flow reconstruction is to trace the flow of each individual particle in an event through the full detector system and use the energy measure of the sub-detector providing best resolution. Instead of classically summing up the total energy deposited in the ECAL and HCAL systems, one exploits the precise momentum measurement of the tracker for all charged particles. Consequently, the energy measure of the ECAL and HCAL system is only used for photons and neutral hadrons, as visualised in Figure 4.9. With this concept, the poor hadronic energy resolution of the HCAL in the order of  $60\%/\sqrt{E}$  [GeV] is in principle omitted for all charged hadrons. Instead, the tracking system precisely measures the momentum, based on the curvature of the charged particle track in the magnetic field, providing an energy measure<sup>3</sup> with an relative

<sup>3</sup>By assuming that the rest mass of the particle is negligible in comparison to its momentum.

energy resolution typically scaling with  $0.01\% \times E$  [GeV] [100]. In final state jets,  $\sim 60\%$  of the energy is carried by charged particles well below 300 GeV, even for collision energies much higher than 1 TeV [101]. The fraction of energy carried by photons and neutral hadrons in such jets typically corresponds to  $\sim 30\%$ ,  $\sim 10\%$  respectively. This demonstrates the potential gain of the particle flow reconstruction towards the desired jet energy resolution, since only a small fraction of the total jet energy still relies on the poor energy measure of the HCAL.

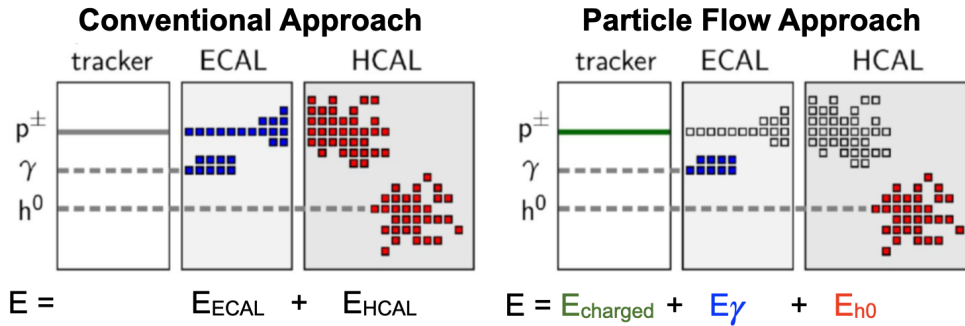


Figure 4.9: Illustration of particle flow reconstruction in comparison to conventional approach for energy reconstruction. Taken and edited from [80].

#### 4.4.2 Limitations

The concept of particle flow requires a precise reconstruction of all individual final state particles within the detector system for each event. This requirement introduces different challenges within the reconstruction resulting in limitations of the concept. While the momentum measure of the tracking system is utilised for all charged particles in a jet, the energy depositions by initiated particle showers still remain in the calorimeter systems. The energy of the charged particles would be counted twice, if both of these measures would be used within the energy reconstruction. Therefore, it is a crucial part of the particle flow reconstruction to precisely identify charged particle energy depositions in the calorimeter systems and subsequently discard them, after a measured track got associated. During the reconstruction, two types of mistakes, in the following referred to as a specific type of confusion, might occur distorting the total energy reconstruction.

##### Lost Neutral Confusion Energy

Energy depositions caused by a neutral particle (e.g. a photon in the ECAL or a neutral hadron in the HCAL) are misclassified as charged particle energy depositions and are subsequently discarded, resulting in a loss of neutral particle energy. Typically this type of confusion appears if a charged and neutral particle shower are situated very close to each other. While Figure 4.10a illustrates a well reconstructed event, this type of confusion is schematically depicted in Figure 4.10b showing a misclassification of all neutral hadron energy depositions in the vicinity of close-by charged hadron energy depositions.

### Double Counted Charged Confusion Energy

Energy depositions caused by a charged particle are misclassified as neutral particle energy depositions. The corresponding energy is counted twice: first from the charged particle track information, second from the utilisation of the calorimetric energy measure. Figure 4.10c illustrates this type of confusion for the case of misclassified charged hadron energy depositions reflecting part of the shower sub-structure.

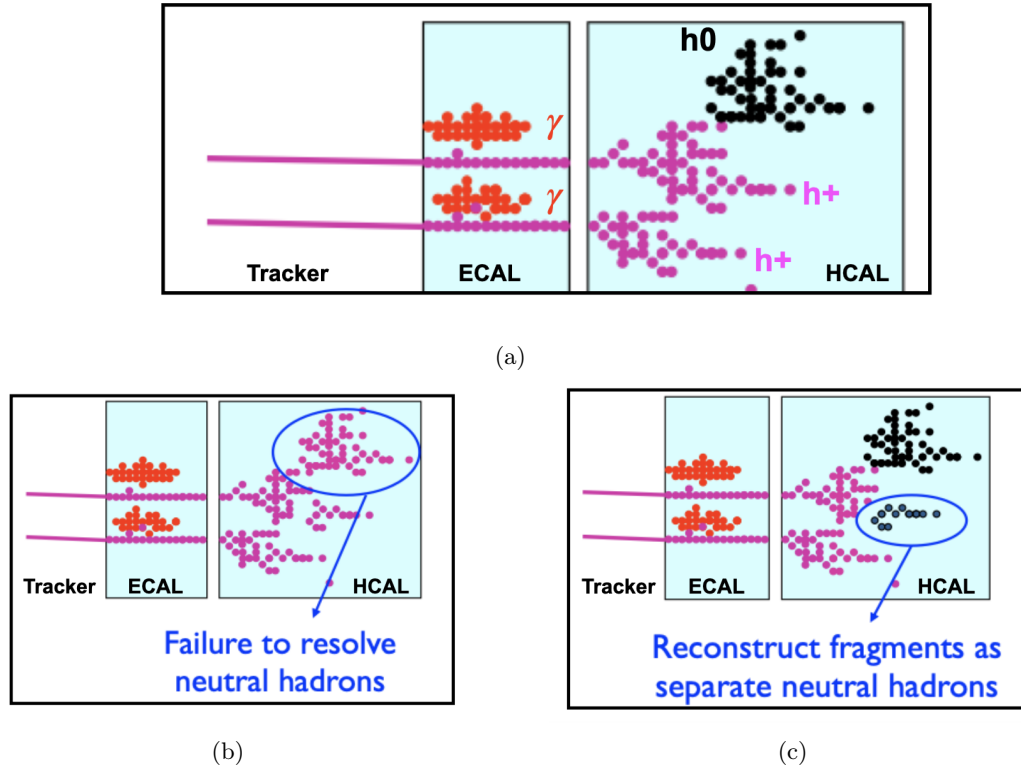


Figure 4.10: Schematic example event illustrating the two types of confusion: **(a)** Correctly reconstructed event reference with labeled photons ( $\gamma$ ), charged ( $h^+$ ) and neutral hadrons ( $h^0$ ). **(b)** Event with lost neutral confusion energy. **(c)** Event with double counted charged confusion energy. Pictures taken and modified from [102].

The combination of the level and balance of the two confusion types impacts the total reconstructed event energy and is therefore one of the driving factors for the achievable jet energy resolution. In general, confusion effects become the limiting factor for jet energies higher than  $\sim 100$  GeV, since the density and multiplicity of particles within jets increase with increasing jet energy. This results in a higher probability of overlapping particle showers in the calorimeter systems. The increased reconstruction complexity of individual energy depositions increase the average probability for confusion and consequently leads to a degradation of the jet energy resolution. For lower jet energies, the particle multiplicity and density within a jet is on average lower as well.

This effectively results in less individual and more separated particle showers in the calorimeter systems. Therefore, in the lower energy range the jet energy resolution is not limited by confusion effects but by the intrinsic energy resolution of the calorimeter systems, mainly dominated by the measurement of neutral hadrons in the HCAL.

In order to minimise the level of confusion effects, it is crucial to correctly assign the tracks of charged particles to their corresponding energy depositions in the calorimeter systems. To succeed with this non-trivial task, specific requirements have to be fulfilled. The calorimeter systems have to be finely segmented to be able to resolve energy depositions from close-by particle showers and sophisticated pattern recognition algorithms have to be employed for a correct classification of the energy depositions of individual particles. Both requirements are discussed in more detail in the next sections.

### 4.4.3 PandoraPFA

The Pandora Particle Flow Algorithm (PandoraPFA) is a highly recursive algorithm chain employing sophisticated pattern recognition algorithms [100, 103]. Despite being originally developed for the application in a future lepton collider experiment over a decade ago, it nowadays finds many other applications like in liquid argon-based detector systems for neutrino experiments [104]. To this day, it is still widely considered as state of the art in particle flow reconstruction<sup>4</sup>. In the following, a brief overview about the main algorithm classes in PandoraPFA and the implementation of the framework for a future lepton collider experiment, relevant for the studies presented in this thesis, is provided.

#### 4.4.3.1 Algorithm Overview

Providing the input of charged particle tracks and calorimeter energy depositions, so-called particle flow objects (PFOs) are reconstructed and given as an output by PandoraPFA. The reconstruction chain can be separated in two preparation steps and six main classes of pattern recognition algorithms, as illustrated in Figure 4.11 and introduced in the following. More details about the individual steps and possible extensions can be found in [99, 100, 107].

#### Track Preparation and Selection

The reconstructed input tracks are prepared for further processing and classified according to their topology. The primary goal at this stage is to identify kinks and  $V^0$  decays<sup>5</sup>. The information gained at this step is used again in the final PFO construction.

#### Calorimeter Hit Preparation

Simulated and digitised calorimeter hits of the various calorimeter sub-systems are read in to the PandoraPFA framework. The hits are sorted into so-called pseudo-layers to minimise dependencies of the algorithm to specific detector geometries. Pseudo-layers are characterised by the integrated thickness of material, in units of  $X_0$  and  $\lambda_n$ , from the centralised interaction point towards the end of the calorimeter systems to serve as a scale for shower development parametrisation within the reconstruction. Furthermore, an energy deposition threshold is applied on calorimeter channel

<sup>4</sup>Parts of the concept were already used in the H1 experiment at HERA [105] and to this day in the CMS experiment at LHC [106]

<sup>5</sup>Like  $K_S^0 \rightarrow \pi^+\pi^-$  or  $\Lambda \rightarrow p\pi^-$

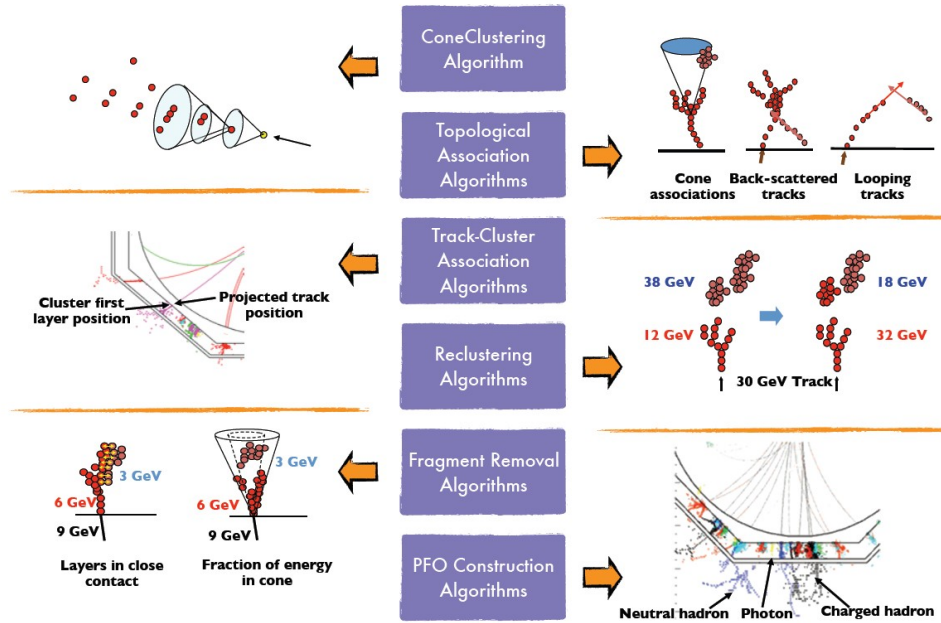


Figure 4.11: Overview of main algorithm classes in PandoraPFA. Taken and edited from [102].

level for noise rejection. In addition, based on topological and energetic conditions, hits are might be flagged as isolated or MIP-like at this stage.

### Initial Cone Clustering

The clustering algorithm is seeded at the point on the ECAL front face where the projection of a charged particle track ends. Looping over all calorimeter hits of a specific pseudo-layer, the algorithm evaluates if a hit is situated within a cone of fixed dimensions lining up with the cluster direction. If this is the case, the hit is added to the cluster. If the hit can not be associated to any of the current calorimeter clusters at all, it is used as a new cluster seed.

### Topological Associations

The initial cone clustering algorithm is configured to rather form smaller and split clusters within a given particle shower than accidentally merging energy depositions originating from different particles showers. In this subsequent step, the clusters are carefully merged according to well-defined topological rules by various topological association algorithms. Energy depositions caused by a back-scattering particle within the shower is subject of these algorithms for example.

### Track to Cluster Associations

This class of algorithm associates the pre-processed tracks to the best current cluster candidate. Within this process the track momentum and cluster energy is compared and the track direction and cluster orientation is taken into account.

### Recursive Re-clustering

Depending on the level of agreement between track momentum and charged cluster energy, a re-clustering iteration is initiated. This includes the employment of a set of specifically tune cone clustering algorithms (with different cone sizes) followed by a re-running of topological and track to cluster association algorithms. This process is repeated recursively until an optimal configuration of tracks and clusters is found. The agreement of track momentum  $p_{track}$  and cluster energy  $E_{cluster}$  is defined as:

$$\chi = \frac{E_{cluster} - p_{track}}{\sigma} \quad (4.8)$$

with  $\sigma = 60\% \sqrt{p_{track} [\text{GeV}] \text{GeV}}$  corresponding to the estimated absolute energy resolution of the calorimeter systems for hadrons of energy  $p_{track}$ . Depending on the specific type of re-clustering algorithm, a re-clustering iteration is typically triggered if the current track to cluster configuration results in  $|\chi| > 2.5-3.0$ . As Equation 4.8 illustrates, the achievable single particle energy resolution (specifically for the HCAL) is beneficial for the pattern recognition performance at this step. If no configuration is found satisfying a minimal requirement on  $\chi$  at all, so-called forced clustering algorithms take over. Those algorithms ignore topological rules of the pattern recognition to a larger extent and are implemented to achieve a reasonable track momentum to cluster energy agreement as a last instance.

### Photon Recovery and Fragment Removal

Based on well-defined electromagnetic shower profiles, topological likelihood data is exploited to identify and flag photon clusters. In addition, photon clusters merged into charged hadron clusters in the previous steps are identified and recovered as neutral particles clusters. In addition, parts of the charged hadron shower sub-structure, potentially misclassified as neutral hadron clusters, are merged back into the parent charged cluster. During this process, the algorithms are constantly taking into account the old and new track momentum to charged cluster energy agreement.

### PFO Construction

Lastly, reconstructed particles in form of PFOs are formed. While the associated track momenta are used for the charged particle clusters, the calorimeter measures are used for the energy reconstruction of the neutral clusters.

Throughout the reconstruction process, energy scale factors are applied on the cluster energy as soon as the type of particle shower is classified. Different scale factors for electromagnetic and hadronic showers are used to correct for non-compensating effects of the different calorimeter systems and cut isolated calorimeter energy depositions in a first step. Details about the PandoraPFA scale factors and their determination are provided in [107]. A more sophisticated compensation method is implemented for hadrons in the HCAL as an optional plugin in addition. Software compensation on hit level, see Section 4.3.3, is used for a more precise comparison of track momenta and cluster energies. This effectively results not only in an improved pattern recognition, but also in an improved intrinsic energy resolution of the identified neutral hadrons and, therefore, the jet energy resolution [108].

#### 4.4.3.2 Implementation

For application to a future lepton collider experiments, PandoraPFA<sup>6</sup> is implemented in the MARLIN C++ framework [109]. DDMarlinPandora<sup>7</sup> serves as the centralised interface processor steering the PandoraPFA algorithms, detector geometry model and the input and output data flow. More details are provided in Section 8.2.1. In recent years, significant developments of the interface and modular application of PandoraPFA have been made. The current implementation features a very high degree of flexibility in the choice of detector geometry, algorithm settings, input and output options and potential usage of plugins. With adaptations in the interface processor and in the steering configurations, it is now possible to test and run PandoraPFA on individual sub-detector components, easily change internal algorithm settings or modify parts of the algorithm itself.

The generic PandoraPFA framework is provided in the public Pandora Software Development Kit (PandoraSDK)<sup>8</sup> allowing for spin-off developments of particle flow pattern recognition algorithms. One example is ArborPFA (now AprilPFA), developed on the basis of a more topology-based reconstruction approach suited for gas-based digital readout calorimeter systems [110].

#### 4.4.4 Requirements for a Particle Flow Detector System

To allow for a sufficient particle flow reconstruction performance, several requirements for the overall detector system are set. In the following, these requirements are briefly summarised describing a particle flow optimised detector system:

- To allow proper track to calorimeter cluster associations, the un-instrumented matter between the central tracking system and the ECAL and the ECAL and HCAL should be minimised. This reduces potential track distortions by multiple scattering.
- As a consequence, the calorimeter systems must be located within the magnetic coil of the experiment. Based on this requirement, the calorimeter systems have to be designed in a compact way to reduce the total volume, consequently the magnetic coil radius and therefore the total costs of the experiment. Passive cooling schemes help to further reduce the volume, which active cooling elements would potentially need.
- Since the calorimeter systems are well placed within the magnetic field of the experiment, all detector components should be highly in-sensitive to magnetic fields.
- In order to sufficiently resolve individual energy depositions of close-by particle showers and fully exploit the pattern recognition within the particle flow algorithms, finely segmented highly granular calorimeter systems are required.

These requirements are fulfilled by the particle flow optimised detector systems introduced in Chapter 3. Different studies based on event simulations in these detector systems and subsequent particle flow reconstruction have been performed to evaluate the projected reconstruction performance at a future lepton collider experiment. One of this studies is exemplarily presented in the next section.

---

<sup>6</sup> <https://github.com/PandoraPFA/LCContent>

<sup>7</sup> <https://github.com/iLCSoft/DDMarlinPandora>

<sup>8</sup> <https://github.com/PandoraPFA/PandoraSDK>

#### 4.4.5 PandoraPFA Jet Energy Resolution for ILD Simulations

Various studies for simulated jets in ILD have been performed to quantify the projected jet energy resolution achievable with PandoraPFA reconstruction [56, 107, 108]. Within this studies, typically simulations of off-shell  $Z$  bosons decaying at rest into light quarks (u,d,s) are utilised resulting in two mono-energetic back-to-back jets, as illustrated in Figure 4.12a. In general, no background is assumed in these benchmarking studies and only events with  $|\cos(\theta)| < 0.7$ , where  $\theta$  is the polar angle of the di-jet system, are taken into account. With these requirements it is ensured, that the overlapping regions of barrel and endcaps are avoided and no energy leaks along the forward/backward beam axis.

If all particle showers would be sufficiently contained in the calorimeters and all track to charged cluster associations would be perfectly made, the reconstructed jet energy spectrum should ideally be Gaussian. In a realistic scenario, due to shower leakage and confusion effects, the distribution is distorted and features tails. Taking into account the whole distribution for a resolution measure would consequently exaggerate the influence of those tails. Therefore,  $Mean_{90}$  and  $RMS_{90}$  are introduced to cancel the effect of these tails and establish a jet energy resolution metric more robust and instructive for various data sets [100]. They are defined as the mean and the root mean square of a specific distribution range, in which a minimal RMS is achieved including 90% of the events. Based on these quantities, the relative single jet energy resolution ( $\sigma_{E_J}/E_J$ ) for the jet energy  $E_J$  is defined as follows:

$$\frac{\sigma_{E_J}}{E_J} = \frac{RMS_{90}(E_J)}{Mean_{90}(E_J)} \quad (4.9)$$

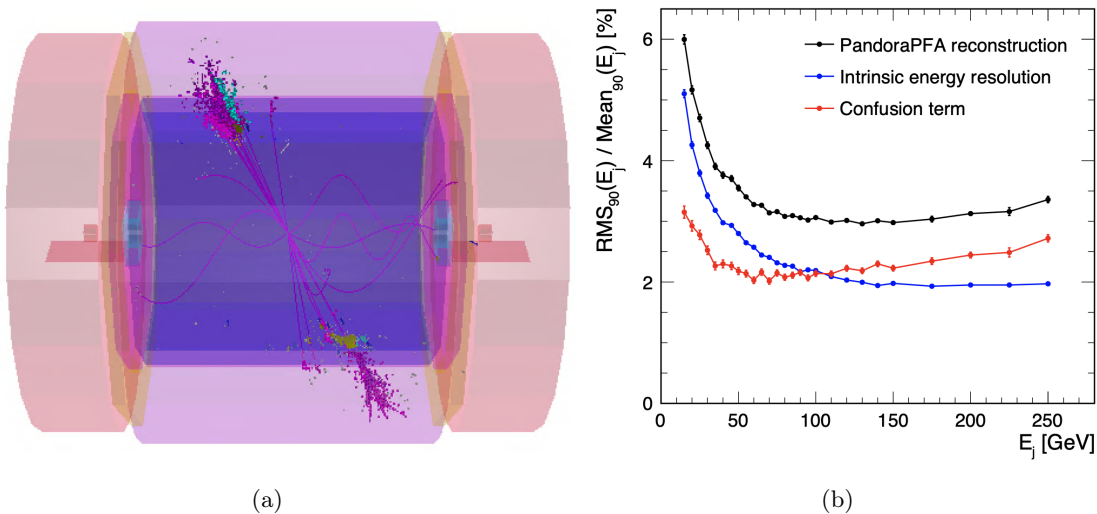


Figure 4.12: (a) Event display of a simulated 500 GeV  $Z \rightarrow qq$  (uds) di-jet event within the ILD detector system. (b) Achieved jet energy resolution over jet energy with PandoraPFA reconstruction for  $Z \rightarrow qq$  (uds) di-jet events in ILD [108].

Figure 4.12b shows the achieved single jet energy resolution with PandoraPFA for investigated di-jet event energies of 40 – 500 GeV in the ILD detector. Additionally, the decomposition of the single jet energy resolution into the contribution of the intrinsic calorimeter system energy

resolution<sup>9</sup> and the contribution caused by confusion effects is presented [108]. In general the observed limitations in this study agree with the expectations discussed in Section 4.4.2. At lower energies, the intrinsic energy resolution of the calorimeter systems, mainly caused by the measurement of neutral hadrons in the HCAL, dominates. With growing energy, the intrinsic energy resolution improves. The confusion term initially improves as well due to the improving track momentum to calorimeter cluster energy comparison provided by the improved intrinsic calorimetric energy resolution. For higher energies, the confusion term becomes the dominant limitation due to the higher particle multiplicity and density within jets resulting in more difficult scenarios for the particle flow reconstruction. Lastly and most importantly, it is shown that the ambitious goal of a relative single jet energy resolution  $< 4\%$  for jet energies of 40-250 GeV at the ILC is achievable.

## 4.5 The CALICE Collaboration and Highly Granular Calorimeters

To fully exploit the benefits of using the particle flow reconstruction at a future linear lepton collider experiment, the CALICE (CALorimeter for LInear Collider Experiment) collaboration leads developments of highly granular electromagnetic and hadronic sampling calorimeters. The collaboration currently consists of  $\sim 336$  physicists and engineers from 60 institutes in 18 countries [111]. The rich spectrum of various detector concepts under investigation differ by the used absorber material and readout technology.

Over the last two decades two generations of calorimeter prototypes have been realised within CALICE. First the physics prototypes, which had the main goal to demonstrate the physics performance of the various detector concepts in particles beams at CERN, Fermilab and DESY. The second generation of technological prototypes is designed to prove successful integration and scalability to a full linear collider detector by significantly raising the number of instrumented channels while keeping the compact layout and demonstrating the desired pulsed power scheme.

Besides the effort of building a particle flow calorimeter for a future lepton collider experiment, a collaboration with the LHC community for the HL-LHC upgrade of the CMS end-cap calorimeter is ongoing. Large parts of the so-called high granularity calorimeter (HGCal) will consist of  $\sim 389000$  CALICE inspired silicon-photomultiplier on scintillating tile channels, benchmarking the next step on the ladder of scalability [112]. In the following sections, a brief overview of the different calorimeter concepts and prototypes of CALICE is provided.

### 4.5.1 Electromagnetic Calorimeters

Two different electromagnetic sampling calorimeter concepts are actively developed by the CALICE collaboration: the silicon tungsten electromagnetic Calorimeter (SiW-ECAL) [113] and the scintillator tungsten electromagnetic calorimeter (ScW-ECAL) [114]. Both calorimeters use tungsten as absorber material due to its relatively small Moliere radius of around 9 mm allowing for compact electromagnetic showers and therefore not only for a compact design, but also for a lower probability of overlapping showers.

The SiW-ECAL physics prototype features 30 active layers consisting of 525  $\mu\text{m}$  thick high-resistivity silicon wafers [113]. Each of the layers has an active area of 18 cm  $\times$  18 cm, with the

<sup>9</sup>Extracted by cheating a perfect pattern recognition without any confusion based on simulated Monte-Carlo truth information.

individual PIN diodes covering this area are of size  $1\text{ cm} \times 1\text{ cm}$ . The prototype features a total of 9720 channels. With an increasing thickness of the tungsten absorber by depth, the prototype features a total of  $24 X_0$ . In various beam test campaigns at DESY and CERN, an energy resolution of  $16.53\%/\sqrt{E} \oplus 1.07\%$  for electrons was achieved [115].

The ScW-ECAL physics prototype consists of 30 active layers alternating with tungsten absorber plates of 3.5 mm thickness summing up to a total of  $20 X_0$  [114]. 18 scintillator strips of the size  $45\text{ mm} \times 10\text{ mm} \times 3\text{ mm}$  in four rows yield as the active material. The emitted scintillation light is guided through wavelength-shifting fibres and read out by silicon photomultipliers, which are discussed in the Section 5.1.1. This makes a total of 2160 readout channels. Since the strips are oriented orthogonally in consecutive layers, an increase of the effective granularity by a strip splitting algorithm (SSA) has been studied extensively [116]. During operation at Fermilab in 2009 the prototype achieved an energy resolution of  $12.5\%/\sqrt{E} \oplus 1.2\%$  for electrons [117].

While the performance of both physics prototypes was extensively studied in particle beams at several beam test campaigns, the technological prototypes are being currently commissioned and prepared for first beam tests.

#### 4.5.2 Hadronic Calorimeters

Similar to the electromagnetic calorimeters, the CALICE collaboration is actively developing different hadronic calorimeter concepts as well. The main differences of these concepts are the level of granularity and the readout technology in terms of processing the amplitude information. While the analog option in the form of the AHCAL, extensively discussed in Chapter 5, is based on the measurement of the full analog information, the digital calorimeter options mainly rely on the counting of the number of energy depositions (calorimeter hits) in their very fine segmented grid of channels.

The digital hadron calorimeter (DHCAL) is based on gaseous resistive plate chamber (RPC) technology [118]. Using a 1-bit readout system, one relies on the first order assumption that the number of hits over a set threshold is proportional to the total energy deposition of the incident particle showering in the calorimeter. One of the earlier prototype configurations features  $\sim 380\text{ k}$  channels, each of the size  $1\text{ cm} \times 1\text{ cm}$ . With an active area of  $\sim 1\text{ m} \times 1\text{ m}$  each, the 38 layers are located within a steel absorber stack of 1.75 cm thickness per layer [119]. During beam test campaigns at Fermilab in 2010-2011, a single particle energy resolution of  $34.6\%/\sqrt{E} \oplus 12.5\%$  for positrons and  $51.5\%/\sqrt{E} \oplus 10.6\%$  for pions were achieved [120, 121].

Using the same technology, the semi-digital hadron calorimeter (SDHCAL) additionally features a 3-bit readout system. Three coarse thresholds for the analog charge can be set internally to have an additional estimate on the number of particles transversing an individual channel and therefore additional information on local energy densities within the shower development can be derived [122]. In 2012, a beam test campaign at the SPS CERN was carried out for the current SDHCAL prototype. It consists of 442368 channels (each  $1\text{ cm} \times 1\text{ cm}$ ) on 48 active layers between 1.5 cm thick steel-absorber plates [122]. For these beam test measurements of 30 GeV charged pions, a relative energy resolution of  $\sim 12.9\%$  and for 80 GeV pions  $\sim 7.7\%$  was reached [123]. More details about the (semi-)digital calorimeters and a detailed comparison study to the analog concept can be found in [124].



# 5 The CALICE Analog Hadron Calorimeter Prototype

The Analog Hadron Calorimeter (AHCAL) concept is a hadronic sampling calorimeter technology developed within the CALICE collaboration. The concept is based on a finely segmented grid of channels, which consist of individual scintillating tiles each coupled to an optical readout in the form of a silicon photomultiplier (SiPM). This allows not only a dedicated spatial reconstruction of an energy deposition within the calorimeter (calorimeter hit coordinate), but also the reconstruction of the deposited energy and the hit time. In contrast to the AHCAL physics prototype [125], the AHCAL technological prototype, in the following simply referred to as AHCAL prototype, features a higher number of channels and a higher degree of uniformity by using the same scintillating tile size and the same type of SiPM for all individual channels. In total the AHCAL prototype features  $\sim 22\,000$  readout channels on 38(39) active layers. These layers are alternating with 1.72 cm thick steel absorber plates adding up to a total of  $\sim 4\lambda_n$ . The high transversal and longitudinal granularity allows for particle shower imaging capabilities to fully exploit particle flow algorithms like PandoraPFA. Central features are the fully integrated front end readout electronics, which can be operated in pulsed power mode providing a passive cooling scheme, and the internal LED system for SiPM calibration. In addition, the AHCAL prototype satisfies spatial constraints for a possible integration into a particle flow optimised full collider detector system like ILD. The scalability of the concept to such a system, where it would feature  $\sim 8\text{M}$  readout channels, is demonstrated by decentralised and fully automatised assembly, quality control and calibration procedures of the individual prototype components [1, 126].

In the following sections, the main components of the AHCAL prototype are introduced in detail starting at the channel level and ending at the assembled base units (Sections 5.1-5.3). After that, an overview about the different beam test campaigns at the SPS CERN and the recorded data with the AHCAL prototype is provided in Section 5.4, which is the basis for the analyses presented within the scope of this thesis. Lastly, the calibration procedure and results of the individual channel calibration is presented in Section 5.5. This includes a detailed uniformity study of the un-calibrated channel properties and the operation and calibration stability of the prototype.

## 5.1 The SiPM-on-Tile Concept

Since the early 2000s, the combination of scintillators and photosensors for usage in highly granular calorimeters has been extensively considered within CALICE [127], mainly due to developments and improvements in the field of pixelated photosensors over the last decades. The combined concept was therefore studied extensively (as in [128, 129]) and excellent results were achieved

e.g. in terms of light yield, response uniformity and signal to noise ratio. As well as the excellent intrinsic performance of the technology, it has multiple advantages like its flexibility in terms of high granularity applications and its insensitivity to magnetic fields. This makes them well suited for use as the active element in a hadronic sampling calorimeter like the AHCAL prototype. Previous AHCAL prototypes used to feature wavelength shifting fibres as an intermediate step between scintillator and photosensor to guide and convert the scintillation light to the required absorption regime [125]. In recent years the paradigm has changed to surface mounted directly coupled components due to various developments in the area of photosensors. In the following sections the two individual components, SiPMs and scintillating tiles, are discussed in more detail.

### 5.1.1 Silicon Photomultipliers

A silicon photomultiplier (SiPM) is a semi-conductor sensor for the detection of photons in the near visible and visible energy range. Since being invented in the 1990's [130] the device has been constantly optimised and is now well established in particle physics and industrial applications. Benefits and driving factors for its development were: the small sensor size (order of  $\text{mm}^3$ ), the single photon detection capabilities, the insensitivity to magnetic fields and the exceptional fast timing properties ( $\sim 100$  ps FWHM for single photons [131]) compared to other types of photosensors. These properties make the SiPM an attractive alternative to photo multiplier tubes (PMTs), which were the conventional photo detectors in particle physics for decades.

A single SiPM pixel consists of an avalanche photo diode (APD), as illustrated in Figure 5.1a, and is based on a pn-junction in silicon. In this junction a depletion region with a strong electric field is created if a bias voltage<sup>1</sup> ( $V_{bias}$ ), which is higher than its specific breakdown voltage ( $V_{breakdown}$ ) is applied to the APD. In this mode a single incident photon is capable of triggering a so-called Geiger discharge. A photon absorbed in the depletion region creates an electron-hole pair by the photo electric effect. The resulting free charge carriers are subsequently accelerated by the electric field and undergo impact ionisation creating more electron-hole pairs and thereby create a charge avalanche. The probability that an incident photon triggers an avalanche process is called the quantum efficiency or photon detection efficiency (PDE). To quench the avalanche, a quenching resistor ( $O(1 \text{ M}\Omega)$ ) is connected in series to reduce the effective voltage of the APD below  $V_{breakdown}$  at a certain point in the avalanche process. The charge generated in this process equals:

$$Q = C_{pixel} \cdot (V_{bias} - V_{breakdown}) \quad (5.1)$$

where  $C_{pixel}$  is the capacitance of the APD (typically on the order of pF).  $Q$  is defined as the intrinsic gain of the SiPM. Depending on the type of SiPM gains of  $10^5 - 10^7$  are achieved, comparable to the gain of a typical PMT. After a Geiger discharge has stopped, the pixels' effective voltage returns to  $V_{bias}$ . The recovery time of a pixel is typically of the order of a hundred nano seconds and therefore corresponds to the time the same pixel is ready for the next photon to trigger an avalanche.

The SiPM consists of an array of APDs (pixels) connected in parallel, as illustrated by the circuit diagram in Figure 5.1b. Therefore, the total output signal of the SiPM is the sum of all quasi simultaneously triggered SiPM pixels resulting in a binary response mode. Since to a first order approximation each pixel on the SiPM releases the same charge if triggered, as illustrated in Equation 5.1, the output signal of the SiPM equals to an integer multiple of this charge, consequently showing how many photons are detected. Due to the capability of single photon sensitivity, the

---

<sup>1</sup>Typically  $V_{bias} = 30 - 60\text{V}$

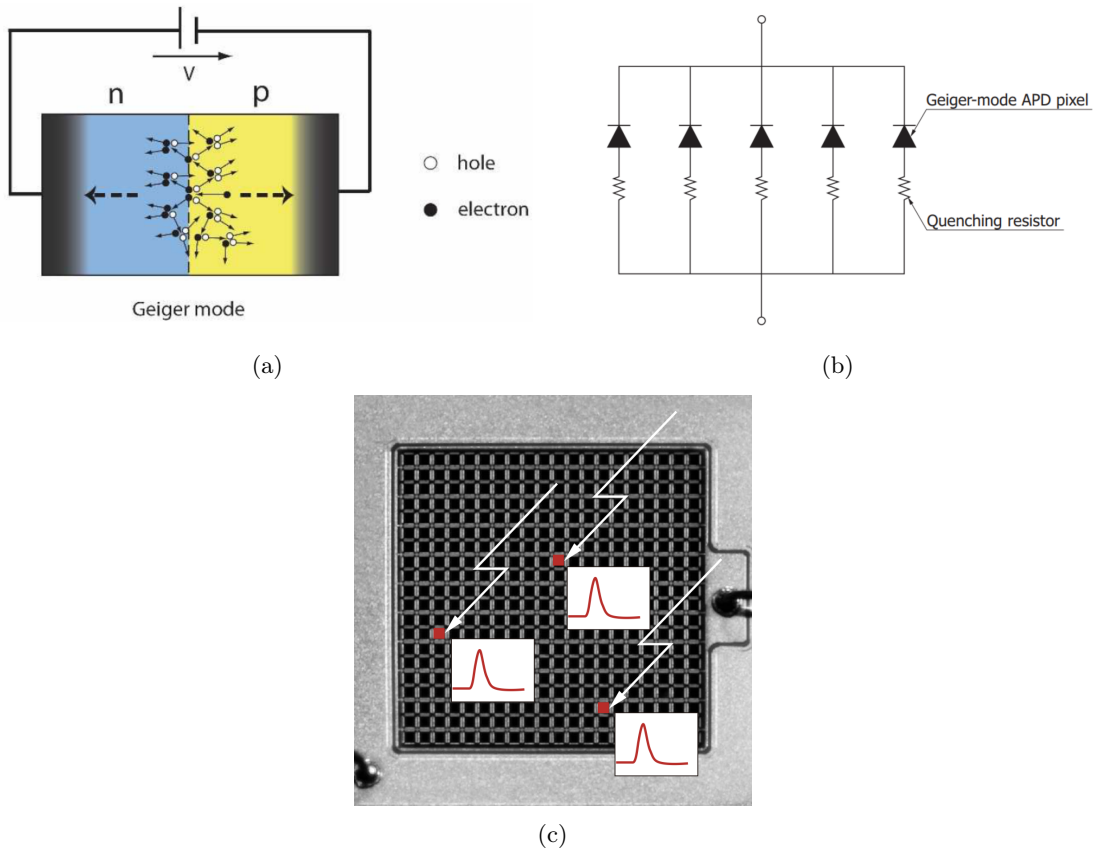


Figure 5.1: Illustration of the working principle of silicon photomultiplier: (a) APD in Geiger mode with a charge avalanche in the depletion area [130]. (b) Circuit diagram of five APDs and quenching resistors connected in series [132]. (c) Close-up picture of a SiPM including illustration of three photons triggering APDs resulting in analog waveforms [132].

SiPM signal is often quoted in units of pe (photon equivalents). This concept is visualised in Figure 5.1c which shows an example SiPM with three incident photons creating a 3 pe signal. Following this concept, one can measure the SiPM gain in-situ<sup>2</sup> by recording single photon spectra while the SiPM is illuminated with light pulses, as explained in Section 5.5.3.

If the finite number of SiPM pixels is too low or the light intensity too high, multiple photons could hit the same SiPM pixel before it has recovered. Since these photons remain undetected, this leads to a non-linear SiPM response in form of a saturation effect, exemplarily depicted in Figure 5.2a. To first order approximation it can be parametrised by:

$$N_{fired}^{sat} = -N_{total} \cdot \left( 1 - e^{-\frac{N_{\gamma} \cdot PDE}{N_{total}}} \right) \quad (5.2)$$

where  $N_{fired}^{sat}$  is the number of fired SiPM pixels,  $N_{total}$  is the total nominal number of SiPM pixels

<sup>2</sup>By assuming a good pixel capacity uniformity and low-noise amplification within the detector system.

and  $N_\gamma$  the number of incident photons. To achieve a linear response, one can apply an inverse function of Equation 5.2 for a de-saturation of the SiPM response, as discussed in Section 5.5.6.

One of the downsides of the SiPM technology is the presence of thermal noise and related lattice effects. Thermally induced crystal lattice excitations (phonons) are able to create electron-hole pairs in the depletion region of the silicon, even if the SiPM is not illuminated by photons at all. These electron-hole pairs are able to trigger a Geiger discharge in the corresponding APD resulting in a thermal noise signal or dark count, which is not distinguishable from a signal triggered by a photon. The dark count rate depends on the specific type of SiPM and is inherently strongly temperature dependent. Another effect is optical inter-pixel cross-talk within a SiPM. It occurs if electrons and holes recombine during the avalanche process creating photons which can propagate to a neighbouring APD and trigger another Geiger discharge almost simultaneously. The probability of this process occurring is typically on the order of a few percent and can be reduced by adding trenches or optical absorbers between the pixels of the SiPM. Lastly, charge carriers trapped in lattice defects within the silicon during the avalanche process and released with a short delay could trigger a secondary slightly delayed avalanche process. These afterpulsing effects typically occur 10 – 100 ns after the start of the initial avalanche.

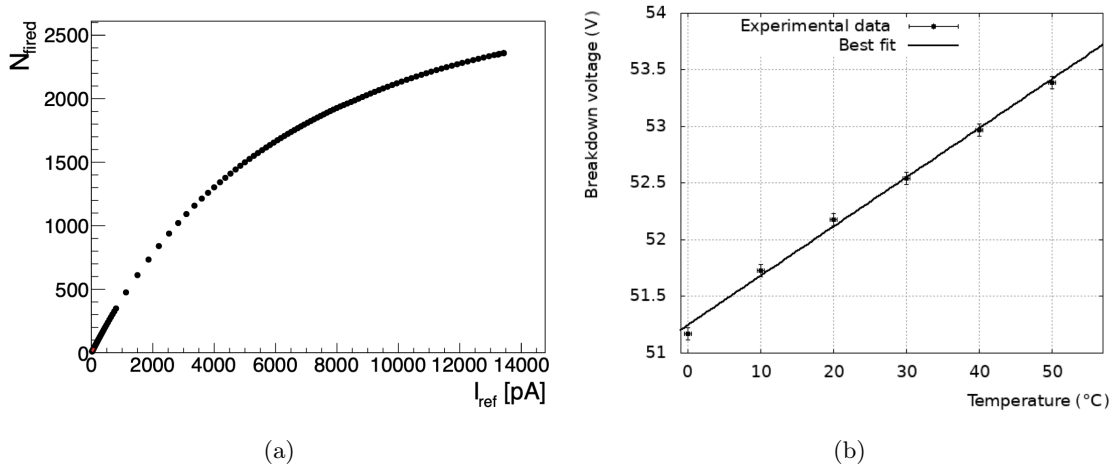


Figure 5.2: (a) Number of fired SiPM (MPPC S13360-1325PE) pixels versus current of illumination diode [133]. (b) Breakdown voltage versus temperature (SiPM: MPPC S13360-1350C) [134].

In general the introduced SiPM characteristics are strongly dependent on the operation temperature [135]. For example the dark count rate decreases typically exponentially with decreasing temperature, due to a decreasing probability of lattice oscillations. Another example is the breakdown voltage  $V_{\text{breakdown}}$ , which increases proportionally with temperature as illustrated in Figure 5.2b. If the bias voltage  $V_{\text{bias}}$  is kept constant in this scenario, the over voltage  $V_{\text{over}}$  decreases according to:

$$V_{\text{over}} = V_{\text{bias}} - V_{\text{breakdown}} \quad (5.3)$$

which will lower the electric field in the depletion region and therefore reduces the gain of the SiPM. This anti-proportional behaviour of gain and temperature is typically on the order of 1%/K. For this reason,  $V_{\text{bias}}$  has to be adapted according to temperature changes in order to keep the SiPM gain constant (see Section 5.4 and 5.5.3).

For the channels of the AHCAL prototype SiPM devices<sup>3</sup> with an active photosensitive area of  $1.3 \text{ mm} \times 1.3 \text{ mm}$  featuring a total of 2668 pixels are used. Figure 5.3 shows a picture of the SiPM and Table 5.1 summarises the most relevant specifications. Among other photosensors from the same producer, it is quoted as having a very fast pixel recovery time of  $\sim 10 \text{ ns}$  and a fast signal rise time in the order of nanoseconds [136, 137]. Regarding noise, this SiPM model features a reduced thermal noise rate on the order of a few 10 kHz and an optical cross talk probability of less than 1% at  $25 \text{ }^\circ\text{C}$  [136]. This results in an effectively noise-free operation of the device when a typical threshold of  $>5 \text{ pe}$  in the AHCAL prototype data acquisition is applied. In addition, the excellent SiPM property uniformity within the same production batches allows a sufficient equipment of the  $\sim 22000$  AHCAL prototype channels. Lastly, this type of SiPM was chosen according to its spectral acceptance range matching the emitted light spectrum of the scintillator, which will be discussed in the following section.

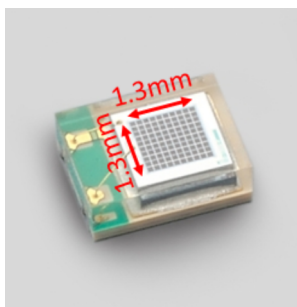


Figure 5.3: Picture of Hamamatsu MPPC-S13360-1325PE SiPM. Adapted from [136].

Parameter	Hamamatsu MPPC-S13360-1325PE
Photosensitive Area	$1.3 \text{ mm} \times 1.3 \text{ mm}$
Number of Pixels	2668
Pixel Pitch	$25 \text{ }\mu\text{m}$
Spectral Acceptance Range	320 nm - 900 nm
Peak Sensitivity Wavelength	450 nm
Typical Breakdown Voltage at $25 \text{ }^\circ\text{C}$	48 V - 58 V
Recommended Operation Voltage	$V_{breakdown} + 5 \text{ V}$
PDE (at Peak Sensitivity Wavelength)	25 %
Typical Gain	$7.0 \times 10^5$

Table 5.1: Main specifications of Hamamatsu MPPC-S13360-1325PE SiPM [136].

### 5.1.2 Scintillator Tiles

The active material of the AHCAL prototype consists of an organic scintillator arranged in a grid of injection-molded tiles, each with a dimension of  $30 \text{ mm} \times 30 \text{ mm} \times 3 \text{ mm}$ . Since the tiles are based

<sup>3</sup>Hamamatsu Photonics: MPPC-S13360-1325PE [136]

on polystyrene and doped with POPOP, the scintillation spectrum ranges from  $\sim 375 - \sim 475$  nm with an emission maximum at 410 nm, corresponding to purple-blue light [1].

The tiles are designed to be directly glued to the printed circuit board (PCB) on top of the SiPMs as depicted in Figure 5.4a. To optimise light collection and reduce inter-channel cross-talk, the tiles are wrapped with a laser-cut mirror foil<sup>4</sup> providing  $>98\%$  reflectivity in the visible light regime [138]. The wrapping of the tiles is fully automated with robotic procedure, without any further surface treatment [126]. In addition, a spherical cavity is engraved in the center of the bottom side of the tile, as shown in Figure 5.4b. On the one hand, this cavity allows an optimal placement of the SiPM surrounded by scintillator, while on the other hand, it further improves the light collection by a photon collection and focusing effect [139]. The cavity design and dimension were studied extensively to optimise the total light yield of the SiPM-on-tile system and the response uniformity for different incident particle positions across the scintillating tile [139, 128].

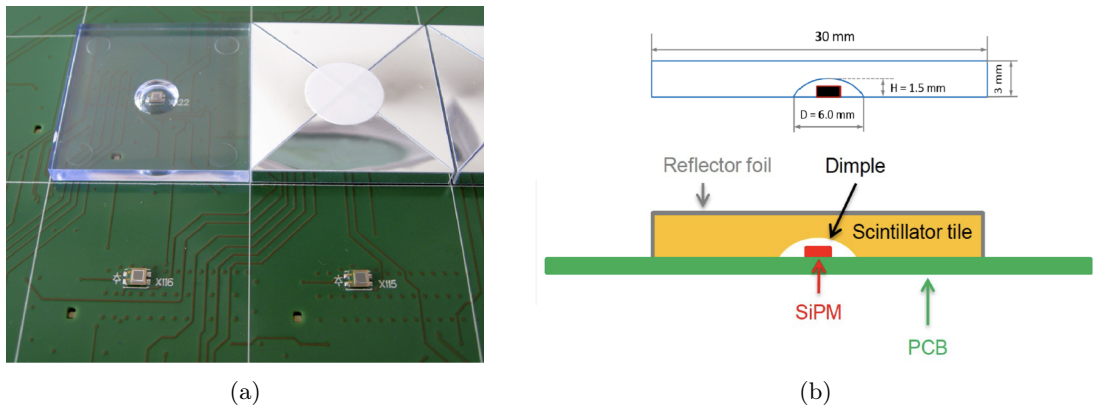


Figure 5.4: (a) Picture of AHCAL prototype channels with unwrapped and wrapped scintillating tiles on top of SiPMs. (b) Sketch of engraved cavity concept for scintillating tiles [139].

With the optimised cavity design, an excellent response uniformity was achieved agreeing well between simulation and test bench measurements. This is presented in Figure 5.5. For both, simulation and measurement, more than  $\sim 97.1\%$  ( $\sim 80.8\%$ ) of the tile area shows a response within 10% (5%) deviation from the average light yield of 22 pe (simulation) and 20.6 pe (data) for MIP like particles [139].

Lastly, the impact of misalignment of the scintillating tiles with respect to the centred SiPM was studied in detail. It was demonstrated, that even if an asymmetry in the spatial response distribution occurs by a misplacement of the tile of up to 1 mm compared to its nominal position, the global tile response does not change [140]. This shows, that potentially small displacements occurring in fully automated assembly procedures have negligible impact on the response and calibration of larger calorimeter systems like the AHCAL prototype.

## 5.2 The SPIROC2E Read-Out Chip

The SiPM integrated readout chip 2E (SPIROC2E) is the latest ASIC generation developed by OMEGA [141] to readout SiPMs in large channel calorimeter applications. It was developed in the

<sup>4</sup>3M Enhanced Specular Reflector (3M ESR)

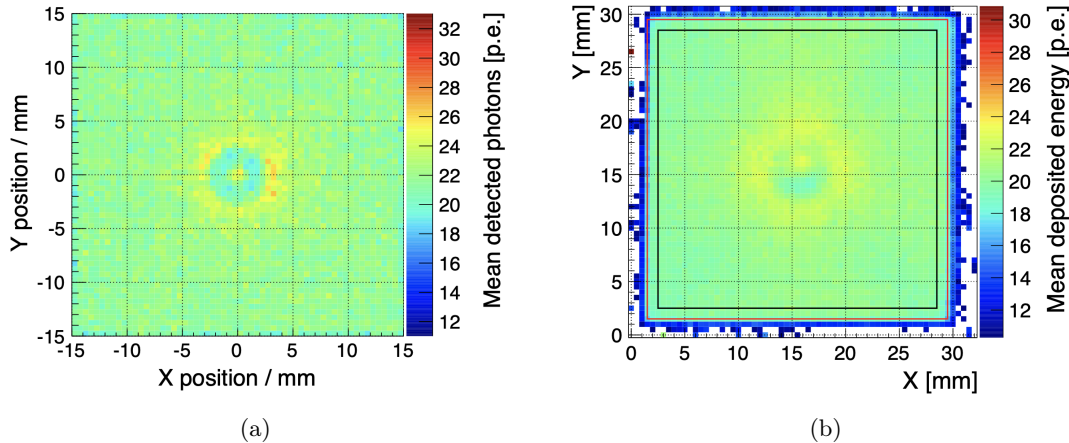


Figure 5.5: SiPM-on-tile response uniformity for particles orthogonally penetrating the scintillating tile at different positions: (a) Simulated 2.28 MeV electrons. (b) Measured  $^{90}\text{Sr}$  electrons [139].

framework of the ILC, specifically the AHCAL concept. A picture of a PCB-soldered readout chip is provided in Figure 5.6. One chip reads out and digitises the signals of 36 SiPM channels with respect to charge and timing information. Its design is optimised to cope with front end integration on top of the active layers and for reduced power consumption ( $\sim 25 \mu\text{W}$  per channel [141]) to avoid the need for active cooling. Other advantages of the chip are the large dynamic range due to a dual amplification scheme and the ability to run in a self-triggering mode (auto-trigger).

In the following, the most important properties of SPIROC2E are explained on the basis of the signal path schematic of an individual channel, as illustrated in Figure 5.6. First of all, the signal of each channel is split and directed towards two configurable low-noise amplifiers for an effective high gain and low gain signal line to achieve a large dynamic range covering signals between single and up to several thousand pe. After passing a slow signal shaper, for both signal lines each channel features an analog memory in the form of a capacitor array (in the following referred to as memory cells) with the ability to store up to 16 events in terms of charge and time measurements. The acquired information is digitised by a 12-bit Wilkinson analog to digital converter (ADC) and transferred out of the chip as soon as all the memory cells of one channel are filled.

In addition and in parallel to the charge output of the SiPM, the corresponding hit time information is sampled from a voltage ramp with respect to the time of the trigger signal and an internal clock cycle. The SPIROC2E features two alternating, superimposed voltage ramps to avoid edge effects and dead times between clock cycles. With clock cycles corresponding to the bunch crossing length of the ILC (200 ns), the voltage ramp has a designed resolution of  $\sim 100$  ps [68]. Subsequently, the sampled charge is also stored in one out of 16 memory cells and later digitised by a 12-bit time to digital Converter (TDC).

The chip can be operated in multiple modes categorised by the desired trigger and digitised output option. In external trigger (ET) mode, an applied external signal triggers the sampling of all channels simultaneously. In combination with the internal LED calibration system introduced in Section 5.3, this mode is used to record the single photon spectra of all channels and measure as well as monitor the SiPM gain. In contrast sampling in auto trigger (AT) mode only occurs, if an internally adjustable channel threshold is exceeded. This is achievable with a fast shaper and

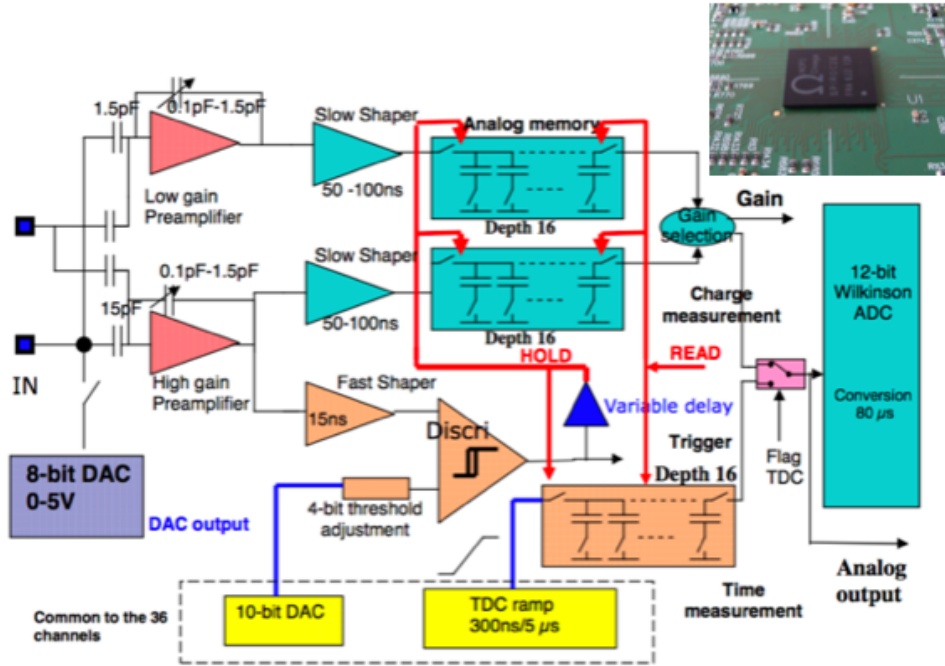


Figure 5.6: Picture and single channel signal path schematic of SPIROC2E readout chip used in the AHCAL prototype [142].

consecutive discriminator for each channel. While a 10-bit digital to analog converter (DAC) sets a common threshold level for all channels on the chip, a 4-bit DAC provides individual channel adjustments of this threshold. If the threshold of a single channel is exceeded by a signal, all 36 channels are sampled. Depending on the exceeded threshold condition of the other 35 channels, the chip assigns either a hitbit = 1 (threshold exceeded, physics signal sampling) or hitbit = 0 (threshold not exceeded, pedestal sampling) to the hit information. In addition, one can choose between the auto gain (AG) and the intercalibration (IC) operation mode. In AG, which is the physics operation mode, either the high or low gain signal is selected in addition to the time information, depending on the sampled charge. On the contrary, in IC mode the time information is neglected and the sampled charge is recorded in HG and LG mode simultaneously, which is mainly used for calibration purposes. More detailed information about the readout chip, quality assurance and characterisation procedures for mass assembly are documented in [3].

### 5.3 The Hadron Calorimeter Base Unit

Designed as the base unit for the AHCAL prototype, the HCAL base unit (HBU) is a  $36\text{ cm} \times 36\text{ cm}$  large PCB equipped with 4 SPIROC2E reading out a total of 144 SiPM-on-tile channels, as shown in Figure 5.7a. With regards to the ILD AHCAL, the HBU was developed to be able to be connected in to a total of 3 slabs featuring 6 HBUs each steered by the same data acquisition (DAQ) interface

modules consisting of a power (POWER), calibration (CALIB) and detector interface board (DIF). For the construction of the AHCAL prototype, 4 HBUs were connected to form a layer with a total of 576 individual channels and one set of DAQ interface modules, as depicted in Figure 5.7b.

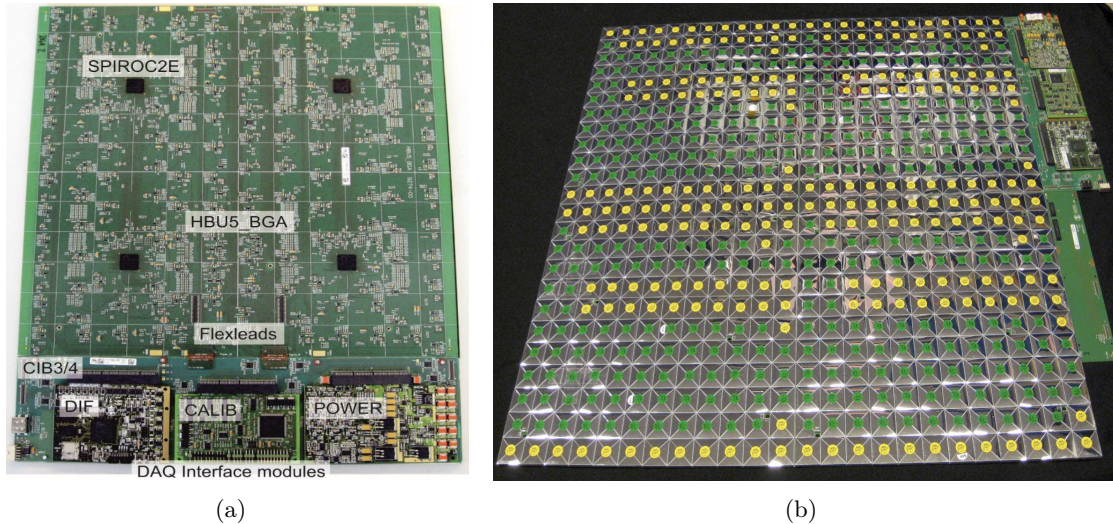


Figure 5.7: **(a)** Top view: HBU with SPIROC2E and DAQ interface modules [3]. **(b)** Bottom view: four HBUs combined to one AHCAL prototype layer showing 576 mounted scintillating tiles.

The POWER board provides the required operation voltages for all front end electronic components, like the SiPMs and SPIROC2E readout chips. In this regard, it is the basis for an active compensation of temperature<sup>5</sup> variations by adapting the common bias voltage of the SiPMs on a HBU in a fully automated way, as explained in Section 5.4. In addition, it steers the desired powering mode - always on or power pulsing. The power pulsing scheme was specifically developed with respect to the bunch train structure of the ILC (200 ms spacing<sup>6</sup>) and is illustrated in Figure 5.8. Major parts of the SPIROC2E, which are not needed in specific phases of the operation cycle are turned off during those phases and the SPIROC2Es are subsequently read out in sets, before the next bunch train arrives. This scheme reduces the power consumption down to  $\sim 25 \mu\text{W}$  per channel. More details and studies about power pulsing operation can be found in [143].

Each HBU features an internal LED calibration system, which is able to illuminate each SiPM-on-tile channel with short LED light pulses (5 – 100ns) of desired intensity. This can be used to record the single photon spectrum for effective gain calibration and monitoring of each channel (see Section 5.5.3) and to study the saturation behaviour of the SiPMs [144]. The CALIB board steers the voltages for the internal LEDs of an AHCAL layer.

Lastly, the DIF board provides and monitors the communication between the individual SPIROC2Es as well as the POWER and CALIB boards through the use of advanced field programmable gate arrays (FPGAs). Furthermore, it collects and organises the acquired data from the individual SPIROC2Es before sending it to higher order DAQ components used for full detector operation, which will be introduced in the next section.

The individual scintillator tiles are mounted on the HBU with a fully automated procedure in a

<sup>5</sup>Measured by temperature sensors implemented on the HBU

<sup>6</sup>With beam spills of 1 ms the ILC duty cycle corresponds to 0.5%.

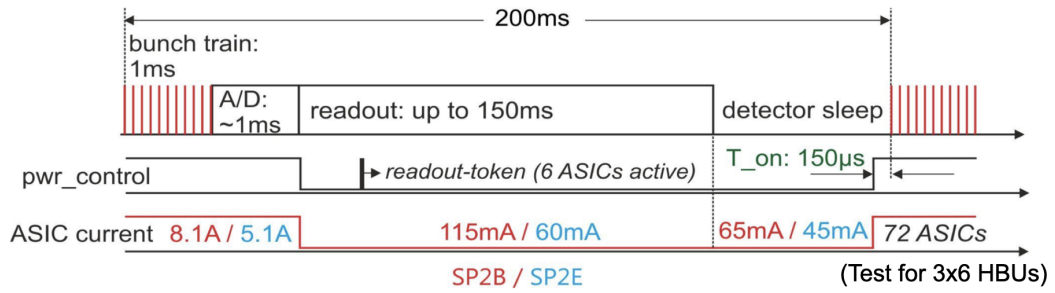


Figure 5.8: Sequences of power pulsing mode between two ILC bunch trains. Given currents correspond to a test with a full ILD slab featuring 18 HBUs (72 SPIROC2B/E) [143].

pick-and-place machine after glue is dispensed by a screen printer. In total  $\sim 170$  HBUs were built during the commissioning effort of the AHCAL prototype [1]. After de-centralised assembly, quality checks and characterisation of the individual HBU components, all HBUs were pre-calibrated in the DESY electron beam before being installed in the AHCAL prototype.

## 5.4 Prototype Commissioning and Test Beam Campaigns 2018

For the AHCAL prototype a total of 38(39) layers were assembled, corresponding to 152 HBUs or 608 SPIROC2Es or a total of  $\sim 22000$  individual SiPM-on-tile channels. The fully commissioned prototype is depicted in Figure 5.9a, after the layers were installed into the steel absorber stack and connected to power distribution, data concentration and active cooling devices.



Figure 5.9: The AHCAL prototype at the SPS CERN in 2018: (a) Close-up top view of the fully assembled 38(39) active layers alternating with steel absorber plates. (b) Top view of the prototype inside its opened light-tight container and on top of a movable stage in the beam test area.

In order to allow a synchronous steering and data acquisition of the full prototype, multiple higher level hardware devices are used, as briefly summarised in the following:

- Clock and control card (CCC): master device. Provides the global reference clock for AHCAL time stamping and steers the global DAQ start and stop by stamped trigger, bunch spill and individual SPIROC2E readiness information.
- Link data aggregator (LDA): combines data packages provided by the individual SPIROC2Es, adds headers with reference information and sends data to the DAQ PCs.
- PCs: multiple computing devices used for slow control operated via a LABView interface, EUDAQ online monitoring and event building, data storage and quasi-online monitoring of basic particle shower quantities and event displays (as illustrated in Figure 5.10)
- Beam interface (BIF): optional device. Receives AHCAL clock from CCC and external beam triggers to allow synchronous operation with external devices e.g. beam telescopes or delay wire chambers for additional beam position information.

In 2018 the AHCAL prototype was installed and operated during three extensive beam test campaigns at the SPS CERN for data taking. As illustrated in Figure 5.9b, the prototype was positioned on a movable stage to achieve different incident particle beam position during operation. Across the different data taking periods, several  $10^7$  events of muons (40 GeV and 120 GeV), electrons (10 – 100 GeV) and pions (10 – 200 GeV) have been recorded. During data taking, the imaging capabilities of the AHCAL prototype could already be exploited by having access to event displays of typical muon (ionising MIP track), electron (dense particle showers in the first layers) and pion (broader particle showers, potentially deeper in the prototype) events in the quasi-online monitoring, as presented in Figure 5.10

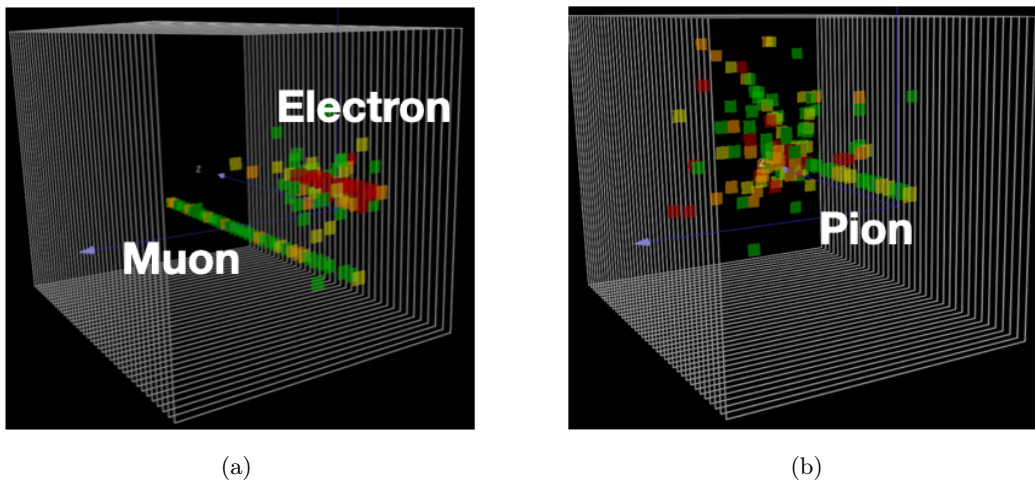


Figure 5.10: Example event displays of particle types recorded with AHCAL prototype in beam test campaigns. **(a)** Muon (40 GeV) and electron shower (10 GeV, initiated in first layer) in the same event. **(b)** Charged pion shower (10 GeV) initiated in layer 20. The color corresponds to calorimeter hit energy: green - low energy (<1.65 MIP), yellow/orange - medium energy (<5.4 MIP) and red - high energy (>5.4 MIP).

Averaged over the  $\sim 5$  s long spills the recorded event rate was up to 400 events per second [126]. In addition, LED calibration data was recorded at least once per day for gain calibration and detector performance monitoring. Expect from these LED runs in ET mode, the prototype was constantly running and taking data in AT mode. In the following, the main differences in terms of hardware and data taking for the different beam test periods are highlighted:

### May 2018 Beam Test Campaign

The standard configuration of the AHCAL prototype was tested. Besides two muon scans, illuminating all channels with a sufficient number of muons by changing the incident beam position with the movable stage, electron and pion beams were recorded centralised with respect to the calorimeter front face. Mostly the always-on powering mode was used during data taking.

### June 2018 Beam Test Campaign

The standard configuration was extended by a so-called pre-shower layer, a Tokyo layer and twelve tail-catcher layers. In order to detect beam particles showering up-stream, the pre-shower layer (a single HBU) was installed in front of the absorber structure, mainly as a veto. The Tokyo layer, a full AHCAL layer with  $6\text{ cm} \times 6\text{ cm}$  instead of the standard  $3\text{ cm} \times 3\text{ cm}$  tiles was installed between layer 37 and 38 with respect to the standard configuration. The twelve tail-catcher layers (a single HBU each) were centrally installed behind the AHCAL main stack in a second steel absorber structure (with absorber thickness  $7.4\text{ cm}$  between the layers), mainly to detect late showering pions not fully contained and therefore leaking out of the AHCAL prototype. Except for a reference muon scan in always-on powering mode, the detector was mostly operated in power pulsing mode during this period. This time, different incident beam positions were not only chosen for muons, but also for electrons and pions (mainly for  $10\text{ GeV}$  and  $30\text{ GeV}$ ).

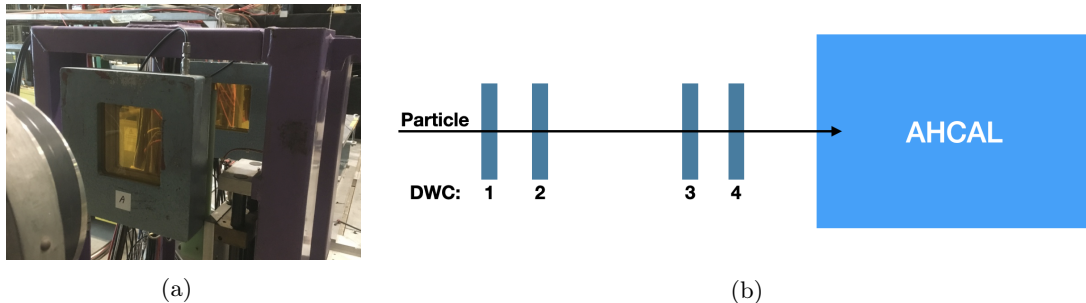


Figure 5.11: **(a)** Picture of two delay wire chambers at the SPS CERN during the June 2018 beam test campaign. **(b)** Sketch of the four delay wire chambers installed in front of the AHCAL prototype. The DWC positions with respect to the AHCAL prototype front face at  $z = 0\text{ m}$ :  $z = -17.69\text{ m}$  (1),  $z = -15.09\text{ m}$  (2),  $z = -2.35\text{ m}$  (3) and  $z = -1.09\text{ m}$  (4) [8].

Lastly, four delay wire chambers (DWC) based on multi wire proportional chamber (MPWC) technology were installed up-stream in front of the AHCAL, as illustrated in Figure 5.11. With a size of  $10\text{ cm}^2 \times 10\text{ cm}^2$  each, they provided four spatial coordinates with a resolution of  $600\text{ }\mu\text{m}$  for most of the single particle events. They were not only used for reconstructing a track for those events with a sub-mm spatial resolution at the AHCAL front face (details about calibration and

track quality in Section 8.1.1), but also for position calibration of the beam with respect to the movable stage and measuring the dimensions of the gaps between the individual scintillator tiles.

## October 2018 Beam Test Campaign

The June configuration of the AHCAL main stack was installed behind the CMS HGCal prototype layers [145], acting as a tail catcher. Therefore, mainly muons and pions, showering late in the CMS HGCal prototype stack were recorded during this period using the power pulsing operation mode.

During all beam test periods, the prototype was running in a fully automated temperature compensation mode. As discussed in Section 5.1.1, SiPM properties are highly temperature dependent. In order to cope with external (day-night cycle) or internal (different operation mode) temperature variations during operation, the automated procedure is based on the adjustment of the bias voltage of all SiPMs according to the internally measured temperature. With respect to Equation 5.3, this procedure aims to keep the over voltage of the SiPM, and therefore SiPM properties like the gain constant. Figure 5.12 shows the resulting SiPM bias voltage adjustment for one AHCAL prototype layer following the temperature trend (with an implemented hysteresis) in one week of data taking during the June 2018 beam test campaign. With an achieved SiPM gain stability within 1%, as presented in Section 5.5.3, the AHCAL prototype operation was stable with respect to temperature variation over the whole data taking period. More details about the temperature compensation can be found in [1]. By assuming an efficient temperature compensation during the acquisition of the data used for calibration purposes, the whole calibration procedure, discussed in the next section, does not include temperature related effects and corrections.

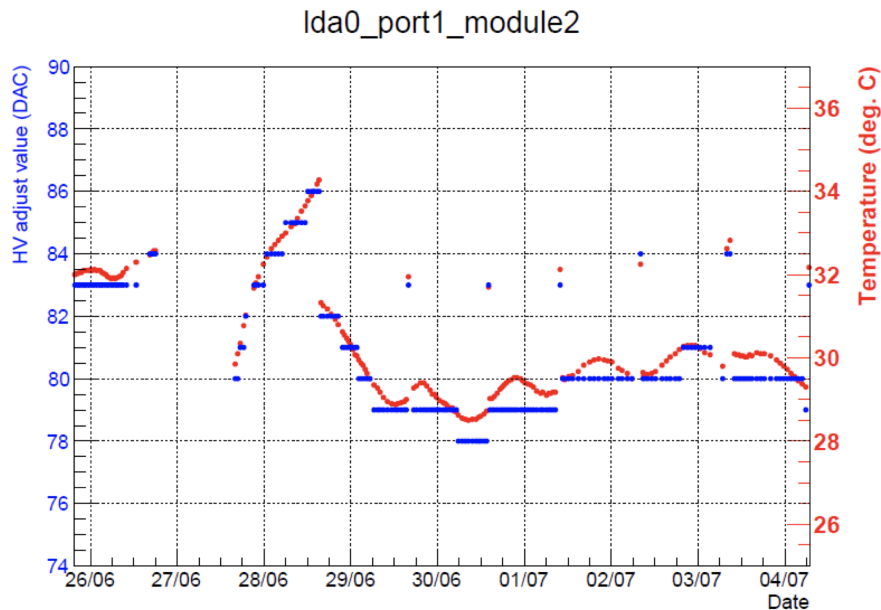


Figure 5.12: Adjusted SiPM bias voltage of one AHCAL prototype layer and measured temperature over time for nine days of data taking during the June 2018 beam test campaign. Achieved SiPM gain stability for the same time period is illustrated in Figure 5.28. Taken from [146].

## 5.5 Prototype Calibration, Uniformity and Stability Studies

The amplitude of the analog output signal of each channel's SiPM is digitised by the SPIROC2E and therefore intrinsically given in units of ADC counts. Statements about the total energy response of the prototype are still inaccurate at this stage, since the measured response of each individual channel is still characterised by its specific electronic and optical properties. With regard to electronic properties, the pedestal level and the SiPM gain can vary from channel-to-channel for example. Examples in terms of optical property variations are the slight quality differences for the wrapping of the scintillating tiles or the different PDEs of the SiPMs, which both have an impact on the total signal amplitude of a channel. To account for these properties and to allow an uniform energy response over all prototype channels, a channel-wise energy calibration has to be performed. The MIP energy scale is chosen as the calibrated energy scale, due to the well-defined standard candle process of MIP energy depositions, as described in detail in Section 4.1.2. In this context, one MIP unit corresponds to the most probable energy a MIP (like a muon) deposits while traversing perpendicularly through a scintillating tile.

The MIP energy scale calibration is performed for each of the  $\sim 22\,000$  channels of the AHCAL prototype and can be expressed as:

$$E_i[MIP] = f_{sat}^{-1}(pixels_i) \cdot \frac{(ADC_i - P_i) \cdot IC_i}{MIP_i} \quad (5.4)$$

where  $E_i[MIP]$  is the calibrated amplitude in units of MIP,  $ADC_i$  is the raw amplitude in units of ADC,  $P_i$  is the pedestal value in units of ADC,  $MIP_i$  is the MIP constant in units of ADC and  $IC_i$  is the intercalibration factor between high and low gain setting of the  $i$ -th channel. Due to the limited number SiPM pixels, as discussed in Section 5.1.1, the signal amplitude saturates for larger energy depositions. This can be corrected by a desaturation function  $f_{sat}^{-1}(pixels_i)$  which is a function of the number of triggered pixels:

$$pixels_i = \frac{(ADC_i - P_i) \cdot IC_i}{G_i} \quad (5.5)$$

where  $G_i$  is the gain constant of the  $i$ -th calorimeter channel.

In the following sections, the calibration procedures for the different calibration constants are explained and the achieved calibration results are discussed and validated. In addition, an uniformity study for the various extracted constants is conducted to explicitly quantify the introduced un-calibrated variations on memory cell, channel, chip and full detector level. Moreover, a stability study of the same constants is performed to check the calibration stability over time and for different detector modes. Both studies will be presented in the dedicated sub-sections as well.

### 5.5.1 Pedestal

The pedestal is defined as the mean electronic baseline level of a specific memory cell or channel. Its extraction is not only crucial for subtraction from the ADC signal amplitude, but also as a prior step for the remaining calibration procedures. Additionally studying a pedestal spectrum helps to quantify if a specific channel and individual memory cells behave well electronically. A spectrum that is too sharp could indicate a dead or dysfunctional channel, while a spectrum that is too broad could indicate a noisy channel. In the scope of this thesis, a fully automated extraction procedure of the pedestal spectra and pedestal properties has been developed on the memory cell ( $\sim 350\,000$ ) and prototype channel level.

### Pedestal Extraction on Memory Cell Level

As explained in Section 5.2, signal amplitude information of a triggered SPIROC2E is either saved as physics hit ( $\text{hitbit} = 1$ ) or no physics hit ( $\text{hitbit} = 0$ ) as a very accurate true zero energy approximation. For the extraction of the pedestal spectra, the full set of 40 GeV muon data from the May and June beam test campaign is used, each featuring a total of  $\sim 14$  million muon events. All ADC amplitudes for hits featuring a  $\text{hitbit} = 0$  flag are sorted into memory cell specific histograms. After two range iterations according to:

$$\text{range}_{new} = \text{mean} \pm 3 \cdot \text{RMS} \quad (5.6)$$

the mean of the pedestal spectrum is extracted as the pedestal value and the RMS as the intrinsic pedestal width. Examples of an expected Gaussian-shaped and a problematic two-peak pedestal spectrum on memory cell level are illustrated in Figure 5.13

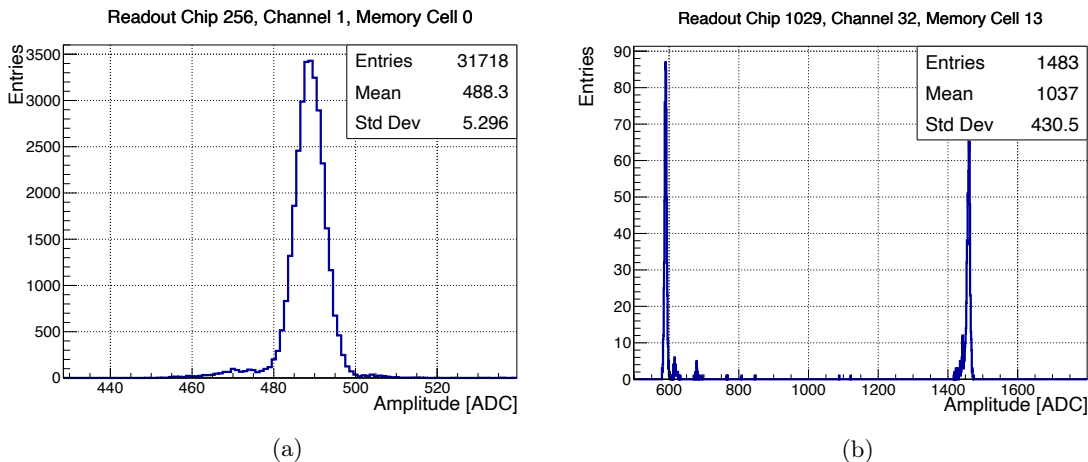


Figure 5.13: Example pedestal spectra of the AHCAL prototype muon data. (a) Gaussian-shaped spectrum. (b) Problematic spectrum with two peaks causing an increase of mean and RMS.

The extracted pedestal values and intrinsic widths of all memory cells for the May beam test period (no power pulsing) and June (power pulsing) are presented in Figure 5.14 and 5.15. For the May beam test period almost all pedestal spectra have the expected narrow Gaussian shape, as presented in Figure 5.13a. This is reflected by the centralised distribution of the pedestal values around a mean of  $\sim 531$  ADC with a total minimum-maximum variation of less than 1 MIP (compare Section 5.5.2) and a width of  $\sim 34$  ADC representing the chip-to-chip variation of the pedestal. In addition, the mean intrinsic width corresponds to  $\sim 4.3$  ADC with only a short tail to higher intrinsic widths showing the very low noise level of the full calorimeter system.

However, for the June beam test period, around 20% of the memory cell pedestal spectra are problematic showing a second peak, as illustrated in Figure 5.13b. This causes a longer tail and therefore an increase of the mean ( $\sim 555$  ADC) and RMS ( $\sim 100$  ADC) within the distribution of extracted pedestal values. In addition, these problematic pedestal spectra give rise to an increase in the mean intrinsic width to  $\sim 6.4$  ADC and  $\sim 10\%$  of intrinsic widths in the overflow bin. This effect is only observed for memory cells higher than 8 (mostly memory cell 9, 12 and 13), while memory cells 0 – 8 are mostly unaffected. Furthermore, this effect predominantly occurs when

the power pulsing mode of the prototype is used and is therefore assumed to originate from the capacitor array or close-by electronic components within the SPIROC2E. In addition, it is only observed on pedestal level and not for physics signals. Therefore, the performance of the AHCAL prototype is not degraded by this effect.

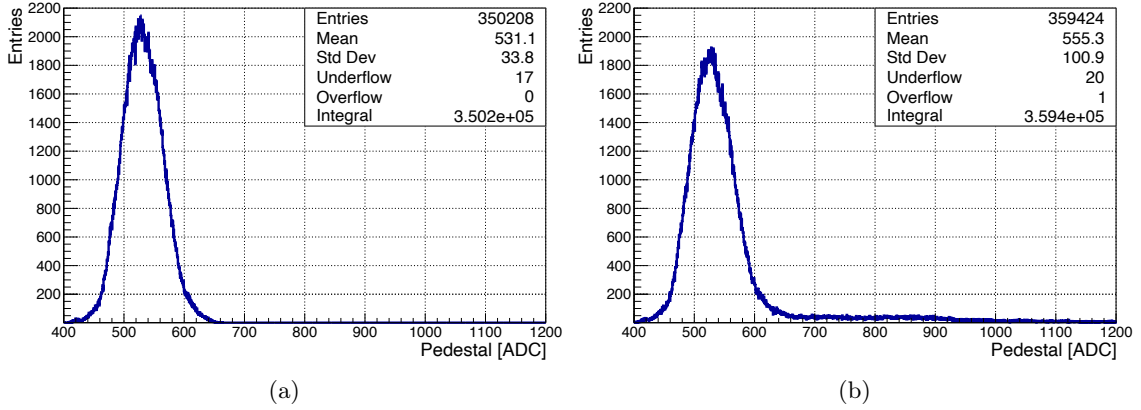


Figure 5.14: Extracted pedestal values (mean of pedestal spectrum) on memory cell level. (a) May beam test (no power pulsing). (b) June beam test (power pulsing).

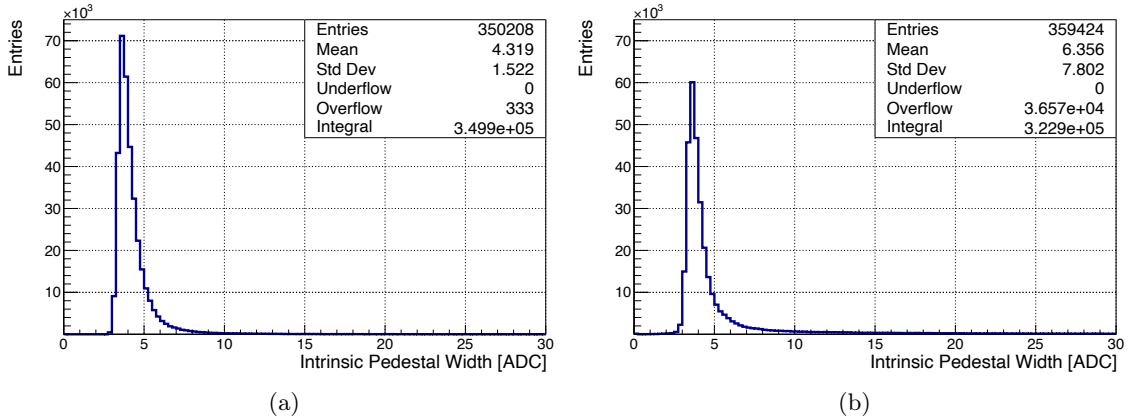


Figure 5.15: Extracted intrinsic pedestal widths (RMS of pedestal spectrum) on memory cell level. (a) May beam test (no power pulsing). (b) June beam test (power pulsing).

### Pedestal Extraction on Channel Level

Due to the effect described in the last section, the extracted individual pedestals of memory cells 0 – 8 are used for energy reconstruction, and for hit amplitude information saved in memory cells 9 – 15 a pedestal according to the average of memory cells 0 – 8 of the corresponding channel is assigned. Following this concept, the pedestal spectra on the channel level are monitored and the

extracted mean and the intrinsic width for both beam test campaigns are shown in Appendix [A.1](#) and [A.2](#). By excluding the information from memory cells 9–15 the mean and RMS of the pedestal distributions for the different operations modes are getting to a comparable level of  $\sim 530$  ADC,  $\sim 33$  ADC respectively, without tails to higher ADC values or entries in the overflow bin. The same applies to the distribution of intrinsic widths with a mean intrinsic width for both operation modes of  $\sim 6.5$  ADC now also including the intrinsic width of the pedestal itself and the cell-to-cell variation of the mean, which is presented in the following.

### Pedestal Variation

For this investigation, the RMS of the pedestals for memory cells 0–15 of each channel is calculated for the May beam test (no power pulsing) and is plotted in Figure [5.16a](#). The mean RMS corresponding to the mean cell-to-cell variation within the same channel is 5.1 ADC. A similar calculation is performed for memory cell 0 across the channels of the individual readout chips giving the mean channel-to-channel variation, which is shown in Figure [5.16b](#), and corresponds to 8.33 ADC. From that, one can conclude that the pedestal variation is a property of the readout chip and not of a specific memory cell, channel number or HBU, as visualised in Figure [5.17](#).

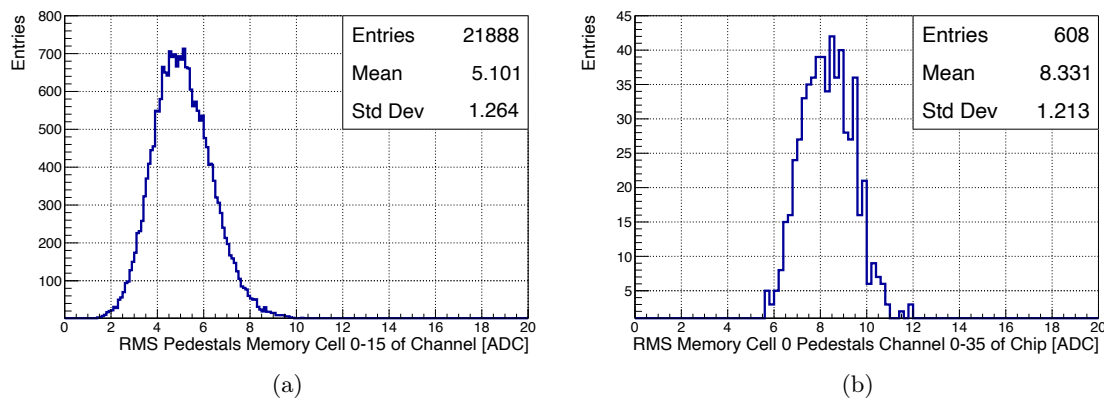


Figure 5.16: (a) Cell-to-cell pedestal variation within the same channel. (b) Channel-to-channel pedestal variation of memory cell 0 within the same readout chip.

### Pedestal Stability

Lastly, the individual pedestals are compared at the channel level for the different beam test periods in the same detector mode (no power pulsing) and different detector modes in the same beam test period to study their stability over time and for different detector modes. The results are presented in Figure [5.18](#), in which the pedestal difference of the same channel is plotted for the investigated scenarios. For both cases studied, the mean difference as well as the width is negligibly small (below 2.2 ADC or 1% of a MIP, compare next section). Therefore, one can conclude that the pedestals are stable on long time scales, as well as for the different detector modes.

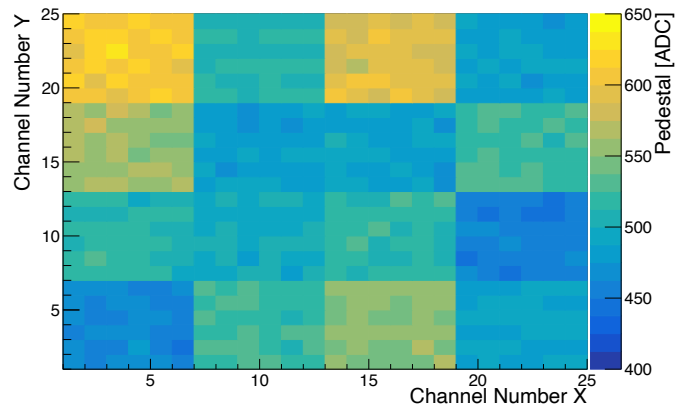


Figure 5.17: Map of pedestals on channel level for AHCAL prototype layer 12 of May beam test.

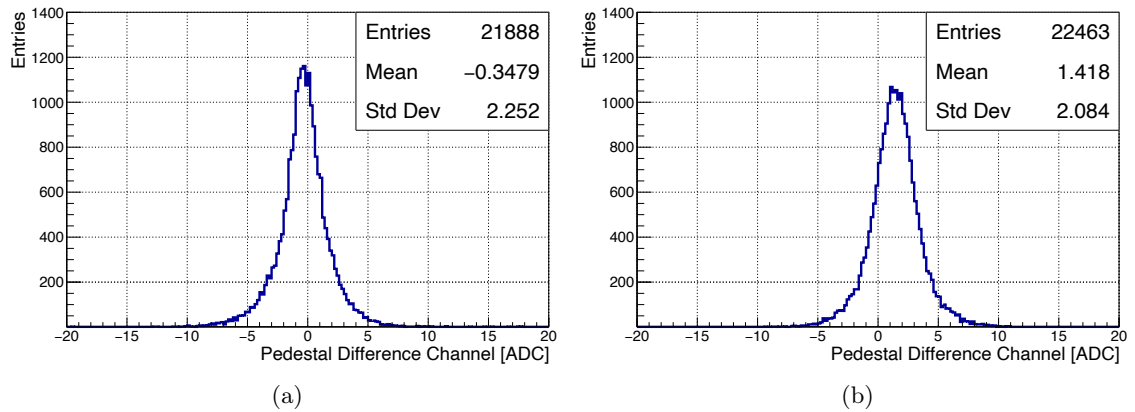


Figure 5.18: Pedestal difference of the same channel for: **(a)** May and June beam test data in the same detector mode (no power pulsing). **(b)** June beam test data in different detector modes (with no power pulsing and with power pulsing).

### 5.5.2 MIP Constants

The MIP constant of an AHCAL prototype channel is defined as the most probable energy deposition, in units of ADC, that a MIP-like particle deposits in the individual channel. After the extraction of the pedestals, the MIP constant for each channel of the AHCAL prototype is determined. Based on work undertaken for previous prototypes of the AHCAL [147-149], a fully automated calibration procedure for all channels has been developed.

#### MIP Calibration Procedure and Results

Like the pedestal extraction, the calibration routine is based on the full 40 GeV muon data set from the May or June beam test campaigns, each featuring a total of  $\sim 14$  million muon events

illuminating all AHCAL prototype channels sufficiently. Due to the low noise level discussed in the previous section, the selected internal SPIROC2E auto-trigger energy threshold for physics hits (see Section 5.2) typically around 0.2 MIP, the very high number of muon events recorded during the MIP scan and the high purity of the SPS muon beam, no additional selection on the raw data is required, in contrast to previous prototype calibrations.

In light of this, only the physics hits (hitbit = 1) are considered and after a memory cell specific pedestal subtraction, the amplitude information is used to fill one histogram per channel. Subsequently, the energy spectra are fitted by a robust 3-step Landau convoluted Gaussian fit in order to obtain the MIP constant as the MPV ( $\sim$ maximum) of this function. A typical example of a fitted MIP spectrum is illustrated in Figure 5.19.

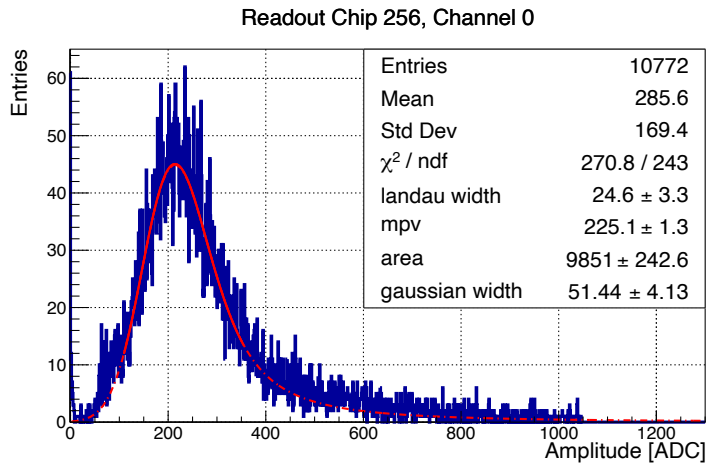


Figure 5.19: Example MIP energy spectrum of an AHCAL prototype channel extracted from the June beam test muon runs. The red line indicates the Landau-Gaussian convoluted fit for the determined MIP constant of 225 ADC for this channel.

Besides the MPV, the fit features the following parameters: the area of the hit energy spectrum, the width of the Landau function and the width of the convoluted Gaussian function. In addition to the fit quality itself, these parameters are monitored channel-wise for quality insurance of the channel response and can be found in Appendix A.3 for the May beam test period. More details about the iterative fitting procedure and optimised initial fit parameters are documented in [148], [149]. The following conditions are defined to evaluate if a channel behaves well in terms of its energy spectrum and fit quality:

- Minimum number of hits: 1000
- $\text{Chi}^2/\text{NDF} < 5$
- No excessive Landau width  $> 60$  ADC
- No excessive Gaussian width  $> 100$  ADC

If a channel does not fulfil one of these criteria, it is considered as a dead channel and excluded from the energy reconstruction. Under these considerations a total of 21868/21888 (May) and 22013/22032 (June) channels are classified as good corresponding to a fraction of  $< 0.1\%$  dead

channels. The extracted MIP constants for both beam test periods are plotted in Figure 5.20. For the May beam test period the mean MIP constant corresponds to 228 ADC, which translates to a signal-over-noise ratio of  $Mean_{MIP}/RMS_{pedestal} = \sim 53$ .

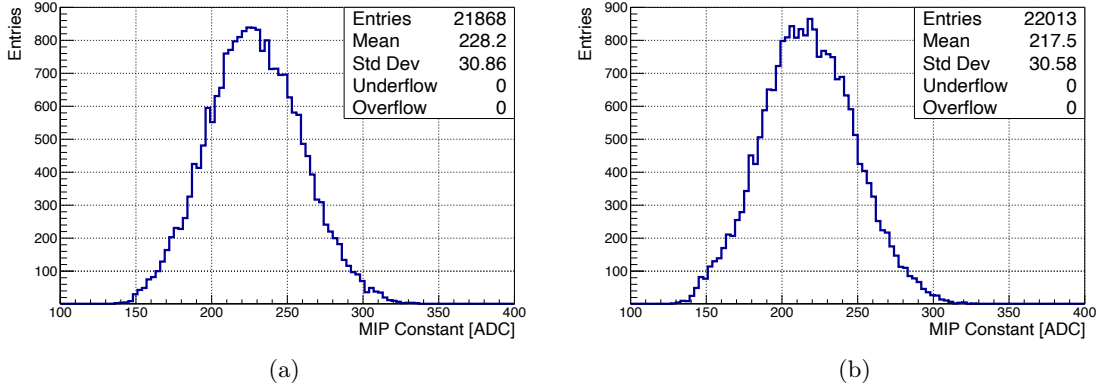


Figure 5.20: Determined MIP constants of AHCAL prototype channels for beam test period: (a) May (no power pulsing). (b) June (power pulsing).

### MIP Constant Variation

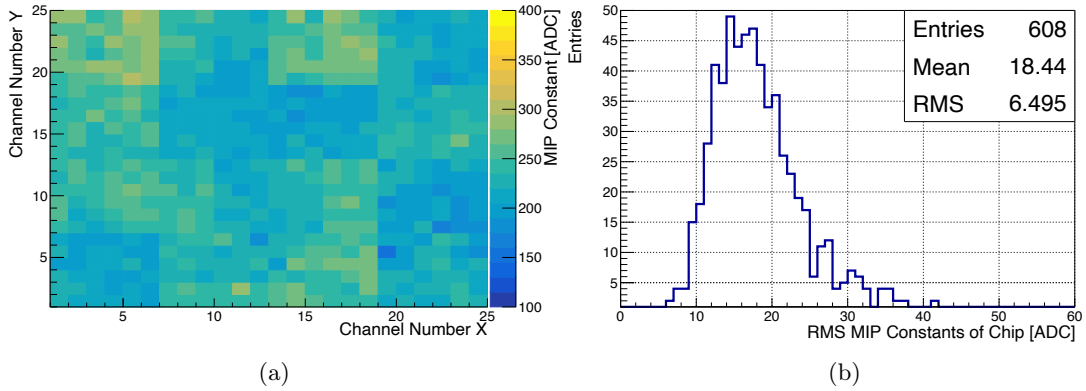


Figure 5.21: MIP constant variation for May beam test beam period (no power pulsing): (a) MIP constant map for layer 12. (b) Channel-to-channel variation within the same readout chip.

As illustrated in Figure 5.20, the RMS of the MIP constant distribution corresponds to  $\sim 31$  ADC for both beam test periods, which resembles a spread over the uncalibrated full AHCAL prototype of  $RMS_{MIP}/Mean_{MIP} = \sim 14\%$ . Like the pedestal, the MIP constant uniformity for channels within the same readout chip improves and corresponds to  $\sim 18.4$  ADC or  $\sim 8.1\%$ , as visualised and shown in Figure 5.21

### MIP Constant Stability

To study the MIP constant stability and evaluate the need for re-calibration of the detector, the MIP calibration procedure is repeated for different data sets and resulting MIP constants are compared channel-wise. First, the stability over time is investigated by checking the ratio of MIP constants extracted from muon data sets in no power pulsing mode from the May and June beam test period. Since the no power pulsing muon scan during the June beam test does not feature sufficiently large statistics, not all of the channels can be fitted successfully in terms of the criteria defined earlier in this section. The result is shown in Figure 5.22a showing a mean MIP constant ratio of 1 within 1% for the two set of MIP constants.

A similar study is performed by comparing MIP constants from no power pulsing mode vs. power pulsing muon data sets for the June beam test period, presented in Figure 5.22b. While the width is approximately the same as in the time stability study, the mean MIP constant ratio is off by  $\sim 4.3\%$ , which also corresponds to the difference between the mean MIP constants presented in Figure 5.20. This global shift in the MIP constants is the result of a well understood electronic effect connected to the temperature compensation of the SiPM bias voltage while running in power pulsing mode, and will not be further discussed in this context. One can conclude that the MIP constants are stable over time, but not for the two investigated detector modes. For the reconstruction of beam test data in no power pulsing and power pulsing detector mode, two individual set of MIP constants are required.

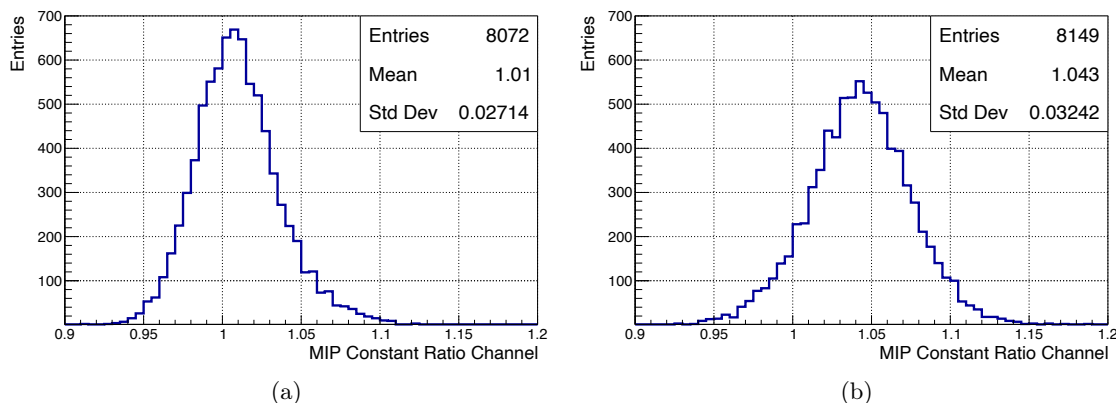


Figure 5.22: MIP constant ratio of the same channel for: (a) May and June beam test data in the same detector mode (no power pulsing). (b) June beam test data in different detector modes (with no power pulsing and with power pulsing).

### MIP Constant and Pedestal Quality Validation

To validate the quality of the extracted MIP constants and pedestals, the energy of a representative sub-sample of the 40 GeV muon data sets from the May and June beam test campaigns is reconstructed in units of MIP using the determined calibration constants for each channel. According to Formula 5.4, the SiPM saturation as well as the inter-calibration plays a minor role in the low energy regime of MIP energy depositions, allowing an intermediate check of the extracted MIP constant and pedestal quality. The reconstructed global hit energy spectra for all channels

from the May (no power pulsing MIP constants) and June (power pulsing MIP constants) beam tests are presented in Figure 5.23. For fitting the spectra, the same Landau-Gaussian fit from the calibration routine is used. An accuracy of a few per-mille to the expected value of 1 MIP is achieved for the MPVs. The same validation procedure is performed for the individual hit energy spectra of all channels for the June beam test muon data set and the resulting MPV distribution is shown in Figure 5.24a. The Gaussian fit results (mean: 1.002 MIP, sigma:  $\sim 0.008$  MIP) indicate that the calibration on channel level is also accurate to below 1%. For these reasons, one can conclude that a self-consistent and accurate implementation of the pedestals and MIP constants has been demonstrated.

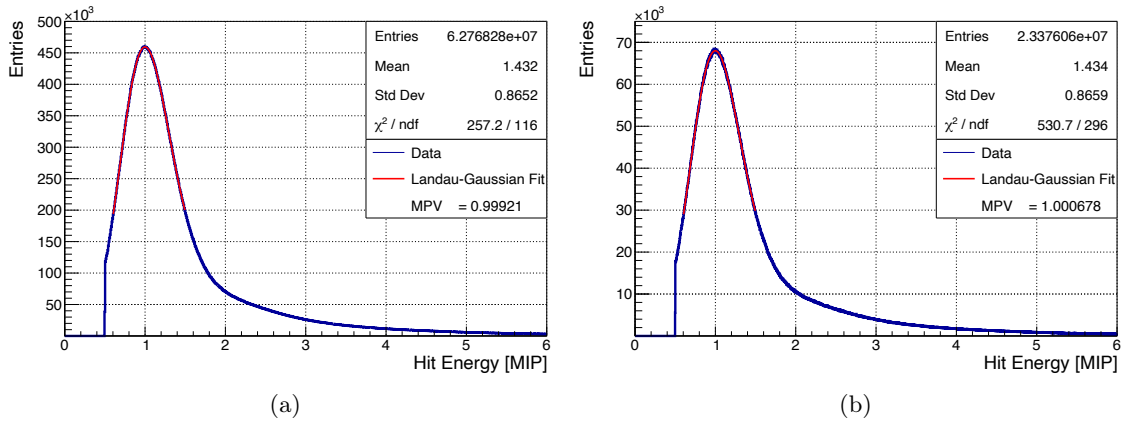


Figure 5.23: Calibrated global hit energy spectra for muon runs of beam test: (a) May (no power pulsing). (b) June (power pulsing).

### MIP Constant and Pedestal Systematic Error

In order to estimate a systematic error on the MIP energy scale calibration, the full calibration procedure for the pedestals and MIP constants, as described in the previous sections, is applied to two individual sets of 40 GeV muon runs. Those two sets have been acquired during the May 2018 beam test campaign, both illuminating all channels sufficiently and in no power pulsing mode, one set recorded at the beginning and the other set at the end of the beam test campaign. Therefore, the systematic error determined with this method is assumed to include the uncertainty of both, the pedestal and MIP calibration routines, as well as temperature and temporal variations. For both sub-sets, the individual channels are fitted with the Landau-Gaussian fit as described previously and the determined MPVs are compared channel-wise by investigating their ratio, as illustrated in Figure 5.24b.

Despite a small shoulder to the left, the mean ratio is found to be equal 1 within 0.3%. A Gaussian is fitted to the spectrum providing similar results for the mean and a sigma of  $\sim 1.22\%$ . However, for the systematic uncertainty the more conservative approach in form of the RMS of the distribution is chosen to incorporate the full impact of the shoulder as well. It corresponds to  $\sim 1.43\%$ . For further studies utilising the systematic uncertainty of the pedestal and MIP constant, a value of 1.5% is assumed, as presented for the electron energy reconstruction performance studies of the AHCAL prototype in Section 7.2.2 for example.

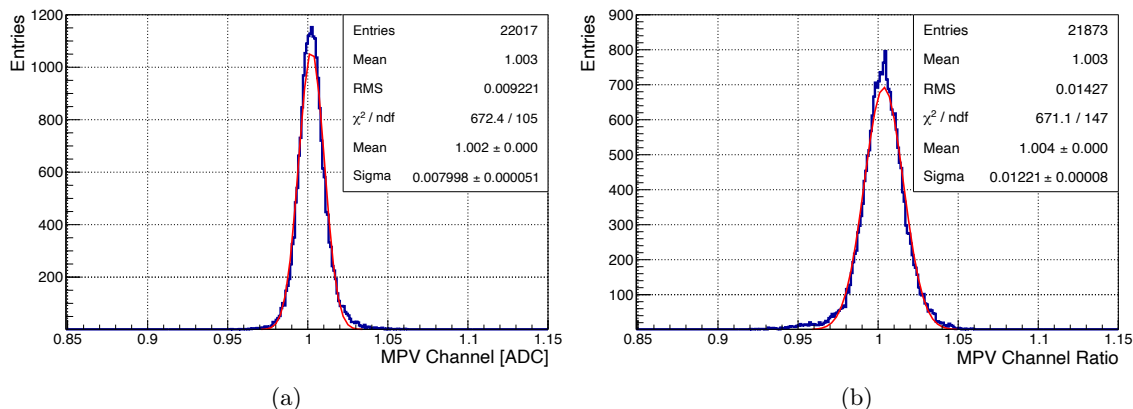


Figure 5.24: (a) Distribution of MPVs extracted from calibrated hit energy spectra for the individual AHCAL prototype channels of the June muon beam test data set (power pulsing mode). (b) Channel-wise ratio of MPVs extracted from individual MIP calibrations of two sets of muon data acquired during the May beam test campaign (no power pulsing).

### 5.5.3 Gain Constants

The gain constant of a channel is defined as the mean measured signal amplitude in units of ADC for one fired SiPM pixel. Therefore, this constant is a combination of the intrinsic amplification factor in the avalanche process of the SiPM (the intrinsic SiPM gain, see Section 5.1.1), the amplification of the pre-amplifier within the SPIROC2E readout chip and the digitisation itself. Due to the dependence of SiPM gain on temperature, the gain constants offer an excellent opportunity to monitor the stability of the full detector system over time. Since the extraction and study of the gain constants for all AHCAL prototype channels is not part of the work performed in the scope of this thesis, corresponding results are only discussed briefly. More details about the calibration procedure and results can be found in [2].

#### Gain Extraction Procedure and Results

The gain calibration is performed by using runs with low intensity light pulses emitted from the internal LED calibration system as described in Section 5.3. The resulting single photon spectra for each individual AHCAL prototype channel are subsequently fitted with a multi-Gaussian fit function as illustrated in Figure 5.25. Within the fit, the distance between neighbouring peaks is left as a single free parameter and corresponds to the gain constant to be extracted. From the daily LED runs during beam test operation, approximately 95% of the channels' gain constants could be extracted according to specific fit quality criteria further described in [2]. The results are presented in Figure 5.26, showing an average gain constant of 16.6 ADC with a spread of about  $\sim 1$  ADC, corresponding to 6%. While the gain constants are compatible for the May and June beam test operation (for both LED runs without power pulsing), for the October period (LED runs with power pulsing) the gain constants are globally shifted by  $\sim 2.2\%$  to lower values due to the same electronic effect as discussed for the MIP constants in power pulsing mode. For this reason, individual set of gain constants are used for the corresponding detector operation mode.

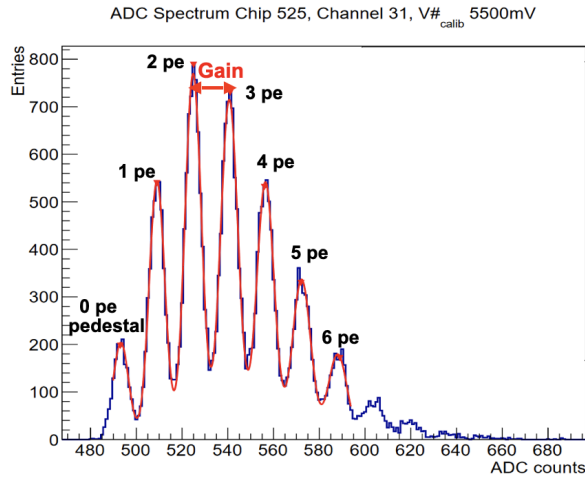


Figure 5.25: Example single photon spectrum of an AHCAL prototype channel. Each peak corresponds to a discrete amount of measured photons (pe). The red line indicates the multi-Gaussian fit to determine the gain constant [150].

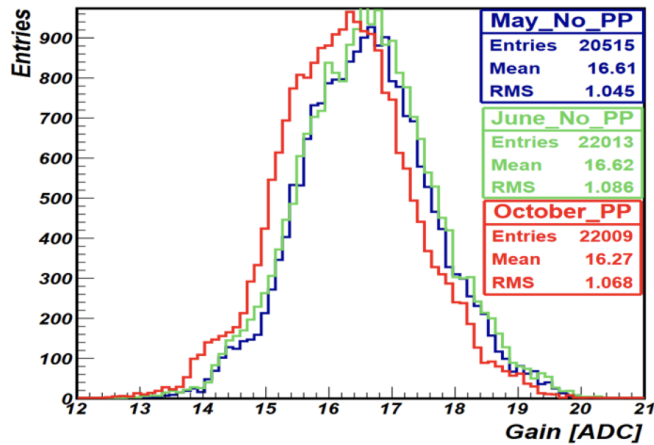


Figure 5.26: Extracted gain constants from LED runs during the May (no power pulsing), June (no power pulsing) and October (power pulsing) beam test [150].

### Gain Variation

As for the pedestal and MIP constants, the gain constant spread from channels of the same SPIRCO2E is significantly smaller than the spread over the full AHCAL prototype and corresponds to  $\sim 2.5\%$ . This shows that the gain constant spread between different SPIROC2E contributes significantly to the overall spread, which is visualised in Figure 5.27. Therefore, for the remaining

5 % of channels with undetermined gain constants the average gain constant of channels within the same readout chip is assigned.

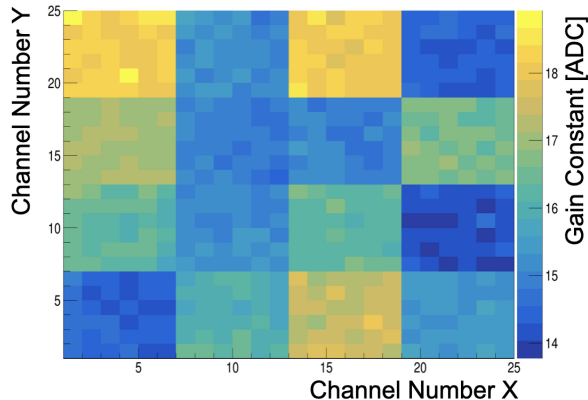


Figure 5.27: Map of gain constants for AHCAL prototype layer 12 of May beam test [2].

### Gain Stability

In the previous sections it has been shown that the gain constants are stable over time for comparing LED runs from the May and June beam test period operated in the same detector mode. Since the gain was monitored for all channels at least on a daily basis in terms of the automated temperature compensation (see Section 5.4) of the full detector system, the time stability can be studied in more detail. As exemplarily illustrated in Figure 5.28 for a single AHCAL channel, the temperature compensation allowed for the gain on the single channel level to be kept constant to within  $\sim 1\%$  over a time period of more than one week.

### 5.5.4 Light Yield

By combining the channel-wise gain and MIP constant, one can determine the light yield of each AHCAL prototype channel to be:

$$LY_i = \frac{MIP_i}{Gain_i} \quad (5.7)$$

The light yield is defined as the most probable number of fired pixels per incident MIP. Since amplification factors and systematic effects cancel with each other it is a purely optical quantity depending on the quality of the wrapped scintillating tiles, photon collection, SiPM properties, etc. only. In Figure 5.29a the distribution of the determined light yields for the AHCAL prototype channels from the May beam test is presented. The mean light yield corresponds to  $\sim 13.8$  pixels/MIP with a spread of around 11.6%. The light yield map of layer 12, shown in Figure 5.29b, demonstrates that the light yield spread is no longer a property of the different read out chips. The visualised inhomogeneities originate mainly from the two different types of tile wrapping used for equipping the AHCAL prototype, in addition to the optical quality features described above.

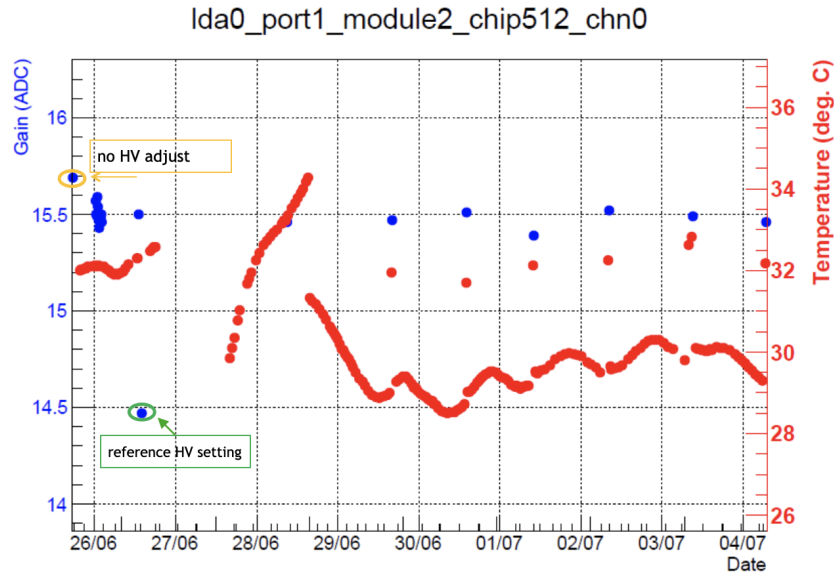


Figure 5.28: Measured gain of a single AHCAL prototype channel and temperature over nine days of beam test operation during the June beam test [151].

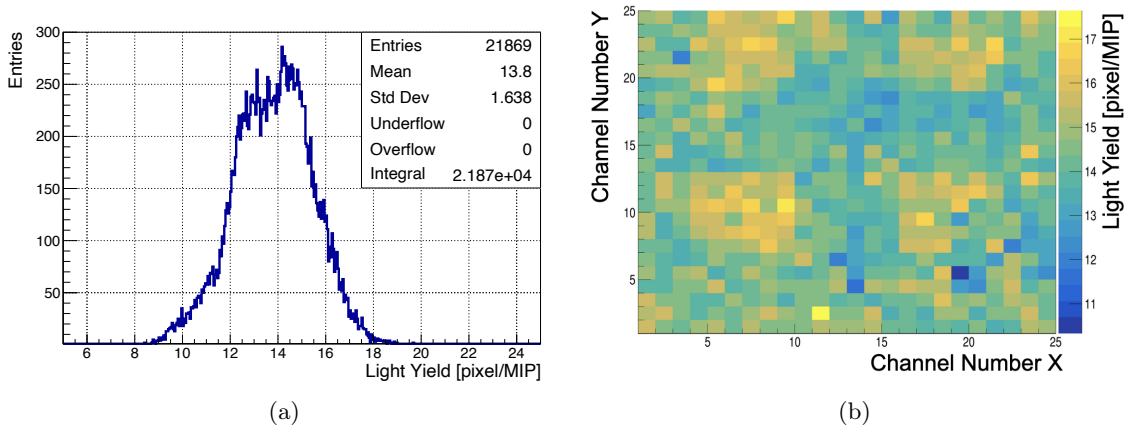


Figure 5.29: Determined light yields on the channel level for the May beam test: (a) Distribution for all channels. (b) Light yield map for layer 12 [2].

### 5.5.5 High Gain - Low Gain Intercalibration

The SPIROC2E features a high and low gain signal readout, as illustrated in the circuit diagram shown in Figure 5.6. Therefore, an intercalibration constant is required to equalise both amplitude outputs and allow for a smooth transition from hit amplitudes recorded in high gain and in low gain mode, as illustrated in Figure 5.30. For each channel the intercalibration constant is assumed to be slightly different, since it depends on the ratio of the capacitances before the two amplifiers in

the high or low gain signal path. Those components have been tuned so that the transition between the two settings typically happens in the energy region around 5 MIP. Since the intercalibration constant extraction is not performed as part of the work presented in this thesis, only a brief overview about one of the extraction methods and the achieved results is provided. More details can be found under [147, 151].

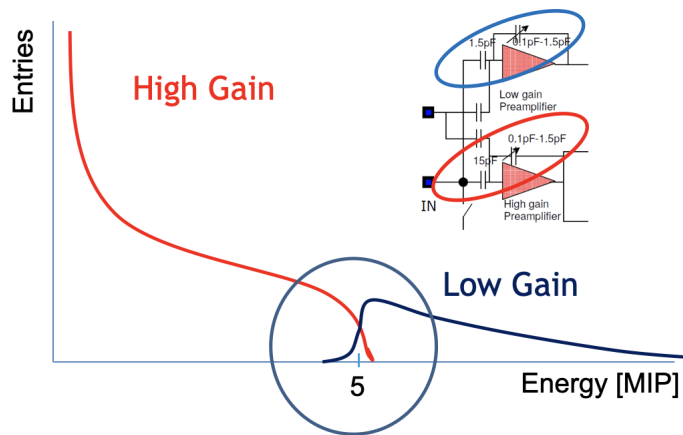


Figure 5.30: Visualisation of the transition from the high gain to the low gain region in a calibrated hit energy spectrum [151].

### Intercalibration Constant Extraction and Results

The intercalibration constant is extracted channel-wise from special LED runs for which both, the high gain as well as the low gain amplitudes, are measured. By varying the LED light intensity, the hit amplitudes (pedestal subtracted) of each channel can be scanned for both modes as illustrated in Figure 5.31a. Since both show a linear behaviour up to the medium energy regime of around 10 MIP, the intercalibration constant of each channel can be extracted as the slope of a linear fit to this regime. The extracted intercalibration constants based on LED runs for the June beam test period for channels passing specific quality criteria are presented in Figure 5.31b. It shows a mean intercalibration constant of 19.46 with a spread of  $\sim 0.67$ , corresponding to an uniformity of about 3.5%. Based on these results, one MIP in low gain mode corresponds to  $\sim 12$  ADC. For the remaining channels, an intercalibration constant calculated from the average over the channels of the same readout chip is used.

### Low Gain Pedestal

During a first look into the electron data, the high gain to low gain transition in the hit energy spectra was not smooth, despite validated intercalibration constants. This was caused by the initial assumption that the pedestal in low gain mode is the same as the pedestal in high gain mode for each channel, shown not to be the case. Therefore, the low gain pedestals are extracted on the memory cell and channel level and the results on the schannel level are presented in Figure 5.32. The average low gain pedestal corresponds to  $\sim 515$  ADC and is therefore 15 ADC lower than the

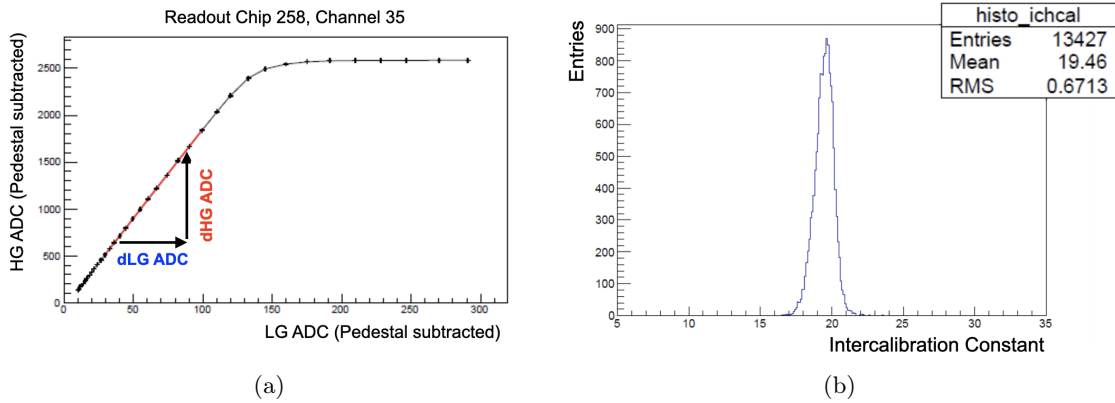


Figure 5.31: (a) Example of intercalibration spectrum of a single AHCAL prototype channel including a linear fit to determine the intercalibration constant. (b) Extracted intercalibration constants for the June beam test passing quality criteria [151].

average high gain pedestal. This corresponds to  $\sim 1.25$  MIP in low gain mode and explains the observed shift in the transition region, while using the high gain pedestal as well for the low gain mode. A description of the extraction method and variation studies for the low gain pedestal, showing results agreeing with those for the high gain pedestals, can be found in [3].

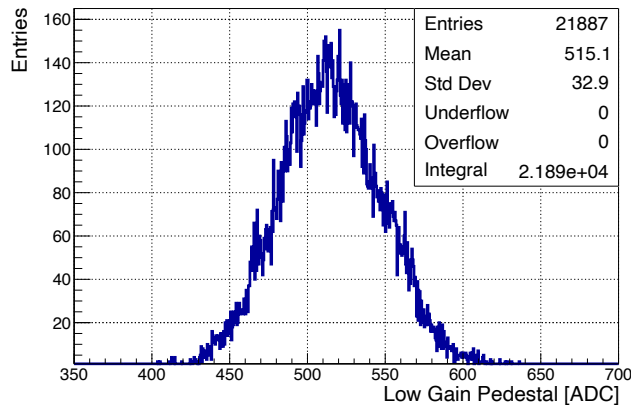


Figure 5.32: Extracted low gain pedestals on the channel level for the May beam test.

### Intercalibration and Low Gain Pedestal Quality Validation

In order to validate the quality of the extracted intercalibration constants and low gain pedestals, the global hit energy spectrum of 100 GeV electron shower data are investigated, offering low and high individual hit energies with sufficient statistics in order to investigate the transition region between high gain and low gain mode. As illustrated in Figure 5.33, the transition region around 5 MIP is found to be smooth on global hit energy level allowing for the accurate reconstruction of

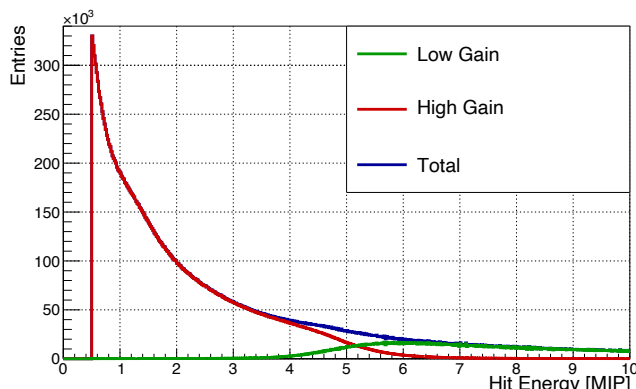


Figure 5.33: Reconstructed global hit energy spectrum of 100 GeV electron showers for the June beam test indicating hit amplitudes measured in high gain or low gain mode. The blue curves (both hit modes added) show a smooth transition around 5 MIP.

individual energy depositions higher than 5 MIP. The same method is used to validate a smooth transition region for the layer, channel and memory cell level, as summarised in [3].

### 5.5.6 SiPM Saturation

In order to reconstruct hit energies higher than 5 MIP accurately, the SiPM pixel saturation described in Section 5.1.1 has to be taken into account. To this end, a de-saturation function is applied for the energy calibration as illustrated in Equation 5.4. It can be parametrised as follows:

$$N_{fired}^{desat} = -N_{eff} \cdot \ln \left( 1 - \frac{N_{fired}^{sat}}{N_{eff}} \right) \quad (5.8)$$

where  $N_{fired}^{desat}$  is the number of de-saturated SiPM pixels,  $N_{fired}^{sat}$  is the number of saturated SiPM pixels and  $N_{eff}$  is the number of effective SiPM pixels. The saturation of the SiPM used within the AHCAL prototype has been precisely measured by illuminating the SiPM with a laser beam [133], featuring a homogenous intensity profile, over almost the full energy range and is presented in Figure 5.34

It was found, that  $N_{eff} = 2553$  provides the best results by comparison to simulations and fitting different functions to the SiPM response with  $N_{eff}$  as a free parameter. This is 10 % less than the nominal SiPM value of 2668 pixels. However, later studies of high energy electron beam test data have shown that  $N_{eff} = 2668$ , corresponding to the nominal pixel value, provides better agreement to simulations over the full energy range of the reconstructed hit energy spectra and the single electron energy resolution [3, 2]. Since the de-saturation function is well described even for the highest number of fired pixels and the calorimeter system is designed to cope with a de-saturated pixel range of up to two times the nominal pixel value of 2668, the effective dynamic range of a single AHCAL prototype channel can be estimated. Based on the determined average light yield of 13.8 pixels/MIP, it corresponds to  $\sim 380$  MIP, which equals  $\sim 10$  GeV with an assumed MIP to GeV conversion factor of 0.028 GeV/MIP (see Section 8.2.3).

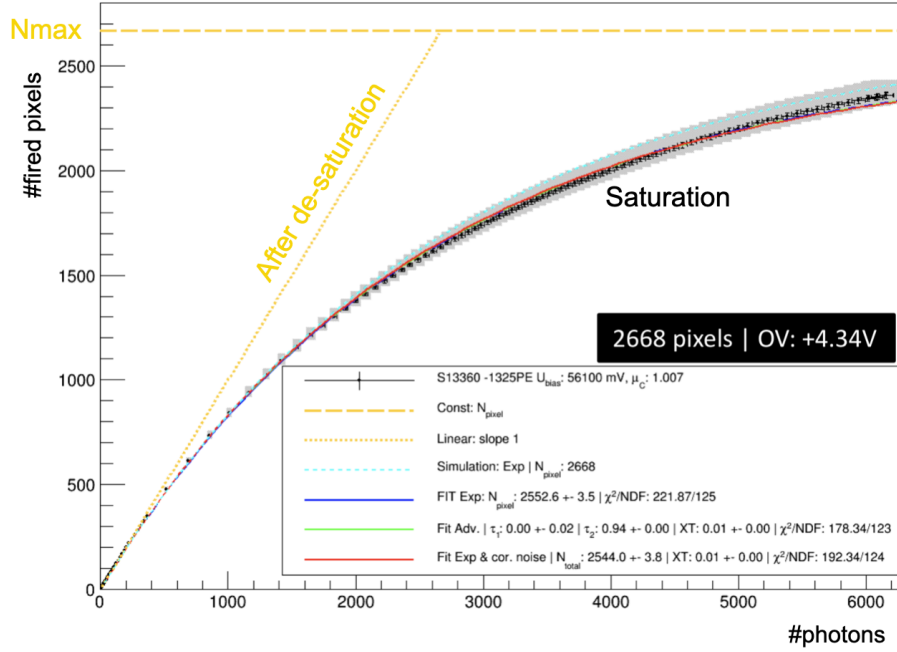


Figure 5.34: Measurement of fired SiPM (MPPC S13360-1325PE) pixels versus incident photons of a laser beam. Next to the desired linear dependence after de-saturation, the response is compared to simulations and fitted with different functions. More details in [133].

### 5.5.7 Hit Time Calibration

Besides the ADC value, the SPIROC2E is capable of saving the time information for each individual hit in the form of a TDC value, as introduced in Section 5.2. Since the time information is not investigated within the scope of this thesis, only a brief overview about the calibration procedure and the achieved single hit time resolution is provided in the following. Details about the time calibration and achieved single hit time resolution results can be found in [1, 68, 152].

In general, the TDC values acquired have to be calibrated against a reference time (external trigger time) for each event. The baseline hit time calibration is performed on muon beam test data and is based on a fitting routine to the TDC slopes provided by the SPIROC2E, as introduced in Section 5.2, on the memory cell and channel level. Also time walk effects are taken into account. Subsequently, the single hit time resolution for muons is investigated to verify a self-consistent time calibration. To this end, the calibrated time difference of muon hits in subsequent AHCAL layers within the same event is calculated. With this method a single hit time resolution of  $\sim 0.780$  ns for muons is obtained matching the ILD AHCAL design goal of 1 ns. In practice the single hit time resolution is specifically limited by the front end readout electronics. For electron and hadron shower data, chip occupancy effects degrading the hit time resolution to a few nano seconds have been observed. To study the intrinsic single hit time resolution of the pure SiPM-on-tile system without those limitations, a simplified telescope-like setup with a 200 ps fast digitiser capable of recording individual waveforms was conducted. Beam test measurements with electrons at DESY resulted in a single hit time resolution of  $\sim 507$  ps [152].

## 5.6 Summary

In this chapter, the AHCAL prototype, a highly granular steel sampling calorimeter with  $\sim 22\,000$  SiPM-on-tile channel, is introduced in detail. After discussing the basic working principles, specifications and features and of the individual hardware components, the beam test campaigns of the commissioned prototype at the SPS CERN in 2018 are summarised. Lastly, procedures and results of the energy and time calibration of the individual calorimeter channels based on corresponding beam test data sets are presented, also with respect to un-calibrated uniformity and stability.

First of all, the AHCAL prototype demonstrates full scalability towards a full collider detector like ILD in terms of design, production, commissioning and operation. This is not only proven by the de-centralised and automated component assembly, quality assurance and calibration, suitable for mass production of prototype base units, but also by stable and well controlled operation during all beam test periods. Within this effort, it is shown that the compact front-end readout electronics are running well in the desired pulsed power scheme and in a fully automated temperature compensation mode with respect to SiPM bias voltage adjustments. Therefore, a successful data acquisition of several million muon, electron and pion events across the different beam test periods is achieved and is ready for detailed analysis.

In the context of the energy calibration of the prototype channels, it is shown that the automated calibration routines developed are robust and calibration constants for almost all channels are extracted successfully. The results show an already good uniformity of the un-calibrated channel properties, excellent signal-to-noise ratio and a low number of dead channels. Non-uniformities are mainly found to originate from spreads between different readout chips. Lastly, variations studies of the acquired calibration constants show that the prototype operates stable over time within and across beam test periods as well as in different powering modes. Deviations of a few percent for the constants recorded in power pulsed mode are understood on the electronics level and corrected for. The main results presented in this chapter are summarised in the Table [5.2](#).

The full set of extracted calibration constants is uploaded to a de-centralised SQL-based database for global event reconstruction and subsequent data analysis accessible to the full collaboration. In the following chapters, the analysis of the recorded beam test in comparison to simulations is presented.

Calibration Class	Parameter / Condition	Rounded Value
Pedestal	Mean (Memory Cell)	531 ADC
	Mean Intrinsic Width (Memory Cell)	4.3 ADC
	Chip-to-Chip Spread	6.41 %
	Channel-to-Channel Spread	1.56 %
	Cell-to-Cell Spread	0.96 %
	Time Variation	<0.42 %
	Powering Mode Variation	<0.42 %
MIP	Mean	228 ADC
	Full Detector Spread	14 %
	Spread within same Readout Chip	8.1 %
	Time Variation	<1 %
	Powering Mode Variation	4.3 %
# Dead Channels	(No MIP Constant Extractable)	<0.1 %
Signal/Noise Ratio	$Mean_{MIP}/RMS_{pedestal}$	$\sim 53$
Gain	Mean	16.6 ADC
	Full Detector Spread	6 %
	Spread within same Readout Chip	2.5 %
	Time Variation	<1 %
	Powering Mode Variation	2.2 %
Light Yield	Mean	13.8 pixels/MIP
	Full Detector Spread	11.6 %
Intercalibration Factor	Mean	19.46
	Full Detector Spread	3.5 %
Low Gain Pedestal	Mean (Channel)	515 ADC
Hit Time Resolution	Muons	$\sim 0.78$ ns
	Showers	Several ns

Table 5.2: Summary of results for AHCAL prototype calibration and uniformity/stability studies.

# 6 AHCAL Prototype Event Simulation and Software Tools

For high energy particle physics and many other fields of research, Monte Carlo simulations have become an essential tool. Simulations do not only provide model predictions to be tested on actual acquired data, but also allow for setting up analysis frameworks before the actual data acquisition starts. This enables the possibility to cost-efficiently project the precision and performance of future experiments and corresponding detector systems. Based on this possibility, simulations are often used to perform a trade-off study between cost and desired performance or help to chose a respective detector technology for an experiment.

With respect to this thesis, simulations play a significant role, since they allow a projection of the particle flow reconstruction performance at a future lepton collider experiment. In general , different simulation models can have an impact on the development of the hadronic shower-substructure resolved by a highly granular calorimeter like the AHCAL prototype. This can consequently affect the pattern recognition and the energy considerations of a particle flow algorithm. Therefore, a detailed understanding and validation of different simulation models by comparison to acquired beam test data is inevitable. Only then, large scale performance projections based on simulations can be trusted to a large extent.

In Section [6.1](#) the software frameworks used within the scope of this thesis are presented. Based on these tools, the focus in Section [6.2](#) is set on the simulations of single particle events in the AHCAL prototype. Lastly, central software tools, which have been developed and optimised on the basis of simulated AHCAL prototype events and utilised for the studies presented within this thesis, are discussed in Section [6.3](#).

## 6.1 Software Frameworks

In the following, the two main software frameworks used for the studies presented in this thesis are briefly introduced: iLCSoft and CALICEsoft.

### 6.1.1 iLCSoft

Over the last two decades, the linear collider community has developed a bright spectrum of software tools and algorithms for Monte Carlo event simulations, physics performance studies, detector

optimisation studies, etc., covering various future experiments like e.g. ILD, SiD and CLIC. All of these software tools are summarised in a common software framework publicly available: iLCSoft<sup>1</sup>.

The baseline event data model used by many different algorithms within iLCSoft is called linear collider I/O (LCIO), considered as reliable and high-performance solution for dedicated event simulation and physics analyses [153]. Based on this event data model, many algorithms, detector concepts and physics analyses can be shared and compared between the different future collider collaborations. Another key feature of iLCSoft is the modular C++ framework MARLIN [109], used for the digitisation, reconstruction and analysis of physics events. MARLIN runs on LCIO files and is configured via XML steering scripts. One of the key benefits of MARLIN is the modular implementation of custom analysis code in the form of so-called processors, which allows a common and independent running of new next to already existing processors.

In the framework of this thesis, software tools and algorithms of iLCSoft v.02-00-01 are used with respect to event simulation, reconstruction and analyses. This includes GEANT4 v.10.3p2, DD4hep v.01-07-01, ROOT v.6.08.06 and MARLIN v.01-16 for example.

### 6.1.2 CALICEsoft

To facilitate the sophisticated simulation efforts and physics analyses of the physics prototypes data, the CALICE collaboration has implemented a common software framework: CALICEsoft. This framework features a collection of standalone algorithms and MARLIN processors for event simulation, digitisation and reconstruction, for prototype calibration and for sophisticated physics analyses of simulation and beam test data. In the context of this thesis, CALICEsoft version v.04-15 is used, which is publicly available on the git-based stash platform provided by DESY<sup>2</sup>. The algorithms developed within the context of this thesis, presented in Section 6.3, are part of this software release.

## 6.2 AHCAL Prototype Event Simulation

For an appropriate comparison to recorded beam test data, the AHCAL prototype and corresponding interactions and energy depositions of incident single particles are simulated. The first part of this section provides an overview about the simulated detector implementation and the different interaction simulations investigated within this thesis. With respect to this, the focus is set on the simulation of the June 2018 setup of the AHCAL prototype at the SPS CERN (see Section 5.4), since the acquired data of this beam test campaign is investigated in the scope of this thesis. In the second part, the further processing of the simulated calorimeter hits is summarised.

### 6.2.1 Geometry Implementation and Interaction Simulation

Providing detailed material descriptions and geometrical implementation of the AHCAL prototype and all further elements in the beam line, the DD4hep [154] framework is used for the event simulations in the scope of this thesis. DD4hep features a full description interface to GEANT4 for the simulation of individual particle interactions in the material. The material description

---

<sup>1</sup> <https://github.com/iLCSoft>

<sup>2</sup> <https://stash.desy.de/projects/CALICE>.

and geometrical setup of the AHCAL prototype and the beam line instrumentation is steered via configurable XML files<sup>3</sup>. Key aspects are briefly summarised in the following.

The simulated material composition of one AHCAL prototype layer is depicted in Figure 6.1a. The thickness of the individual parts in Figure 6.1a corresponds to the measured average dimensions over all layers: 17.2 mm of steel absorber plate, 1.285 mm of air-gap, 0.5 mm of steel cassette hosting the active layers, 1.5 mm of simulated cable mix of elements on top of the PCB, 0.7 mm of PCB, 0.115 mm of polystyrene simulating the reflective foil wrapping of the scintillating tile, 3.0 mm polystyrene scintillator, 0.115 mm of polystyrene foil, 0.5 mm of steel cassette and again 1.285 mm of air-gap.

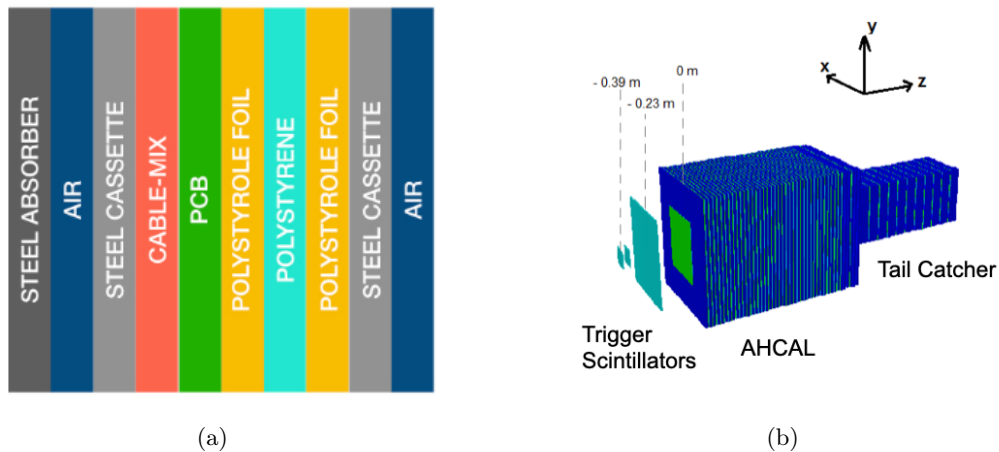


Figure 6.1: **(a)** Material decomposition of one AHCAL prototype layer. Dimensions are not to scale. Taken from [68]. **(b)** DD4hep geometry model of the AHCAL prototype setup for the June 2018 beam test at SPS CERN: steel absorber (dark blue), active layers (green), pre-shower layer (green square). Taken and adapted from [3].

A picture of the full AHCAL prototype model for the June 2018 beam test setup in DD4hep is presented in Figure 6.1b. The dimensions of the air-gaps between the two main slabs per layer (featuring two HBUs each) and the layer offsets in X and Y with respect to the first AHCAL layer are accurately simulated based on the measurements with the DWCs during the beam test campaign [3]. Instead of the trapezoidal shape of the steel absorber stack, only the quadratic steel absorber between the active layers of the AHCAL prototype are simulated, which is expected to have no impact on the simulations. The active layers are arranged in the same slots of the steel absorber stack as for the beam test campaign.

The coordinate system is chosen to have its origin  $Z = 0$  mm at the start of the pre-shower layer. Next to the trigger scintillators, the material of the full beam instrumentation upstream the SPS beam line is simulated including a Cherenkov counter not used during the beam test campaign. At  $Z = -47$  m additional 2 mm of steel are simulated in order to compensate for missing upstream material. The thickness of this extra steel plate is optimised on the agreement of the energy weighted center of gravity in Z for electrons showers of 30 – 90 GeV in data and simulation [3]. Lastly, the beam gun is located at  $Z = -50$  m with a set X/Y coordinate and profile according

<sup>3</sup>For the June 2018 beam test setup: [https://stash.desy.de/projects/CALICE/repos/calice\\_dd\\_testbeams/browse/2018\\_SPS\\_June\\_AHCAL](https://stash.desy.de/projects/CALICE/repos/calice_dd_testbeams/browse/2018_SPS_June_AHCAL)

to run-specific beam test conditions determined as presented in Section 7.1. A discrete particle momentum is chosen according to the desired beam energy.

Next to the individual interaction simulations, also effects of particles traversing the scintillating material are simulated by GEANT4 according to Birks' law:

$$\frac{dL}{dx} = \frac{dE}{dx} \cdot \frac{1}{1 + k_B \frac{dE}{dx}} \quad (6.1)$$

with  $\frac{dL}{dx}$  the light yield per length unit,  $\frac{dE}{dx}$  the specific energy loss per length unit via ionisation processes and Birks' constant  $k_B$ . This empirical law takes into account that the differential light yield in the scintillating material does not scale linear with very high energy loss rates.  $k_B$  is material specific and for the utilised simulation setup fixed to  $0.151 \text{ mm MeV}^{-1}$  based on optimisation studies for charged pion showers [2].

In the context of this thesis, single particle events are simulated either with the QGSP\_BERT\_HP or FTFP\_BERT\_HP physics list within GEANT4 v.10.3p2, as described in Section 4.2.3. With respect to the studies presented in Chapter 7, 8 and 9, only the simulated energy depositions in the main 39 layer AHCAL prototype are considered without the simulated pre-shower layer and tail catcher information.

## 6.2.2 Digitisation Chain and Reconstruction

In order to mimic a realistic detector response, including electronic and device specific effects, a data driven digitisation is applied on the simulated calorimeter hits. Figure 6.2 provides an overview about the digitisation chain. The individual steps are briefly discussed in the following. More details can be found in [88].

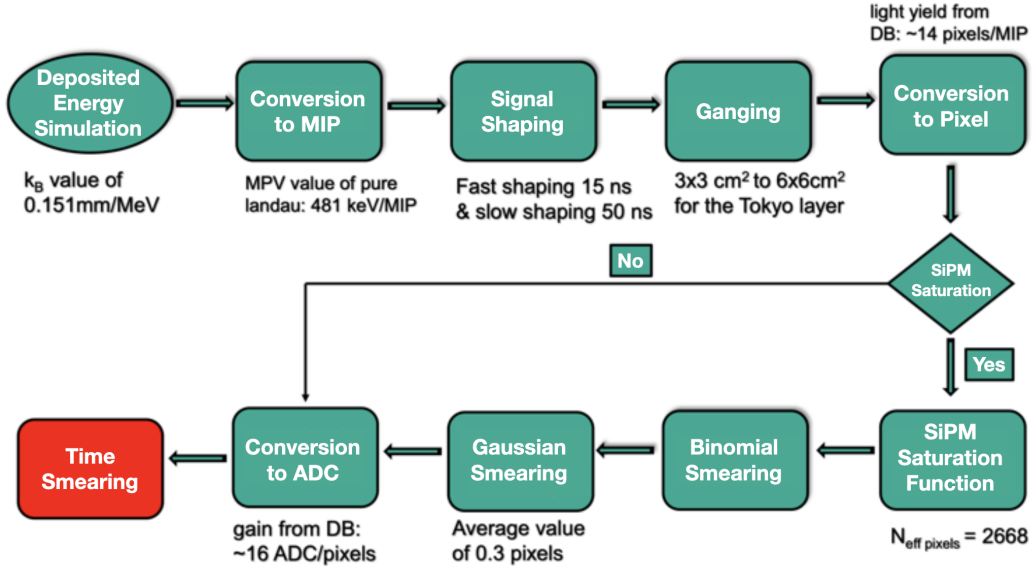


Figure 6.2: Digitisation chain for simulated energy depositions in AHCAL prototype channels. Taken and modified from [2].

In a first step, the deposited hit energy in units of GeV is converted to units of MIP in order to achieve the same energy scale as for the beam test data once calibrated. The conversion constant of 481 keV/MIP is determined by the MPV of a fitted energy deposition spectrum of simulated muons traversing the AHCAL in units of GeV. According to the discussions in Section 4.1.2, the shape of the spectrum follows a pure Landau function due to the good approximation of the scintillator tiles as a thin material and the absence of electronic effects at this point.

The next step includes the simulation of the fast and slow signal shaping of the SPIROC2E readout chip and the so-called ganging procedure, which combines the deposited energy information of four  $3\text{ cm} \times 3\text{ cm}$  AHCAL channels to mimic the  $6\text{ cm} \times 6\text{ cm}$  granularity of the Tokyo layer.

After that, the hit energy in units of MIP is converted into units of SiPM pixels with a light yield in the order of  $\sim 14$  pixels/MIP. This conversion is done channel-wise according to the light yields extracted from the beam test data for each channel and saved in the data base (DB). In the next step, the SiPM pixel saturation is simulated by applying a saturation function of the inverse form as shown by Equation 5.8. The number of effective SiPM pixels utilised within this function corresponds to the same number of effective SiPM pixels  $N_{eff,pixels} = 2668$  found in an optimisation study comparing the simulated and beam test data response of the AHCAL prototype to electron showers, as presented in 2. Subsequently, a binomial smearing is applied to mimic the statistical fluctuations of photons hitting and triggering a SiPM pixel, including e.g. the effect of the photon detection efficiency of the SiPM.

Lastly, a Gaussian smearing of 0.3 pixels is applied to mimic overall noise in the readout electronics. Again, this value is tuned by the agreement of reconstructed hit energy spectra for simulated and recorded electron shower data of various energies 3, 2. In the final step, a channel-wise conversion to units of ADC is performed by multiplying the gain constants saved in the data base. Since the focus of this thesis is not set on the timing performance of the AHCAL prototype, a smearing of the simulated hit time is disabled and will be investigated in future studies.

After the process of digitisation, the simulated calorimeter hits have the same format as the raw calorimeter hits of the recorded beam test data. The same reconstruction software chain is applied to the simulated events, including the channel-by-channel hit energy calibration with the same calibration constants as described in Section 5.5.

## 6.3 Central Software Tools

With sophisticated event simulations, pure event samples of specific particle types traversing the AHCAL prototype can be generated including truth interaction information. On the basis of this information, different algorithms have been developed for event reconstruction, selection and preparation for subsequent high level analyses. Except from the multi-variate particle identification, all central software tools presented in this section have been developed as preparatory steps for the presented studies with the AHCAL prototype data and simulations in the context of this thesis. However, those centralised algorithms find their application in collaboration wide analyses and are the baseline option in many studies. A special focus in this section is set on the developed hadronic shower start finding algorithm, which provides crucial information exploited by the other presented algorithms. All optimisation and validation studies for simulated samples in this section are based on the QGSP\_BERT\_HP physics list of GEANT4 v.10.3p2.

### 6.3.1 Hadronic Shower Start Finding Algorithm

The initiation of a hadronic shower by a hard in-elastic interaction of the primary incident hadron and a nucleus (see Section 4.1.3) typically happens in the absorber material of the calorimeter. With regard to the AHCAL prototype, the hadronic shower start layer is defined as the active layer following the absorber layer in which this interaction happened. Before this interaction, a perpendicular traversing charged primary hadron typically deposits MIP-like energies in form of a straight line in the calorimeter channels of the prior layers, which is referred to as primary ionising track in the following. Within this interaction, a bunch of secondary particles are generated typically resulting in a steep increase of both the number of triggered calorimeter channels and the deposited energy in the subsequent calorimeter layers. This is visualised in Figure 6.3 which shows a recorded 10 GeV charged pion data event in the AHCAL prototype highlighting the reconstructed hadronic shower start layer. The algorithm to determine the hadronic shower start layer is based on finding this sudden excess of the number of calorimeter hits and energy in subsequent calorimeter layers. A similar algorithm was developed and used for the AHCAL physics prototype [155, 88]. For the development of an efficient hadronic shower start finding algorithm for the AHCAL prototype, the basic concept and optimisation idea were reused, as explained in the following.

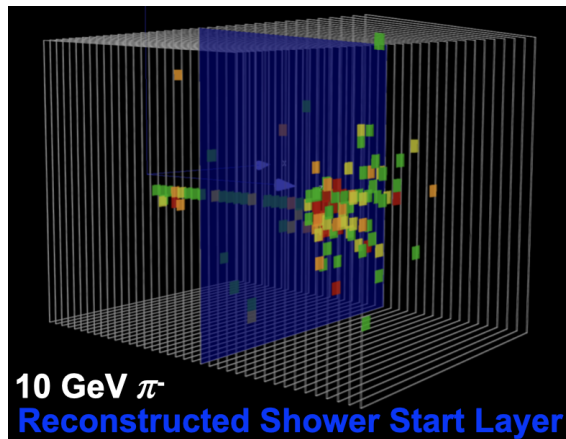


Figure 6.3: Event display of a 10 GeV charged pion shower in the AHCAL prototype from the May 2018 beam test. The blue layer highlights the determined hadronic shower start layer.

#### 6.3.1.1 Basic Concept

The basic principle of the hadronic shower start finding algorithm is based on a summed energy and number of hits criterium. For each layer of the AHCAL prototype event, two variables are calculated:  $M_i$ , which corresponds to the mean layer energy calculated from five subsequent layers up to the  $i$ -th layer, and  $N_i$  the number of hits in the  $i$ -th layer. The algorithm starts to iterate from the first calorimeter layer and checks the following conditions:  $(M_i + M_{i+1}) > E_{thr}$  and  $(N_i + N_{i+1}) > N_{thr}$  with an energy threshold  $E_{thr}$  and a number of hit threshold  $N_{thr}$ , as illustrated in Figure 6.4. As soon as both conditions are satisfied simultaneously the first time, the  $i$ -th layer is determined as the hadronic shower start layer. The five layer energy average is employed in order to suppress the effect of calorimeter hits caused by back-scattered particles or thermalised neutrons in the hadronic shower, potentially causing a misidentified too early hadronic

shower start layer. For the iteration through the first four layers of the calorimeter, virtual layers, each featuring 1 hit and a hit energy of 1.4 MIP, are implemented in order to mimic primary ionising MIP-like energy depositions. After a hadronic shower start is determined in the  $i$ -th layer, a steepness criterium is subsequently applied, which scans the steepness of the energy increase up to layer  $i + 4$  and decides if the  $i$ -th layer is kept or if layer  $i + 1$  is determined as the hadronic shower start layer. If none of the layers satisfy both conditions at the same time, the shower start variable is set to 100 indicating sail-through non-showering events for the processing in subsequent algorithms. Both thresholds,  $E_{thr}$  and  $N_{thr}$ , which are in general parametrised as a function of the input particle energy, are subject to the optimisation of the algorithm performance described in the next section.

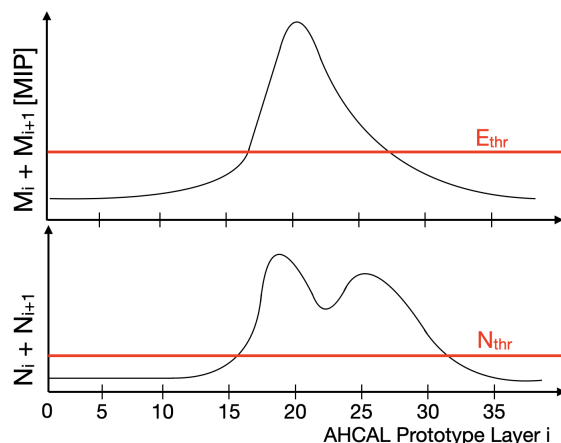


Figure 6.4: Illustration of the calculated energy and number of hit conditions of the hadronic shower start finding algorithm. The red lines demonstrate the threshold levels to be optimised.

### 6.3.1.2 Threshold Optimisation

In order to tune the energy and hit thresholds with respect to an optimised performance of the hadronic shower start finding algorithm, the MC truth hadronic shower start layer information within the simulation samples is exploited. This information can be extracted from the MCParticle LCIO collection<sup>4</sup>. In this collection the full particle and interaction history of the simulated event on GEANT4 level is saved including interaction types (hadronic, electromagnetic, decays,...) and parameters (momentum, kinetic energy, particle type, startpoint, endpoint, ...) of the primary incident particle and all particles generated in the hadronic shower development. However, to simply take the primary particles endpoint position in  $z$  as the MC truth hadronic shower start position for all events is not sufficient, due to its inadequate definition for hadronic shower. A considerable fraction of these interactions, which define the primary particles endpoint, are of elastic or soft in-elastic nature, leading only to a minor decrease of the primary hadrons energy. In addition, sometimes the initial hadron has an endpoint in connection with the appearance of a single hadron in the second generation with almost identical properties as the initial hadron before the interaction process.

<sup>4</sup> [http://lcio.desy.de/v01-07/doc/doxygen\\_api/html/classEVENT\\_1\\_1MCParticle.html](http://lcio.desy.de/v01-07/doc/doxygen_api/html/classEVENT_1_1MCParticle.html)

To be able to tune the thresholds accurately, those elastic and soft in-elastic interacting events as exemplarily depicted in Figure 6.5a, have to be rejected from the simulated event samples. This is done by introducing a hardness-criterion to explicitly select events with a sufficiently hard interaction and a subsequent hadronic shower start, as illustrated in Figure 6.5b. The hardness of the primary interaction is characterised by the effective kinetic energy sum of generated secondary particles without the leading hadron ( $E_{kin,gen}$ ) via:

$$E_{kin,gen} = \sum E_{kin,sec} - E_{kin,hlead} \quad (6.2)$$

with  $\sum E_{kin,sec}$  the kinetic energy sum of all particles in the second generation and  $E_{kin,hlead}$  the kinetic energy sum of the leading hadron in the second generation. The leading hadron is defined as the one secondary hadron with the same particle type as the primary hadron and the highest momentum projected onto the incident primary hadron direction.

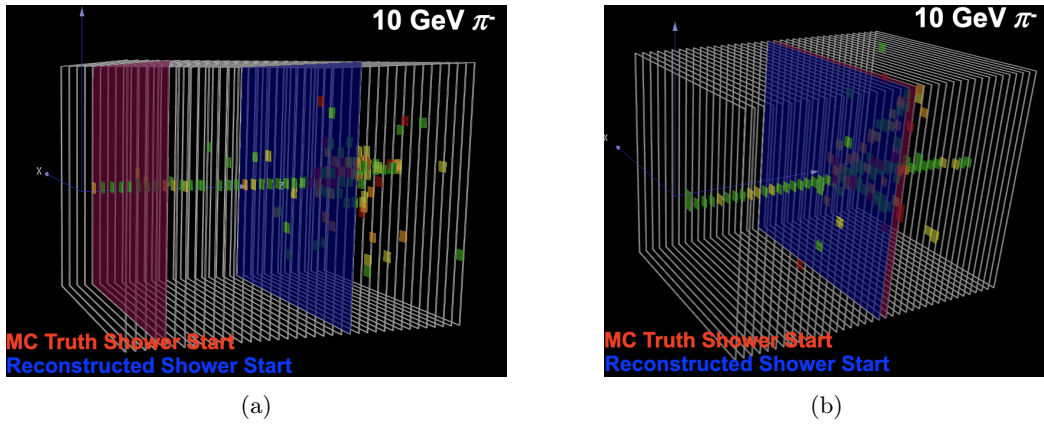


Figure 6.5: Event displays for simulated 10 GeV charged pions: (a) Soft primary particle interaction causing a distorted primary particle endpoint and an inadequate MC truth shower start layer. (b) Hard in-elastic primary particle interaction resulting in an accurate primary particle endpoint.

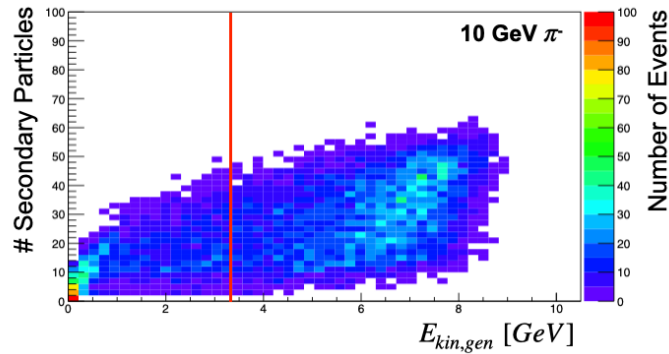


Figure 6.6: Number of generated secondary particles over  $E_{kin,gen}$  for a sample of 10 GeV simulated charged pions. The red line illustrates the hardness cut of  $E_{kin,gen} > \frac{1}{3} E_{primary}$ .

Figure 6.6 shows the correlation plot for the number of secondary particles and  $E_{kin,gen}$  for the example of a sample with 10k simulated charged pion. The large population at very low number of secondary particles and negligible  $E_{kin,gen}$  are representing elastic primary interactions. A hardness cut of  $E_{kin,gen} > \frac{1}{3}E_{primary}$  is chosen with  $E_{primary}$  the kinetic energy of the primary incident hadron. This allows to sufficiently reject the elastic and soft in-elastic events (left the red line in Figure 6.6), while keeping the event with hard in-elastic interactions (right the red line in Figure 6.6). These feature a considerable number of secondary particles and a significant fraction of energy transferred into the particles of the later generation. Furthermore, events which feature a primary particle endpoint definition outside the AHCAL volume are rejected. In a last step, the endpoint position in z is converted into the respective AHCAL prototype layer for determining the MC truth hadronic shower start layer.

With clean simulation samples at hand, the energy and hit thresholds are tuned individually for simulated 10 GeV and 30 GeV charged pions, both featuring 50 k events. Applying the hardness cut results in an event rejection of roughly 44 % for 10 GeV and 27 % for the 30 GeV charged pion samples. The parameter space of both thresholds is scanned simultaneously and tuned against a maximised efficiency of the hadronic shower start finder  $\epsilon_{SSF}$  according to:

$$\epsilon_{SSF} = \frac{\#Events(st = MC_{st} \pm 2)}{\#Events} \quad (6.3)$$

with  $\#Events(st = MC_{st} \pm 2)$  the number of events for which the determined shower start layer agrees with the MC truth shower start layer within  $\pm 2$  layers and  $\#Events$  the number of all events.

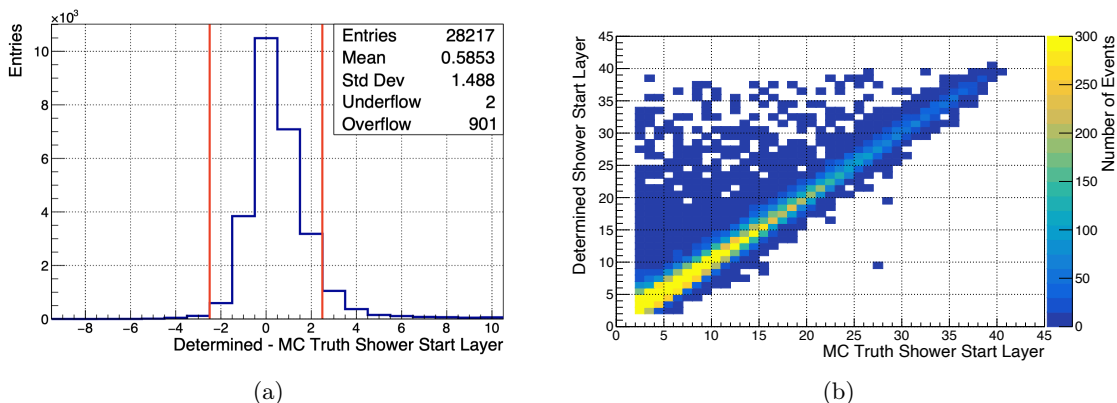


Figure 6.7: Results for optimised hadronic shower start finding algorithm for simulated 10 GeV charged pion showers with respect to MC truth shower start layer: (a) Difference distribution with red lines indicating bins considered for the efficiency optimisation. (b) Correlation.

For the 10 GeV (30 GeV) charged pion sample the maximal efficiency is found for  $E_{thr} = 17$  MIP ( $E_{thr} = 25$  MIP). Additionally, it is observed that for the optimised energy threshold the impact of  $N_{thr}$  on  $\epsilon_{SSF}$  becomes negligible. Therefore, in contrast to the original concept of the algorithm for the AHCAL physics prototype,  $N_{thr}$  is dropped and only the energy criterium is considered further within the algorithm. The distribution of the difference between the determined shower start layer and the MC truth shower start layer is depicted in Figure 6.7a and the correlation between both quantities is illustrated in Figure 6.7b with the optimised energy threshold for the 10 GeV

charged pion sample. An efficiency  $\epsilon_{SSF}$  of around 90% is found. The off-diagonal elements in the correlation plot originate from a very few remaining semi-hard interactions with  $E_{kin,gen}$  between  $0.33 - 0.4 E_{primary}$ . For the tuned  $E_{thr}$  of the two investigated energy points, a linear extrapolation is performed serving as a linear parametrisation of the energy threshold in dependence of the input beam energy according to  $E_{thr} = 13 \text{ MIP} + 0.4 \text{ MIP/GeV} \cdot E_{beam}[\text{GeV}]$ .

### 6.3.1.3 Validation and Results

To accurately validate and quantify the performance of the optimised hadronic shower start finding algorithm over a wide energy range, the optimised algorithm is applied to 10 – 100 GeV simulated charged pion samples featuring 10k events each. The achieved efficiencies, calculated by the agreement to the MC truth shower start layer as described by Equation 6.3, are plotted over the respective charged pion energies in Figure 6.8.

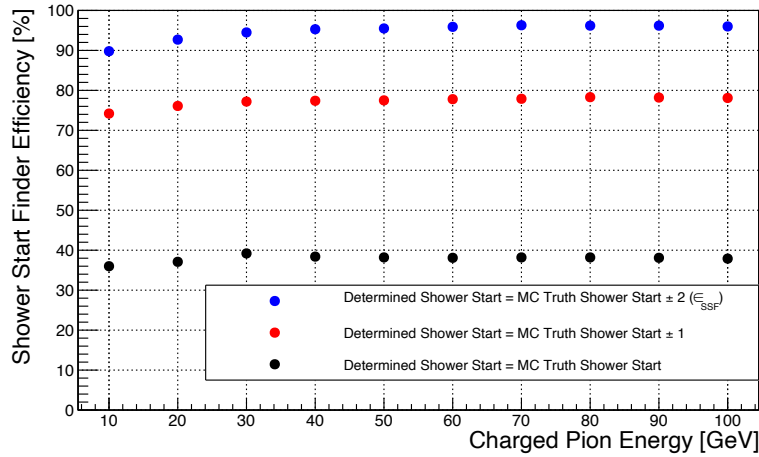


Figure 6.8: Achieved efficiencies of optimised hadronic shower start finding algorithm for 10 – 100 GeV simulated charged pion showers. Only events with a sufficiently hard primary interaction ( $E_{kin,gen} > \frac{1}{3} E_{primary}$ ) are considered, see Equation 6.2.

Over all charged pion energies, the algorithm provides a  $\pm 2$  layer agreement efficiency above 89%. The achieved efficiencies show an increasing trend with increasing charged pion energy up to 30 GeV. This is based on the steeper rise of deposited energy right after the in-elastic hard hadronic interaction for particle showers with higher energy, which is detected more efficiently by the algorithm. For higher energies, this effect saturates and results in almost constant efficiencies at the level of 96% for the  $\pm 2$  layer agreement, 78% for the  $\pm 1$  layer agreement and 38% for the exact agreement.

Similar efficiencies are achieved for the previous version of the hadronic shower start finding algorithm, developed for the AHCAL physics prototype [155, 88, 156], applied on the same AHCAL prototype simulation samples. In comparison to the version presented in this thesis, it features different parameters for the energy threshold parametrisation, a logarithmic parametrisation of the number of hits threshold with the particle energy and a mean layer energy window of six to ten instead of five layers. This results in a slightly better efficiency for the  $\pm 1$  layer agreement

( $\sim 76\%$ ) for 10 GeV charged pions and a better data to simulation agreement for the found shower start distribution in the first 3 layers of the AHCAL prototype. However, this comes at the costs of an increased total RMS of roughly  $0.2 - 0.3$  layers in the difference distributions of determined shower start layer and the MC truth shower start layer for all investigated charged pion energies.

A typical hadronic shower start layer distribution of 10 GeV charged pions for a June 2018 beam test data and a simulated sample<sup>5</sup>, both featuring 100k events, is depicted in Figure 6.9. In general, the distribution follows the expected exponentially decaying behaviour defined by the nuclear (pion) interaction length, as introduced in Section 4.1.3. Only the first two and last two layers are exceptional, due to intrinsic edge effects of the algorithm and the AHCAL prototype itself. The assumed MIP-like tracks for the virtual layers before the first AHCAL layer and the last layer being instrumented after two empty slots behind the last to last layer within the AHCAL steel absorber stack for the June 2018 beam test. Except from these outer layers, an excellent data to simulation agreement is observed.

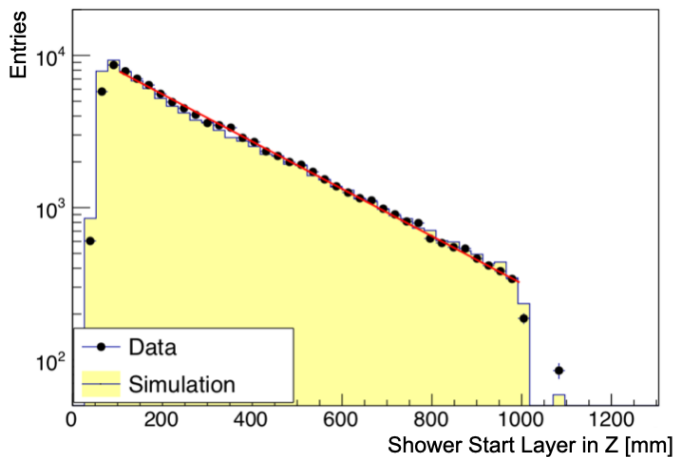
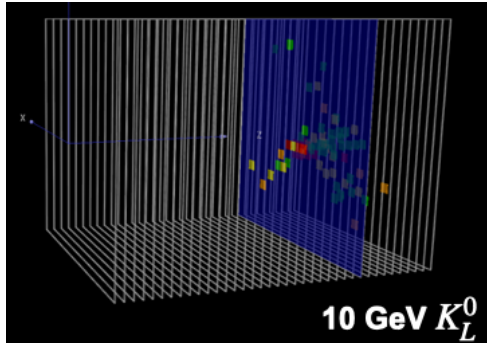


Figure 6.9: Determined shower start layer distribution ( $z$  coordinate of AHCAL layer) for 10 GeV charged pion samples of the June 2018 beam test data and simulation. The red line indicates a fit to determine the pion interaction length characterising the exponential decay. More details in [6].

Furthermore, the performance of the optimised algorithm is evaluated with simulated 10 GeV and 30 GeV neutral hadron samples ( $K_L^0$ ), each featuring 10k events. Neutral particles are missing the primary ionising track of MIP-like calorimeter hits before the first in-elastic hard hadronic interaction, as illustrated in Figure 6.10a for a 10 GeV  $K_L^0$  event. This results in an intrinsically steeper energy increase during the layer iteration and therefore an improved algorithm efficiency in comparison to charged hadron showers. Resulting efficiencies for different layer agreements to the MC truth shower start layer are summarised in Table 6.10b.

Lastly, the optimised hadronic shower start finding algorithm is applied to simulated 40 GeV muon and 10 GeV electron samples with 10k events each to evaluate the performance of the algorithm for showers of different particle types. The determined shower start layer distributions are presented in Figure 6.11. For  $\sim 1\%$  of the muon events a shower start is found in the AHCAL prototype. This can be caused by a low energy electromagnetic shower initiated e.g. by a radiated

<sup>5</sup>With removed beam contamination via PID, see Section 6.3.4.



(a)

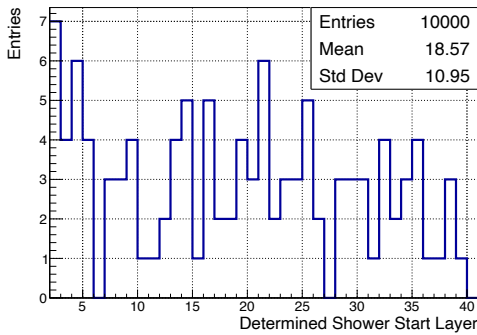
Efficiency [%]	10 GeV $K_L^0$	30 GeV $K_L^0$
Agreement	40.2	42.0
Agreement $\pm 1$	79.1	82.1
Agreement $\pm 2$	94.0	96.7

(b)

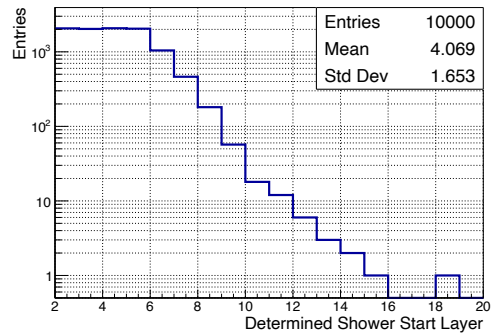
Figure 6.10: **(a)** Event display for simulated 10 GeV  $K_L^0$  with blue layer indicating determined shower start layer. **(b)** Achieved efficiencies of optimised hadronic shower start finding algorithm for 10 GeV and 30 GeV simulated  $K_L^0$ .

bremsstrahlung photon subsequently undergoing pair creation and agrees with the studies presented in [7]. Since one AHCAL prototype layer corresponds to  $\sim 1 X_0$ , the shower start is expected to happen in the first layers for basically all electrons. This is confirmed by the observed  $\sim 90\%$  of electron events with a determined shower start layer in the first five layers of the AHCAL prototype, despite the fact that the algorithm is not optimised for electromagnetic showers.

Based on the performance results for charged (neutral) hadrons, muons and electrons, the developed and tuned shower start finding algorithm is considered as evaluated. Therefore, the determined shower start layer information can be exploited in subsequent algorithms and analyses.



(a)



(b)

Figure 6.11: Distributions of determined shower start layer for simulated samples of: **(a)** 40 GeV muons. If no shower start layer is found, the value is assigned to 100. **(b)** 10 GeV electrons. For the June 2018 beam test setup the layer counting for the AHCAL prototype starts at 2, since layer 1 is assigned to the pre-shower layer.

### 6.3.2 Pseudo-Neutral Hadron Generation Algorithm

During the beam test campaigns in 2018, no neutral hadron data was recorded with the AHCAL prototype at the SPS CERN. However, for the two particle separation studies with PandoraPFA, presented in Section 8.4, neutral hadron showers are required. For these reasons a simple cut-based algorithm has been developed, which generates pseudo-neutral hadron showers based on recorded and simulated charged pion showers in the AHCAL prototype. Main objective of this algorithm is to remove the calorimeter hits of the primary ionising track caused by the incident charged pion before the first in-elastic hard interaction happens. The following conditions are defined to remove calorimeter hits of the primary ionising track on an event-by-event basis. All three conditions have to be true in order for an individual hit to be removed from the event:

- Hit located in layer  $\leq$  shower start layer - 2
- Hit located in cylinder with radius  $< 60$  mm around central shower axis defined by energy-weighted center of gravity in the transversal plane:

$$cog_x = \frac{\sum_{i=1}^{nHits} hitPositionX_i \cdot hitEnergy_i}{\sum_{i=1}^{nHits} hitEnergy_i} \quad (6.4)$$

$$cog_y = \frac{\sum_{i=1}^{nHits} hitPositionY_i \cdot hitEnergy_i}{\sum_{i=1}^{nHits} hitEnergy_i} \quad (6.5)$$

- Hit energy  $< 3$  MIP

The conditions are motivated by the following reasons: The calorimeter hits corresponding to the primary ionising track have to be removed only before the truth hadronic shower start layer. Based on the demonstrated shower start finding algorithm efficiency of at least 90% to determine the shower start layer within  $\pm 2$  layers from the MC truth shower start, the chosen condition minimises the chance of removing shower hits caused by a slightly too late determined shower start layer. Furthermore, the incident pions are assumed to enter the AHCAL prototype perpendicular with respect to the calorimeter front face. However, the applied 60 mm radius allows the primary particle to cross 2 AHCAL channels transversally over the full detector length caused by a slight incident angle. Lastly, the energy cut of 3 MIP allows to remove most of the Landau energy tail for the expected MIP-like energy depositions of the primary ionising calorimeter hits without removing too much of the high energy depositions caused by the electromagnetic shower core, if the shower start position is not found accurately. Figure 6.12 illustrates an example event of a 20 GeV charged pion shower, before and after applying the pseudo-neutral hadron generation algorithm.

The algorithm performance and the quality of the generated pseudo-neutral hadrons are validated in two steps with 20 GeV simulation samples of charged pions and  $K_L^0$ , both featuring 10k events. First of all, the number of cut hits by the algorithm is investigated for the determined shower start layer of the charged pions events, as illustrated in Figure 6.13. A clear correlation is found agreeing with the expectations of on average one MIP-like hit per layer removed by the algorithm. The later the hadronic shower start is located in the AHCAL prototype, the more MIP-like hits are removed in the previous layers.

In a second step, the energy response and topology of the generated pseudo-neutral hadron showers are validated by comparing basic calorimetric observables to those of simulated real neutral hadrons  $K_L^0$ . The comparison of the number of shower hits, hit energy sum and the mean

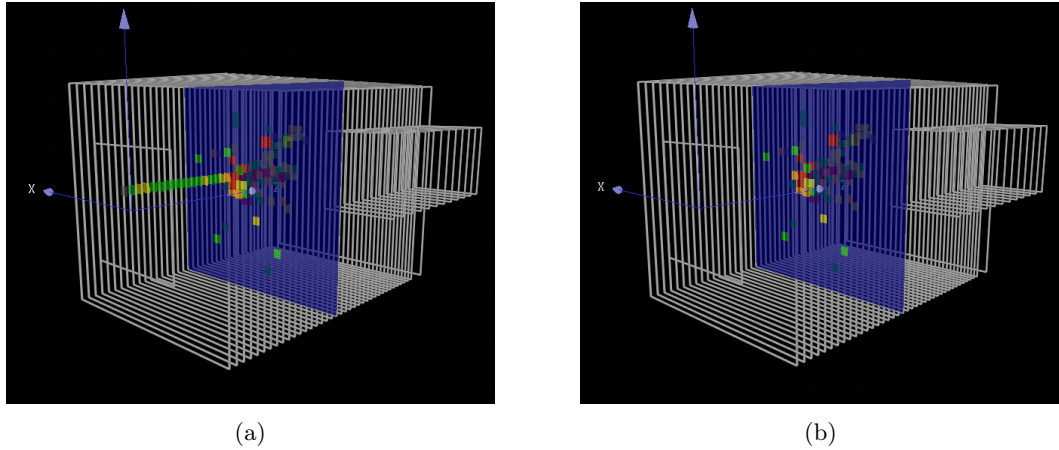


Figure 6.12: Event displays illustrating pseudo-neutral hadron generation algorithm for simulated 20 GeV charged pion with indicated shower start layer (blue): (a) Before applying algorithm. (b) After applying algorithm.

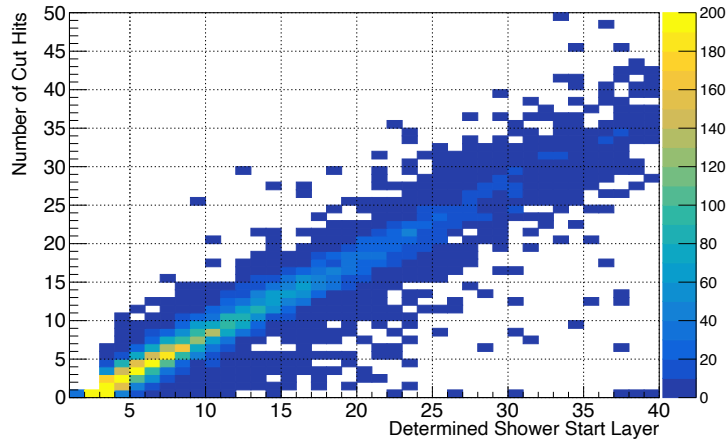


Figure 6.13: Number of cut hits by pseudo-neutral hadron generation algorithm over determined shower start layer for 20 GeV simulated charged pion events.

longitudinal and radial shower energy profiles are illustrated in Figure 6.14. An excellent agreement between the two types of showers is observed. On average the pseudo-neutral hadron shower consists only of about 7 hits less than the  $K_L^0$  showers. A similar observation is made energy-wise, since the pseudo-neutral hadron showers features on average only about 0.3 GeV less energy. Most of this energy deficit can be explained by the removed primary ionising track hits. With an assumed conversion constant of 0.028 MIP/GeV (see Section 8.2.3) about 7 – 8 removed MIP-like hits are on average causing the observed energy deficit. The mean longitudinal and radial energy profiles for both shower types agree within 20%. Additional validations studies are performed by comparing the same observables for the algorithm applied on  $K_L^0$  showers in comparison to un-

touched  $K_L^0$  showers. As expected, much better agreements mostly within 5% are found as shown in Figure B.1, showing that the application of the algorithm on real neutral hadron showers keeps those mostly unaffected. Bases on these studies, it is concluded that the quality of the generated pseudo-neutral hadrons is validated with respect to their energy and shower topology. Therefore, they are considered to accurately mimic real neutral hadrons in the simulation and recorded with the AHCAL prototype, suitable for the two particle separation studies with PandoraPFA.

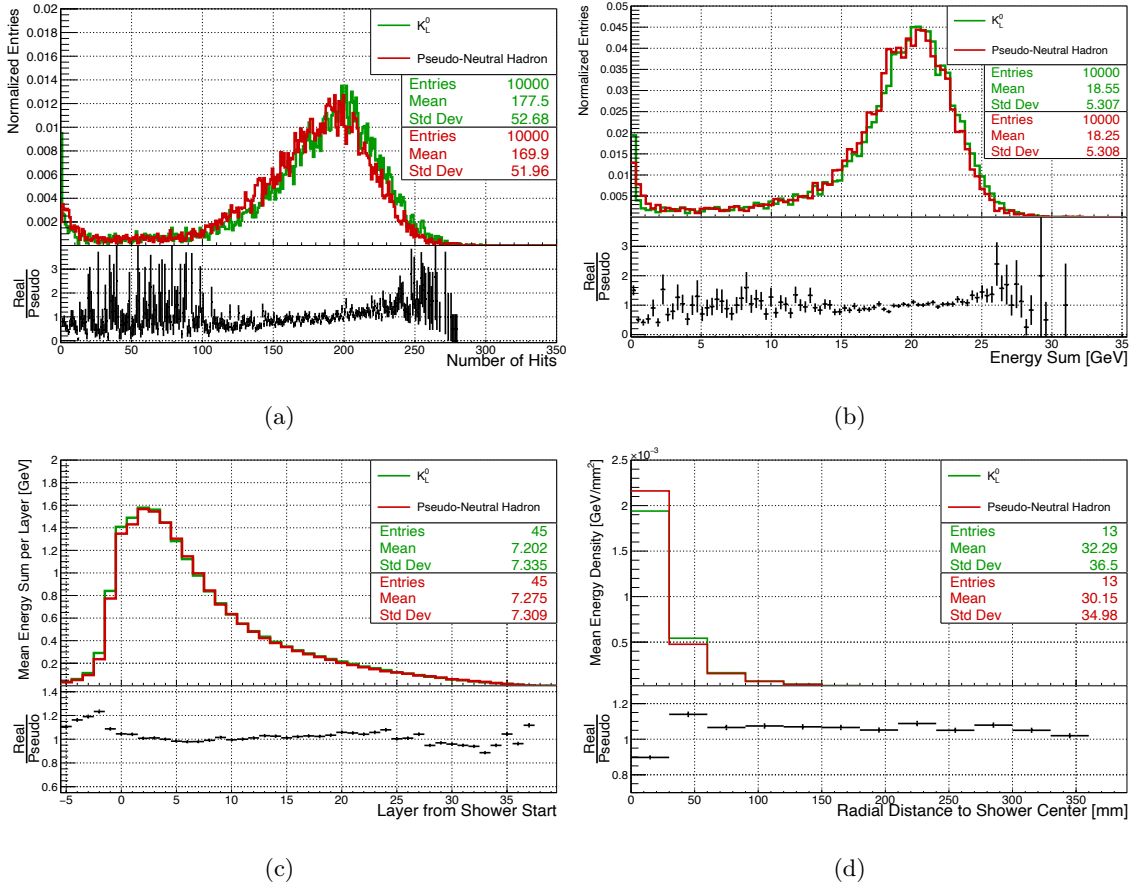


Figure 6.14: Calorimetric observables for 20 GeV simulated samples of  $K_L^0$  and generated pseudo-neutral hadrons based on charged pions (QGSP\_BERT\_HP): (a) Number of shower hits. (b) Hit energy sum. (c) Mean longitudinal energy profile. (d) Mean radial energy profile.

### 6.3.3 Event Overlay Algorithm

In order to study the two particle separation performance of PandoraPFA based on AHCAL prototype events, as presented in Section 8.4, an event overlay algorithm has been developed for the generation of dedicated two particle event samples. An illustration of the event overlay on the basis of event displays is exemplarily illustrated in Figure 6.15, showing a 10 GeV pseudo-neutral hadron

overlaid with a 30 GeV charged pion shower. Basic functionalities of the developed algorithm are summarised in the following:

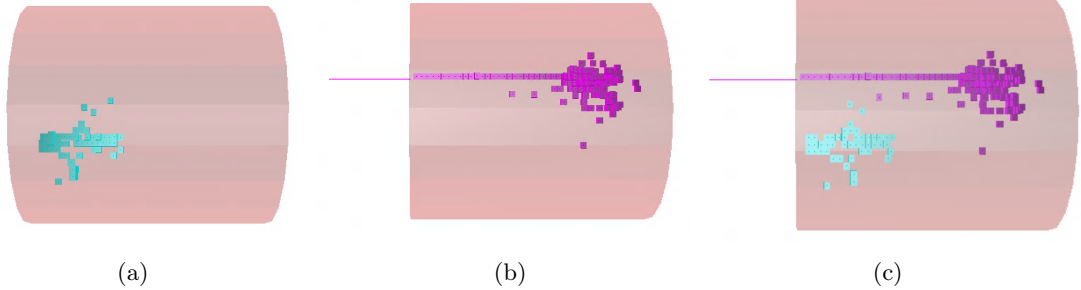


Figure 6.15: Illustration of event overlay algorithm for a simulated 10 GeV pseudo-neutral hadron (cyan) and a 30 GeV charged pion shower (magenta): **(a)** Pseudo-neutral shower hits before overlay. **(b)** Charged pion shower hits before overlay. **(c)** Pseudo-neutral and charged pion shower hits overlaid. Further information about the PandoraPFA event display can be found in Section [8.2.5.1](#).

- **Input and output:** The algorithm requires two input samples with single particle events (typically one with pseudo-neutral hadrons and the other with charged pion events) and provides one output sample containing the overlaid events.
- **Overlay modes:** Different overlay modes handle the event matching within the algorithm. For the studies presented within this thesis, a subsequent overlay mode is used, which overlays event 1 from sample 1 with event 1 from sample 2 and so on until the last event of either sample 1 or 2 is utilised. This is done in order to maximise statistics and ensure at the same time that no event of the two input samples is used twice in the overlaid event sample.
- **Hit by hit overlay:** The algorithm loops over all channels of the AHCAL prototype and checks if there is an energy deposition saved for the event of sample 1 and the event of sample 2. If this is the case for either of the cases, the energy deposition is saved for this channel. If both events feature an energy deposition for the same respective channel, the energy depositions are summed.
- **Hit flagging:** Each hit in the overlaid event is flagged to originate from the event of sample 1, the event of sample 2 or both events (in the framework of these studies: neutral, charged or mixed). For the case of a mixed hit, the fractional hit energies are also saved.
- **Threshold considerations:** After the overlay procedure, each hit of the overlaid sample is examined and rejected if it does not exceed the analysis hit energy threshold of 0.5 MIP. The application of a threshold only at this late stage allows to keep hits, which only exceeded this threshold by the overlay of a hit from the second event in the same channel. This allows to mimic real two particle events with calorimeter energy depositions in the same data acquisition time window.
- **Control parameters:** For each matched event pair the radial distance between the centralised shower axes of the two showers and the energy sum of both showers are saved.

To quantify the number of low energy ( $<0.5$  MIP) and overlaid hits with respect to the samples investigated later in this thesis, a study on representative data and simulation samples is performed. For this study, AHCAL prototype data of the June 2018 beam test and simulations<sup>6</sup> are used in order to generate two particle samples of a 10 GeV pseudo-neutral hadron, overlaid with a charged pion shower of 10 GeV or 30 GeV at radial distance of 25–75 mm and 175–225 mm. At input level, the samples feature a hit energy threshold level of 0.2 MIP. Table 6.1 summarises the results for the found mean number of low energy hits  $\langle nHits_L \rangle$ , the mean number of overlaid hits  $\langle nHits_O \rangle$ , the mean number of hits exceeding the 0.5 MIP threshold only after the overlay procedure with an hit of the other event  $\langle nHits_{new} \rangle$  and the mean number of hits removed by the 0.5 MIP threshold requirement  $\langle nHits_{cut} \rangle$  in the overlaid samples.

	10 GeV		10 GeV		10 GeV		10 GeV	
	+		+		+		+	
	10 GeV		10 GeV		30 GeV		30 GeV	
	25 – 75 mm		175 – 255 mm		25 – 75 mm		175 – 225 mm	
	Data   MC		Data   MC		Data   MC		Data   MC	
$\langle nHits_L \rangle$	16.3	52.9	16.4	51.7	26.5	90.6	27.1	86.4
$\langle nHits_O \rangle$	6.7	7.6	0.6	0.9	14.1	16.1	1.2	2.0
$\langle nHits_{new} \rangle$	0.02	0.13	0.01	0.04	0.04	0.29	0.01	0.09
$\langle nHits_{cut} \rangle$	15.6	50.9	16.3	51.2	25.1	86.2	26.8	83.0

Table 6.1: Summary of hit studies for overlaid data and MC samples featuring a 10 GeV pseudo-neutral hadron and a 10 GeV or 30 GeV charged pion shower for different radial shower distances.

In general, more low energy hits are observed for the investigated simulation samples in contrast to the beam test data samples. In addition, the number of low energy hits is higher for the scenarios including a 30 GeV instead of a 10 GeV charged pion shower, as expected. Also the trends for the observed overlaid hits agrees with the expectations. On average more overlaid hits are observed for the close-by shower scenarios and for the scenarios including a 30 GeV instead of a 10 GeV charged pion shower. From the determined values for  $\langle nHits_{new} \rangle$  below 0.3 for all data and simulation scenarios one can conclude that the impact from overlaid hits, which exceed the threshold of 0.5 MIP only after the overlay procedure, is negligible. Lastly, from the mean number of cut low energy hits  $\langle nHits_{cut} \rangle$ , one can see that most of the initial low energy hits  $\langle nHits_L \rangle$  are cut after the overlay procedure. Only a few low energy hits (maximal 2 – 4) overcome the threshold, since they are merged with a hit  $>0.5$  MIP from the second event. However, the maximal additional energy in the event caused by those low energy hits corresponds  $4 \cdot 0.5 \text{ MIP} \cdot 0.028 \text{ GeV/MIP} = 0.056 \text{ GeV}$  on average and is therefore considered as negligible.

In summary, the implemented overlay algorithm is considered as reliable and well suited to generate the two particle samples required for the studies presented in this thesis. Based on the presented studies, the trends for low energy and overlaid hits agree with the expectations for the various investigated scenarios and the effect of overlaid low energy hits is found to be negligible with respect to the investigated shower energies and topologies.

<sup>6</sup>For all samples the BDT particle identification for hadrons is applied, see next section.

### 6.3.4 Particle Identification

In the beam test data recorded with the AHCAL prototype in the beam line of the SPS CERN, a significant fraction of events within a run do not contain the desired particle type, specifically for the lower energies of 10 – 40 GeV. Visible from basic calorimetric event observables, the recorded beam test data can be studied with respect to particle contamination in the beam, as illustrated in Figure 6.16 for events recorded during a 10 GeV charged pion run. In the plotted phase space of the number of calorimeter hits and energy-weighted center of gravity in  $z$  ( $cog_z$ ) for the un-selected event sample, three different populations are present: muons, which are characterised by  $cog_z$  in the middle of the AHCAL prototype and a number of hits corresponding roughly to the number of AHCAL prototype layers; electrons, which typically shower in the first AHCAL layers and feature a low  $cog_z$ ; pions, which are typically widely spread in this phase space and feature a larger number of hits.

In order to investigate the detector response to single particles of a specific type, a particle identification (PID) has to be applied in order to remove the contamination events from the sample. For the event selection applied within the studies of this thesis, a multi-variate technique is employed based on gradient boosted decision trees. Since the implementation and study of this PID is not subject to the work presented in the context of this thesis, only key features and main performance results are presented in this section. Detailed information can be found in [5, 157].

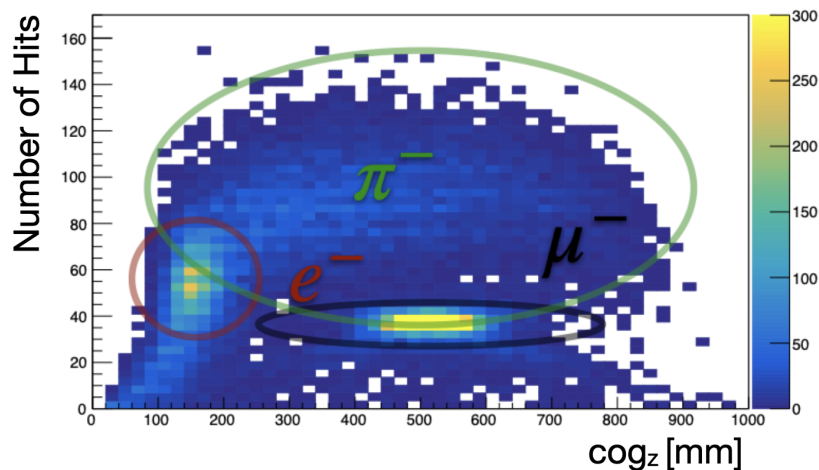


Figure 6.16: Number of hits over energy-weighted center of gravity in  $z$  for the events of a 10 GeV charged pion beam test sample illustrating beam particle contamination. Figure taken from [157].

Before the application of the multi-variate algorithm, several pre-analysis steps are performed in order to calculate calorimetric observables and to perform an initial event filtering. This includes a shower sub-structure track and cluster finding algorithm. Additionally, multi-particle and upstream showering events are rejected on specific requirements, like the number of calorimeter hits in the event or the number of found primary ionising tracks or calorimeter clusters.

After that, a multi-class gradient boosted decision tree (BDT) is utilised with a multi log loss function based on the LightGBM package<sup>7</sup>. The method of gradient boosting allows the combi-

<sup>7</sup> <https://lightgbm.readthedocs.io/en/latest/>

nation of several sequential decision trees with weights, which are tuned during the training with respect to the gradient of the loss function. The following calorimetric event observables are used for the training: number of hits, shower start layer, event (shower) radius, center of gravity in  $z$ , fraction of energy deposited in the first 22 layers, in the shower center and the shower core, the number of found sub-structure track hits, the fraction of found sub-structure track hits over all hits in the event, the mean hit energy after the shower start layer and the number of layers after the last five calorimeter layers subsequently containing hits. For the training and test samples, pions, electrons and muons of energies 10 – 200 GeV are simulated for the June 2018 setup of the AHCAL prototype. The simulated samples are split in half for training and testing purpose, featuring  $\sim 200$  k events each.

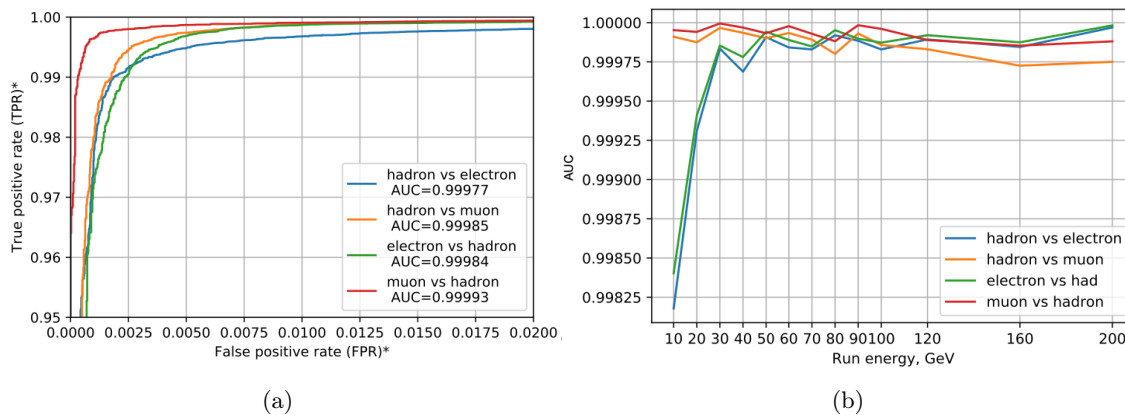


Figure 6.17: Evaluation of event classification performance by trained gradient BDT: **(a)** ROC curves for input test samples vs. trained classifiers. **(b)** AUC for input test samples vs. trained classifiers over particle energies. Figures taken from [157].

For performance evaluation of the event classification, the receiver operating characteristic (ROC) curves and the area under ROC curves (AUC) for different particle energies are presented in Figure 6.17 for different input test samples investigated by the three trained classifiers: muon, electron and hadron-like. The AUC for each of the three classifiers differs from 1 only in the fourth order, which shows that a wrong classification only happens in rare cases. The muon-hadron classification is the most efficient, the hadron-electron classification performance is only slightly lower in comparison. This behaviour originates from the fact that early showering low energy hadrons ( $\sim 10$  GeV) can topologically and energetically be very similar to electron showers. This is supported by the slightly degraded AUC at the lowest investigated beam energies for the hadron-electron classification, reaching the AUC level of the other classifications only at roughly  $\sim 30$  GeV. To summarise, the efficiency of a successful hadron classification of hadrons corresponds to 99.3% over the entire energy range and the probability to mis-classify electron or muons as hadrons is lower than 0.3% and 0.2%, respectively [5].



# 7 AHCAL Prototype Performance and Simulation Validation

The next parts of this thesis investigate the high-level PandoraPFA reconstruction performance of the AHCAL prototype for both, beam test data and simulation. This chapter lays the basis for this study by presenting the conventional calorimetric energy response of the AHCAL prototype to individual particles in beam test data and simulation, and validating the agreement between those two. Section 7.1 of this chapter describes the method of data-based beam profile extraction for tuning the simulated particle beam. After that, the calibrated AHCAL prototype response to single muons, electrons and pions for both, data and simulation, is presented and briefly discussed in Section 7.2. In the scope of this thesis, the investigation of the muon response is performed to validate the channel-wise MIP energy scale calibration for data and simulation. The goal of the electron and pion response investigation is to check if the details of the simulation and digitisation models results in a proper description of the data and to quantify the conventional calorimetric energy reconstruction performance on the basis of energy linearity and relative energy resolution.

Most of the studies presented in this chapter have not been conducted within the scope of this thesis and are excerpts of much more detailed investigations of the energetic and topological responses of the AHCAL prototype to the three investigated types of particles. All of these studies commonly utilise the introduced BDT-PID (see Section 6.3.4) to reject particle contamination within the beam and the same physics lists QGSP\_BERT\_HP and FTFP\_BERT\_HP within GEANT4 v.10.3p2. For further information, e.g. on the exact event selection and uncertainty calculations, see for 7 muons, 3 for electrons and 2 for pions.

## 7.1 Beam Positions and Profiles

In order to avoid a channel-specific bias in the comparison between data and simulations, one has to ensure that on average the same prototype channels are hit by the real or simulated particle beams. This is achieved by tuning the position and the width of the beam gun within the simulation procedure in  $x$  and  $y$  to match the beam position and width of the particle beam in the experiment.

For this purpose, the energy-weighted center of gravity distributions in  $x$  ( $cog_X$ ) and  $y$  ( $cog_Y$ ), calculated as shown by Equations 6.4 and 6.5, are used to estimate the beam position and beam width for the data samples of the different particle beams. This is considered as a sufficient estimate with respect to the real beam parameters, since the AHCAL prototype features less than 0.1% dead channels and operates at a very low noise level, as described in Section 5.2. For data samples of all investigated energies and particle types, muons, electrons and pions, the mean and RMS of the  $cog_X$  and  $cog_Y$  distributions are extracted and used as the input of beam position and

width of the simulated particle gun. The resulting  $cog_X$  and  $cog_Y$  distributions of the simulation samples are subsequently compared to the corresponding distributions of the data samples. For a 60 GeV pion run this comparison is exemplarily illustrated in Figure 7.1. An acceptable agreement between data and simulation is achieved for both coordinates. The peak-like features within the distributions originate from the equidistant 30 mm scintillating tile positions. For muons, electrons and low energy pions a significant better agreement is achieved due to the lower spatial fluctuation of the respective energy depositions in contrast to high energy pion showers. Thus, the shown distributions represent the most conservative agreement achieved in the presented work.

For each of the simulated pion samples investigated in the scope of this thesis, see Section 8.1.4, the beam position and profile have been tuned with this method to match the beam position and profile of the corresponding data sample.

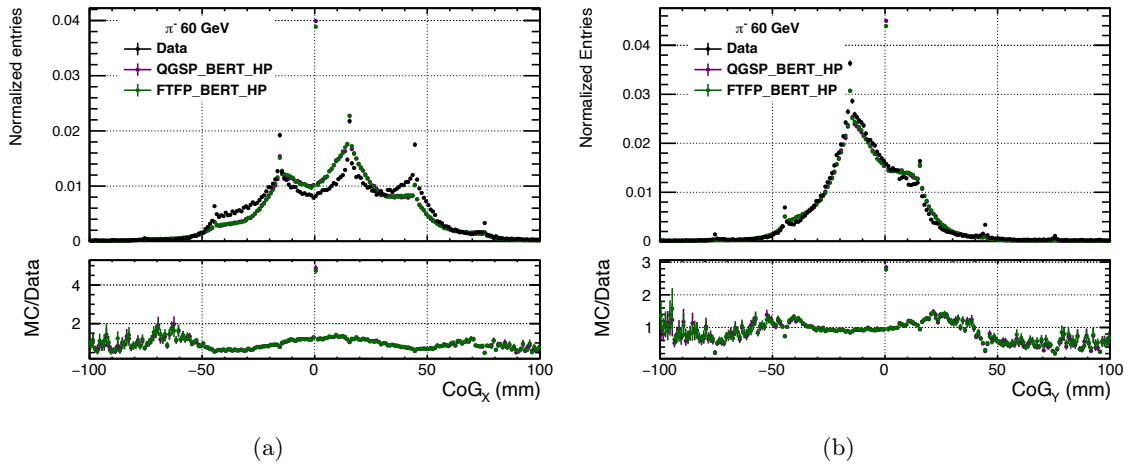


Figure 7.1: Beam profiles acquired with the AHCAL prototype for 60 GeV charged pions of a June 2018 beam test data run and corresponding simulations. (a)  $cog_X$ . (b)  $cog_Y$ . Taken from [2].

## 7.2 Energy Response

In the following, the calibrated conventional calorimetric energy response of the AHCAL prototype is presented for the full set of 40 GeV muons [7] of the May 2018 beam test and 10 – 100 GeV electrons [3] and 10 – 200 GeV charged pions [2] of the June 2018 beam test. For the comparison to the simulated response, the QGSP\_BERT\_HP is used for muons and electrons, while QGSP\_BERT\_HP and FTFP\_BERT\_HP are both investigated for pions.

### 7.2.1 Muons

As extensively discussed in Section 5.5, the energy deposited by MIPs is utilised as the energy deposition scale after calibration. In order to compare results and perform further conversions to different energy scales, it is crucial to validate the achieved MIP energy scale for data and simulation. In Figure 7.2a the global hit energy spectrum of all AHCAL channels is plotted for data and simulation.

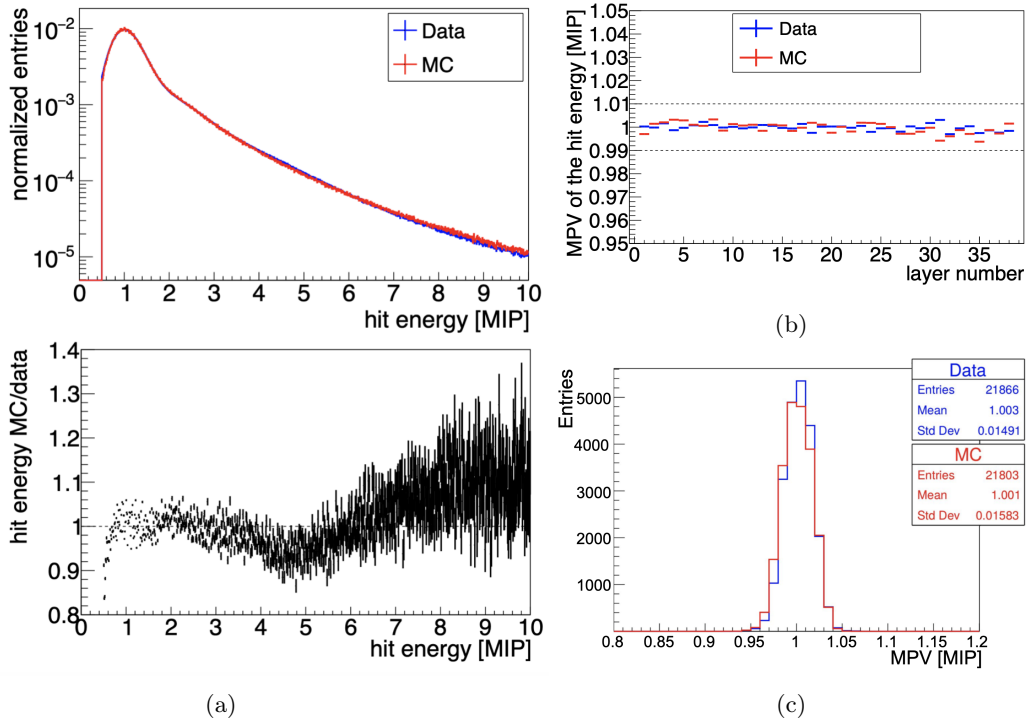


Figure 7.2: AHCAL prototype response to 40 GeV muons of May 2018 beam test data and simulations. (a) Global hit energy spectrum [7]. MPVs extracted from Landau convoluted Gaussian fits to layer-wise (b) [7] and channel-wise (c) hit energy spectra.

Both distributions accurately peak at 1 MIP and the general shapes agree very well between data and simulation. Only at very low hit energies close to the analysis threshold of 0.5 MIP and in the Landau tail above 4 MIP higher deviations up to 20% are observed. The most probably values (MPVs) of the energy depositions in the AHCAL channels of a specific layer are depicted in Figure 7.2b. It shows an excellent agreement between data and simulation, and validates the simulation within less than 1%. Furthermore, the precise and successful calibration procedure is further validated by all MPVs agreeing within 1% to 1 MIP. This is additionally supported by Figure 7.2c on individual channel level. Both MPV distributions peak at 1 MIP within 1% and show a spread which agrees within 5% between data and simulation. All in all, this shows the excellent calibration on channel level achieved for both, data and simulation, and the validation of the simulation at the lowest energies.

## 7.2.2 Electrons

Since the interactions within electromagnetic shower are well understood and simulated with high precision, the investigation of the AHCAL prototype response to electrons allows to further validate the simulation in many aspects. This includes not only the exact material composition and the geometry of the detector, but also the general calibration and the response to highest energies. Incident high energy electrons typically shower immediately in the AHCAL prototype and deposit

most of the energy in a few channels due to the compactness of electron showers. This emphasizes the role of the SiPM pixel saturation of individual channels with respect to the total energy reconstruction. Detailed studies about the SiPM saturation for the AHCAL prototype have been conducted with respect to tuning the applied saturation and de-saturation functions for simulated events and the estimation of systematic uncertainties. Details can be found in [3, 2].

Figure 7.3a shows the achieved energy linearity for electron shower samples of data and simulation. The AHCAL prototype is found to respond linearly over the investigated electron energy range, within 2% for beam test data and within 1% for simulated electrons. While the agreement between data and simulation is found to be within 2% for energies up to 30 GeV, the discrepancy grows up to 4–5% for highest energies. This can only be partly explained by the systematic error on the simulation, which is mostly dominated by the effects of SiPM saturation.

The relative energy resolution is plotted in Figure 7.3b for the same energy range. The AHCAL prototype achieves a single electron energy resolution of about  $22.6\%/\sqrt{E_{beam}} \oplus 1.0\%$  for beam test data based on the parametrisation introduced in Section 4.3.2. The same resolution is achieved for the simulation within 5%, while for all but the 10 GeV point the discrepancy lies within the systematic error band of the simulation.

The achieved accuracy level of simulated electron showers describing data is considered as satisfying for the PandoraPFA studies of 10–80 GeV pion showers (Section 8.3), since the total deposited energy is distributed over a larger number of channels and SiPM saturation effects play a smaller role for pion showers in comparison to electron showers.

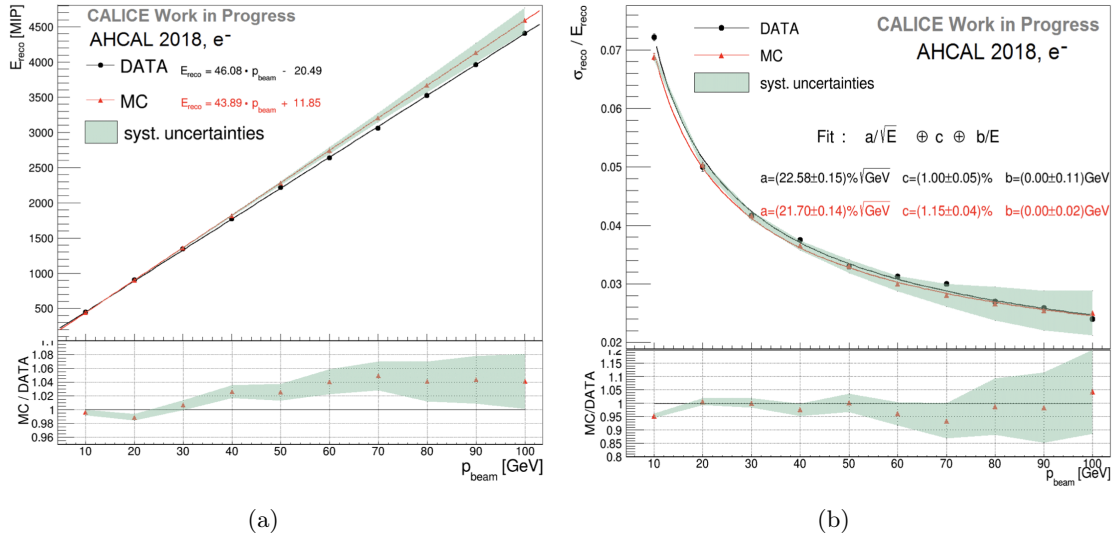


Figure 7.3: AHCAL prototype response to 10–100 GeV electrons for June 2018 beam test data and simulations. (a) Energy linearity. (b) Relative energy resolution. Taken from [3].

### 7.2.3 Charged Pions

After the validation of an excellent calibration and a well tuned simulation on the basis of the investigated MIP and electromagnetic shower response, lastly and most importantly for the studies presented in the scope of this thesis, the energy response of the AHCAL prototype to charged pion

showers is investigated for data and simulations [2]. In order to reduce the bias caused by leakage events, a hadronic shower start in the first six AHCAL prototype layers is required for these studies.

Figure 7.4a shows the energy linearity for the investigated data and simulation samples. An overall response linearity within 5% is achieved over all energies, except for the lowest energy of 10 GeV for which a linearity within 10% is observed. Data and both simulated physics lists agree almost within 2% over the full energy range, while again for 10 GeV the discrepancy corresponds to 2% for both physics lists. This observed discrepancies are reproduced for the 10 – 80 GeV charged pion samples on the GeV energy scale level, which are utilised for the studies presented within this thesis, see Section 8.1.4.

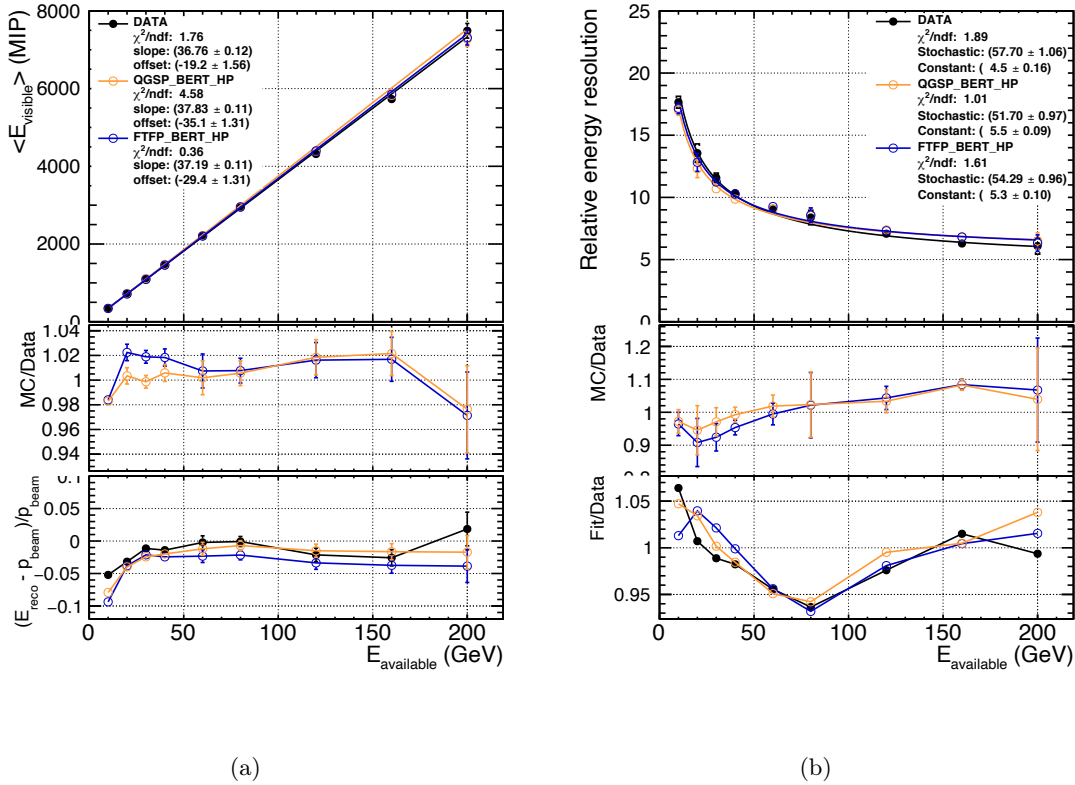


Figure 7.4: AHCAL prototype response to 10 – 200 GeV pions for June 2018 beam test data and simulations. **(a)** Energy linearity. **(b)** Relative energy resolution. Taken from [2].

The relative energy resolution over the same energy range is depicted in Figure 7.4b. For the beam test data, the AHCAL prototype achieves a single charged pion energy resolution of  $57.7\%/\sqrt{E_{\text{beam}}} \oplus 1.06\%$  based on the same parametrised function as used for the electron resolution. The simulated relative energy resolution agrees within 10% over the full energy range for both physics lists, while the deviations from the fit function are approximately within 5% over the full energy range.

Based on this results, the data to simulation agreement of the conventional calorimetric energy

response for charged pion showers in the AHCAL is considered suitable for the PandoraPFA studies presented next. Furthermore, a very good performance with respect to the energy linearity and resolution for hadron showers has been validated. These conventional calorimetric performances still play a significant role not only in the remaining conventionally reconstructed neutral cluster energies, but also in the accuracy of the track momentum to charged cluster energy comparison within the PandoraPFA reconstruction.

# 8 PandoraPFA Studies with AHCAL Prototype Data

The projected jet energy resolution achievable with particle flow reconstruction in a future lepton collider experiment relies on the accurate hadronic shower modelling in the utilised Monte Carlo simulations. Details of these simulations, like the topology or energy dissipation in the hadronic shower development, are expected to have a significant impact on the limiting effects and therefore the achievable performance of the particle flow reconstruction. Furthermore, the performance of real detector systems in such experiments may differ from the idealised Monte Carlo modelling.

The studies presented in this chapter have the goal of investigating the performance of particle flow reconstruction on acquired beam test data of a state of the art highly granular hadronic calorimeter prototype and of validating the performance for corresponding Monte Carlo simulations. This validation would provide further proof that the projected particle flow reconstruction performance at a future lepton collider experiment, based on similar Monte Carlo simulations, is realistic and reliable. In addition, this study aims to disentangle the two types of confusion energy in the particle flow reconstruction: double counted charged and lost neutral confusion energy. A detailed investigation of the level and balance of the two confusion types for different particle distances and energies helps to gain a deeper understanding of the limitations and their impact on the particle flow reconstruction performance. Lastly, this study offers the unique opportunity to test the feasibility and confirm the technical implementation of a particle flow algorithm framework on a calorimeter in a standalone application, in contrast to a fully hermetic collider detector system.

To achieve these goals, the ILD default PandoraPFA algorithm framework is adapted and applied to AHCAL prototype beam test data and simulation samples. In a first step, the PandoraPFA reconstruction of single charged pion showers of various energies is investigated. This allows the exclusive study of double counted charged confusion energy and to benchmark the single charged pion particle flow reconstruction performance. After that, the focus is set on the PandoraPFA reconstruction of two particle events, consisting of a pseudo-neutral hadron overlaid with a charged pion shower of different energies at varying radial distances, in order to study the two particle separation performance.

In Section [8.1](#) the event preparation and selection are summarised, complemented by an overview of the utilised hadronic shower samples. Setup-specific adaptations of the PandoraPFA framework to allow a reconstruction of the AHCAL prototype events are described in Section [8.2](#). Finally, the results of the single and two particle reconstruction studies are presented and discussed in Section [8.3](#) and [8.4](#).

## 8.1 Event Preparation, Selection and Sample Overview

To allow a reliable and sufficient application of PandoraPFA to the AHCAL prototype events, beam test data and simulated samples have to be prepared and selected in an initial step. A schematic overview of these procedures is provided by Figure 8.1

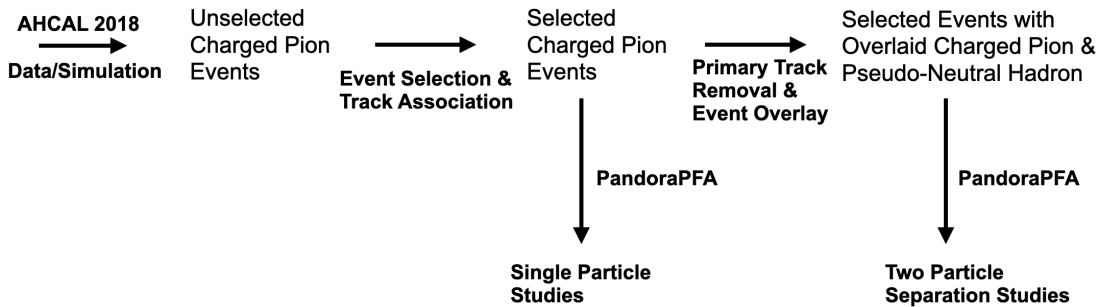


Figure 8.1: Overview of AHCAL prototype event preparation and selection for single and two particle PandoraPFA studies.

First of all, charged particle tracks are added to the charged pion shower events followed by dedicated event selection. After these steps, the samples are ready to be reconstructed by PandoraPFA for the single particle study. In a second step, selected charged pion events are the basis for the generation of two particle events, including a charged pion and a generated pseudo-neutral hadron shower. After this procedure, the events samples are ready to be reconstructed by PandoraPFA to study the case of two particle separation. The individual steps are discussed in the following sections and an overview of the utilised samples is provided.

### 8.1.1 Track Implementation and Quality Validation

Charged particle tracks are an essential part of the particle flow reconstruction. For this reason, a crucial first step is a track implementation for each charged pion shower event in the AHCAL prototype. Due to the beam test operation of the prototype in the SPS beam line without a magnetic field, a well defined beam direction and beam particles featuring almost only a momentum in the  $z$ -component, the tracks are assumed to be straight. Based on this assumption, the tracks align with the  $z$ -axis and end at the prototype front face perpendicularly, as illustrated by Figure 8.2. In this section, the spatial track implementation for beam test and simulated events is discussed in detail. A momentum is manually associated to the track during the interface instance, as described in Section 8.2

#### Tracks for Beam Test Data

As discussed in Section 5.4, four DWCs were installed upstream during the beam test operation of the AHCAL prototype in June 2018. Thus, in principle four measured coordinates per traversing charged particle could be used for a spatial track reconstruction and extrapolation to the AHCAL prototype front face. Detailed descriptions of the DWC calibration, track reconstruction and

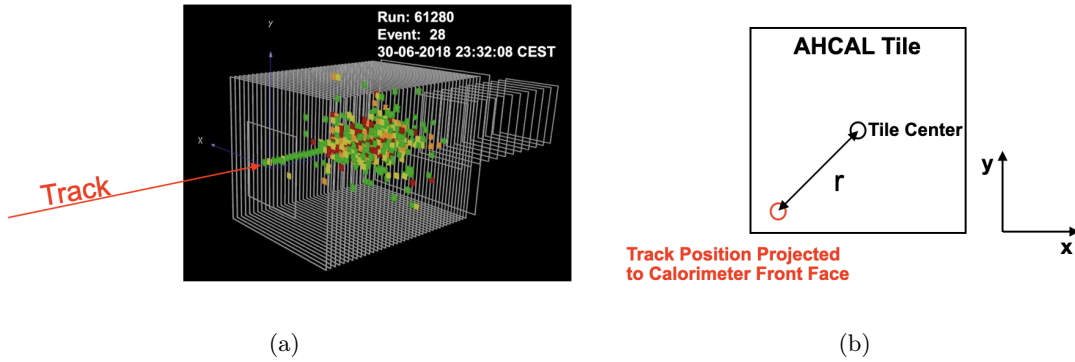


Figure 8.2: Visualisation of track implementation for AHCAL prototype events: **(a)** Illustrated track and hadronic shower of an 80 GeV charged pion in the AHCAL prototype. **(b)** Track projection to the AHCAL front face illustrating distance measure to tile center of an AHCAL channel.

synchronisation with the AHCAL prototype are provided in [8, 9]. In the following, only the key aspects most important for the presented studies are summarised.

In a first step, the alignment of the four DWCs with respect to each other is calibrated with a high statistics ( $\sim 120$  k) 160 GeV pion sample. The first DWC is chosen as the reference and the  $x$  and  $y$  offsets for the other DWCs are calculated. This is done by tuning the offsets for the respective DWC offline, so that the beam center is located at the same  $x$  and  $y$  position as for the reference DWC. In a second step, linear functions are fitted to the  $x$  and  $y$  coordinates individually, corrected by the offsets determined in step one, for a track reconstruction. Subsequently, the average hit to track position residuals for each DWC are minimised for a more precise second order offset correction. An example of the achieved hit to re-fitted track residuals after this initial calibration procedure is shown for the second downstream DWC in Figure 8.3.

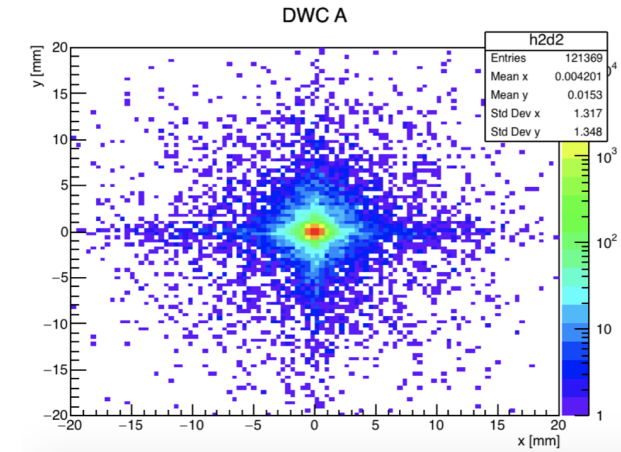


Figure 8.3: Residuals of hit and fitted track position of  $x$  and  $y$  coordinate for second downstream DWC for 160 GeV pions after inter-DWC calibration [9].

The final track is reconstructed by fitting the x and y coordinates of the measured four spatial points, which are corrected for the respective chamber alignment, individually with a linear fit, as shown for the x coordinate in Figure 8.4. In combination with the x and y coordinate at the calorimeter front face (fit intersection at  $z = 0$ ), the two determined slopes provide a full three-dimensional description of the charged particle track according to:

$$x(z) = \text{slope}X \cdot z + \text{intersection}X \quad (8.1)$$

$$y(z) = \text{slope}Y \cdot z + \text{intersection}Y \quad (8.2)$$

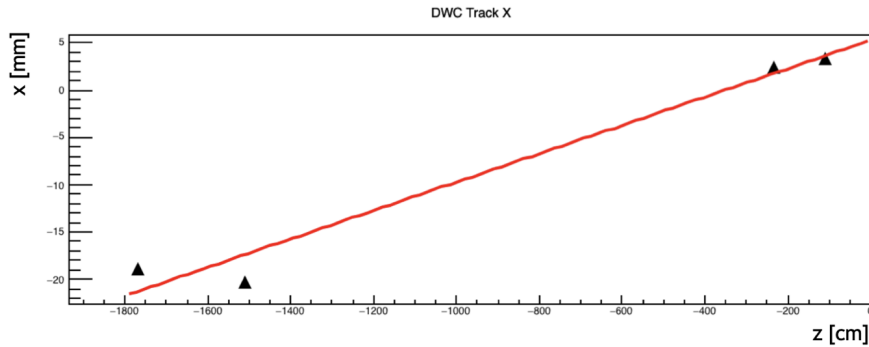


Figure 8.4: DWC measurements of x coordinate over position of the four operated DWCs in z for a traversing 160 GeV charged pion. For track reconstruction a linear fit is applied [8].

For each event, the two intersections and the two slopes are saved in a LCIO collection for further processing and analysis. In addition, a track quality flag is stored indicating events with a missing measurement in at least one DWC or multiple measurements in the same DWC resulting from multi-particle or noise events. Figure 8.5 shows the reconstructed x and y slopes for a 80 GeV charged pion sample. As for all investigated samples in the scope of this thesis, for more than 99 % of events both absolute slope values are lower than 0.001. This corresponds to a maximal shift in the x or y direction of roughly 17 mm for a z distance of 17 m (distance from first DWC to AHCAL prototype front face), validating the assumption of quasi straight tracks on average.

Lastly, a run-specific alignment calibration of the DWC system with respect to the AHCAL prototype is required in order to correct for the relative position of the AHCAL, which was located on a moveable stage during beam test operation. Thus, for each run the correlation of the reconstructed track position at the AHCAL front face and the energy-weighted center of gravity *cog* for each event is monitored individually for the x and y coordinate. By fitting a linear function with slope 1 to the correlation distributions, the global alignment offset for the x and y coordinate is determined and saved for each individual beam test run. Figure 8.6 illustrates an example of this procedure for the x coordinate correlation of a 40 GeV muon run with a determined x offset of  $\sim -100$  mm. The extracted offsets are used to shift the reconstructed tracks into the reference coordinate system of the AHCAL prototype according to the beam test run number. Table C.1 summarises the determined offsets for all beam test runs investigated in the scope of this thesis.

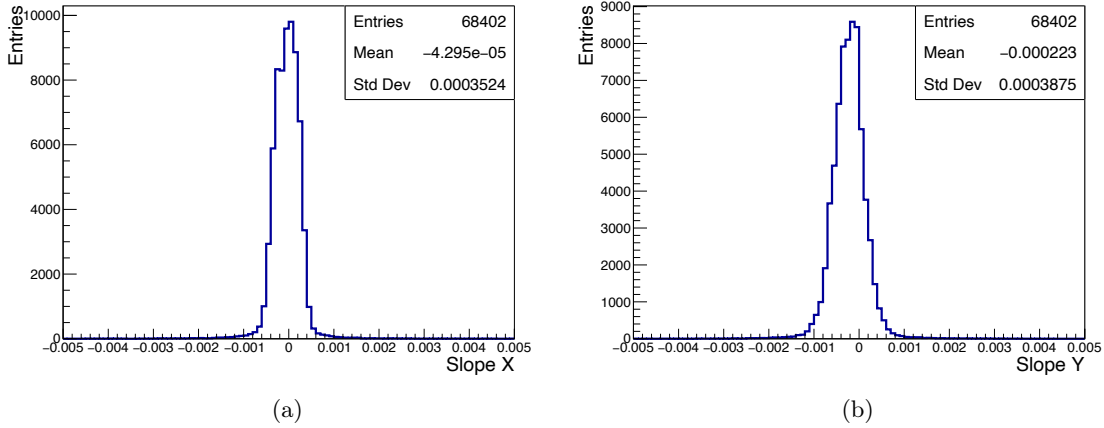


Figure 8.5: Reconstructed DWC track slopes in x (a) and y (b) for an 80 GeV charged pion sample.

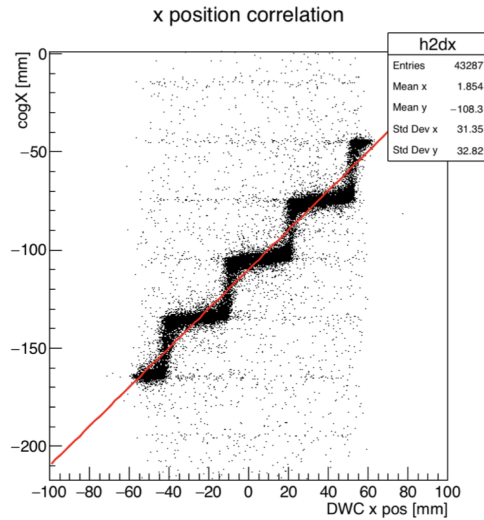


Figure 8.6: Correlation of the energy-weighted center of gravity in x for the hits in the AHCAL prototype and track intersection at the calorimeter front face in x reconstructed by DWCs for 40 GeV muon events [9]. The step-like structure originates from the scintillating tile dimensions.

### Tracks for Simulated Events

In order to generate tracks for simulated events, the Monte Carlo truth information of the GEANT4 simulation is accessed for each event. As introduced in Section 6.3.1.2 the MCParticle history is investigated and the endpoint coordinates of the primary particle are extracted. Those coordinates in x and y serve as the assumed track intersection at the calorimeter front face and straight tracks are extrapolated to the volume in front of the AHCAL prototype with constant functions as:

$$x(z) = intersectionX = endpointX \tag{8.3}$$

$$y(z) = \text{intersection}Y = \text{endpoint}Y \quad (8.4)$$

By default, the *slopeX* and *slopeY* parameters are set to zero, which is justified by the quasi straight track validation for the reconstructed DWC tracks of the beam test data. To match the output format of the beam test data tracks, a similar LCIO collection is generated for each simulated event. No global alignment offset calibration is needed for the simulated events, since the simulation itself happens in the coordinate system of the AHCAL prototype.

### Track Quality Validation

A precise track reconstruction is a crucial requirement in order to allow an appropriate track to charged cluster association within the particle flow reconstruction. For this reason, the quality of the implemented tracks needs to be validated for the AHCAL prototype charged pion events. To quantify the track quality for beam test and simulated events, two metrics according to the following questions are defined:

1. How well is the track position at the calorimeter front face agreeing with the energy-weighted center of gravity of the event? For how many events is the projected radial distance

$$r_{cog} = \sqrt{(x_{track} - x_{cog})^2 + (y_{track} - y_{cog})^2} \quad (8.5)$$

smaller than 30 mm, corresponding to the scintillating tile dimension of a channel?

2. Is the track position at the calorimeter front face agreeing with the position of a triggered AHCAL channel in the first three layers? For how many events is the projected radial distance

$$r_{hit} = \sqrt{(x_{track} - x_{hit})^2 + (y_{track} - y_{hit})^2} \quad (8.6)$$

to the closest calorimeter hit smaller than 22 mm, corresponding to the scintillating tile center to corner distance as illustrated by Figure [8.2b](#)?

The track quality is representatively investigated for a 10 GeV charged pion sample of the June 2018 beam test and a corresponding simulation sample based on the QGSP\_BERT\_HP physics list, both featuring  $\sim 100$  k events and a centralised beam position. The lowest particle energy studied in the scope of this thesis corresponds to 10 GeV. Since these low energy charged pion samples show the largest fraction of beam contamination and are mostly affected by upstream material in comparison to higher particle energies, the determined track quality for these samples resembles the lower limit of quality. A simple event filter based on the BDT-PID (see Section [6.3.4](#)) to select charged pion events is applied for both samples. Furthermore, at least one triggered AHCAL channel in one of the first three prototype layers is required for each event to allow the calculation of the second quality metric.

Figure [8.7](#) shows the results of the track quality investigation. For 65.3% (data) and 67.8% (MC) of events, the track position agrees with the energy-weighted center of gravity of the event within the dimension of one AHCAL channel. In addition, for 97.5% (data) and 98.6% (MC) of the events, there is a track to AHCAL channel position match in one of the first three layers. All in all, the achieved results show the excellent track quality achieved by the sophisticated calibration and reconstruction of the DWC tracks for the data samples and the dedicated implementation of the tracks for the simulation samples.

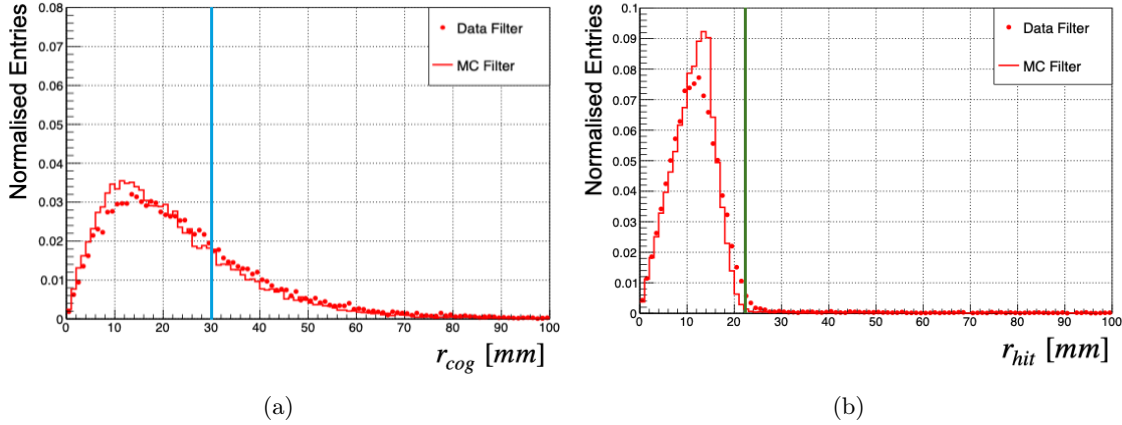


Figure 8.7: Investigated track quality metrics for selected AHCAL data and simulation samples of 10 GeV charged pions: (a)  $r_{cog}$ . The blue line indicates the scintillating tile dimension (30 mm). (b)  $r_{hit}$ . The green line indicates the center to corner distance of a scintillating tile (22 mm).

### 8.1.2 Basic Event Selection

To provide clean and suitable samples to the PandoraPFA reconstruction, a sophisticated event selection is applied to the charged pion samples of both, data and simulation. The overall goal of this procedure is to select events with single charged pions showering in the AHCAL prototype, reject beam contamination and multi particle events and establish a basis for a proper initial track association to a calorimeter cluster on particle flow reconstruction level. Due to the absence of an ECAL in front of the AHCAL prototype in the presented studies, the last criterium is substantial to reject events for which the particle flow reconstruction technically fails. A detailed motivation for these setup-specific selection criteria and visualised consequences are discussed in Section [8.2.5.5](#). On purpose, no restriction on the hadronic shower start layer is set in order to study the impact of shower leakage for the single particle reconstruction and to enable the full longitudinal shower separation for the two particle reconstruction. The event selection criteria applied to all charged pion samples investigated within this chapter are summarised in the following:

- Event classified as a hadron by the BDT-PID (see Section [6.3.4](#)).
- Event featuring a hadronic shower start in the AHCAL prototype (see Section [6.3.1](#)).
- Only one reconstructed track for the event.
- Track must not hit HBU gap of AHCAL layers ( $|x_{track}| > 1$  mm with the gap center at 0 mm in the x-plane of the AHCAL).
- At least one track to hit position match in one of the first three AHCAL layers (see Section [8.1.1](#)).
- At least 10 % of calorimetric charged pion energy associated to the track by PandoraPFA (applied after PandoraPFA reconstruction)

Corresponding selection efficiencies for data and simulation samples are provided in Tables [C.2](#) and [C.5](#).

### 8.1.3 Generation and Classification of Two Particle Event Samples

In the scope of this thesis, the two particle reconstruction performance with PandoraPFA is studied for events consisting of a charged pion next to a neutral hadron shower. Since no neutral hadron beam was available during the beam test campaigns in 2018, these events are generated artificially for both, data and simulation. In a first step, the pseudo-neutral hadron generation algorithm, discussed in Section 6.3.2 is applied to samples of selected charged pion events. Subsequently, the event overlay algorithm, introduced in Section 6.3.3 is employed to overlay the generated pseudo-neutral hadrons with charged pion showers. At input level, the samples feature a hit energy threshold of 0.2 MIP and only after the hit overlay procedure the default analysis hit energy threshold of 0.5 MIP is applied. This is done to explicitly consider hits which exceed 0.5 MIP only after the overlay with a hit of the other event in the same channel. Afterwards, the generated two particle event samples are classified according to the following conditions:

- Particle energy: A 10 GeV pseudo-neutral hadron is overlaid with either a 10 GeV or 30 GeV charged pion shower including the respective track.
- Radial shower distance: According to the transversal distance of the pseudo-neutral hadrons and charged pions energy-weighted center of gravity in the x-y plane, the events are sorted into the following distance bins:  $0 - 25$  mm,  $50 \pm 25$  mm,  $100 \pm 25$  mm,  $150 \pm 25$  mm,  $200 \pm 25$  mm,  $250 \pm 25$  mm and  $300 \pm 25$  mm.

With this method, the events in a radial distance bin originate from several sample combinations featuring charged pion shower positions spread isotropically across all of the incident calorimeter positions. As a result of this procedure, a position dependent bias is omitted.

### 8.1.4 Sample Overview and Quality Validation

For the studies presented in this chapter, data samples from the June 2018 beam test campaign and corresponding simulation samples are utilised. The simulation samples are based on the physics list QGSP\_BERT\_HP and FTFP\_BERT\_HP in GEANT4 v.10.3p2. In the following, an overview of the samples used for the single and two particle reconstruction study is provided. The conventional calorimetric reconstruction performance of the AHCAL prototype for hadrons has been summarised in Section 7.2.3. To validate the quality of the selected hadron samples, basic calorimetric observables are monitored and compared for centralised and most de-centralised incident beam positions as well as for the different radial shower distance bins in Appendix C.

#### 8.1.4.1 Single Particle Events

For the single particle reconstruction study centralised charged pion samples of energies between 10 – 80 GeV are investigated. In addition, de-centralised charged pion simulation samples of the same beam energies are investigated, while for beam test data only de-centralised samples for 10 GeV and 30 GeV are available. Tables C.2 and C.3 provide an overview about the sample sizes and tuned beam positions and profiles.

Figures C.1 and C.2 show the distributions of the hit energy sum and number of shower hits for the investigated centralised and de-centralised samples of selected charged pions. Corresponding mean shower energy profiles are depicted in Figures C.3 and C.4. In general, the shape of the distributions and profiles as well as the mean and RMS agree well to within 5% when data is compared to the two simulated physics lists, and for comparing centralised and de-centralised beam positions.

The imperfect energy linearity for data as well as simulation, summarised in Section 7.2.3, causes a maximal deviation of around 5% from the nominal calorimetric energy sum studied for 10 GeV charged pions, while for the higher energies the deviation decreases to 1 – 2%. However, with respect to the energy comparison to the track momentum within the particle flow reconstruction, these discrepancies to the nominal beam energies are considered to be tolerable. The same goes for the deviations between centralised and de-centralised beam positions, which originate from transversal shower leakage. With 1 – 2% less energy and 2 – 3% less hits for all investigated de-centralised charged pion samples, the effect is relatively small and in the same order as the data to simulation discrepancy. Since the investigated de-centralised samples feature the outermost beam positions of all samples investigated within this thesis, the observed discrepancies represent upper limits for the effect of transversal shower leakage.

One can conclude, that the quality of the selected single charged pion samples for data and simulation is validated with respect to energy and topology reconstruction. Therefore, they are considered well suited for the PandoraPFA reconstruction study and for the further processing towards two particle events.

#### 8.1.4.2 Two Particle Events

For the two particle studies, events featuring a pseudo-neutral hadron shower of 10 GeV and a charged pion shower of 10 GeV or 30 GeV with transversal shower distances varying from 0 mm to 325 mm are generated for data and simulation, as introduced in Section 8.1.3. Table C.4 summarises the charged pion samples and Table C.5 the pseudo-neutral hadron samples utilised for the two particle event generation, including tuned beam positions and profiles.

The quality of the charged pion samples for 10 GeV and 30 GeV has been validated for the central and outermost beam positions in the last section. Therefore, only the quality of the generated pseudo-neutral hadron samples is left to be validated. Figure C.5 shows the energy sum and number of shower hits distributions and the mean energy profiles for the generated pseudo-neutral hadron samples for a centralised and the outermost investigated beam position. With respect to the comparison of data and both simulated physics lists as well as central and outermost beam position, again an agreement within 5% is achieved. In addition, on average 0.3 – 0.4 GeV and 8 – 9 fewer shower hits are observed in comparison to the charged pion samples of the same energy. This agrees well with the results found for the validation of the pseudo-neutral hadron generation algorithm presented in Section 6.3.2.

In order to monitor the statistics of the generated two particle samples in each radial distance bin, the number of events in each bin is checked and summarised in Table C.6. Furthermore, Figure 8.8 shows the radial shower distance distributions of all generated two particle event samples for data and simulation for both energy scenarios in order to monitor the inter-bin distribution of radial shower distances. The bias towards lower or higher radial shower distances within the same distance bin is found to be roughly equal for data and simulation samples. The peak in Figure 8.8b is caused by an extra iteration of the two particle event generation for a radial distance of 0 mm – 25 mm, initially showing a too low number of events in the respective bin. Most of the radial distance bins feature more than 30 k events for both investigated energy scenarios.

In a last step, the quality of the generated two particle samples within the respective radial distance bins is validated. For this validation, the reconstructed energy sum, which is considered as most important for the comparison of track momentum and charged cluster energy in PandoraPFA, is investigated. Thus, the mean and RMS of the individual energy sum spectra for the events in each radial shower distance bin are monitored for the overlaid pseudo-neutral hadrons and charged

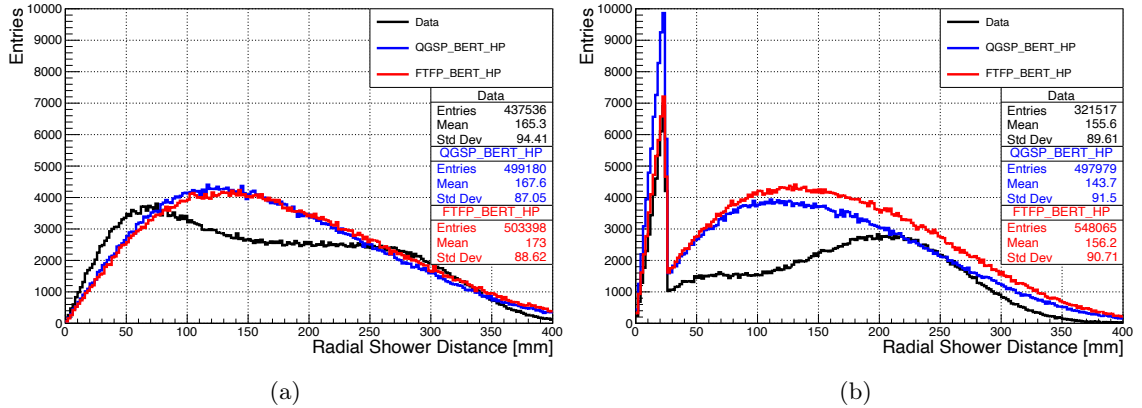


Figure 8.8: Distribution of radial shower distances for generated two particle event samples of overlaid 10 GeV pseudo-neutral hadrons and 10 GeV (a) or 30 GeV (b) charged pion showers.

pions separately, as presented in Figure C.6 and C.7. While for the 30 GeV charged pions a slight energy deficit of  $\sim 1.5$  GeV due to shower leakage is observed, as expected, the 10 GeV pseudo-neutral hadrons show an energy deficit of  $\sim 0.3$  GeV caused by the generation algorithm itself, as discussed previously. The RMS for the 10 GeV pseudo-neutral hadrons and 10 GeV charged pion samples agree well at 2 GeV. This is not the case for the RMS of the 30 GeV charged pions, where the FTFP\_BERT\_HP simulation differs from the QGSP\_BERT\_HP simulation and for data up to 5%, similar to the observations in Section 7.2.3.

Most importantly, it is observed that the mean as well as the RMS is constant over all radial shower distance bins of the respective energy scenario for the data and the simulation samples. This verifies the equal quality of the generated two particle samples and proves that the sorting of the events into respective distance bins does not create any type of bias. Corresponding evaluations of the  $Mean_{90}$  and  $RMS_{90}$  suppressing leakage effects and individual energy spectra can be found in Figures C.8-C.16.

## 8.2 Adaptations of PandoraPFA Framework for AHCAL Prototype Study

Since a particle flow algorithm framework, like PandoraPFA, is implemented and optimised for a collider detector system like ILD, several adaptations are necessary to allow a sufficient reconstruction of AHCAL prototype events. Several of these required adaptations are related to the AHCAL prototype specific geometry and data format. In addition, an accurate prototype specific energy calibration and conversion has to be provided. Lastly, parameters of basic PandoraPFA algorithms need to be adapted to avoid setup-specific reconstruction limitations mainly caused by the AHCAL standalone application without an ECAL installed, no fully hermetic detector concept and no magnetic field applied. If not explicitly stated otherwise, the PandoraPFA framework and parameters used for the default ILD reconstruction are used. An overview of the reconstruction framework and the internal data flow is provided by Figure 8.9 and individual instances are discussed in the following Sections.

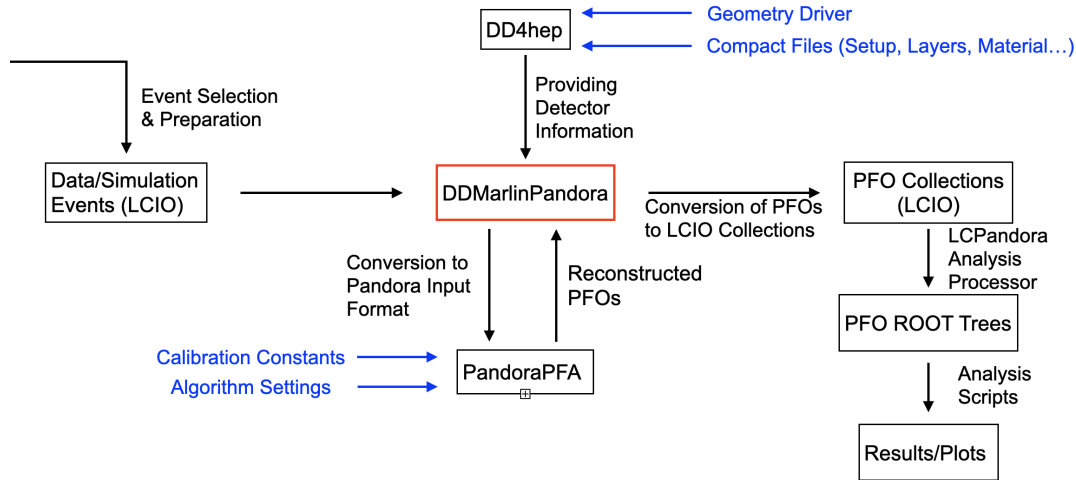


Figure 8.9: Framework and data flow diagram for PandoraPFA AHCAL prototype studies.

### 8.2.1 DDMarlinPandora Interface Processor

DDMarlinPandora<sup>1</sup> is the central processor of the reconstruction framework providing an interface to the detector geometry and material description via DD4hep and the PandoraPFA algorithms. The processor prepares the infrastructure and converts input data to the required format in order to apply the generic PandoraPFA algorithms. Afterwards, the final PFO reconstruction output is converted back to LCIO format by the processor for subsequent data analysis.

In order to allow the reconstruction of AHCAL prototype events, several processor components are adapted. First of all, simple adaptations incorporating the AHCAL prototype geometry, energy calibration and output formats are done for the geometry, calorimeter hit and PFO creator. The pre-defined HCAL endcap class is utilised for treating the AHCAL prototype calorimeter hits. The HCAL barrel class is avoided due to barrel specific treatments and calculations in further instances of DDMarlinPandora. Additionally, the pre-defined classes of ECAL barrel and endcaps, HCAL barrel, muon detector and forward calorimeters are fully disabled without any consequences for the reconstruction of AHCAL prototype events.

Due to the absence of a magnetic field during the beam test campaigns of the AHCAL prototype, the default magnetic field map of ILD is disabled in the B-field plugin of DDMarlinPandora. Instead, the plugin is adapted to provide a constant output of  $10^{-5}$  T, which is on the order of the earth's magnetic field, for all positions within the detector. The magnetic field is chosen to be negligibly small in terms of bending charged particle trajectories, but not equal to zero. This prevents several topological association algorithms within PandoraPFA from crashing.

Furthermore, the pseudo-layer plugin of DDMarlinPandora is re-defined in order to incorporate the geometry of the AHCAL prototype. Since the prototype features a simple and uniform sampling calorimeter geometry without any barrel to endcap or ECAL to HCAL transition regions, the plugin is configured to provide the AHCAL layer number for a given calorimeter hit coordinate.

Lastly, the track creator of DDMarlinPandora is modified in order generate continuous charged

<sup>1</sup> <https://github.com/iLCSoft/DDMarlinPandora>

particle tracks from the track information provided by the DWC LCIO collection, as introduced in Section 8.1.1. Based on the x and y intersection positions and slope parameters, a basically straight track is constructed ranging from  $Z = -1.0$  m to  $Z = -0.1$  m with respect to the calorimeter front face at  $Z = 0.0$  m. The global DWC offset to the AHCAL prototype for each beam test run is considered at this point as well. A sharp track momentum corresponding to the beam energy, or the simulated primary particle energy respectively, is assigned and the track is defined to originate from a charged pion with respect to the PandoraPFA internal mass, charge and particle identification.

## 8.2.2 Detector Geometry and Material Description

The geometry and material description of the AHCAL prototype is provided by a DD4hep interface through the DDMarlinPandora processor. This instance is very similar to the one for the AHCAL prototype GEANT4 simulations, as described in Section 6.2.1. However, several modifications to the geometry driver and compact files are necessary in order to provide additional information required by PandoraPFA subsequently. First of all, the basic implementation is changed to the DDDRec class of DD4hep<sup>2</sup> and the AHCAL prototype input is sorted into the HCAL endcap class. For this implementation, different parameters like the endcap inner (0 mm) and outer radius (510 mm)<sup>3</sup> and the Z coordinates of start (0 mm) and end of the endcap (1100 mm)<sup>4</sup> are provided for the AHCAL prototype. These parameters are mainly required for the visualisation of the event reconstruction. Finally, next to minor format-specific adaptations, the integrated radiation lengths ( $X_0$ ) and nuclear interaction lengths ( $\lambda_n$ ) at each calorimeter layer up to the center of the active medium and up to the end of the layer are calculated and implemented<sup>5</sup>.

## 8.2.3 MIP to GeV Calibration

On the input level, PandoraPFA requires individual calorimeter hit energy information in units of GeV. As described in Section 5.5, the calibrated AHCAL prototype hit energy information is saved in units of MIP in the LCIO collections. Therefore, a MIP to GeV conversion on the hit energy level is implemented within the calorimeter hit creator of DDMarlinPandora after the MIP threshold check. Due to the fact, that the AHCAL prototype is an under-compensating calorimeter, the average response to hadrons is smaller in comparison to electron or photons of the same energy. With respect to this, the conversion factor depends on the choice of the desired energy scale. Since for the AHCAL prototype studies only hadrons are investigated, the conversion from MIP to the hadronic GeV scale is chosen.

To determine the conversion factor, samples of  $K_L^0$  are simulated with the QGSP\_BERT\_HP physics list of GEANT4 and reconstructed in the same manner as described in Section 6.2. Samples with energies ranging from 5 – 30 GeV in 5 GeV steps, each featuring 10 k events, are used with centralised beam positions. Higher energies are omitted and a shower start in the first ten layers of the prototype is required in order to minimise a potential bias by energy leakage. For each energy sum distribution, the  $Mean_{90}$  (defined in Section 4.4.5) is calculated and plotted versus the truth particle energy in units of GeV, as presented in Figure 8.10. Subsequently, a linear fit is applied without any parameter restrictions and a slope of 35.72 MIP/GeV is extracted corresponding to a hadronic MIP to GeV factor of 0.028 GeV/MIP for the AHCAL prototype.

<sup>2</sup>See: <https://github.com/AIDASoft/DD4hep/tree/master/DDRec>

<sup>3</sup>AHCAL prototype layer center to layer corner distance.

<sup>4</sup>Roughly the total AHCAL prototype absorber length

<sup>5</sup>Values are used for calculations, e.g. shower profiles, in the PandoraPFA algorithms.

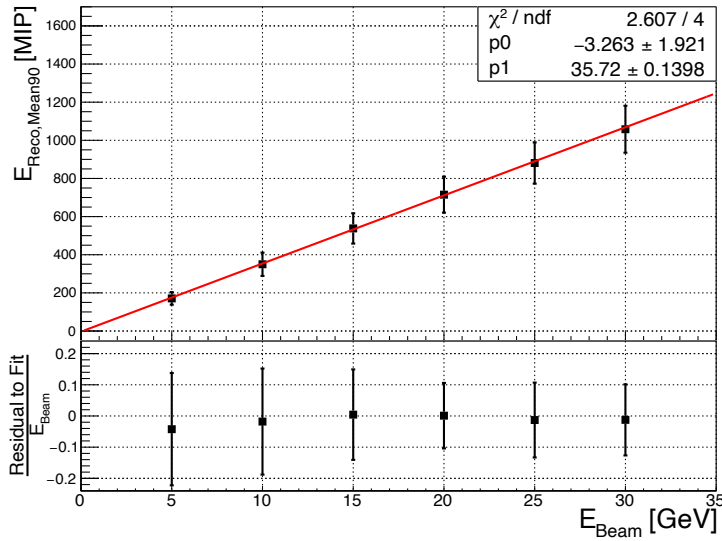


Figure 8.10:  $Mean_{90}$  of energy sum spectra over the truth beam energy for simulated  $K_L^0$  in the AHCAL prototype. A linear fit is applied to determine the hadronic MIP to GeV conversion factor.

### 8.2.4 Internal PandoraPFA Energy Scale Calibration

As introduced in Section 4.4.3.1, a dedicated calibration of the internal PandoraPFA scale factors is required. Since the studied setup does not include an ECAL, no barrel detector systems and only hadron showers are investigated in the scope of this thesis, the set of five calibration factors for ILD-like setups reduces to only one effective calibration factor for the AHCAL prototype study: *PandoraHcalToHadScale*, which corrects for the average energy loss caused by hit isolation cuts in the different instances of the clustering algorithms for the investigated setup. Based on this reason, the respective calibration procedure for the AHCAL prototype is simplified with respect to the ILD default calibration [6]. Since hadrons are only able to shower in the AHCAL prototype for the studied setup, *PandoraHcalToHadScale* is simply tuned on the agreement of the reconstructed neutral PFO energy in the AHCAL and the beam energy of simulated neutral hadrons.

For the calibration procedure a recommended simulation sample of 10 GeV  $K_L^0$  featuring 10k events with a centralised beam position is utilised. The simulation is based on the QGSP\_BERT\_HP physics list of GEANT4, processed as explained in Section 6.2 and subsequently reconstructed by PandoraPFA. The reconstructed neutral PFO energy is plotted and fitted with a Gaussian. This procedure is repeated iteratively for different *PandoraHcalToHadScale* factors until the mean of the fitted Gaussian agrees for 10 GeV within a per-mille. The *PandoraHcalToHadScale* factor is determined to be 1.03 for the AHCAL prototype setup. Figure 8.11 shows the tuned distribution of the reconstructed neutral PFO energy.

<sup>6</sup>See <https://github.com/iLCSoft/LCCalibration/tree/master/doc>

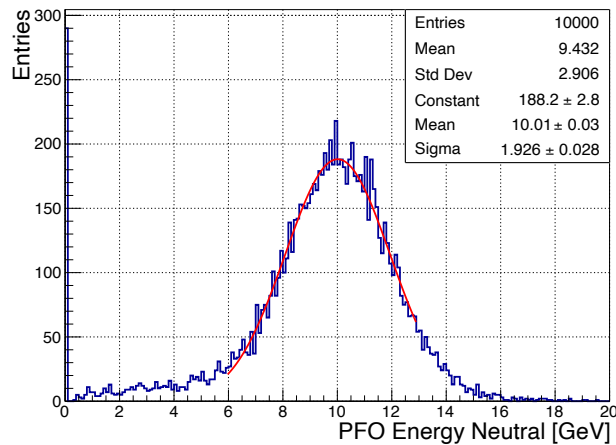


Figure 8.11: Neutral PFO energy for simulated 10 GeV  $K_L^0$  reconstructed by PandoraPFA with  $PandoraHcalToHadScale = 1.03$  for the AHCAL prototype study.

## 8.2.5 PandoraPFA Algorithms

With respect to the PandoraPFA algorithms, only minor modifications are necessary to allow a sufficient application to the AHCAL prototype events. Most of these adaptations are based on the absence of an ECAL with higher granularity installed in front of the AHCAL prototype and on geometrical and setup-specific limitations. In the following, the individual adaptations are discussed and exemplarily visualised with the PandoraPFA internal visual event monitoring. If not stated otherwise, the ILD default PandoraPFA algorithm settings are used, except for the hadronic software compensation plugin [7].

### 8.2.5.1 PandoraPFA Visual Monitoring

The PandoraPFA internal visual monitoring algorithm [8] features an interactive graphical user interface for displaying event reconstruction by PandoraPFA including reconstructed tracks and calorimeter hits. In addition to the possibility to hide/show all individual PFOs separately, the algorithm features full information on reconstructed track momentum and calorimeter cluster energies for different energy scales, reconstructed particle types indicated by different colors and the total reconstructed energy of the event. Furthermore, it can be initiated after each PandoraPFA sub-algorithm allowing a continuous visualisation of all individual reconstruction steps. For this reason, it has been extensively exploited for the validation of the AHCAL prototype setup implementation, problem identification, determination of algorithm adaptations and the visualisation of the reconstruction performance within the scope of this thesis.

Figure 8.12 demonstrates the visual output at the final reconstruction step for an AHCAL prototype two particle data event. Magenta (cyan) calorimeter hits indicate the classified charged

<sup>7</sup>See: <https://github.com/iLCSoft/ILDConfig/blob/master/StandardConfig/production/PandoraSettings/PandoraSettingsDefault.xml>

<sup>8</sup>See: <https://github.com/PandoraPFA/LCContent/blob/master/include/LCMonitoring/VisualMonitoringAlgorithm.h>

(neutral) cluster hits by PandoraPFA. Grey hits represent unclustered calorimeter hits, not further used in the reconstruction. The magenta line corresponds to the charged pion track. Since the geometrical implementation of the AHCAL prototype utilises the HCAL endcap class, the calorimeter hits are located within a visualised cylinder.

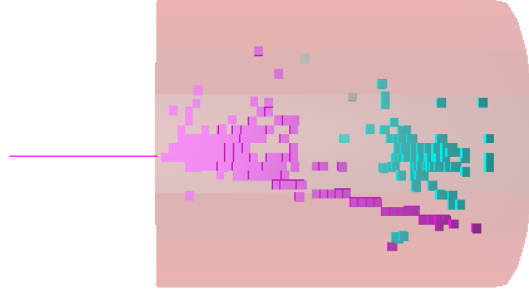


Figure 8.12: PandoraPFA event display for an AHCAL prototype data event featuring a 10 GeV pseudo-neutral hadron and a 10 GeV charged pion shower after completed PandoraPFA reconstruction. Magenta (cyan) hits correspond to classified charged (neutral) cluster hits.

### 8.2.5.2 Track to Cluster Association Algorithm

The basic track to cluster association algorithm within PandoraPFA features several steerable parameters, for example the maximal track to cluster distance limit for considering a suitable track to cluster association<sup>9</sup>. For the ILD PandoraPFA default settings this parameter is set to 10 mm corresponding to two times the cell size of the planned SiW-ECAL. Therefore, only if the distance between the track projection to the calorimeter front face is within 10 mm to the transversal center of a potential cluster candidate, a track to cluster association is considered. For a single hit in a respective layer, this parameter corresponds to the radial distance between the track projection and the center of the triggered calorimeter channel.

However, the AHCAL prototype features an uniform cell size of 30 mm × 30 mm. Therefore, as soon as the distance of the track projection to the position of a triggered calorimeter channel (or to the transversal center of gravity of the respective cluster for the case of multiple hits in a layer) is larger than 10 mm, the track to cluster association is not considered even if the track directly hits a triggered calorimeter channel in the AHCAL. Without an initial track to cluster association, basically all re-clustering algorithms within PandoraPFA are omitted and as one of the last instances the track is associated to the closest cluster found right before the reconstruction is finished. As a consequence, either all or a significant number of charged pion shower hits are classified as neutral by PandoraPFA, resulting in a large excess of double counted charged energy in those events. This problematic final reconstruction state is observed for 2-3% of the charged pions events, as illustrated by Figure 8.13a.

In order to avoid this setup specific technical limitation, the parameter is set to 22 mm corresponding to the AHCAL channel center to corner distance. This resembles the track projection

<sup>9</sup>See: <https://github.com/PandoraPFA/LCContent/blob/master/src/LCTrackClusterAssociation/TrackClusterAssociationAlgorithm.cc>

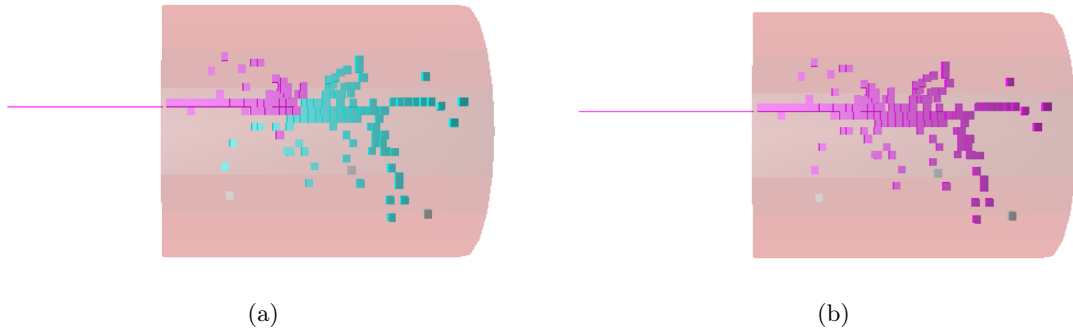


Figure 8.13: AHCAL prototype event featuring a 20 GeV charged pion shower after completed PandoraPFA reconstruction for different settings of the  $MaxTrackClusterDistance$  parameter in the track to cluster association algorithm: (a) 10 mm (ILD default). (b) 22 mm (AHCAL prototype).

matching with the position of an individual AHCAL channel, which is the case for roughly 98% of events, as validated in Section 8.1.1. With the changed parameter, a proper initial track to cluster association is achieved and the re-clustering iterations of PandoraPFA are exploited resulting in significantly better final reconstruction states, with illustrative examples shown in Figure 8.13b.

### 8.2.5.3 Track Driven Merging Algorithm

As introduced in Section 4.4.3.1, re-clustering considerations are mainly based on the track momentum to charged cluster energy comparison. According to Equation 4.8, a potential re-clustering is considered if the discrepancy exceeds the  $\chi$ -threshold. The track driven merging algorithm<sup>[10]</sup> is one of the basic re-clustering algorithms within PandoraPFA. It is implemented to handle topologically simple cases and to consider a re-clustering if the merging of a close-by neutral cluster into the charged cluster under investigation would improve the agreement to the associated track momentum. The PandoraPFA ILD default value for considering a re-clustering by this algorithm is  $\chi = 2.5$ . For the example of a 30 GeV charged pion event the currently associated charged calorimeter cluster must have an energy lower than  $\sim 21.8$  GeV so that a re-clustering consideration by this algorithm would be triggered. If the new configuration is better than the previous, the re-clustering is performed, otherwise the old configuration is kept.

For approximately 1% of the AHCAL prototype charged pion events an unsatisfying final reconstruction state has been observed. Despite being topologically well connected and in summation corresponding well to the associated track momentum, the charged pion hits are split and classified as a charged and an extra neutral cluster, as exemplarily illustrated in Figure 8.14a. The additional identified neutral hadron cluster, resulting in a large excess of double counted charged energy, most probably originates from the missing ECAL in front of the AHCAL prototype. Less topological information, due to the missing MIP-like track in the ECAL, affects the cone clustering as well as the subsequent topological association algorithms. For these events the  $\chi = 2.5$  threshold of the track driven merging algorithm is not exceeded and a re-clustering is not considered.

In order to minimise this technical limitation, the  $\chi$ -threshold for the track driven merging algorithm is lowered to  $\chi = 1.5$  for the AHCAL prototype study. As a result, for a 30 GeV (10 GeV)

<sup>10</sup>See: <https://github.com/PandoraPFA/LCContent/blob/master/src/LCReclustering/TrackDrivenMergingAlg.cc>

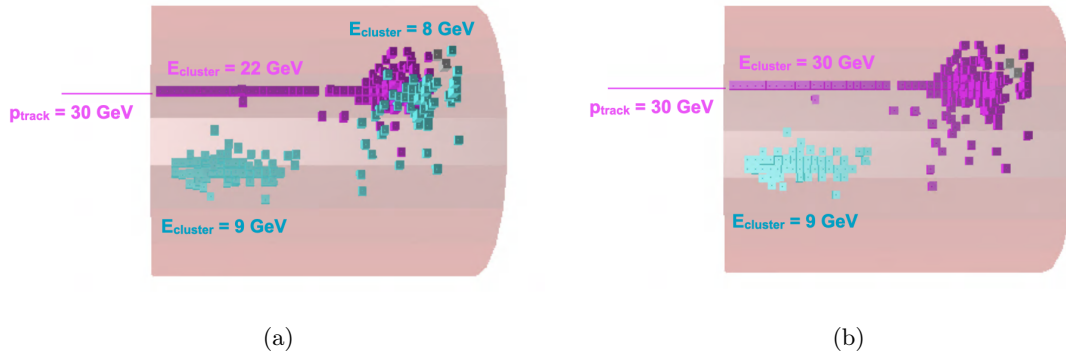


Figure 8.14: AHCAL prototype event featuring a 10 GeV pseudo-neutral hadron and a 30 GeV charged pion shower after completed PandoraPFA reconstruction for different  $\chi$ -thresholds in the track driven merging algorithm: **(a)**  $\chi = 2.5$  (ILD default). **(b)**  $\chi = 1.5$  (AHCAL prototype).

charged pion, a potential re-clustering is now considered if the currently associated charged cluster has an energy lower than  $\sim 25 \text{ GeV}$  ( $\sim 7.2 \text{ GeV}$ ). With this adaption, PandoraPFA achieves significantly improved reconstruction states for roughly 90% of the observed problematic events, as exemplarily depicted by the example event in Figure [8.14b](#).

#### 8.2.5.4 Impact of Outer Sampling Layer Definition on Re-clustering Algorithms

Before any of the re-clustering algorithms is executed, PandoraPFA checks if any hit of the currently associated charged cluster is located in the outer sampling layers of the calorimeters. If this is the case, the potential re-clustering consideration is not initiated. This mechanism is implemented to prevent the absorption of nearby neutral clusters into charged clusters, if the charged hadron shower leaks out of the calorimeter and the charged cluster energy is significantly lower than the associated track momentum<sup>[\[11\]](#)</sup>. For the default PandoraPFA settings for ILD the last three longitudinal and transversal pseudo-layers are defined as the outer sampling layers.

Depending on the the incident beam position and the energy of the charged pion, for  $\sim 0.5\text{-}2\%$  of the studied single and two particle AHCAL prototype events an unsatisfying final reconstruction state is observed. In general, these events feature a nearly perfect agreement of the track momentum and the energy of a topologically well connected calorimeter cluster. However, the associated charged cluster features only a small fraction of the truth charged energy and the remaining truth charged hits are classified as an extra neutral cluster by PandoraPFA, as illustrated in Figure [8.15a](#). Again, this leads to a large excess of double counted charged energy. This is caused by one or several hits, which are located in the defined outer sampling layers, preventing the re-clustering algorithms from being initiated.

Due to the fact that the investigated charged pions feature only momentum in the longitudinal direction of the calorimeter and the incident beam position is separated at least 18 cm transversally from the calorimeter edge, all of the investigated events feature negligible transversal shower leakage, as shown and discussed in Section [8.1.4.1](#). Based on this assumption, the outer sampling layers are redefined for the AHCAL prototype study. No transversal pseudo layers are considered at all

<sup>11</sup>See: `ClusterHelper::IsClusterLeavingDetector` in <https://github.com/PandoraPFA/LCContent/blob/master/src/LCHelpers/ClusterHelper.cc>

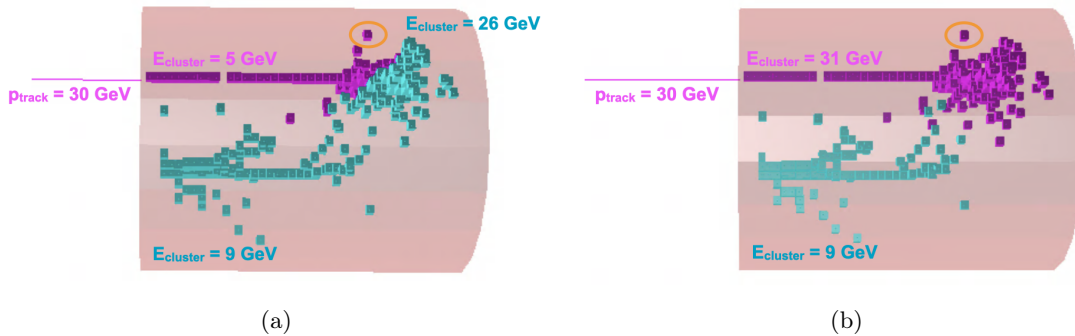


Figure 8.15: AHCAL prototype event featuring a 10 GeV pseudo-neutral hadron and a 30 GeV charged pion shower after completed PandoraPFA reconstruction for different outer sampling layer definitions: (a) Last three transversal and longitudinal pseudo-layers (ILD default). The yellow marked outermost calorimeter hit is classified to be located in the outer sampling layers preventing a re-clustering consideration. (b) Last longitudinal pseudo layer (AHCAL prototype).

and only the last longitudinal pseudo layer is defined as the outer sampling layer of the setup. As a consequence, the full spectrum of re-clustering algorithms is enabled for this type of problematic events. Figure 8.15b shows the significantly improved reconstruction for the introduced example event by enabling the re-clustering consideration of the track driven merging algorithm.

### 8.2.5.5 Isolated Hit Merging Algorithm

After the adaption of the PandoraPFA algorithm parameters described in previous sections, a few per-mille of events are still observed to show a non working track to charged cluster association in the final reconstruction state, as shown for an example event in Figure 8.16a. As a result, these events feature a classified neutral hadron next to an un-associated track and PandoraPFA counts all calorimeter hits of the charged pion shower effectively twice. In general two categories of these events are observed. Events for which there is no calorimeter hit at all in the first AHCAL layers at the position of the track projection and events, which feature a gap in the ionising MIP-like track before the shower is initiated by a hard interaction in later layers. Those missing hits can be caused by the charged pion traversing un-instrumented volume, like the  $\sim 1 \text{ mm}$  gap between HBU configuration in a layer or the  $\sim 10 \mu\text{m}$  gap between individual scintillator tiles. Furthermore, the deposited hit energy could be below the analysis hit energy threshold of 0.5 MIP.

For more than half of those events PandoraPFA is initially still able to associate the track to an initial cluster consisting of a few calorimeter hits in the first layers. However, this track to cluster association is broken afterwards by the isolated hit merging algorithm<sup>[12]</sup>. As part of the topological association algorithms, it is designed to consider a merging of both, individual hits and small clusters of up to 3 hits, to nearby larger clusters. Since a few hits in the first layers are topologically isolated for the observed gap-like events, they are exposed to this algorithm and in many cases topologically not considered further in the reconstruction process, as illustrated in Figure 8.16b.

<sup>12</sup>See: <https://github.com/PandoraPFA/LCContent/blob/master/src/LCTopologicalAssociation/IsolatedHitMergingAlgorithm.cc>

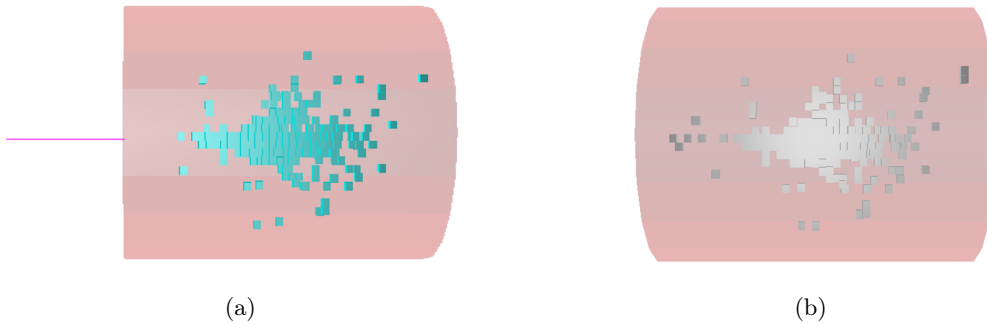


Figure 8.16: AHCAL prototype event featuring a 30 GeV charged pion shower for different PandoraPFA reconstruction steps: (a) Final reconstruction level. (b) Calorimeter hit input level.

This setup specific limitation is caused by the non existent ECAL in front of the AHCAL prototype, which would provide a larger number of hits in the initial charged cluster based on the extended primary ionising track in the ECAL. Within the scope of this work, different tests have been performed changing the parameters of the isolated hit merging algorithm or disabling it completely. While the performance for the observed problematic events could be improved, the reconstruction for all other events is affected as well. Therefore, instead of changing or disabling this algorithm within PandoraPFA for the AHCAL prototype studies, the quality criteria for a proper initial track to charged cluster association are introduced in the event selection, as summarised in Section 8.1.2. Those selection criteria ensure not only the rejection of the events affected by the isolated hit merging algorithm, but all gap-like events for which the track to charged cluster association completely fails.

### 8.2.6 PFO Analysis Chain

The LCIO based reconstruction output provided by DDMarlinPandora is subsequently converted into n-tuple ROOT trees. This is done by the LCPandoraAnalysis processor<sup>13</sup>, which is modified in order cope with the AHCAL prototype setup and to provide output ROOT trees featuring all calorimeter input and PFO output observables needed for subsequent analyses. In a last step, developed case-specific analysis scripts calculate and plot higher level observables.

## 8.3 Reconstruction of Single Particle Events

As an initial step, the PandoraPFA reconstruction of single charged pion samples for AHCAL prototype data and simulations is studied due to multiple reasons. First of all, the reconstruction of single charged pion events offers the unique opportunity to study double counted charged confusion energy exclusively. For increasing particle energies, the charged pion shower development becomes on average topologically more complex, diverse and spatially spread out. It is expected that this results in a higher potential for the misclassification of charged pion calorimeter hits as additional neutral clusters by PandoraPFA. Depending on the accuracy of the modelled hadronic shower sub-structure details in the simulations, the level of this expected effect might differ for data and

<sup>13</sup> <https://github.com/PandoraPFA/LCPandoraAnalysis>

simulated charged pion samples, which is worth an investigation. Furthermore, the performance of PandoraPFA is optimised for dense particle environments like jets in future lepton collider experiments. Significant part of this optimisation typically aims to balance the two types of confusion energy on average. For these reasons, the single charged particle reconstruction performance of PandoraPFA is of high interest, since it shows how the internal algorithm interplay copes with the exclusive presence of double counted charged confusion energy. Lastly, the investigation of single charged pions is required for the subsequent two particle studies. An evaluation of several aspects within the PandoraPFA reconstruction, like the initial clustering, the track to cluster association or the re-clustering iterations, provides a profound basis to study the reconstruction performance for events, which feature a pseudo-neutral hadron in addition.

For the studies presented in this section, the single charged pion data and simulation samples of energies between 10–80 GeV, introduced in Section 8.1.4.1 are reconstructed with PandoraPFA. If not explicitly stated otherwise, the samples with centralised beam position are investigated. First, the different classes of reconstructed events are introduced by examples. After that, the double counted charged confusion energy and the total energy reconstruction performance is investigated. Lastly, selected parts of these studies are repeated for restrictions on the hadronic shower start layer of the charged pions in order to study the potential impact of longitudinal shower leakage.

### 8.3.1 Reconstructed Event Classes

Four different event classes are observed for the reconstructed single charged pion events, which are defined by distinctly populated areas in the correlation plot of the reconstructed PFO and conventional calorimetric energy sum. Figure 8.17 illustrates the correlation plot for the reconstructed 40 GeV charged pion data sample, including the four labeled populations. An example event display for each of the classes is provided in Figure 8.18 and further described in the following:

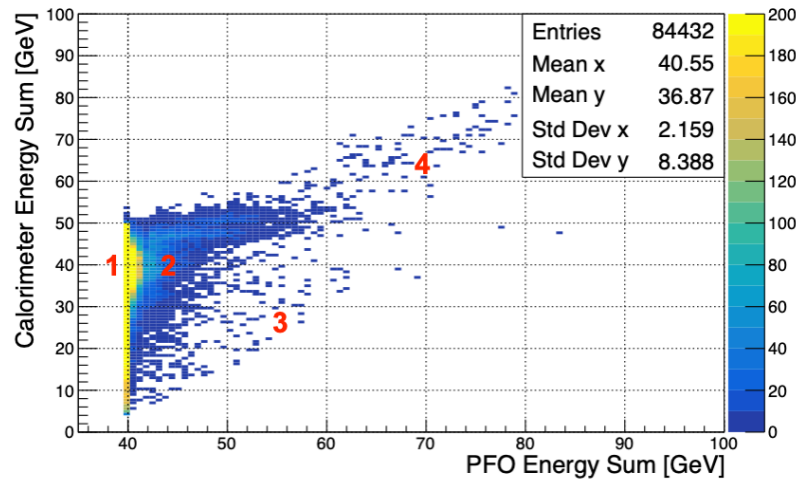


Figure 8.17: Correlation of reconstructed PFO and conventional calorimetric energy sum for the 40 GeV charged pion data sample. Numbers indicate the different populations of reconstructed event classes: (1) Well reconstructed events. (2) Events with double counted charged confusion energy. (3) Events with track to cluster association failure. (4) Multi-particle and high energy contamination events.

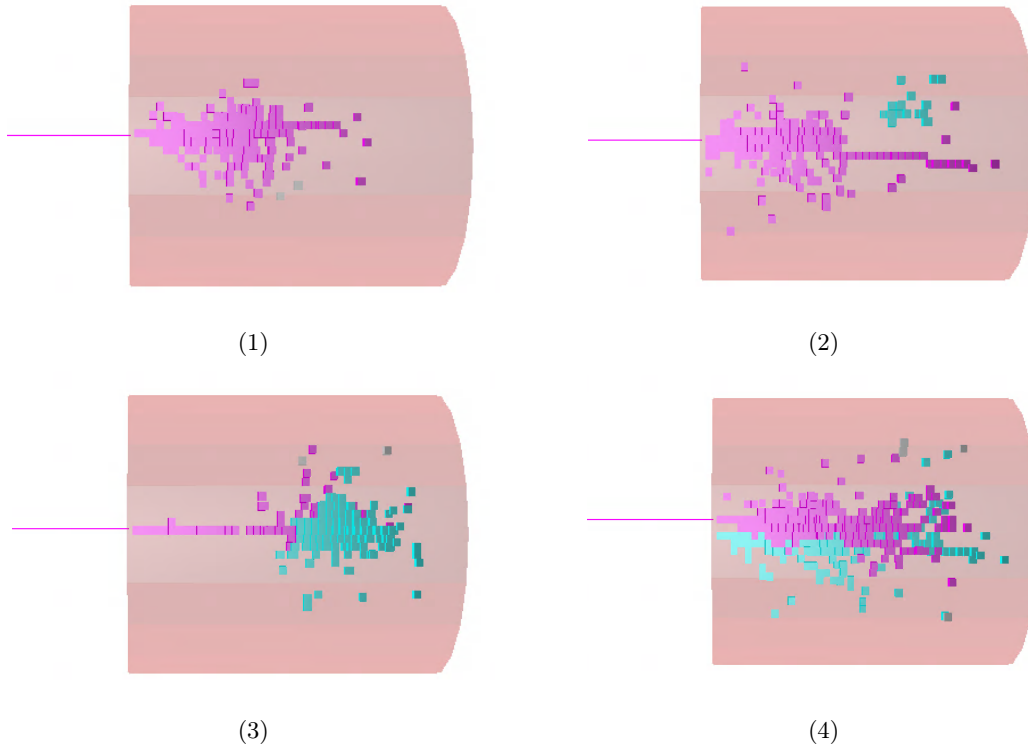


Figure 8.18: Event displays illustrating reconstructed single particle event classes. According to the number, each display shows a representative event of the populations labeled in Figure [8.17](#).

1. Well reconstructed events: Basically all of the charged pion shower hits (except for potentially a few isolated) are combined in a single charged cluster with a correctly associated track. The event does not feature any confusion energy. Therefore, the total reconstructed energy corresponds to the fixed track momentum, while the energy measure of the charged calorimeter hits is ignored. By utilising the momentum measure of the track, PandoraPFA is able to compensate occurring shower leakage for a considerable fraction events.
2. Confusion events: Next to a charged cluster with associated track, one or multiple neutral clusters are reconstructed by PandoraPFA. The energy sum of the hits within those neutral clusters, consisting of misclassified charged hits, corresponds to the double counted charged confusion energy. For the total reconstructed energy of the event, the confusion energy is added to the momentum of the associated track, effectively counting the energy of the misclassified hits twice.
3. Track-cluster association failure events: The track got associated to a charged cluster featuring 10 – 40% of the calorimetric charged pion event energy and survives the selection cuts introduced in Section [8.1.2](#). The remaining hits are identified as part of one or multiple neutral clusters. Therefore, those events feature double counted charged confusion energy on the order of 60 – 90% of the charged pion calorimetric energy. It is assumed, that the failure

is caused by topological gaps or other topology anomalies in the development of the charged pion shower. However, the observed fraction of this event class is less than a per-mille for all investigated samples and is therefore considered to be negligible.

4. Multi-particle high energy contamination events: This class only occurs for data samples and is based on close-by multi-particle events not rejected by the BDT-PID, which cause an excessive calorimetric energy. In this dense hit environment, PandoraPFA typically associates the track to a charged cluster featuring a total energy close to the track momentum. Since only one track is reconstructed, the remaining hits are clustered and classified as neutral providing a total reconstructed energy close to the calorimetric energy measure. Again, the observed fraction of events is less than a per-mille for all investigated data samples and is therefore considered to be negligible.

### 8.3.2 Confusion for Different Particle Energies

The found fraction of events for which double counted charged confusion energy appears is plotted in Figure 8.19 over the charged pion energy of the reconstructed data and simulation samples. It is observed that the fraction of events featuring confusion increases for increasing charged pion energy from  $\sim 10\%$  at 10 GeV to  $\sim 30 - 45\%$  at 80 GeV. This agrees with the discussed expectations of on average topologically more complicated and spatially spread out particle showers with increasing particle energy, providing a higher potential for PandoraPFA to reconstruct additional neutral clusters in the extended charged shower sub-structure.

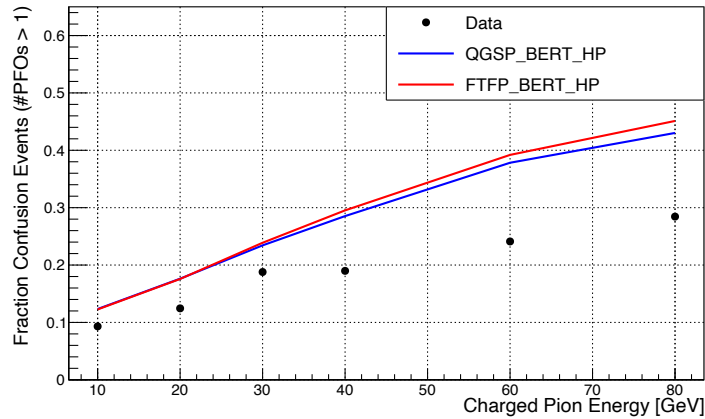


Figure 8.19: Relative number of confusion events over charged pion energy. An event is classified as confusion event if it features at least one neutral PFO in addition to the charged PFO.

Additionally, it is observed that confusion appears more frequently in the reconstruction of simulated charged pion showers. While for lower energies the fraction of confusion events is on a comparable level for both, data and simulation, the simulations feature up to a factor 1.5 more confusion events for reconstructed 80 GeV charged pion samples. To investigate this observation in more detail, the mean number and energy of the reconstructed neutral clusters as well as the impact on the reconstructed charged cluster is studied in the following.

### 8.3.2.1 Neutral PFO Multiplicity and Energy

The number of reconstructed neutral clusters, in the following referred to as the neutral PFO multiplicity, is shown in Figure 8.20 for the 10 GeV and 60 GeV charged pion samples of data and simulation. Well reconstructed events with no neutral clusters are represented by a neutral PFO multiplicity of 0 and correspond to the opposite fraction of events presented in Figure 8.19.

Comparing the two energies, one observes an increase of the mean neutral PFO multiplicity. This increase mainly originates from confusion events featuring a single neutral cluster. However, the higher the charged pion energy gets, the larger is the fraction of events with multiple neutral clusters: For 10 GeV charged pions, confusion events feature almost exclusively one neutral cluster, while for 60 GeV  $\sim 5\%$  of the events include a second, and  $\sim 1\%$  contain a third neutral cluster. As the distribution for 60 GeV shows, the fractionally higher number of confusion events for the simulated in comparison to the data samples mostly feature only one additional reconstructed neutral cluster.

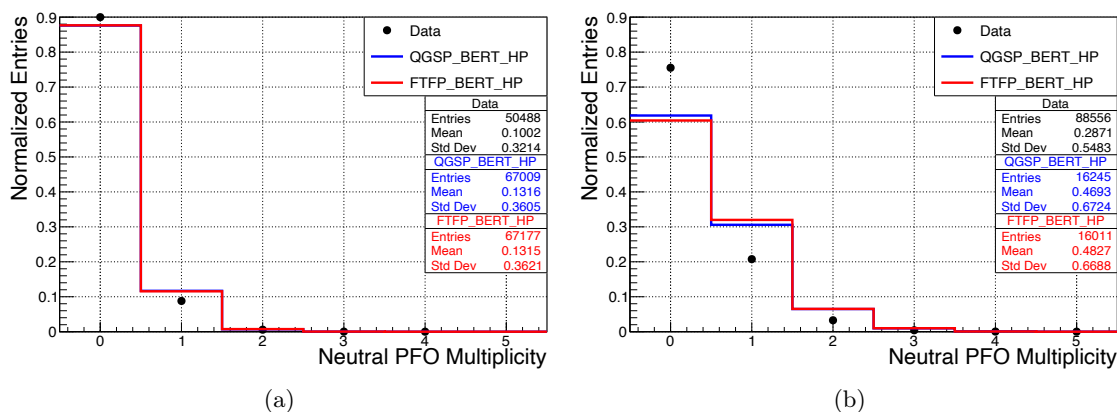


Figure 8.20: Distributions showing the number of reconstructed neutral PFOs for data and simulation samples of charged pions with energy: (a) 10 GeV. (b) 60 GeV.

In order to compare the level of confusion for all investigated charged pion energies, the mean neutral PFO multiplicity is plotted over the charged pion energy in Figure 8.21a. In addition, the corresponding mean energy sum of all neutral PFOs in an event, equivalent to the mean double counted confusion energy, is presented for the different charged pion energies in Figure 8.21b. One can see that both, the average number of neutral PFOs as well as the total double counted confusion energy increases with charged pion energy. This validates the expectation that with increasing charged pion energy the shower sub-structure becomes topologically more complex and spatially spread out. This consequently leads to more and energetically larger parts of the charged shower sub-structure, which are on average misclassified as neutral clusters by PandoraPFA. However, the total energy carried by all neutral clusters in an event is on average relatively small with respect to the total event energy: It corresponds to  $\sim 1\%$  for 10 GeV and  $<4\%$  for 80 GeV.

Lastly, an excess of both observables for the simulation samples is found, which increases with charged pion energy. While the excess for the neutral PFO multiplicity corresponds to  $\sim 30\%$  for 10 GeV and  $\sim 60\%$  for 80 GeV, a good agreement within  $\sim 5\%$  for the mean double counted charged confusion energy up to 30 GeV and an excess of up to 65% is observed for 80 GeV. In

addition, this excess for both observables is slightly more pronounced for the simulation based on the FTFP\_BERT\_HP physics list. It can be concluded, that PandoraPFA tends to reconstruct significantly more neutral clusters as well as double counted charged confusion energy for the simulated charged pion showers in comparison to real charged pion showers, particularly at higher energies. This result hints towards a slightly more spatially spread out and complex shower sub-structure topology for the simulated charged pion showers on average.

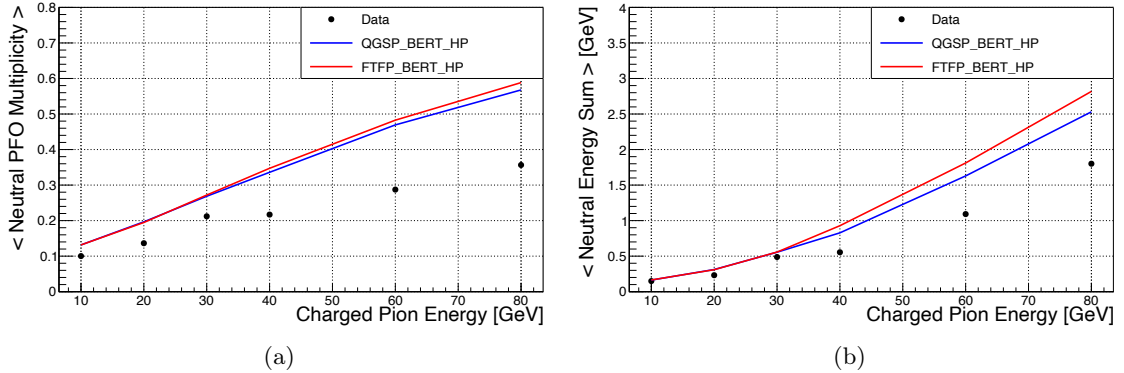


Figure 8.21: Mean number of neutral PFOs (a) and mean energy sum of neutral PFOs (double counted charged confusion energy) (b) versus charged pion energy for data and simulation samples.

### 8.3.2.2 Charged Hit Clustering Efficiency

An imperfect reconstruction of the charged pion shower can not only originate from charged calorimeter hits misidentified as neutral, but also from the internal PandoraPFA clustering isolation cuts resulting in hits not further considered in the reconstruction process. Therefore, the impact of confusion and the PandoraPFA internal isolation cuts on the reconstructed charged cluster energy is investigated in the following. In order to quantify the quality of the charged cluster reconstruction, the hit clustering efficiency  $\epsilon_{hit}$  and the energy clustering efficiency  $\epsilon_{energy}$  are defined as:

$$\epsilon_{hit} = \frac{nHits_{charged}}{nHits_{total}} \quad (8.7)$$

$$\epsilon_{energy} = \frac{E_{charged}}{E_{total}} \quad (8.8)$$

with  $nHits_{charged}$  the number of hits in the reconstructed charged cluster,  $nHits_{total}$  the number of all hits in the event,  $E_{charged}$  the calorimetric energy sum of charged cluster hits and  $E_{total}$  the total calorimetric energy sum of the event. Figures 8.22a and 8.22b show the mean hit and mean energy clustering efficiencies for the investigated single charged pion data and simulation samples.

Except for the charged pion energy of 10 GeV, for both quantities a slight decrease with increasing charged pion energy is observed. In general, these observations agree well with the observed increasing number and energy of the neutral clusters, presented in the previous section. Classified neutral hits and neutral energy is missing in the charged cluster consequently. However, a mean hit clustering efficiency greater than 90% and a mean energy clustering efficiency of greater than 95% is observed over all charged pion energies. This shows that there is on average very efficient

clustering performed by PandoraPFA with respect to the charged pion hits in the vicinity of a track. Furthermore, this proves that the occurring confusion energy as well as the energy lost by the clustering isolation cuts is on average small with respect to the total event energy and maximally corresponds to  $\sim 4\%$ . Because of that, the impact on the total single particle energy reconstruction is on average small, as shown in the next section.

For the comparison of data and simulation it can be concluded that trends in accordance with the results for the neutral clusters are observed. For the data samples, a higher mean hit as well as a higher mean energy efficiency in comparison to the simulated samples is found, particularly at the highest investigated energies. However, the observed discrepancies between data and simulation samples are rather small: Over all energies an agreement within 5% is found for both physics lists.

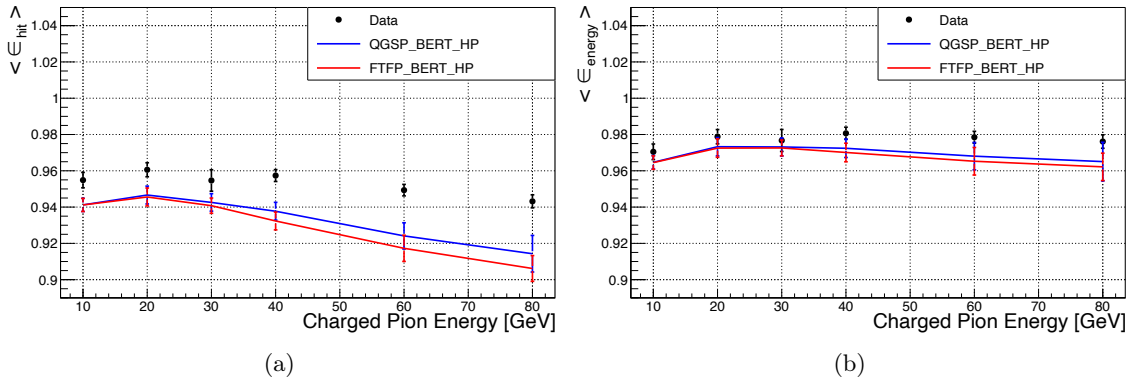


Figure 8.22: Mean charged hit clustering efficiency ( $\epsilon_{hit}$ ) (a) and mean charged energy clustering efficiency ( $\epsilon_{energy}$ ) (b) for reconstructed data and simulation samples over charged pion energy.

### 8.3.3 Total Energy Reconstruction Performance

Finally, the total PandoraPFA energy reconstruction performance for the single charged pion events is evaluated and compared to the conventional calorimetric approach. In the particle flow paradigm, the total energy of the single charged pion event is reconstructed as:

$$E_{PFA} = E_{track} + E_{confusion} \quad (8.9)$$

with  $E_{track}$  the energy provided by the track momentum and  $E_{confusion}$  the double counted charged confusion energy. In general, a significant improvement for the energy linearity and energy resolution is expected for the reconstruction with PandoraPFA, due to exploitation of the sharp track momentum and the observed low fraction of confusion energy with respect to the total event energy, as presented in the last section.

The reconstructed energy spectra of  $E_{PFA}$  for the investigated charged pion samples of 10 GeV and 60 GeV are shown in Figure 8.23. As one can observe, the spectra are dominated by the sharp peak at the respective track momentum corresponding to well reconstructed events. The tail to the right represents the events, which feature double counted charged confusion energy. Agreeing with the observations in the previous sections, the fraction of events in the tail grows with increasing charged pion energy and is higher for both simulations in comparison to the data samples. Since

these spectra are of non Gaussian nature and the impact of the confusion events in the tails are of high interest, the full mean and RMS are calculated to quantify the mean reconstructed energy and the relative energy resolution.

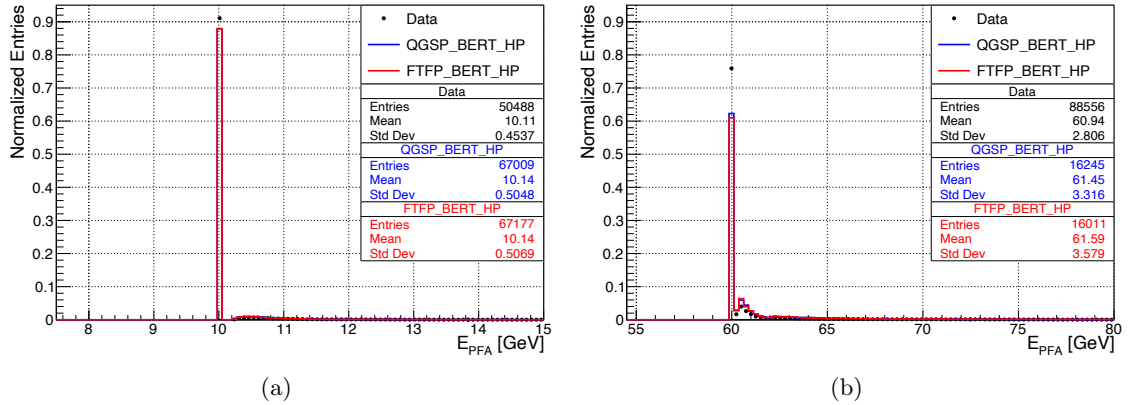


Figure 8.23: Distributions showing total reconstructed PFO energy for charged pion data and simulation samples of energies: **(a)** 10 GeV. **(b)** 60 GeV.

The mean reconstructed energy  $E_{mean}$  against the charged pion energy is presented in Figure 8.24. For comparison of the energy linearity, the mean of the conventionally reconstructed calorimetric energy spectrum is shown and the relative deviation from energy linearity is denoted. As expected, the PandoraPFA reconstruction provides an excellent energy linearity within 4% over the full energy range. The observed mean energy excess originates from double counted charged confusion energy, which slightly grows for increasing charged pion energy as shown in the previous sections. An opposing trend is found for the conventional calorimetric energy measure in form of an increasing mean energy deficit with increasing charged pion energy. It corresponds to an average of  $\sim 4\%$  less energy for 10 GeV and up to 10% less energy for 80 GeV and can be explained by the increasing fraction of events with shower leakage. These events are intrinsically compensated in the PandoraPFA reconstruction by utilising the track momentum. For both mean energy measures an excellent data to MC agreement within 4% over all charged pion energies is observed.

The relative energy resolution  $E_{rms}/E_{mean}$  for both, PandoraPFA and conventional energy reconstruction, is shown in Figure 8.25. In comparison to the conventional calorimetric approach an improvement by approximately a factor 3 is achieved for the PandoraPFA reconstruction over all investigated charged pion energies. After an improving trend up to 20 GeV for the PandoraPFA reconstruction, a slight degradation of up to 2.5% points for increasing charged pion energy is observed, which is caused by the increasing mean double counted charged confusion energy. The conventional calorimetric energy resolution is dominated by the impact of leakage events, fractionally increasing with increasing particle energy. Therefore, it does not follow the parametrisation introduced in Section 4.3.2 but continuously degrades instead. A data to simulation agreement of 10% is observed for both observable over all investigated charged pion energies. Again, the FTFP\_BERT\_HP physics list shows a larger trend towards slightly worse energy resolution, agreeing with the observations discussed in Section 8.3.2 and 7.2.3.

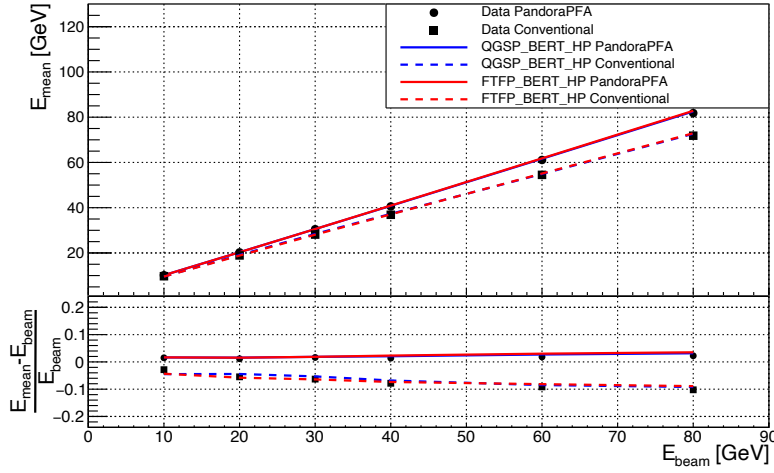


Figure 8.24: Mean reconstructed event energy  $E_{\text{mean}}$  with PandoraPFA and conventional calorimetric approach over charged pion energy for data and simulation samples.  $(E_{\text{mean}} - E_{\text{beam}}) / E_{\text{beam}}$  denotes the relative deviation from energy linearity.

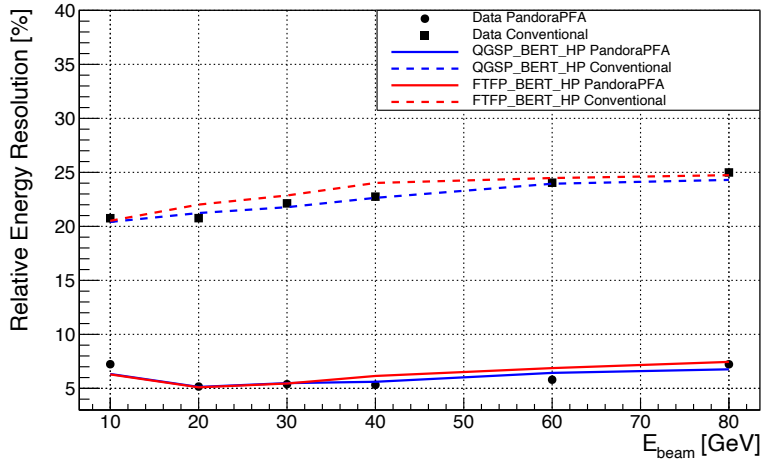


Figure 8.25: Relative energy resolution  $E_{\text{rms}} / E_{\text{mean}}$  achieved with PandoraPFA and conventional calorimetric approach over charged pion energy for data and simulation samples.

### 8.3.4 Impact of Shower Leakage

To study the impact of shower leakage on the mean double counted charged confusion energy in the PandoraPFA single charged pion reconstruction, the samples are subdivided in two categories:

1. Events with a hadronic shower start in the first 10 layers for reduced shower leakage.
2. Events with a hadronic shower start later than layer 10 for enhanced shower leakage.

The two sub-samples are reconstructed individually with PandoraPFA and subsequently the mean double counted charged confusion energy is investigated as described in the previous sections and presented in Figure 8.26

For pion showers initiated in the first quarter of the calorimeter an enhancement of  $\sim 20 - 60\%$  for the simulations and up to a factor of 2 for the data samples is observed for all charged pion energies in comparison to the inverted scenario. This result agrees well with the expectations. If the charged pion starts to shower early in the calorimeter, the particle shower is able to fully develop topologically in the subsequent layers, the full energy is deposited on average and there is a certain chance that PandoraPFA identifies a neutral cluster within the charged shower sub-structure. However, events with enhanced shower leakage feature an intrinsic energy deficit in the calorimetric energy measure. Since the re-clustering iterations of PandoraPFA aim for an optimal agreement between track momentum and associated cluster energy, the misclassification of charged hits as neutral clusters, which would cause an even worse agreement, is suppressed in the leakage case. With increasing charged pion energy the mean energy leakage grows and the absolute discrepancy of the double counted charged confusion energy between the two sub-samples increases on average based on this effect.

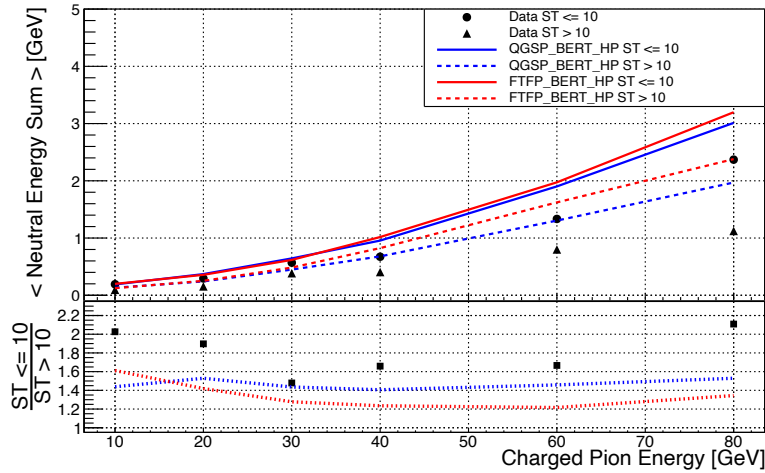


Figure 8.26: Mean double counted charged confusion energy over charged pion energy for data and simulation samples with hadronic shower start in first 10 AHCAL layers ( $ST \leq 10$ ) and AHCAL layers  $> 10$  ( $ST > 10$ ).

## 8.4 Reconstruction of Two Particle Events

Due to the fluctuating nature of the hadronic shower development, the hadron-hadron shower separation is in general a challenging task particularly in dense particle environments. In comparison to hadron-photon separation, for which average energy profiles of photon showers can be utilised, only event-by-event hadronic shower topology and energy dissipation can be exploited by a particle flow algorithm like PandoraPFA. Therefore, the hadronic shower sub-structure details play a significant

role in the pattern recognition and energy considerations within the PandoraPFA reconstruction and have a large impact on how efficiently close-by hadronic showers can be separated.

In the scope of this thesis, the hadron-hadron separation with PandoraPFA is studied on the basis of AHCAL two particle events featuring a pseudo-neutral hadron next to a charged pion shower. One possibility to quantify the separation capability for this scenario is to investigate the recovered neutral energy. A complementary approach is to focus on the two types of confusion energy occurring in the reconstruction: double counted charged and lost neutral confusion energy. Both, the level and balance of the two confusion type are driving factors for the total energy reconstruction performance and thereby the ability to efficiently separate the two hadron showers.

For the studies presented in this section, the two particle data and simulation samples of overlaid 10 GeV pseudo-neutral hadrons and 10 GeV or 30 GeV charged pions at radial distances of 0 – 325 mm, as introduced in Section 8.1.4.2, are reconstructed with PandoraPFA. The chosen energies are considered as being representative for the reconstruction environment typically created by a 100 GeV jet [158]. Therefore, the level of data to simulation agreement for the investigated observables allows to draw direct conclusions on the reliability of performance projections in a future lepton collider experiment. The found results can be considered as a pessimistic lower limit in comparison to the anticipated reconstruction performance in a future lepton collider experiment, due to the absence of a magnetic field. Typically, the presence of a magnetic field intrinsically helps in separating the charged from the neutral particle shower in such a scenario.

First of all in this section, an overview of the reconstructed two particle event classes is provided. After that, the recovery of the pseudo-neutral hadron energy in the vicinity of the charged pion shower is studied including a comparison to previous studies for the AHCAL physics prototype. Afterwards, the focus is set on the study of the two disentangled types of confusion and their impact of on the total energy reconstruction performance, which is compared to the classical calorimetric approach. Lastly, the impact of longitudinal shower separation on the two particle reconstruction performance is investigated.

### 8.4.1 Reconstructed Event Classes

Seven different reconstructed event classes are observed for the two particle studies, which are defined by distinctly populated areas in the correlation plot of the reconstructed PFO and calorimetric energy sum. The different event classes are illustrated in the correlation plot for the data sample of 10 GeV pseudo-neutral hadrons overlaid with 30 GeV charged pions at radial distances of 175 – 225 mm in Figure 8.27. For the five classes specific to the two particle reconstruction, example event displays are provided in Figure 8.28 and discussed in the following:

1. Well reconstructed events: PandoraPFA successfully separates the pseudo-neutral hadron and charged pion shower. The charged pion shower hits are combined into a single charged cluster with a correctly associated track. In addition, the hits of the pseudo-neutral hadron shower are clustered into one or multiple neutral clusters. The total reconstructed energy consists of the sum of the track momentum for the charged pion cluster and the calorimetric measure for the reconstructed neutral cluster(s).
2. Events with maximal lost neutral confusion energy: All hits of the pseudo-neutral hadron shower are clustered into a large charged cluster together with the hits of the charged pion shower. For the total reconstructed event energy only the associated track momentum is considered. The calorimetric energy measure of the pseudo-neutral hadron hits is fully lost.

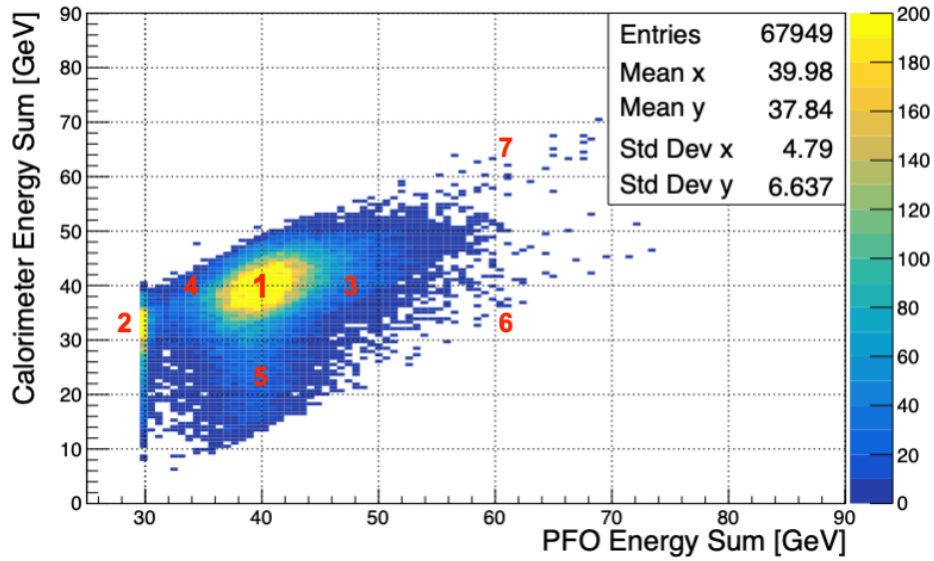


Figure 8.27: Correlation of reconstructed PFO and conventional calorimetric energy sum for data sample of 10 GeV pseudo-neutral hadrons overlaid with 30 GeV charged pions at a radial distance of 175 – 225 mm. The numbers indicate the different populations of reconstructed event classes: (1) Well reconstructed events. (2) Events with maximal lost neutral confusion energy. (3) Events with an excess of double counted charged confusion energy. (4) Events with an excess of lost neutral confusion energy. (5) Well reconstructed events with compensated leakage for charged pion. (6) Events with track to cluster association failure. (7) Multi-particle and high energy contamination events.

3. Events with excess of double counted charged confusion energy: Same case as for 1., but in addition several charged pion shower hits are classified as one or multiple additional neutral clusters by PandoraPFA. This results in an excess of double counted charged confusion energy in the total reconstructed event energy, equivalent to the confusion case studied for the single charged pion reconstruction.
4. Events with excess of lost neutral confusion energy: Same case as for 1., but in addition several pseudo-neutral hadron shower hits are classified to be part of the charged cluster by PandoraPFA. Since the track momentum is utilised instead of the charged clusters calorimetric measure, the energy of the misclassified pseudo-neutral hadron hits is lost and not considered in the reconstructed total event energy.
5. Well reconstructed events with leakage compensation for charged pion shower: Same case as for 1., but in addition the lost calorimetric energy measure of the charged pion shower due to shower leakage is fully compensated by utilising the associated track momentum.
6. Track-cluster association failure events: See single particle event classes in Section [8.3.1](#)
7. Multi-particle high energy contamination events (only for data samples): See single particle event classes in Section [8.3.1](#)

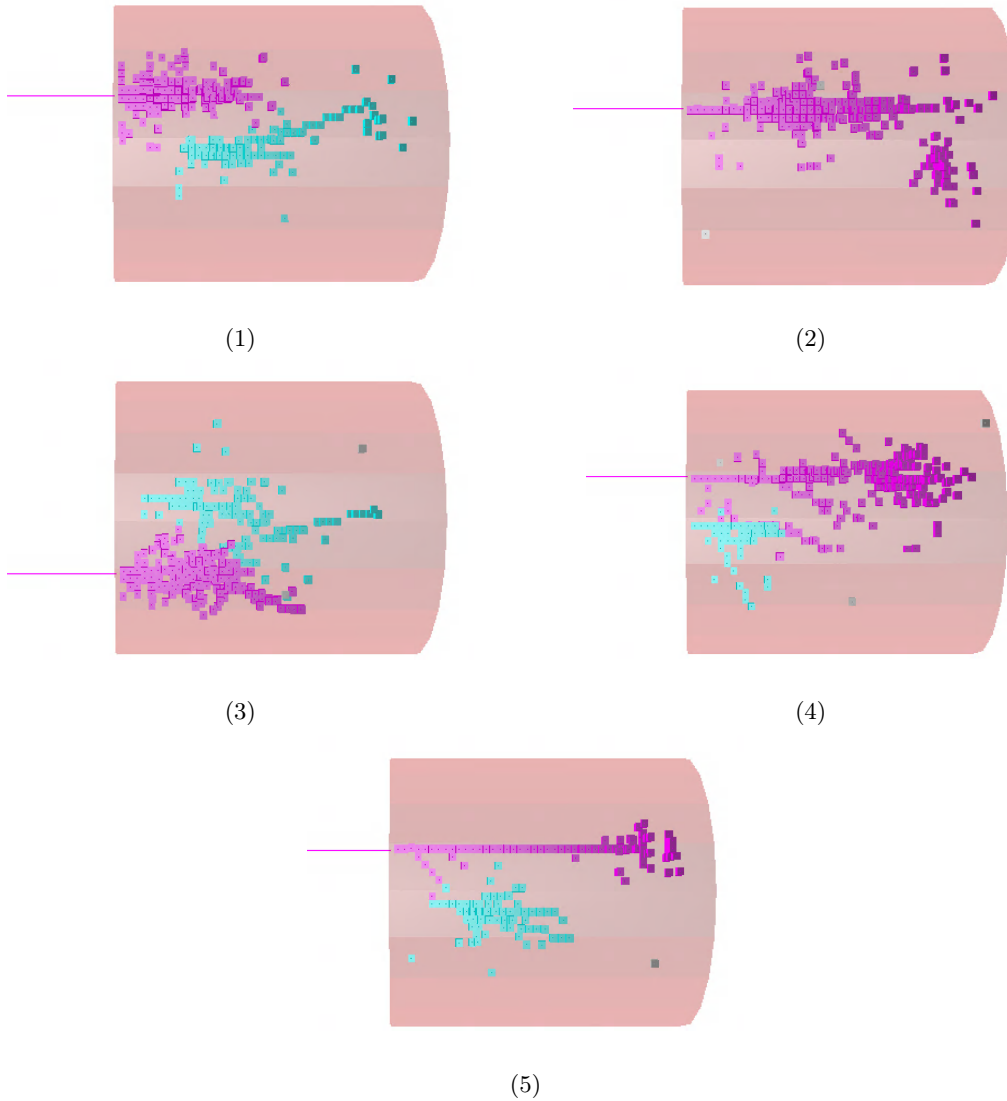


Figure 8.28: Event displays illustrating reconstructed two particle event classes. According to the number, each display shows a representative event of the populations labeled in Figure 8.27.

#### 8.4.2 Pseudo-Neutral Hadron Energy Recovery for Different Shower Distances and Energies

To accurately quantify the recovery of the pseudo-neutral hadron energy, the neutral energy reconstructed with PandoraPFA is compared to the input calorimetric neutral energy for each event. This is done by investigating the spectra showing the difference of those two energy measures for all distance and energy scenarios. Figure 8.29 shows the spectra for a radial shower distance of

25 – 75 mm and 275 – 325 mm for the overlaid 10 GeV and 30 GeV charged pion scenarios. The respective spectra for all other distance and energy scenarios can be found in Appendix [D.1](#)–[D.7](#).

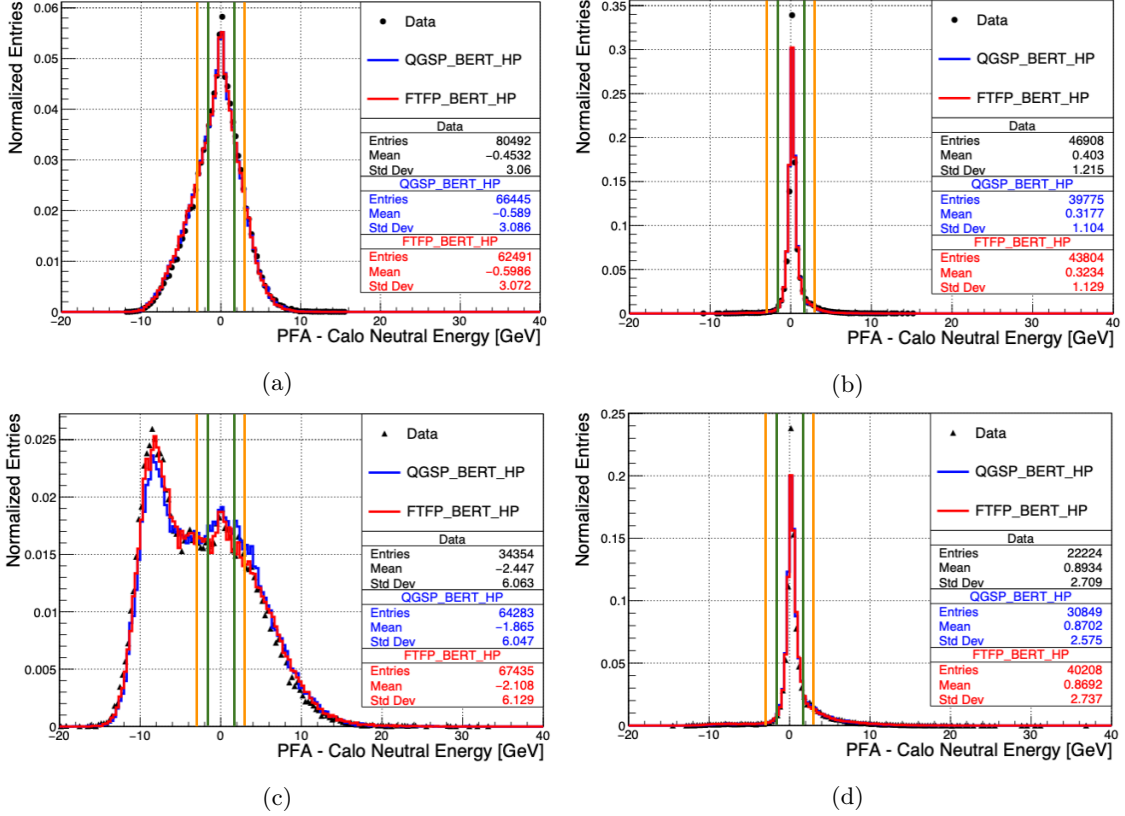


Figure 8.29: Spectra of differences between neutral PFO energy sum and input neutral calorimetric energy sum for beam test data and simulations samples of overlaid pseudo-neutral hadron and charged pion shower at different radial distances: (a) 10 GeV + 10 GeV at 25 – 75 mm. (b) 10 GeV + 10 GeV at 275 – 325 mm. (c) 10 GeV + 30 GeV at 25 – 75 mm. (d) 10 GeV + 30 GeV at 275 – 325 mm. The green lines indicate the  $2\sigma$  and the orange lines the  $3\sigma$  limits.

For all investigated spectra an excellent data to simulation agreement is observed. At the largest shower distances a sharp peak around 0 GeV demonstrates the precise recovery of the pseudo-neutral hadron energy for the vicinity of both, a 10 GeV and 30 GeV overlaid charged pion shower. If the shower distance decreases, the reconstruction of the pseudo-neutral hadron energy becomes more difficult. This is reflected by distributions with a growing spread around 0 GeV for both energy scenarios. In addition, a shoulder to the left and a second peak at around  $-9$  GeV are observed for the close-by charged pion scenarios. Both are resulting from events, in which either all or parts of the pseudo-neutral hadron hits are classified as charged and their energy is lost (compare event class 2. and 4.). This type of events are more frequent in the case of a 30 GeV overlaid charged pion shower. The same applies to the right shoulder, representing events with too much reconstructed neutral energy in the form of double counted charged pion hit energies misclassified as neutral (compare event class 3.).

To quantify the spread accurately and include both tail effects for comparison between the different energy and distance scenarios, the  $3\sigma$  and  $2\sigma$  recovery probabilities of the pseudo-neutral hadron energy are defined as follows:

$$P_{3\sigma} = \frac{N_{events}|_{E_{PFO}-E_{Calo}|<3\sigma}}{N_{events}_{total}} \quad (8.10)$$

$$P_{2\sigma} = \frac{N_{events}|_{E_{PFO}-E_{Calo}|<2\sigma}}{N_{events}_{total}} \quad (8.11)$$

with  $N_{events}|_{E_{PFO}-E_{Calo}|<3\sigma}$  and  $N_{events}|_{E_{PFO}-E_{Calo}|<2\sigma}$  the number of events within the  $3\sigma$  and  $2\sigma$  limits and  $N_{events}_{total}$  the total number of reconstructed events.  $\sigma$  is defined as the absolute resolution of the input pseudo-neutral hadron calorimetric energy and is determined by the  $\sigma$  of a Gaussian fitted to the respective energy sum spectrum, as illustrated by Figure 8.30. The  $\sigma$  determination is done for data and simulation samples of all pseudo-neutral energy sum spectra of each distance bin and energy scenario individually. Over all scenarios, the mean  $\sigma$  corresponds to  $\sim 1.9$  GeV. The corresponding  $3\sigma$  and  $2\sigma$  limits are illustrated in Figure 8.29 as well.

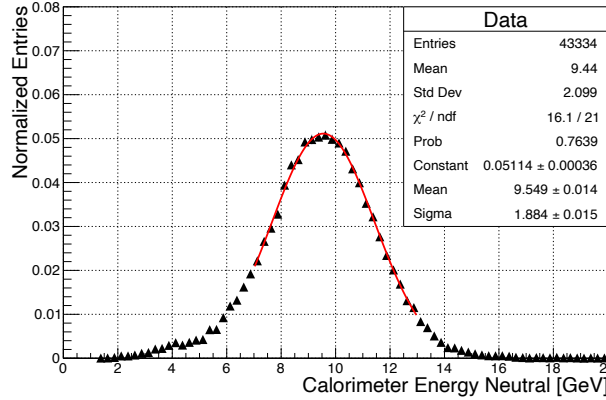


Figure 8.30: Calorimetric energy sum spectrum of 10 GeV pseudo-neutral hadrons in the vicinity of 30 GeV charged pion showers at 0 – 25 mm distance for the data sample. A Gaussian is fitted to extract the  $\sigma$  for the pseudo-neutral hadron recovery probability calculation.

The calculated  $3\sigma$  recovery probability  $P_{3\sigma}$  is plotted in Figure 8.31 over all investigated distances and both charged pion energy scenarios. As expected, the best recovery probability is achieved for the largest shower distances for both energy scenarios. As soon as the showers are getting closer to each other, the recovery probability decreases. For both energy scenarios, a turning point is located at a radial shower distance of around 125 – 175 mm. In addition, it can be observed that the recovery of the 10 GeV pseudo-neutral hadron is significantly better in the vicinity of a 10 GeV in comparison to a 30 GeV charged pion shower. While for the first case a  $3\sigma$  recovery probability of over 95 % (60 %) is reached for the largest (smallest) shower distances, for the second case only 85 % (25 %) is achieved. This is due to the increase of both confusion types for the on average topologically more spread out 30 GeV in comparison to 10 GeV charged pion showers. Again, an excellent data to simulation agreement within 5 % is observed for both physics lists.

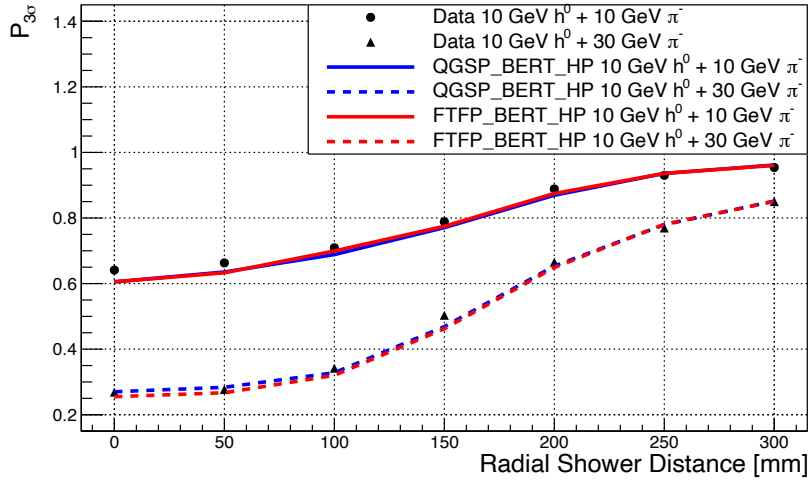


Figure 8.31:  $3\sigma$  recovery probability of 10 GeV pseudo-neutral hadron energy in the vicinity of a 10 GeV or 30 GeV charged pion shower over radial shower distance for data and simulation samples.

#### 8.4.2.1 Comparison to Previous Studies

In a previous study by CALICE [156], the two particle separation performance with PandoraPFA in the form of the pseudo-neutral hadron energy recovery has been investigated as well. However, the environment and samples utilised in the previous work are significantly different from the ones presented in the context of this thesis. First of all, the combined beam test data of an ECAL and the AHCAL physics prototypes, featuring different granularities for different layers, is used. Second, since an older and less modular version of PandoraPFA was used, a projection to the geometry and granularity of the ILD barrel was required. Lastly, older GEANT4 simulation models (v.04.09.2) were used in comparison to the ones investigated in this thesis. Except from that, the analysis strategy applied was similar and events with overlaid pseudo-neutral hadron showers of 10 GeV and charged pion showers of 10 GeV or 30 GeV at radial shower distances of 0 – 300 mm were investigated, too. To further evaluate the quality of the latest AHCAL prototype events, the reliability and technical feasibility of the adapted PandoraPFA framework and to understand the impact of the different datasets and setups on the two particle separation performance, the results for both studies are compared in the following.

Figure D.8 illustrates the neutral energy difference spectra of the previous studies for the same distance and energy scenarios as presented in Figure 8.29. If the respective spectra are compared between the two studies, the same qualitative features and trends with respect to the two confusion types for increasing charged pion energy and decreasing radial shower distance can be observed.

To compare the individual spectra quantitatively, the calculated  $2\sigma$  recovery probability of the pseudo-neutral hadron energy for both studies is shown in Figure 8.32. In general, the same decreasing trends of the  $2\sigma$  recovery probability for decreasing radial shower distances and increasing charged pion energy are observed in both studies. The achieved recovery probability for the current study is approximately 10 – 20 percentage points lower for the smallest to medium and 5 – 10 percentage points lower for the largest radial shower distances in both energy scenarios. This is

predominantly caused by a found enhanced number of events with double counted charged confusion energy in comparison to the previous study. Furthermore, a steeper drop with decreasing shower distance is observed for the previous study in comparison to the more saturated behaviour for the lowest shower distances of the current study. In addition, for the current study a turning point in the region 100 – 200 mm is observed.

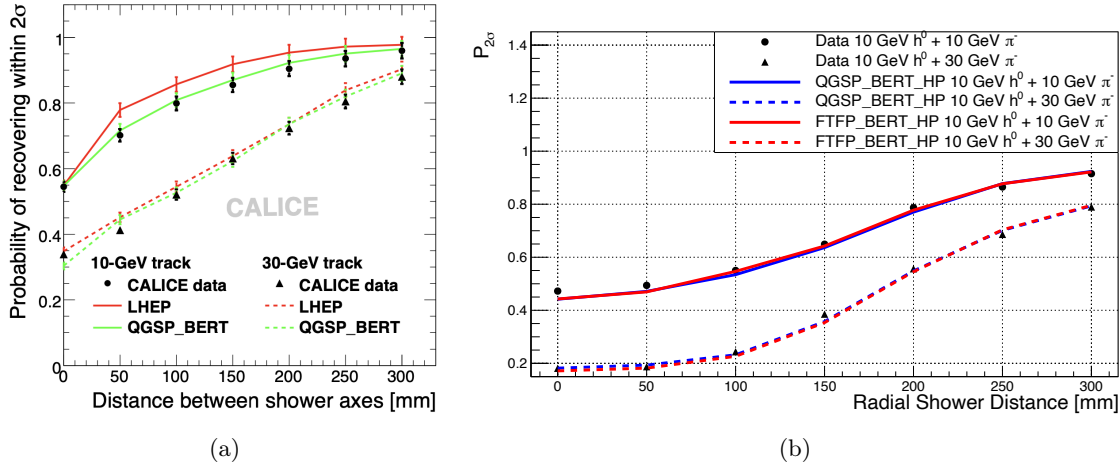


Figure 8.32:  $2\sigma$  recovery probability of 10 GeV pseudo-neutral hadron in the vicinity of a 10 GeV or 30 GeV charged pion shower over radial shower distance for data and simulation samples of (a) CALICE SiW-ECAL + AHCAL 2007 prototype studies [156]. (b) AHCAL prototype studies.

These observations agree with the trends and absolute values for the mean and RMS of the neutral energy difference spectra for both studies, which are compared in Figures D.9 and D.10. For the lowest radial shower distances, lower absolute values for the mean and RMS are observed for the current study, which potentially indicate a slightly better confusion type balance and a lower total confusion level. All compared observables show a good data to simulation agreement within 15% or better for both physics list of the current study, similar to the agreement achieved for the data and QGSP\_BERT simulation of the previous study.

To sum up, with the combination of the current PandoraPFA framework implementation and the AHCAL prototype events almost the same performance level as for the previous studies is reached, despite the fundamentally different setups. Similar, but slightly smoother trends for the recovery of the pseudo-neutral hadron energy are observed. The main difference in the studied observables originates from the enhanced number of events with double counted charged confusion energy in the current study. One can conclude that the high quality data of the AHCAL prototype, with respect to the reduced noise levels and higher and more uniform granularity, and the sophisticated implementation of the PandoraPFA framework, allowed to compensate the performance gains by the combination of ECAL and AHCAL data for the previous studies to a large extent. With an ECAL in front of the current AHCAL prototype, improvements of the general performance are expected, particularly at the lowest shower distances. This is based on the improved initial clustering and track to cluster association a combined setup would offer, which is beneficial for the subsequent re-clustering iterations of PandoraPFA, as discussed in the previous sections.

### 8.4.3 Confusion for Different Shower Distances and Energies

Up to now the reconstruction performance has been quantified by comparing the PandoraPFA reconstructed neutral energy, independent of their origin, to the input calorimetric neutral energy. In this section, the reconstruction performance is quantitatively investigated by focusing on the correct classification of individual neutral or charged shower hits by PandoraPFA. As described in Section 6.3.3 in the overlay procedure the truth origin is flagged for each hit in an event. This allows to evaluate for each neutral or charged calorimeter input hit if it is reconstructed correctly or incorrectly as a neutral or charged hit by PandoraPFA. As a result, not only the correctly classified energy can be quantified, but also the two individual types of confusion can be disentangled.

In the first part of this section, the mean energy reconstruction efficiency and purity of both, the pseudo-neutral and charged pion showers, are investigated with this method. After that, the absolute energy for each confusion type, the resulting type balance and the total confusion energy per event is studied in detail for the investigated distance and energy scenarios.

#### 8.4.3.1 Energy Reconstruction Efficiency and Purity

In order to quantify the correctly identified charged or neutral energy and the purity of the reconstructed charged or neutral PFOs on hit level, the energy reconstruction efficiency and purity are defined as follows:

$$\epsilon = \frac{Esum_{reco,correct}}{Esum_{input,total}} \quad (8.12)$$

$$\rho = \frac{Esum_{reco,correct}}{Esum_{reco,total}} \quad (8.13)$$

with  $Esum_{reco,correct}$  the energy sum of the hits within the respective PFO correctly identified by PandoraPFA as neutral or charged,  $Esum_{input,total}$  the energy sum of the neutral or charged calorimeter input hits and  $Esum_{reco,total}$  the energy sum of all hits within the reconstructed neutral or charged PFO. For overlaid hits, which have a truth energy contribution from the charged pion and pseudo-neutral hadron shower, only the corresponding truth fraction of energy is used. The determined mean energy reconstruction efficiency and purity for the pseudo-neutral hadron are plotted in Figure 8.33 over the radial shower distance for the two energy scenarios and for the charged pion showers in Figure 8.34 respectively. Complementary plots for the two quantities defined on the number of hit level can be found in Appendix D.11 and D.12

For the pseudo-neutral hadron showers the maximal mean reconstruction efficiency and purity, both above 90%, are found for the largest shower separations. As anticipated, both observables decrease with decreasing radial shower distance, due to the increasing confusion energy. Truth neutral hits, misclassified as charged, lower the reconstruction efficiency on the one hand. The misclassification of charged shower hits as neutral reduces the reconstruction purity of the pseudo-neutral hadron on the other hand. In general, the impact of these effects is more enhanced for the vicinity of a 30 GeV charged pion shower, due to the more complex and spatially spread out shower topology causing more difficult PandoraPFA reconstruction of the pseudo-neutral hadron. For decreasing shower distances this effect is further enhanced, which results in a factor 2 less mean reconstruction efficiency and purity in comparison to the overlaid 10 GeV charged pion shower scenario. Both observables do not saturate at 1 for the largest shower distances. For the mean reconstruction efficiency this is caused by a few events, which are either affected from PandoraPFAs isolation cuts or still feature a few misclassified hits. The mean purity of the pseudo-neutral hadron is limited by the occurring double counted charged confusion energy. As observed

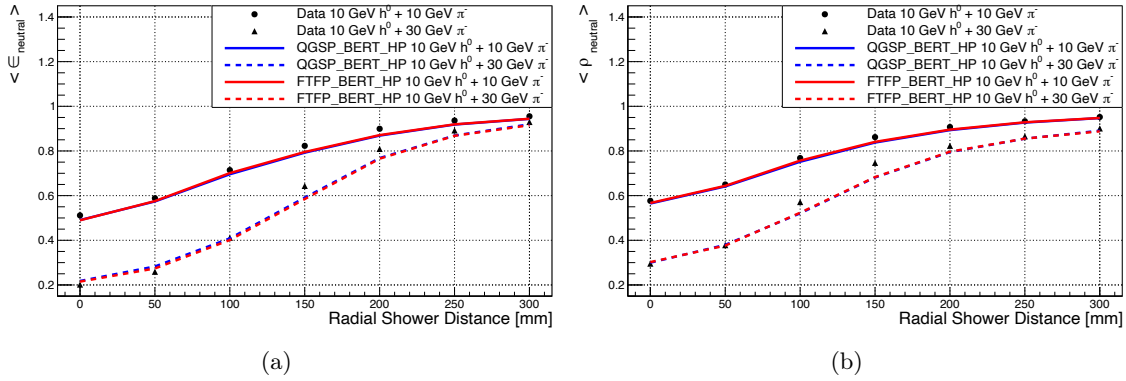


Figure 8.33: Mean energy reconstruction efficiency (a) and purity (b) for 10 GeV pseudo-neutral hadron in the vicinity of 10 GeV or 30 GeV charged pion showers over radial shower distance for data and simulation samples.

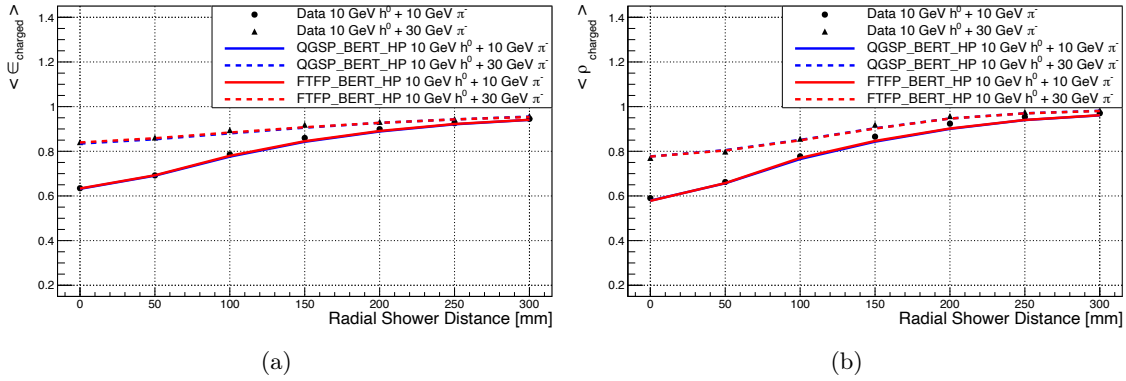


Figure 8.34: Mean energy reconstruction efficiency (a) and purity (b) for 10 GeV or 30 GeV charged pion in the vicinity of 10 GeV pseudo-neutral hadron showers over radial shower distance for data and simulation samples.

in the previous sections, this is more dominant for the 30 GeV in comparison to a 10 GeV charged pion shower, agreeing with the observed trends. For the lowest shower distances, the found mean purity approximately corresponds to a random mixture of charged and neutral shower hit energies according to the neutral energy fraction of the total event energy.

The same trend for decreasing shower distance is observed for the mean reconstruction efficiency and purity of the charged pion shower. However, now the confusion scenarios are inverted. Truth charged hits, mis-classified as neutral hits, decrease the reconstruction efficiency on the one hand. The misclassification of neutral shower hits as charged hits lowers the reconstruction purity on the other hand. In general, both observables feature higher absolute values in comparison to the ones for the pseudo-neutral hadrons. This is based on the track association from which the charged hit clustering in PandoraPFA benefits even at the lowest shower distances. This also explains, why the

30 GeV charged pion scenario shows better efficiencies and purities in comparison to the 10 GeV case. The confusion caused by the vicinity of the 10 GeV pseudo-neutral hadron is fractionally small in comparison to the total charged energy in the event, of which most is reconstructed correctly. For the largest distances the mean efficiency saturates at a level lower than 1, due to the occurring double counted charged confusion energy. The mean energy purity saturates close to 1, since the impact of lost neutral confusion energy is significantly reduced for the largest shower separations.

A good data to simulation agreement within 10% is observed for all observables, all studied scenarios and for both physics lists.

#### 8.4.3.2 Confusion Level and Type Balance

Determined with the method described in Section 8.4.3, the found mean absolute doubled counted charged and lost neutral confusion energies are presented in Figure 8.35 over all investigated shower distance and energy scenarios.

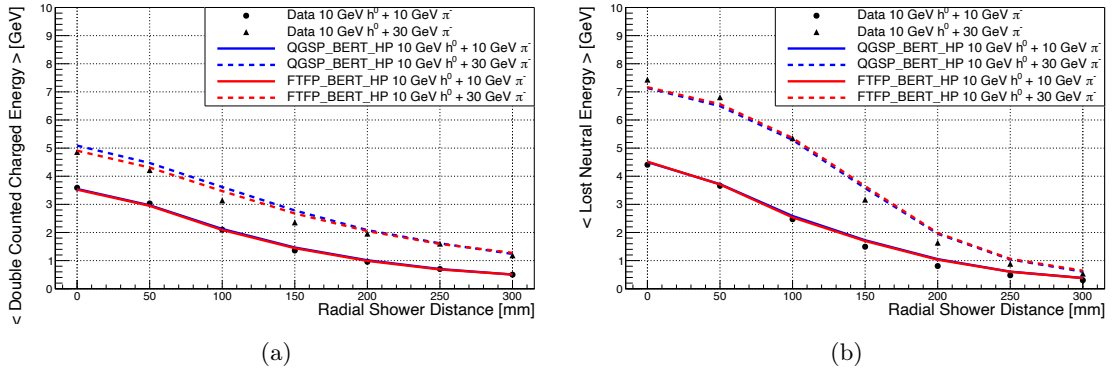


Figure 8.35: Mean absolute confusion energies over radial shower distance for data and simulation samples: (a) Double counted charged confusion energy. (b) Lost neutral confusion energy.

For both types of confusion, an increasing trend for the confusion energy with decreasing shower distance is observed. As expected, the absolute confusion energy for both types is higher for the 30 GeV charged pion scenario, due to spatially more spread out topology within the charged pion shower development. With regard to the double counted charged confusion energy, this causes an enhanced probability for PandoraPFA to reconstruct parts of the charged shower sub-structure as neutral clusters, as discussed for the single particle study. In general, this effect is assumed to be constant with the charged pion energy. The observed increasing trend for lower shower distances can be explained by an increasing charged/neutral hit mixing probability in the PandoraPFA reconstruction. The enhanced lost neutral confusion energy originates from a higher probability of the charged pion shower to be topologically connected to the pseudo-neutral hadron shower. This causes the pattern recognition within PandoraPFA to reconstruct some or all of the neutral shower hits to be part of the charged cluster with a higher chance. Furthermore, this explains the observed behaviour for largest shower distances. The showers are transversally well separated and even the larger spatial shower dimension of the 30 GeV charged pion shower is not large enough for a topological shower connection on average. Therefore, for both energy scenarios the lost neutral confusion energy saturates at the same low level of  $\sim 0.5$  GeV. On the other hand, the

double counted charged confusion energy becomes the dominant confusion type particularly for the 30 GeV charged pion shower scenario at largest shower distances.

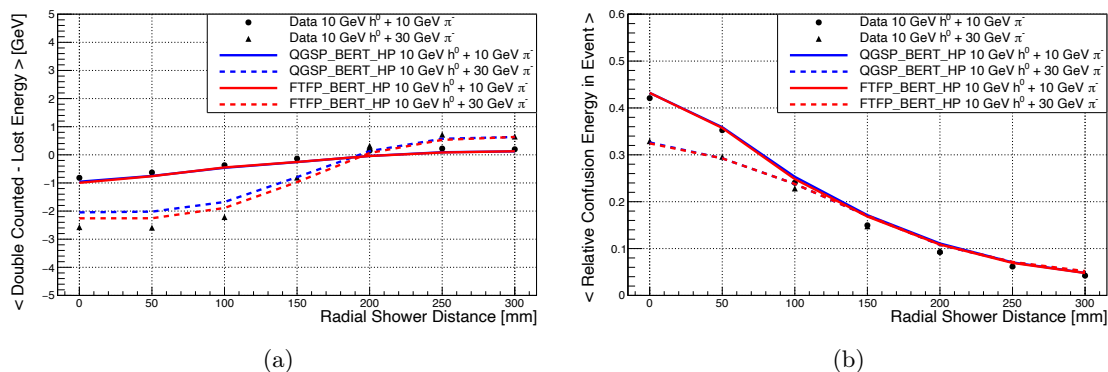


Figure 8.36: Mean absolute confusion type difference of double counted charged and lost neutral energy (a) and mean fraction of confusion energy (b) in two particle events featuring 10 GeV pseudo-neutral hadron in the vicinity of 10 GeV or 30 GeV charged pion showers over radial shower distance for data and simulation samples.

These observations are further validated by Figure 8.36a showing the mean absolute confusion type difference of double counted charged and lost neutral confusion energy against the radial shower distances. While for the 10 GeV charged pion scenario a mean confusion balance within  $\sim 1$  GeV is observed, the confusion balance for the 30 GeV charged pion scenario is only within  $\sim 2.5$  GeV. For the largest shower distances a dominance of double counted charged confusion energy and for the lowest shower distances a dominance of lost neutral confusion energy is found, which are both more enhanced for the 30 GeV charged pion scenario.

Another driving factor for the total energy reconstruction performance is the total fraction of confusion energy in the event. The mean fraction of confusion energy normalised to the event energy versus the radial shower distances is illustrated in Figure 8.36b. The fraction of confusion energy is far below 10% for the largest shower distances and increases on average with decreasing shower distance. For distances below 100 mm, the confusion energy is fractionally lower for the 30 GeV charged pion scenario, since a larger fraction of the 30 GeV charged pion energy is reconstructed correctly on average in contrast to the 10 GeV charged pion scenario.

Again, for all investigated observables of all studied scenarios within this section a good data to simulation agreement within 15% is observed for both physics lists.

One can conclude, that with decreasing shower distance the total level of confusion as well as the confusion type imbalance increases. This is particularly the case for the 30 GeV charged pion scenario, despite the fact that the relative confusion with respect to the event energy is lower in comparison to the 10 GeV charged pion scenario. Since the correctly and incorrectly reconstructed energies of neutral and charged particles are determined individually, confusion matrices are constructed to further visualise the conclusions of this section. Figure D.13 compares the mean confusion matrices normalised to the event energy for 10 GeV pseudo-neutral hadrons and 30 GeV charged pion showers at the closest and largest shower distances for the data samples.

### 8.4.4 Total Energy Reconstruction Performance

After the extensive study of the individual confusion types and the total confusion level, the impact on the total reconstructed energy balance for the two particle events is investigated and compared to the conventional calorimetric approach. The total event energy reconstructed by PandoraPFA  $E_{PFA}$  for the two particle events corresponds to:

$$E_{PFA} = E_{track} + E_{DCC} + E_{neutral} - E_{LN} \quad (8.14)$$

with  $E_{track}$  the energy provided by the associated track momentum,  $E_{DCC}$  the double counted charged confusion energy,  $E_{neutral}$  the calorimetric input energy of the pseudo-neutral hadron and  $E_{LN}$  the lost neutral confusion energy. Since the ILD default settings for PandoraPFA are not optimised on the reconstruction of simple two particle events, a non ideal reconstruction performance is expected, due to emerging confusion energy particularly at the lowest radial shower distances. Only for larger radial shower distances, and thereby a sufficient separation of the charged and neutral particle showers on average, a significant improvement in comparison to the conventional calorimetric approach is expected. This is again based on the exploitation of the sharp track momentum for the charged pion shower.

The reconstructed energy spectra of  $E_{PFA}$  for close-by and well separated particle showers are illustrated in Figure 8.37 for the example of the 10 GeV pseudo-neutral hadron overlaid with 30 GeV charged pion shower scenario. The peak around 40 GeV represents the events with a well reconstructed energy balance. The tail and the peak to the left represent events with an excess of or maximal lost neutral confusion energy. The tail to the right features events with an excess of double counted charged confusion energy. In general, an excellent data to simulation agreement on individual spectra level is observed. Agreeing with the confusion trends studied in the previous sections, the reconstructed total energy balance is improving on average with increasing radial shower distance. Events in both tails get fractionally less and the peak around 40 GeV gets more pronounced. Again, due to the non Gaussian nature of the spectra for the lowest radial shower distances and the focus on the impact of the tail events, the full mean and RMS are chosen to quantify the total energy reconstruction performance for the different scenarios.

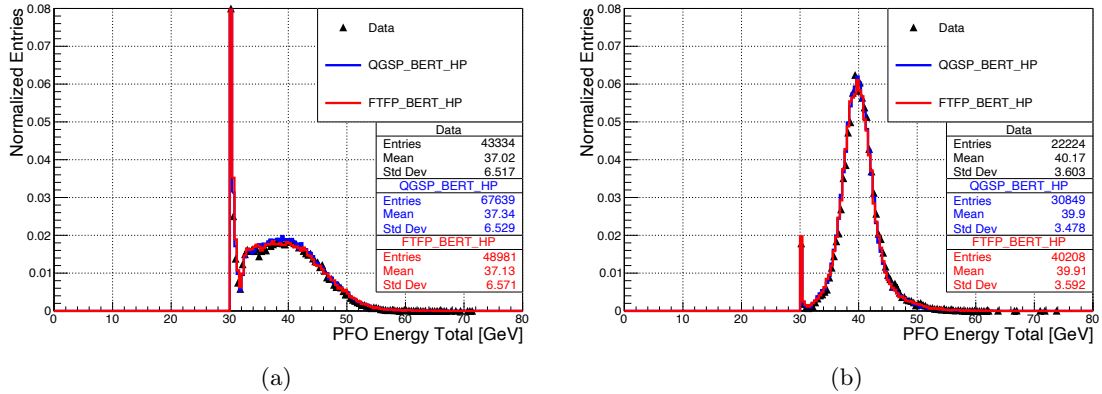


Figure 8.37: Distributions showing total reconstructed PFO energy ( $E_{PFA}$ ) for reconstructed data and simulation samples of 10 GeV pseudo-neutral hadron + 30 GeV charged pion shower at radial distances: (a) 0 – 25 mm. (b) 275 – 325 mm.

Figure 8.38 shows the mean of the individual  $E_{PFA}$  spectra in comparison to the mean calorimetric energy sum of all investigated scenarios. As expected, for the calorimetric measure a constant mean, slightly below the total two particle event energy of 20 GeV and 40 GeV is observed for all radial shower distances, due to the impact of shower leakage. Conversely, the mean of the  $E_{PFA}$  spectra for the highest radial shower distances shows more accurately recovered energies of 20 GeV and 40 GeV, due to the intrinsic leakage compensation by PandoraPFA, as discussed for the single particle case in Section 8.3.3. The excess of double counted charged confusion energy found for the largest radial shower separations does not have a significant impact on the total reconstructed energy balance. However, for decreasing shower distances the impact of lost neutral confusion energy becomes dominant. The mean slightly decreases about 1 GeV for the 20 GeV and about 2.5 GeV for the 40 GeV scenario.

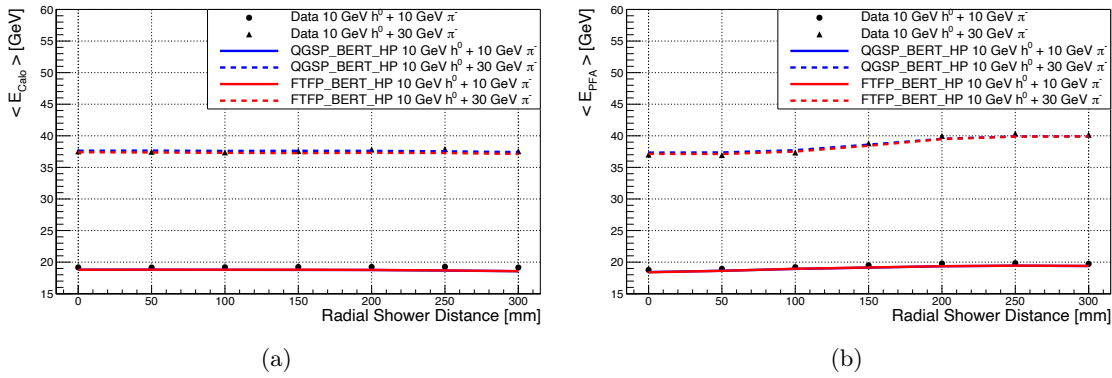


Figure 8.38: Mean reconstructed total event energy of two particle events featuring 10 GeV pseudo-neutral hadrons in the vicinity of 10 GeV or 30 GeV charged pion showers over radial shower distance for data and simulation samples: (a) Conventional calorimetric approach. (b) PandoraPFA.

Lastly, the relative energy resolution is calculated and presented in Figure 8.39. For the conventional calorimetric energy resolution of the 20 GeV and 40 GeV events, a constant behaviour over all radial shower distances is observed, as expected. The relative energy resolution for 40 GeV is dominated by leakage effects for the 30 GeV charged pion shower and for this reason is higher than the respective resolution for the 20 GeV events. In contrast to that, the relative energy resolution for the PandoraPFA reconstruction improves for increasing radial shower distance, due to the decreasing confusion level. With respect to the total event energy, the confusion effects are fractionally larger for the 20 GeV scenario resulting in a worse overall energy resolution in comparison to the 40 GeV scenario, for which most of the 30 GeV charged pion energy is correctly associated to the track and thereby reconstructed precisely. In addition, the shower leakage is intrinsically compensated by PandoraPFA to a large extent. These are as well the reasons, why for the 40 GeV scenario the relative energy resolution is on the same level for smallest and up to 90% better for largest shower distances for the PandoraPFA reconstruction in comparison to the conventional calorimetric approach. For the 20 GeV scenario, a better energy resolution is only achieved at shower distances larger than 200 mm. For both, the mean reconstructed total energy and the relative energy resolution of the PandoraPFA reconstruction, an excellent data to simulation agreement within 5% for both physics lists is observed.

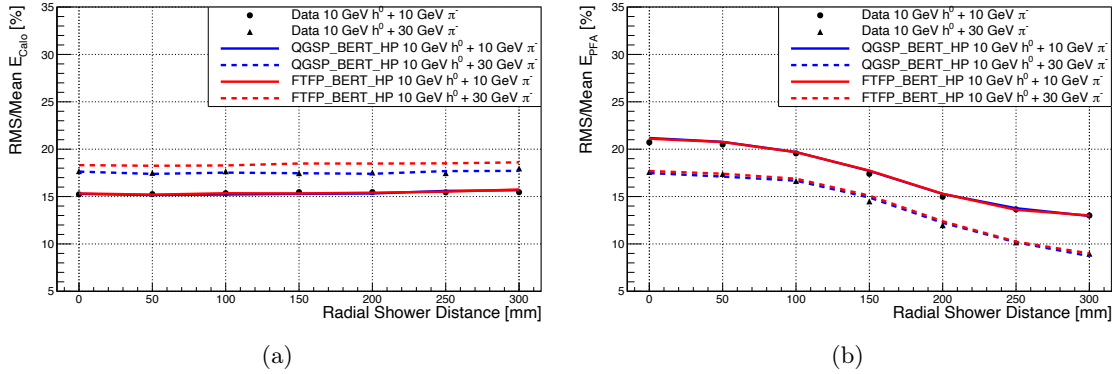


Figure 8.39: Relative energy resolution for two particle events featuring 10 GeV pseudo-neutral hadrons in the vicinity of 10 GeV or 30 GeV charged pion showers over radial shower distance for data and simulation samples: (a) Conventional calorimetric approach. (b) PandoraPFA.

#### 8.4.5 Impact of Longitudinal Shower Separation

The high granularity of the AHCAL prototype with respect to the channels per layer and the total number of layers does not only allow to study the separation of hadron showers in the transversal, but also longitudinal plane. If one of the hadrons showers in one of the first layers of the AHCAL and the other one a significant number of layers later, well beyond the scale of the first hadronic shower development, an effective longitudinal shower separation is achieved, as illustrated in Figure 8.40. It is expected that the longitudinal shower separation additionally helps PandoraPFA to separate the two particles more efficiently and to decrease the overall level of confusion.

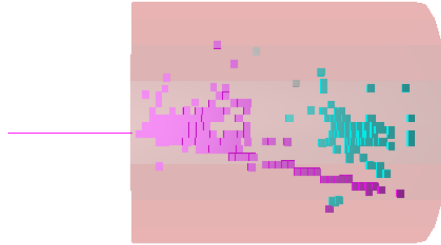


Figure 8.40: Event display featuring a 10 GeV pseudo-neutral hadron (shower start in layer 29) in the vicinity of a 30 GeV charged pion (shower start in layer 2) after PandoraPFA reconstruction.

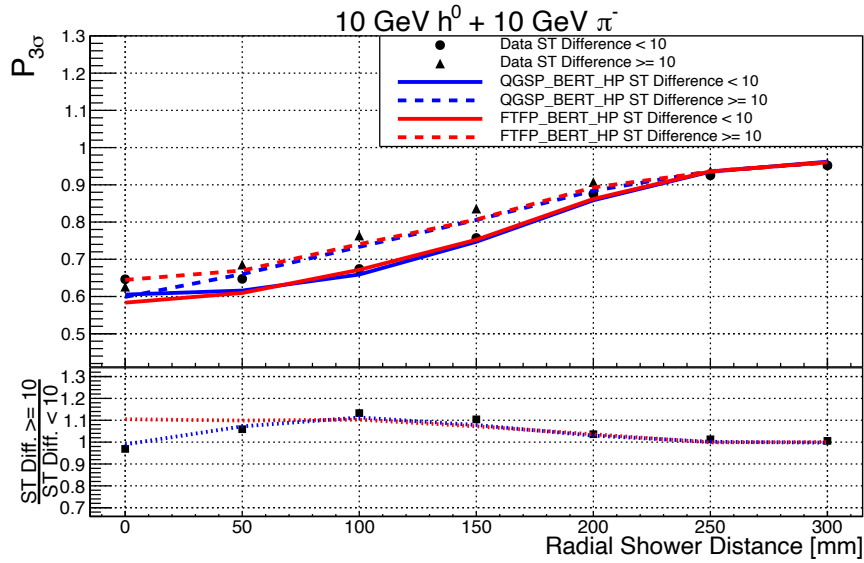
In order to confirm this expectation, the impact of longitudinal shower separation on the recovery probability of the pseudo-neutral hadron energy is investigated in the following. For this purpose, the two particle samples are sub-divided into two categories:

1. Events for which the pseudo-neutral hadron and the charged pion shower start layer difference is not larger than 9 layers to generate samples with reduced longitudinal shower separation.

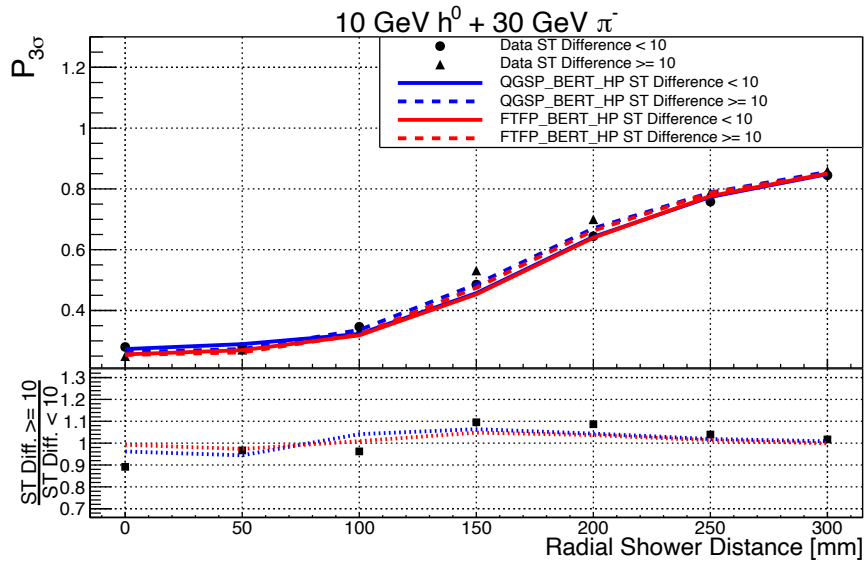
2. Events for which the pseudo-neutral hadron and the charged pion shower start layer difference is equal or larger than 10 layers to generate samples with enhanced longitudinal shower separation.

The  $3\sigma$  pseudo-neutral hadron energy recovery probability is plotted over the radial shower distance for both energy scenarios and sub-samples in Figure [8.41](#). For the largest radial shower distances an agreement within 2 percent is observed between the two longitudinal separation scenarios for both energy scenarios. For the lowest radial shower distance of the 10 GeV charged pion scenario a similar observation is made and for the 30 GeV charged pion scenario a slight degradation of the recovery probability of up to 10 percent is observed. However, particularly for the intermediate radial shower distances an improvement of the recovery probability of up to 8–10% is observed for the samples with enhanced longitudinal shower separation, which is more pronounced for the 10 GeV charged pion scenario. This agrees well with the combined observations for the individual confusion types, the mean confusion type difference and the mean fraction of confusion energy studied for the two sub-samples, as illustrated in Figures [D.14](#)–[D.17](#).

One can conclude that additional longitudinal shower separation particularly helps at intermediate transversal shower distances of 50 – 250 mm to further improve the two particle separation performance of PandoraPFA by up to 10%. At the largest investigated radial shower distances, the transversal separation is too large in order to see an effect by additional longitudinal shower separation. For the lowest radial shower distances, an improvement of the two particle separation is mostly prevented by an enhanced confusion type imbalance for the case of longitudinally separated showers, despite the fact that the total fraction of confusion energy in the event is lower. As expected, the improvement is in general better for the 10 GeV compared to the 30 GeV charged pion shower scenario, due a more compact and less topologically spread out shower development.



(a)



(b)

Figure 8.41:  $3\sigma$  recovery probability of 10 GeV pseudo-neutral hadron energy in the vicinity of a 10 GeV (a) or 30 GeV (b) charged pion shower over radial shower distance for data and simulation samples with shower start difference of pseudo-neutral hadron and charged pion < 10 layers (ST Difference < 10) and  $\geq$  10 layers (ST Difference  $\geq$  10).

# 9 Studies of Different PandoraPFA Settings and Hit Energy Thresholds

In the last chapter, the reconstruction performance with PandoraPFA ILD default settings for AHCAL prototype single and two particle events has been studied extensively. Besides the observed overall good agreement of data and simulations, one of the key observations is that the limitations by confusion increase with decreasing hadron shower distance and increasing hadron energy. In this chapter, the performance with different PandoraPFA settings is studied on the basis of more complex simulated ILD di-jet events in a similar manner. For the first part of this study, the most confusion sensitive PandoraPFA parameters and algorithms are changed or disabled completely. In the second part, the hit energy thresholds are increased to simulate the consequences of increased noise levels in calorimeter systems e.g. caused by radiation damage. In general, these studies are motivated by the following central goals:

- Gain a deeper understanding and insights into PandoraPFAs multi-algorithm interplay and the exploitation of shower sub-structure details.
- Validate the confusion-sensitivity for specific PandoraPFA algorithms and parameters. Confirm the expected changes on the basis of confusion type levels and the resulting overall reconstruction performance.
- Investigate the impact of an effectively reduced shower-substructure topology level in the calorimeter systems on the particle flow reconstruction performance.
- Show similar trends for limiting effects in the reconstruction of ILD di-jet simulations and less complex AHCAL prototype two particle data events for further reliability validation of the projected particle flow reconstruction performance.

In a first step, the investigated ILD di-jet simulation samples are introduced and the optimised reconstruction performance with PandoraPFA ILD default settings is validated (Section 9.1). After that, studies of limiting effects and the overall reconstruction performance for different PandoraPFA algorithm settings (Section 9.2) and hit energy thresholds (Section 9.3) are presented. The ILD di-jet results of each section are subsequently compared to observed performance trends for AHCAL prototype two particle data events with the same changes applied.

## 9.1 ILD Di-Jet Samples

In order to study the PandoraPFA reconstruction performance for more complex and dense particle scenarios, simulated ILD di-jet event samples are utilised. For the processing of the simulated raw events, the standardised reconstruction procedure provided within the iLCSoft framework<sup>1</sup> is used. This section briefly introduces the studied samples and summarises the global event reconstruction and selection. Furthermore, the jet energy reconstruction performance for the default ILD detector model, default reconstruction settings and default PandoraPFA settings is reproduced and validated. More details about the individual steps can be found in [68, 159, 160].

### 9.1.1 Simulation, Reconstruction and Event Selection

For the presented studies, the latest iLCsoft version (v02-00-02) is used featuring GEANT4 v10.03.p02 and DD4hep v01-07-02, as a framework to realistically model the full ILD detector and simulate particle interactions and energy depositions. The implemented detector model (ILD\_l5\_o1\_v02) represents the baseline ILD configuration with a SiW-ECAL and AHCAL as calorimeter options (see Section 3.2.2.1) and incorporates detailed descriptions of mechanical support structures, non-instrumented volumes and detector gaps. All ILD simulations in this chapter are based on the QGSP\_BERT physics list. Simulated di-jet events based on  $Z \rightarrow q\bar{q}$  with the  $Z$  boson decaying at rest with twice of the desired single jet energy are chosen for this study<sup>2</sup>. Only the decay into quarks of lighter generations (up, down and strange quarks) is considered. In the simulation, the quarks propagate isotropically back-to-back towards the detector systems. In this simplified environment, higher order effects like radiated initial state photons and the need for dedicated jet clustering algorithms are omitted allowing to benchmark the unbiased jet energy resolution. Five di-jet energies (40 GeV, 91 GeV, 200 GeV, 350 GeV and 500 GeV) are investigated with samples of 5 k events each. The event reconstruction is separated into the following steps:

- Tracking: For each of the tracking systems corresponding hits are digitised to include electronic noise and digitisation effects to mimic realistic data. After that, track segments are reconstructed by pattern recognition algorithms and are consecutively used for track fitting based on Kalman filters [161] to identify curved trajectories of the charged particles in the magnetic field. For each reconstructed track, the momentum and charge of the corresponding particle, the direction and origin are assigned and saved.
- Calorimeter hit digitisation: The simulated energy depositions in the individual calorimeter channels of ECAL, HCAL and muon detector are digitised to achieve realistic hit energy measurements. Within this process technology-specific effects are integrated resembling SiPM-on-tile and silicon-specific readout characteristics. In addition, lower limit thresholds are set and Gaussian electronic noise smearing is applied. More details about the corresponding Marlin processor and validation studies in [88].
- Since it has no effect on the presented studies, the reconstruction for the BeamCAL and FoCAL (see Section 3.2.2.1) is disabled.
- PandoraPFA: The reconstructed tracks and digitised calorimeter hits serve as the input for PandoraPFA. For the ILD event reconstruction the default version of the DDMarlinPandora

<sup>1</sup>See: <https://github.com/iLCSoft/ILDConfig/tree/master/StandardConfig/production>

<sup>2</sup>These samples are typically used to benchmark the PandoraPFA performance with respect to an optimised jet energy resolution by the ILD collaboration [159].

interface processor is used. The full PandoraPFA algorithm chain, as introduced in Section 4.4.3, is applied with calibration constants according to the specific detector model and optimised for the jet energy resolution performance<sup>3</sup>.

- High level reconstruction: Optional algorithms like vertex finding, time-of-flight estimators or particle identification running on the output PFO collections. These algorithms are not used within the scope of this study and are therefore not further discussed.
- Output generation: Different output processor run on the reconstructed LCIO PFO output collections to generate output formats for further analysis e.g. ROOT files. In this context, particularly the LCPandoraAnalysis<sup>4</sup> package is exploited.

Since no background events are overlaid with the simulated di-jet events, the event selection only features a  $|\cos(\theta)| < 0.7$  requirement according to ILD selection standards (see Section 4.4.5). This cut rejects events with jets predominantly in the forward region or in the transition areas between barrel and endcaps. Two example PandoraPFA event displays for reconstructed ILD di-jet events of different energies are visualised in Figure 9.1.

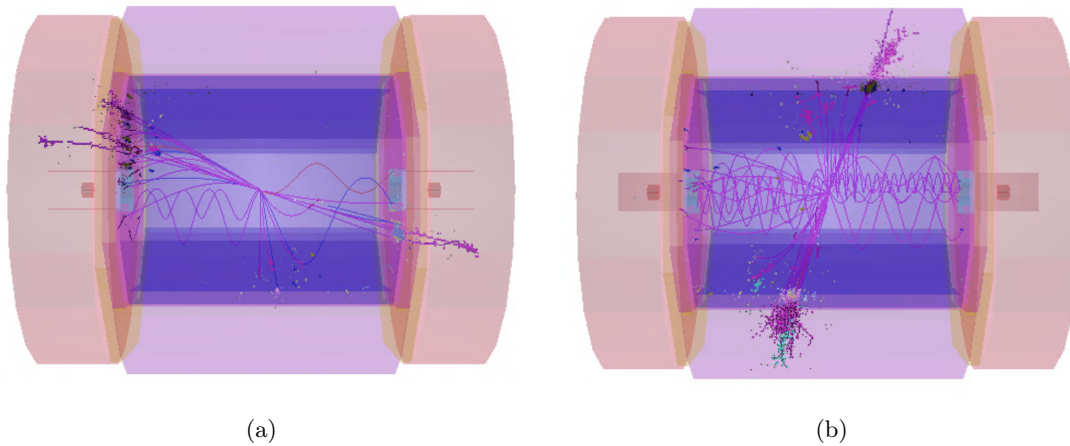


Figure 9.1: Example PandoraPFA events displays for studied ILD back-to-back di-jet events with light quark generations ( $uds$ ): (a) 200 GeV with  $|\cos(\theta)| > 0.7$ . (b) 500 GeV with  $|\cos(\theta)| < 0.7$ .

### 9.1.2 Performance Validation for Default PandoraPFA Settings

To evaluate the performance for the default PandoraPFA settings on the introduced ILD di-jet event samples, the reconstructed mean jet energy and relative jet energy resolution are studied and compared to the results presented in the ILD Interim Design Report [159]. To obtain these quantities, the  $Mean_{90}$  and  $RMS_{90}$  (see Section 4.4.5) are calculated for each sample<sup>5</sup>. Subsequently, the relative single jet energy resolution is determined according to Equation 4.9.

<sup>3</sup>See: <https://github.com/iLCSoft/ILDConfig/blob/master/StandardConfig/production/PandoraSettings/PandoraSettingsDefault.xml>.

<sup>4</sup>See: <https://github.com/PandoraPFA/LCPandoraAnalysis>.

<sup>5</sup>The UdsAnalysis package of iLCsoft is used: <https://github.com/iLCSoft/ILDPerformance/tree/master/UdsAnalysis>

Figures 9.2a and 9.2b show the calculated observables over the corresponding jet energy. A reconstructed jet energy linearity within 4–5% is achieved. Furthermore, the achieved jet energy resolution is better than 4% for  $E_{jet} > 45$  GeV. Both results are well in line with the results presented in the ILD Interim Design Report and satisfy the ILD performance requirements. Based on this performance evaluation, the used software and reconstruction framework is considered validated and suited for the performance studies with different PandoraPFA settings investigated in the following.

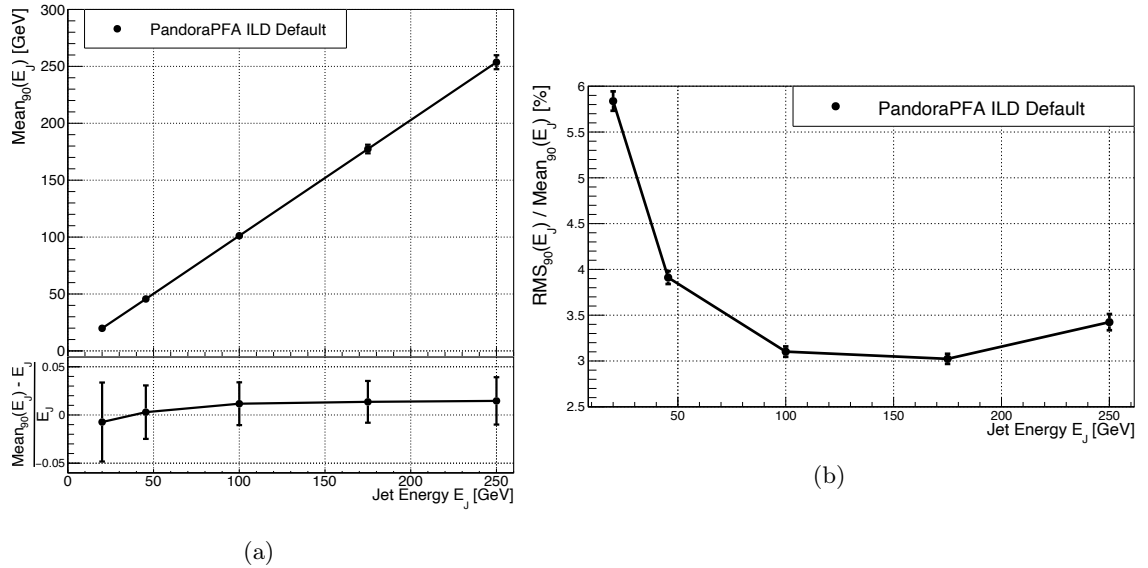


Figure 9.2: Single jet energy reconstruction for simulated ILD di-jet events over jet energy for PandoraPFA ILD default settings: (a) Jet energy linearity. (b) Relative jet energy resolution.

## 9.2 Confusion Sensitive Algorithms and Parameters

As discussed in Section 4.4.3.1, PandoraPFA features a large number of sub-algorithms working recursively. Those algorithms' parameters and sequences are tuned for an optimised reconstruction performance at specific experiments like the ILD at ILC, as presented in the last section. One of the key aspects in this optimisation procedure is the minimisation and energy balancing of the two confusion types. This is required in order to minimise the degrading impact on the jet energy resolution by confusion particularly for jet energies higher than  $\sim 100 - 200$  GeV. Consequently, a change of algorithm parameters or disabling of algorithms is expected to significantly influence the level and balance of confusion energy types and thereby the achievable jet energy resolution. To study the internal algorithm inter-play and understand which algorithm affects which type of confusion to what extent, the most confusion sensitive algorithms are changed or completely disabled. The investigated changes of the PandoraPFA algorithm settings and expected consequences are summarised in the following:

## Disabling of re-clustering algorithms

For this setting all re-clustering algorithms are disabled. Thus, the track momentum to cluster energy comparison and crucial parts of the pattern recognition are omitted to a large extent. Only the topological association and first track to cluster association algorithms are applied after the initial clustering iteration. These algorithms typically merge the initially identified smaller energy clusters to nearby charged clusters with an associated track, resulting in an excess of charged cluster energy in comparison to the associated track momentum on average. Without the broad spectrum of re-clustering algorithms, the merged larger charged clusters are not split up again in a potential re-clustering consideration. As a consequence, a trend towards lost neutral confusion energy is expected.

## Disabling of fragmental removal algorithms

This setting features the disabling of all fragment removal algorithms right before the PFO construction. Since classified neutral clusters, which might actually be parts of the charged shower sub-structures, are not considered to be merged into close-by charged clusters anymore, an excess of doubled counted charged confusion energy is expected.

## Adaption of thresholds within re-clustering algorithms to $|\chi| = 1.5$

For this setting no algorithms are disabled, but the internal threshold of the re-clustering algorithms<sup>6</sup> is changed from  $|\chi| = 2.0 - 3.0$  to  $|\chi| = 1.5$ . As defined by Equation 4.8,  $\chi$  steers the threshold of a potential re-clustering consideration by comparing the agreement of track momentum and the energy of the currently associated cluster. By lowering this threshold, a re-clustering iteration is triggered for smaller track momentum to cluster energy discrepancies. However, splitting up the hits of a charged cluster to effectively reduce its energy is in principle always possible. In contrary the merging of a neutral cluster to effectively increase the charged cluster energy is only possible if this neutral cluster is relatively close-by. Therefore, a slight excess of double counted charged confusion energy is expected for this setting.

### 9.2.1 Impact on Level of Confusion

In the following, the impact of the different PandoraPFA settings on the level and type balance of confusion energy is studied for the ILD di-jet samples. In a similar approach as for the AHCAL prototype studies in Section 8.4.3.2 the Monte Carlo truth information<sup>7</sup> is utilised, to check for each calorimeter hit the correct or incorrect classification as charged or neutral by PandoraPFA.

The calculated mean fraction of lost neutral and double counted charged confusion energy with respect to the full event energy over the di-jet energy for the different PandoraPFA settings are presented in Figure 9.3. Complementary plots for correctly reconstructed energies can be found in E.1. For the different PandoraPFA settings the two types of confusion show opposite behaviour: While the lost neutral confusion energy is higher for the no re-clustering setting in comparison to the default setting, the double counted charged energy behaves vice versa. For the no fragment removal setting the opposing trend is observed. Lastly, the  $|\chi| = 1.5$  setting shows only a slight

<sup>6</sup>Default value depending on the specific re-clustering algorithm.

<sup>7</sup>Based on the LCIO::MCPARTICLE collection [http://lcio.desy.de/v02-09/doc/doxygen\\_api/html/classEVENT\\_1\\_1MCParticle.html](http://lcio.desy.de/v02-09/doc/doxygen_api/html/classEVENT_1_1MCParticle.html)

deviation from the default setting towards double counted charged energy. These observations agree well with the expectations for the confusion type trends discussed in the last section.

Furthermore, an increase for both types of confusion energy over the di-jet energy for all investigated settings is observed. This agrees well with the expectation of more difficult reconstruction scenarios based on increasing particle densities and multiplicities in higher energetic jets. Whereas the ratio to the default setting is almost constant within for the no fragment removal and the  $|\chi| = 1.5$  setting, it significantly changes with increasing di-jet energy for the no re-clustering setting for both confusion types. This reflects the importance of the re-clustering algorithms to disentangle individual particles in a particle environment, which becomes denser with higher jet energies. Lastly, for the lowest jet energies the different settings seem to play a minor role for the individual confusion types indicating an efficient initial clustering algorithm and the reduced need for re-clustering in less dense particle environments. Only the fragment removal algorithms seem to play an important role to merge misidentified neutral clusters back to close-by charged clusters.

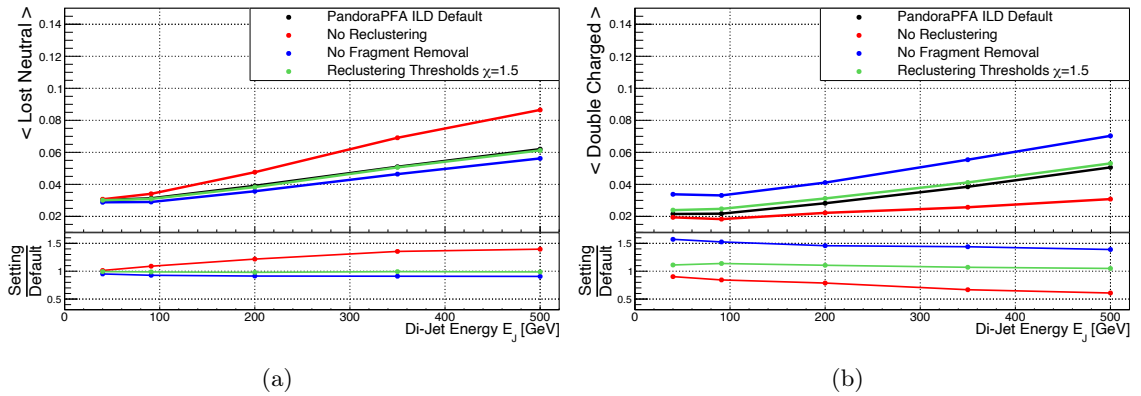


Figure 9.3: Mean fraction of confusion energy in event over di-jet energy of simulated ILD di-jet events for different PandoraPFA algorithm settings: (a) Lost neutral confusion energy. (b) Double counted charged confusion energy.

The mean absolute confusion type balance and the total level of confusion for the different PandoraPFA settings are presented in Figure 9.4a and 9.4b. Over all di-jet energies the obtained results evaluate that the PandoraPFA ILD default settings are indeed optimised with respect to the combination of confusion balance and total fraction of confusion energy in the event. For the no re-clustering setting an increasing mean energy deficit of up to 30 GeV for di-jet energies of 500 GeV is observed caused by the excess of lost neutral confusion energy. The total mean fraction of confusion is largely unaffected and agrees within 5% to the default settings over all di-jet energies. In contrary for the no fragment removal setting an increasing mean energy excess of up to 8 GeV for di-jet energies of 500 GeV is found caused by the excess of double counted charged confusion energy. The mean confusion type balance is better in comparison to the no re-clustering setting, but the mean total confusion fraction is 10 – 20% higher than for the default settings. Finally, the  $|\chi| = 1.5$  setting shows a comparable performance to the default settings: The confusion energy types are balanced slightly better by up to 1 GeV on average, while the mean total confusion fraction is increased by 2 – 3% with respect to the default settings. The impact of these observed trends on the jet energy reconstruction performance for the different PandoraPFA settings is investigated next.

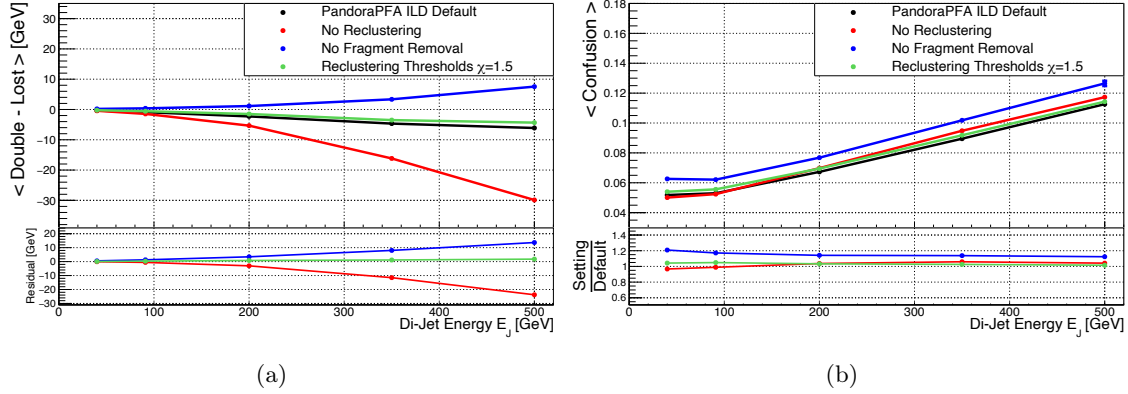


Figure 9.4: Confusion observables over di-jet energy of simulated ILD di-jet events for different PandoraPFA algorithm settings: (a) Mean absolute difference of double counted charged and lost neutral confusion energy. (b) Mean fraction of confusion energy in events.

### 9.2.2 Impact on Jet Energy Linearity and Resolution

The mean jet energy and relative jet energy resolution, calculated as in Section 9.1.2, for the different PandoraPFA settings are plotted over the jet energy in Figures 9.5a and 9.5b.

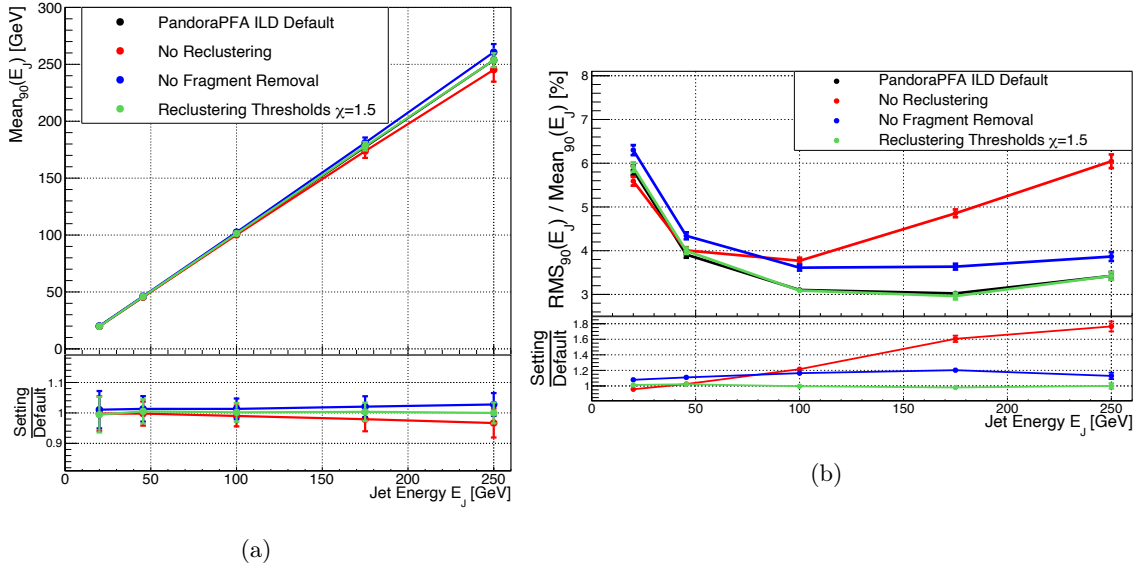


Figure 9.5: Energy reconstruction of single jets for simulated ILD di-jet events over jet energy for different PandoraPFA settings: (a) Jet energy linearity. (b) Relative jet energy resolution.

In general, trends of an energy deficit for the no re-clustering setting and an energy excess for the no fragment removal setting with increasing jet energy is observed, agreeing with the trends on

confusion level as presented in the last section. While the deviation from default setting is smaller than 2% for jet energies of 20 GeV, it increases up to 5% for jet energies of 250 GeV. As expected, the  $|\chi| = 1.5$  setting agrees well with the default settings over the full energy range.

With respect to the relative jet energy resolution, the  $|\chi| = 1.5$  setting agrees with the default settings within the statistical uncertainties. Furthermore, for the no fragment removal setting a degradation of the jet energy resolution by 10–20% is observed over all jet energies. Lastly, for the no re-clustering setting an increasing degradation of the jet energy resolution with increasing jet energy up to 80% for 250 GeV is found underlining the importance of the re-clustering algorithms in dense and high multiplicity particles environments to keep the overall confusion on a considerable level. In general, the observed trends for the jet energy resolution agree with the expectations derived from the observations of the confusion type balance and total confusion level.

### 9.2.3 Comparison to AHCAL Prototype Data

In the following, the same algorithm changes in PandoraPFA are studied for less complex scenarios based on beam test data acquired with the AHCAL prototype. For this purpose, representative sub-samples of 10 GeV pseudo-neutral hadrons overlaid with 30 GeV or 60 GeV charged pions at radial distances of 0–50 mm and 125–175 mm are generated from the June 2018 beam test data based on the same selection criteria and with the same procedure as introduced in Section 8.1.3. For each scenario a sample of 10 k events is investigated.

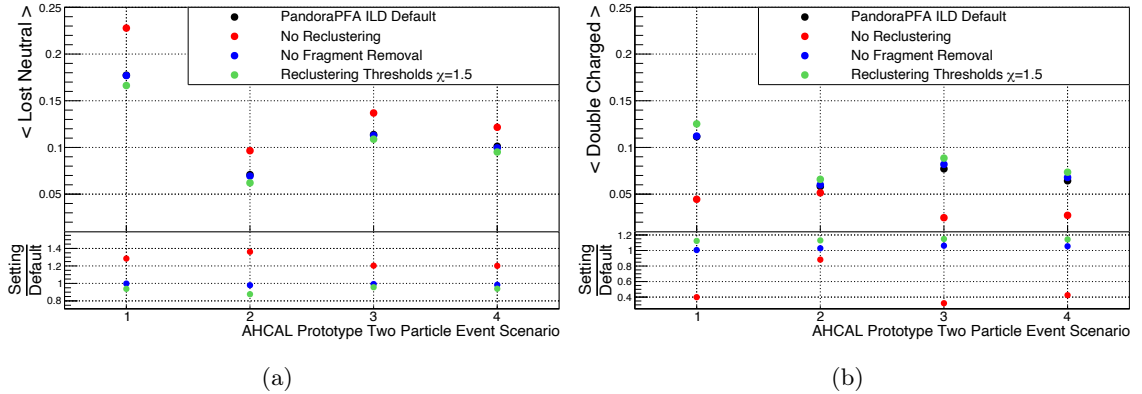


Figure 9.6: Mean fraction of confusion energy over AHCAL two particle event scenario for different PandoraPFA algorithm settings: **(a)** Lost neutral energy. **(b)** Double counted charged energy.  
 1: 10 GeV  $h^0$  + 30 GeV  $\pi^-$ ,  $r = 0 - 50$  mm    2: 10 GeV  $h^0$  + 30 GeV  $\pi^-$ ,  $r = 125 - 175$  mm  
 3: 10 GeV  $h^0$  + 60 GeV  $\pi^-$ ,  $r = 0 - 50$  mm    4: 10 GeV  $h^0$  + 60 GeV  $\pi^-$ ,  $r = 125 - 175$  mm

Figure 9.6 shows the mean fraction of lost neutral energy and double counted charged confusion energy versus the two particle AHCAL event scenarios for the different PandoraPFA settings. With respect to the default setting, for the no re-clustering setting a trend towards higher lost neutral confusion energy and less double counted charged confusion energy is observed. Both, the no fragment removal and  $|\chi| = 1.5$  setting show the opposite trend. However, the no fragment removal setting has not a large impact and agrees with the default setting within 5%. This is based on the fact that for the AHCAL two particle events on average not many misidentified neutral clusters are located close-by to the charged cluster in contrast to the ILD di-jet events.

By comparing the results for the different 10 GeV + 30 GeV scenarios, it can be concluded that an increased radial shower distance helps to reduce both types of confusion energies by roughly a factor 2 for all investigated PandoraPFA settings. For the 10 GeV + 60 GeV scenario the improvement is significantly smaller. This is caused by the spatially more spread out 60 GeV charged pion shower topology connecting charged and neutral shower sub-structures to a higher degree and thereby causing a higher fractional level of both confusion energies on average, even at larger radial shower distances.

It can be concluded that for both confusion types the same trends as for the ILD di-jet events are observed for the investigated different PandoraPFA settings. The same agreement of trends is as well observed for the mean confusion type balance and mean fraction of confusion energy in the event, which are depicted in Figure [E.3a](#) and [E.3b](#).

### 9.2.4 Conclusions

In the presented studies, the qualitatively expected trends for the different types of confusion, the confusion type balance and the total level of confusion for the changed PandoraPFA settings are quantitatively validated. The opposite trends towards an excess of lost neutral or double counted charged confusion energy for the no re-clustering and the no fragment removal setting demonstrate the individual PandoraPFA algorithm designs aiming to reduce a specific type of confusion. Furthermore, the impact on the reconstructed mean jet energy and the relative jet energy resolution aligns well with the expectations for the different algorithm settings and the observed confusion trends. While, the  $|\chi| = 1.5$  setting has a negligible impact in comparison to the default settings, the enhancement of lost neutral confusion energy and double counted charged confusion energy for the no re-clustering and no fragment removal setting impacts the reconstructed mean jet energy and leads to a significant degradation of the relative jet energy resolution.

As expected, the largest degradation is observed for the no re-clustering setting at highest jet energies. This is based on the fact, that the disabled comparison of track momentum to cluster energy and the pattern recognition approaches are most crucial in these dense and high particle multiplicity environments. Consequently, this validates that the multi-algorithm chain of PandoraPFA is particularly tuned and optimised for this type of dense scenarios, validated as well by performance for the PandoraPFA default settings. By disabling or changing specific parts in this algorithm chain, this study has gained a detailed insight into the algorithm interplay and connected the impact of specific algorithm classes on limiting effects of the reconstruction.

Lastly, the same trends for confusion type parameters are observed for the reconstruction of representative two particle AHCAL prototype data events with the same applied PandoraPFA settings. The achieved results demonstrate that the limiting effects of the PandoraPFA reconstruction are well understood and behave similar on different levels of complexity and are reproducible on prototype data. This is considered as a further evaluation of the reliability of performance projections for a future lepton collider experiment with special respect to the achievable jet energy resolution.

## 9.3 Hit Energy Thresholds

A highly granular calorimeter system operated in a high radiation experimental environment, like the CMS HGCAL in the context of the HL-LHC [\[112\]](#), suffers from increasing radiation damage over its lifetime. For a SiPM-on-tile based calorimeter system this radiation damage is expected lead to an increase of the dark count rate of the SiPMs for example. Different studies have

shown these degrading effects for the SiPM characteristics after neutron irradiation in the order of  $\Phi_{eq} = 10^{11} - 10^{14} \text{ cm}^{-2}$  [162].

One option to be able to operate individual calorimeter channels sufficiently above the increased noise levels is to increase the hit energy thresholds on channel level. However, by increasing the hit energy thresholds not only noise but also low energy physics hits might be suppressed. This consequently reduces the number of triggered calorimeter channels in a physics event on average, as illustrated in Figure 9.7 for the example of a simulated 500 GeV di-jet event in ILD. Depending on the level of the threshold, this could have a large impact on the shower sub-structure topology resolved by highly granular calorimeters and reduces the total reconstructed event energy by the calorimeter systems. While the lost energy information can mostly be regained with a dedicated energy re-calibration, the topological information can not be recovered. However, detailed topology information of the shower sub-structure is one of the crucial requirements for achieving a high reconstruction performance with pattern-recognition based particle flow algorithms like PandoraPFA. Altogether these assumptions motivate to investigate if a highly granular calorimeter system in a high radiation environment is capable of achieving adequate particle flow reconstruction performance over its full time of operation.

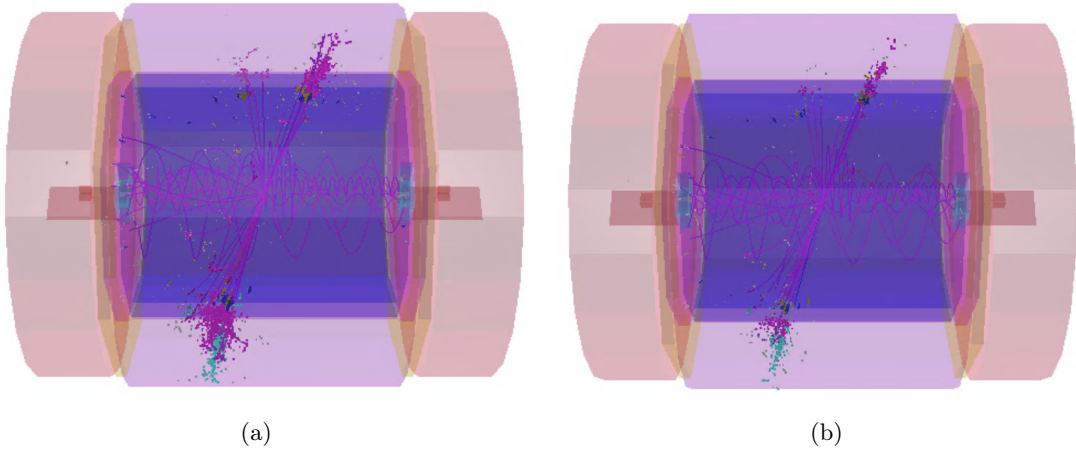


Figure 9.7: Example event displays of studied ILD back-to-back di-jet events for different hit energy thresholds: **(a)** Default (ECAL: 0.5 MIP, HCAL: 0.3 MIP). **(b)** ECAL and HCAL: 3 MIP.

In order to simulate the consequences of increased noise levels on calorimeter channel level, the hit energy thresholds for the introduced ILD di-jet samples are increased and subsequently the impact on the PandoraPFA reconstruction performance is investigated. Next to the impact on the confusion parameters, the achieved jet energy linearity and relative jet energy resolution is studied for increased hit energy thresholds of 1 MIP, 2 MIP and 3 MIP (both ECAL and HCAL) in comparison to the ILD default thresholds (ECAL: 0.5 MIP, HCAL: 0.3 MIP) in this section. However, to compensate for the loss of energy information, an internal energy re-calibration is mandatory to allow e.g. a fair track momentum to cluster energy comparison within PandoraPFA.

### 9.3.1 PandoraPFA Re-Calibration

As part of the iLCsoft framework, the LCCalibration package<sup>8</sup> offers a fully automated calibration procedure for particle flow designed multi purpose detector systems like ILD. The package features the calibration of the following classes of energy constants for the different sub-detector systems:

1. MIP scale calibration: Extraction of constants for conversion of simulated energy depositions to units of MIP.
2. GeV scale calibration: Similar procedure as for MIP scale calibration but for conversion to units of GeV based on energy depositions of photons in ECAL and neutral hadrons in HCAL.
3. GeV to MIP scale calibration for PandoraPFA: Extraction of GeV to MIP factors based on muon samples reconstructed with previously determined GeV calibration factors.
4. PandoraPFA EM scale calibration: Determination of electromagnetic energy scale for electron and photon PFOs.
5. PandoraPFA HAD scale calibration: Determination of hadronic energy scale for charged and neutral hadron PFOs.
6. PandoraPFA software compensation calibration: Determination of the weights for PandoraPFA internal software compensation for hadrons. More details in [108].

Except for step 1 and 6, the calibration steps are implemented recursively to adapt the calibration constants until a desired agreement (default: 1%) with the MC truth energy is accomplished. For the different steps of the calibration procedure samples of single muons, photons and  $K_L^0$  with 20k events each, simulated with the same physics list and detector model are recommended. More detailed descriptions of the individual calibration steps can be found in [107, 163].

The calorimeter hit energy threshold is implemented in the DDCaloHitCreator of the interface processor DDMarlinPandora right before a hit is potentially read in into PandoraPFA. Therefore, the calibration constants determined in step 1-3 are unaffected by increased hit energy thresholds and only re-calibration steps 4 and 5 are mandatory. The PandoraPFA internal software compensation weights are not re-calibrated in the scope of this work, since the effect on the track momentum to cluster energy comparison in PandoraPFA is expected to be small.

The calibration samples are simulated with the QGSP\_BERT physics list, the ILD\_15\_o1\_v02 detector model and with the same software framework as introduced for the ILD di-jet samples in Section 9.1. For the recursive calibration routines an agreement of 2% is chosen for a fast convergence of the individual steps. In a first step, calibration steps 1-3 are performed for each of the chosen hit energy thresholds to evaluate the independence of the calibration constants and demonstrate reproducibility with respect to the ILD default constants<sup>9</sup>. For all threshold settings, calibration constants agreeing within a per mille to the ILD default constants are obtained. Therefore, for all threshold settings the ILD default calibration constants according to step 1-3 are used, which are summarised in Table E.1. The obtained calibration constants for calibration steps 4 and 5 are summarised in Table 9.1 for the different hit energy thresholds. It can be observed that with increasing hit energy threshold the absolute values of all calibration constants increase, which reflects the expected need for lost hit energy compensation. Figure 9.8 illustrates the tuned

<sup>8</sup>See: <https://github.com/iLCSoft/LCCalibration/tree/master/doc>

<sup>9</sup>See in ILD default calibration file: [https://github.com/iLCSoft/ILDConfig/blob/master/StandardConfig/production/Calibration/Calibration\\_ILD\\_15\\_o1\\_v02.xml](https://github.com/iLCSoft/ILDConfig/blob/master/StandardConfig/production/Calibration/Calibration_ILD_15_o1_v02.xml)

plots of the reconstructed photon PFO energy in the ECAL and the reconstructed neutral hadron PFO energy in ECAL and HCAL for the hit energy threshold of 3 MIP with the final calibration constants applied.

Calibration Constant	Default	1 MIP	2 MIP	3 MIP
PandoraEcalToEMScale	1.0	1.0249	1.089	1.169
PandoraHcalToEMScale	1.0	1.0249	1.089	1.169
PandoraEcalToHadBarrelScale	1.173	1.244	1.425	1.639
PandoraEcalToHadEndcapScale	1.173	1.244	1.425	1.639
PandoraHcalToHadScale	1.028	1.134	1.330	1.520

Table 9.1: Obtained calibration constants of PandoraPFA internal energy scales for increased hit energy thresholds based on ILD model ILD\_l5\_o1\_v02 and QGSP\_BERT physics list.

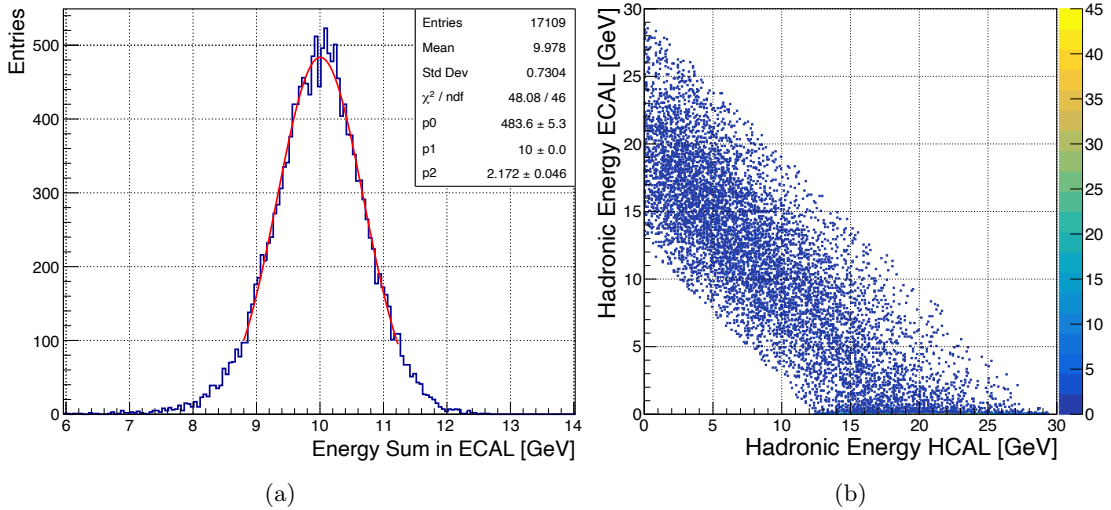


Figure 9.8: PandoraPFA EM and HAD scale calibration for 3 MIP internal hit energy threshold. (a) Electromagnetic PFO energy of 10 GeV  $\gamma$  sample in the ECAL. (b) Hadronic PFO energy of 20 GeV  $K_L^0$  sample deposited in the HCAL over the deposited energy in the ECAL.

### 9.3.2 Impact on Level of Confusion

With the same method as introduced in Section 9.2.1, the mean fraction of confusion energy for the individual confusion types is extracted for the ILD di-jet samples reconstructed with increased hit energy thresholds and presented in Figure 9.9. Complementary plots showing the mean fraction of correctly reconstructed energies can be found in E.4. First of all, for all investigated hit energy thresholds an increasing confusion level is observed for increasing di-jet energy as extensively discussed in Section 9.2.1. In comparison to the default thresholds, the mean fraction of confusion

energy for both types is on the same level or 10-20 % lower for the thresholds of 1 MIP and 2 MIP over all di-jet energies. For the threshold of 3 MIP, however, the trend inverts and a 10-40 % higher fraction of confusion energy is observed for both confusion types for all di-jet energies higher than 200 GeV.

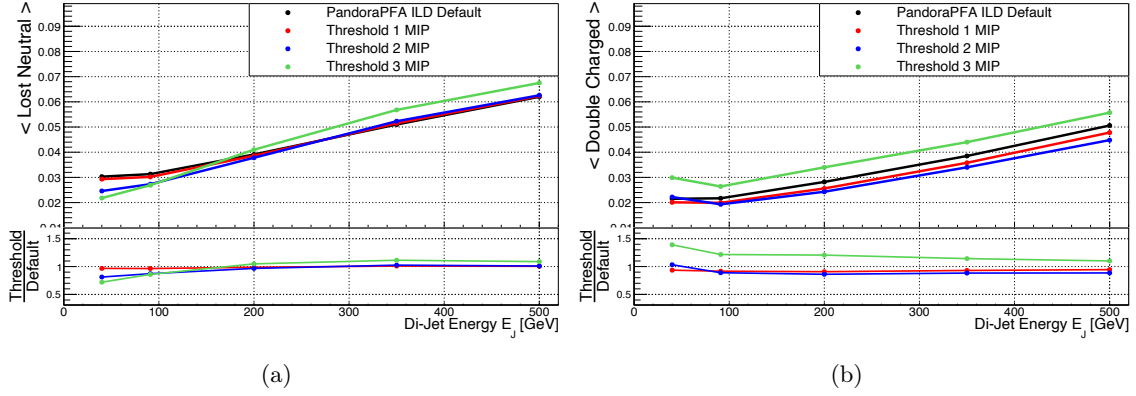


Figure 9.9: Mean fraction of confusion energy over di-jet energy of simulated ILD di-jet events for different hit energy thresholds: (a) Lost neutral energy. (b) Double counted charged energy.

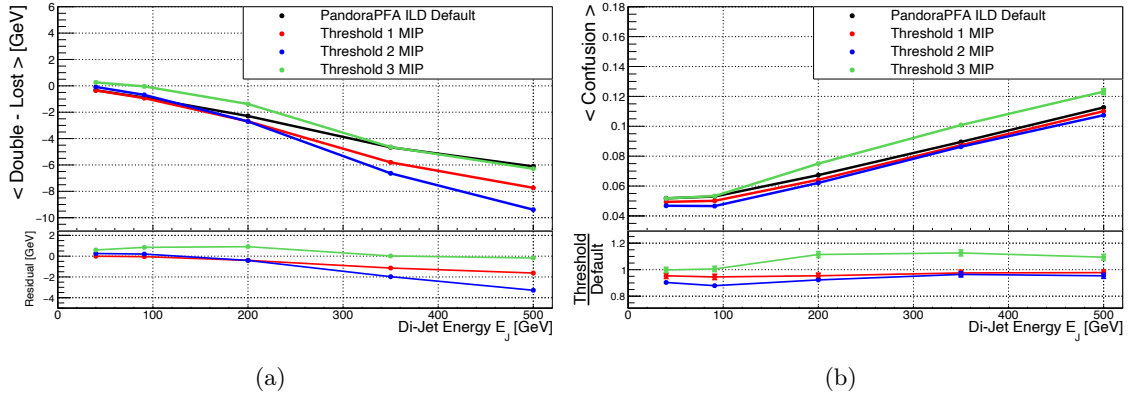


Figure 9.10: Confusion observables over di-jet energy of simulated ILD di-jet events for different hit energy thresholds: (a) Mean absolute difference of double counted charged and lost neutral confusion energy. (b) Mean fraction of confusion energy in events.

This inverted trend is preserved if both types of confusion are combined into the mean absolute confusion type balance and the total mean confusion energy fraction, as depicted in Figure 9.10. While for the thresholds of 1 MIP and 2 MIP an increasing trend towards lost neutral confusion energy with increasing di-jet energy is observed, for the 3 MIP threshold a comparable or up to 1 GeV better confusion type balance with respect to the default settings is observed. The overall determined imbalances are relatively small (maximum:  $\sim 9.5$  GeV) in comparison to the studies with changed PandoraPFA settings (maximum:  $\sim 30$  GeV). Furthermore, for the 1 MIP and 2 MIP

threshold settings the total confusion fraction is up to 10 % lower compared to the default settings, in contrast to the 3 MIP threshold, for which an increasing mean confusion fraction up to 15 % is observed for di-jet energies higher than 100 GeV.

It can be summarised that the confusion type imbalance suffers and the total fraction of confusion improves for the 1 MIP and 2 MIP thresholds, while for the 3 MIP threshold the trend is inverted.

### 9.3.3 Impact on Jet Energy Linearity and Resolution

The jet energy linearity and relative jet energy resolution for the ILD di-jet samples reconstructed with different hit energy thresholds are depicted in Figure 9.11a and 9.11b.

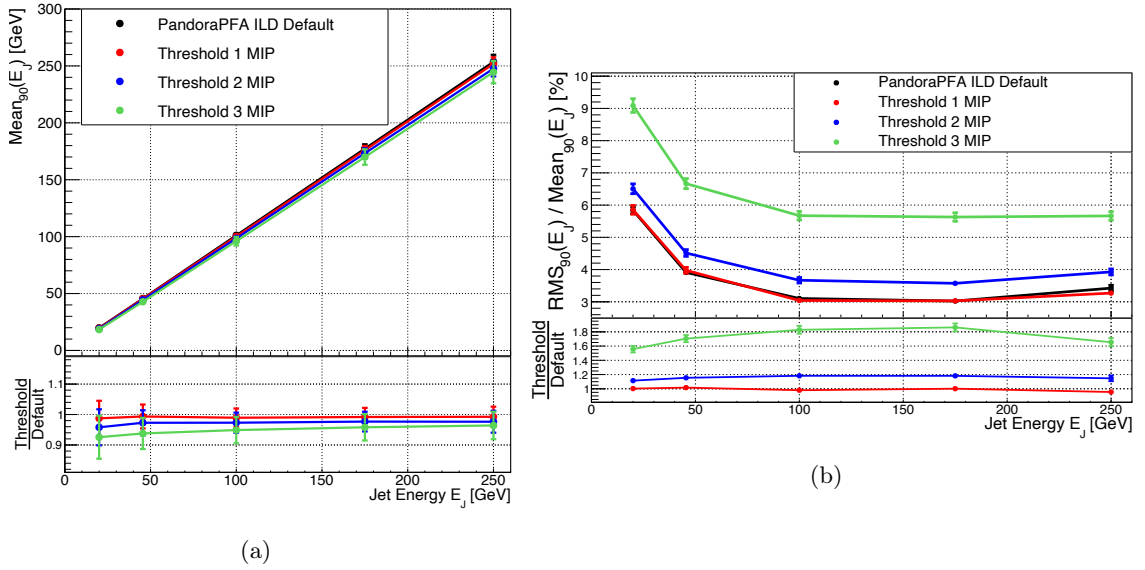


Figure 9.11: Energy reconstruction of individual jets from simulated ILD di-jet events over jet energy for different hit energy thresholds: (a) Jet energy linearity. (b) Relative jet energy resolution.

With the re-calibration procedure a jet energy linearity within 8 % is achieved over all thresholds, close to the 5 % level observed for the ILD default hit energy thresholds. Whereas the 1 MIP threshold setting agrees within 1 % to the default threshold setting, for the threshold settings of 2 MIP and 3 MIP the linear energy up-weighting of the remaining hits by simple calibration factors is not completely sufficient, particularly for the lowest jet energies. This is mainly caused by the number of hits below the respective hit energy thresholds, which does not scale linearly with decreasing jet energy and is fractionally larger for the lowest jet energies.

The increased energy threshold of 1 MIP does not have a degrading impact on relative jet energy resolution, since it agrees with the default threshold setting within the statistical uncertainties. For the 2 MIP threshold an almost constant relative degradation of ~15-20 % and for the 3 MIP threshold a relative degradation of ~50-80 % of the relative jet energy resolution is observed. These observed levels of performance degradation are evaluated and discussed in detail in Section 9.3.5.

### 9.3.4 Comparison to AHCAL Prototype Data

Lastly, the impact of different hit energy thresholds on the reconstruction performance is studied for the less complex AHCAL prototype data events. The impact of increased hit energy thresholds on the event topologies is qualitatively visualised for an overlaid 10 GeV pseudo-neutral and a 30 GeV charged pion shower in Figure 9.12. The number of shower hits is significantly reduced and mostly the electromagnetic shower core and a few high energy satellite hits are left for an increased hit energy threshold of 3 MIP. In addition, most hits of the primary ionising MIP track before the charged hadron shower start layer are cut. As a consequence, for up to 20% of events a non working initial track to cluster association is observed resulting in a maximum of double counted charged confusion energy since all hits are classified as neutral. Due to the application of the same event selection criteria as introduced in Section 8.1, these events are rejected within the presented study.

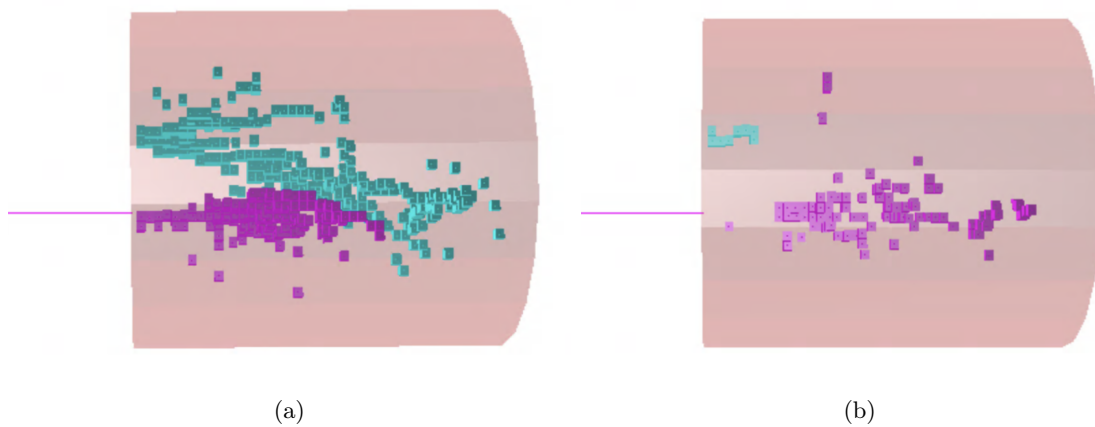


Figure 9.12: Example event displays of an AHCAL prototype data event featuring a 10 GeV pseudo-neutral hadron and a 30 GeV charged pion shower reconstructed with different hit energy thresholds: (a) Default (0.5 MIP). (b) 3 MIP.

Similar as for the ILD di-jet study, an energy re-calibration of the PandoraPFA internal energy scale is required to compensate for the decreasing event energy. According to the calibration procedure, as introduced in Section 8.2.4, only the hadronic energy scale within the AHCAL needs to be re-calibrated for the different hit energy thresholds. Since a non linear behaviour is expected for the dependency of the number of hits below a certain hit energy threshold and the energy of the particle, simulation samples of both, 10 GeV and 30 GeV,  $K_0^L$ , each featuring 10 k events, are used for the calibration. The calibration factor is tuned by minimising the deviation of the mean, extracted by a Gaussian fit to the neutral PFO energy distribution, and the truth  $K_0^L$  energy for both energies simultaneously. The tuned neutral PFO energies for the hit energy threshold of 1 MIP are presented in Figure 9.13 and the calibration results for all hit energy thresholds are summarised in Table 9.2. In general a re-calibration of the mean energy within 10% to the truth energy is achieved. Only for the 3 MIP threshold the achieved re-calibration is less accurate (-16%) for 10 GeV due to the large number of low energy hits being removed.

For this study the full set of two particle data samples, introduced in Section 8.1.4.2, are reconstructed with the same increased hit energy threshold as for the ILD di-jet study. As an observable

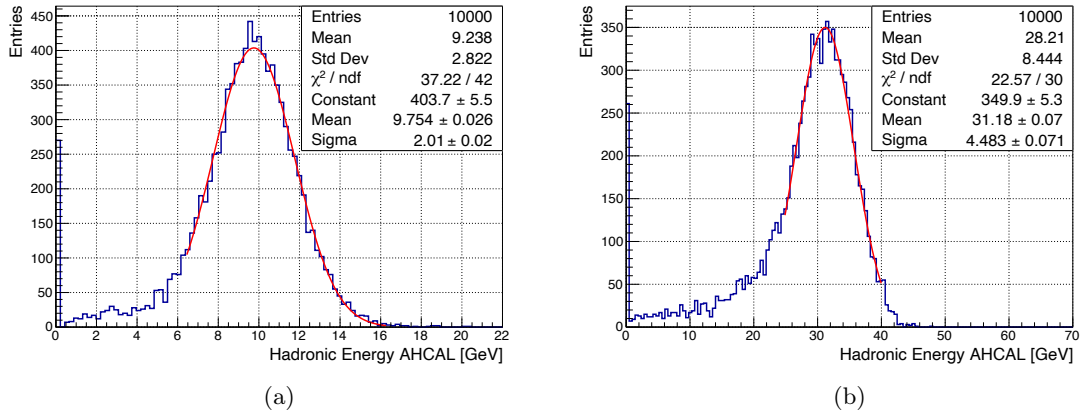


Figure 9.13: Reconstructed neutral PFO energy distributions of  $K_0^L$  samples in the AHCAL prototype for tuning PandoraPFA hadronic energy scale constant (PandoraHcalToHadScale) for 1 MIP hit energy threshold simultaneously for: (a) 10 GeV. (b) 30 GeV.

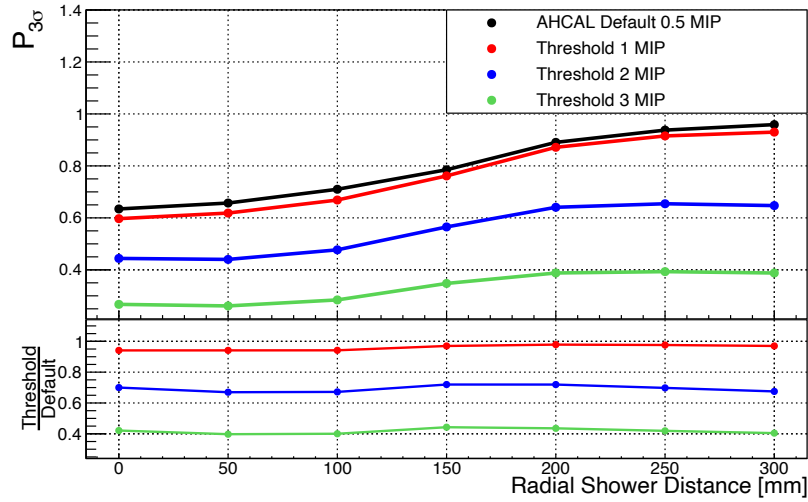
	Default	1 MIP	2 MIP	3 MIP
PandoraHcalToHadScale	1.030	1.085	1.262	1.431
Deviation of Mean from 10 GeV [%]	-0.9	-2.5	-7.7	-16.0
Deviation of Mean from 30 GeV [%]	3.6	3.9	5.6	3.2

Table 9.2: Obtained PandoraPFA hadronic energy scale calibration constants for AHCAL data events reconstructed with increased hit energy thresholds.

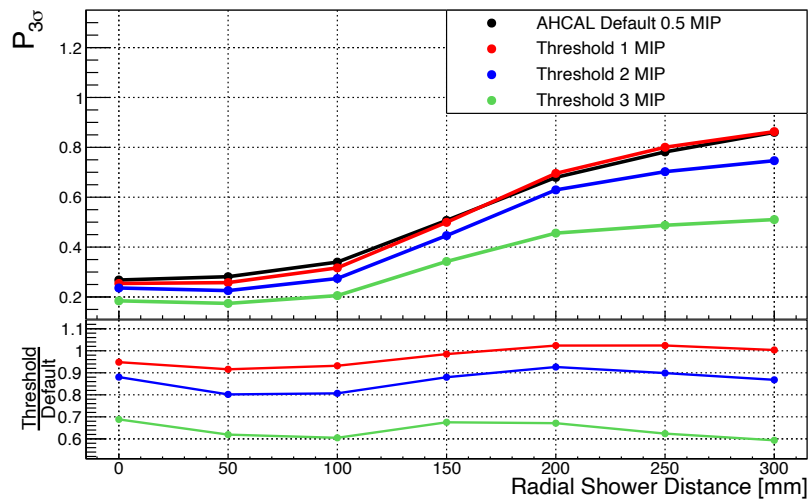
to compare the PandoraPFA reconstruction performance between the different hit energy thresholds for the AHCAL two particle events, the  $3\sigma$  recovery probability of the pseudo-neutral hadron energy, as defined in Section 8.4.2, is chosen. It incorporates the impacts by the two types of confusion equally and the comparison of neutral calorimetric input and neutral PFO output is unaffected by the energy calibration for the pseudo-neutral hadrons. The obtained  $3\sigma$  recovery probability over the radial distance to the charged pion shower for the different hit energy thresholds is presented for both energy scenarios in Figures 9.14a and 9.14b.

For both energy scenarios it can be observed, that the  $3\sigma$  recovery probability degrades with increasing hit energy threshold over all radial shower distances. It is observed that the 1 MIP threshold setting agrees with the default threshold setting within 10% for all investigated scenarios. The relative degradation for the 2 MIP threshold corresponds to 30 – 45% and for the 3 MIP threshold up to more than a factor 2 worse recovery probabilities are observed over the full shower distance range. One can conclude that the two particle separation becomes more difficult with increasing hit energy threshold level agreeing with the performance degradation trends observed in the ILD di-jet study.

Furthermore, the obtained results show that the recovery probability improves with radial shower distance for all hit energy threshold settings proving that shower separation is still helps in recovering the pseudo neutral hadron energy. However, even for the largest shower separations the



(a)



(b)

Figure 9.14:  $3\sigma$  recovery probability of 10 GeV pseudo neutral hadron in the vicinity of a 10 GeV (a) or 30 GeV (b) charged pion shower over radial shower distance for different hit energy thresholds.

recovery probability is significantly lower for the hit energy thresholds of 2 MIP and 3 MIP in comparison to the default threshold setting. This demonstrates that spatial shower separation alone does not compensate the massive loss of shower-substructure topology information degrading the reconstruction performance of PandoraPFA.

### 9.3.5 Conclusions

The presented studies show that the simulated loss of topology information in the shower sub-structure can be compensated to a large extent by the powerful implementation of PandoraPFA. For an increased hit energy threshold of 1 MIP no significant degradation in comparison to the default threshold setting (ECAL: 0.5 MIP, HCAL: 0.3 MIP) is observed for the ILD jet energy resolution. For the case of the CMS HGCAL, a required increase of the hit energy threshold level higher than 1 MIP close to end of the detectors lifetime is a pessimistic estimation. Therefore, one can conclude that with a powerful particle flow algorithm like PandoraPFA the jet energy reconstruction performance is not expected to significantly degrade by this effect.

For higher hit energy thresholds of 2 MIP and 3 MIP a non negligible degradation of the relative jet energy resolution is observed. With an energy threshold this high in both, ECAL and HCAL, basically all MIP like primary ionising hits before the charged hadrons start showering and within the shower sub-structure are cut and mostly the electromagnetic shower core remains. On the basis of this assumption, two observations are positively surprising. Firstly, that PandoraPFA is on average still capable to form appropriate track to charged cluster associations. Secondly, that the large loss of topology information seems to be compensated by the algorithm chain to a large extent. This is reflected by the obtained relative jet energy resolution, which relatively degrades only by  $\sim 20\%$  for the 2 MIP and  $\sim 60 - 80\%$  for the 3 MIP thresholds with respect to the default threshold setting. It is suspected that for the hit energy threshold of 3 MIP a PandoraPFA internal limit is exceeded, where specific forced clustering algorithms implemented within PandoraPFA<sup>10</sup> are activated within the reconstruction. These algorithms are designed to intervene at a very unsatisfying level of topological associations and track momentum to cluster energy agreement. As a last instance, they force a calorimeter hit clustering only based on the agreement to the track momentum. A potential indication for this internally changed reconstruction strategy is observed for the studied threshold settings of 2 MIP and 3 MIP with respect to the found trends for the confusion type balance and the total confusion level: Both observables show an inverted trend in comparison to the default threshold by increasing the hit energy threshold from 2 MIP to 3 MIP.

With the same hit energy thresholds applied to the AHCAL prototype data, the same trends for the PandoraPFA performance degradations are observed for less complex scenarios and for real particles showers. Again, these reproduced trends further validate the reliability of performance projections based on simulated shower sub-structure details for future lepton collider experiments.

Lastly, the obtained results raise several questions with respect to the interplay of the particle flow algorithm and the highly granular calorimeter systems. Firstly, if optimised detector effects like e.g. highly suppressed noise levels or ultra high granularity could potentially be less crucial for the achievable reconstruction performance than a highly optimised and powerful particle flow algorithm. Over-engineering of individual detector components or over-designing the level of granularity could be avoided, saving development and production costs, if an optimised particle flow algorithm would compensate the degradation of the reconstruction performance. Secondly, if the provided high level topology information by the highly granular calorimeters could be further exploited by PandoraPFA. On the one hand, topology based alternatives for the forced clustering algorithms might provide room for further improvements. On the other hand, potential improvements could be achieved by adding topology-based criteria within the track to cluster comparison iterations, like tree-structure developing probabilities<sup>11</sup> or comparisons to average 3-dimensional hadronic shower profiles.

<sup>10</sup>See: <https://github.com/PandoraPFA/LCContent/blob/master/include/LCclustering/ForcedClusteringAlgorithm.h>

<sup>11</sup>Similar to the approaches of APRIL PFA developed for a semi-digital calorimeter system [\[110\]](#).

# 10 Summary, Conclusions and Outlook

## 10.1 Summary and Conclusions

Future lepton collider experiments can play an important role in high precision measurements and aim to complement measurements at the high energy frontier, such as the LHC experiments. In order to reach the ambitious precision levels in such experiments, like ILC or CLIC, an unprecedented jet energy resolution of 3 – 4% is required. Key item to achieve this goal is to utilise the particle flow reconstruction concept and optimised detector designs accordingly. Particle flow algorithms (PFAs) aim to reconstruct each individual particle in a jet and use the energy measure of the sub-detector providing best resolution. Thus, in principle for all charged hadrons in a jet the much preciser momentum measure of the tracker can be exploited omitting the intrinsically poor energy resolution of the hadronic calorimeter systems. However, wrong association of charged and neutral particle showers by those algorithms gives rise to an intrinsic limit of this reconstruction concept in form of the confusion term. To allow for an efficient particle flow reconstruction performance, stringent requirements on the detector systems are set. Next to an excellent momentum resolution of the tracking system, highly granular calorimeters are crucial. Extensive simulation studies have shown that the ambitious jet energy resolution is reachable with the concept of particle flow reconstruction and the employment of optimised detector systems. However, the projected performance is highly dependent on the sub-structure details of the simulated particle showers, revealed by the highly granular calorimeters and exploited by the pattern recognition of the PFAs.

For the potential employment of a  $\sim 8$ M channel hadronic calorimeter in the ILD detector system, the CALICE collaboration has developed the highly granular Analog Hadron Calorimeter (AHCAL) concept. The latest AHCAL prototype is a steel sampling calorimeter with  $\sim 22\,000$  readout channels consisting of  $3\text{ cm} \times 3\text{ cm}$  scintillating tiles coupled to silicon photomultipliers (SiPMs). During extensive beam test campaigns at the SPS CERN in 2018, the AHCAL prototype has been commissioned and operated in muon, electron and pion beams of energies between 10 – 200 GeV recording several ten million of individual particle events.

In the first part of this thesis, the prototype energy calibration is presented including response uniformity and stabilities studies. The focus in this thesis is set on the pedestals and MIP constants, extracted by a fully automatised and robust calibration routine on the basis of recorded muon beam test data, implemented by the author. In total, more than 99.9% of the channels are found to be fully functional and are calibrated successfully with an excellent observed mean signal to noise ratio of  $\sim 53$ . The chip-to-chip variation of  $\sim 6.4\%$  is found to be the dominant spread for the pedestals in the prototype. Variation studies have shown that the pedestal is constant within  $<0.5\%$  over

time and for different powering modes. For the MIP constant, a spread of  $\sim 14\%$  over all channels is found, reflecting the outstanding uniformity on the uncalibrated level. Over the different beam test periods in 2018, the studies have shown that the MIP constant is stable within  $1\%$  for the same powering mode. For different powering modes a variation of  $\sim 4.3\%$  is found, which is well understood and taken into account for the calibration constants of the specific beam test period. In addition, the self consistency of the energy calibration is successfully validated on single channel level by the investigation of the calibrated energy spectra for muon events. Based on these studies, it can be concluded that the AHCAL prototype has been successfully commissioned and calibrated. Therefore, the recorded beam test data is considered well suited for high level physics analyses.

In the second part of this thesis, the conventional calorimetric prototype response to muons, electrons and pions is evaluated to agree within  $10\% - 15\%$  or better to Monte Carlo simulations. Furthermore, in preparation for the main analysis part of this thesis, different developed algorithms to determine or exploit aspects of the hadronic shower development are presented and validated. This includes a hadronic shower start finding algorithm with shows an accuracy of better than  $\sim 89\%$  to find the truth shower start layer within  $\pm 2$  layers for charged pions with energies between  $10 - 100$  GeV. Besides an event overlay algorithm, also a pseudo-neutral hadron generation algorithm has been developed. This allows to generate pseudo-neutral hadrons from charged pion events agreeing with simulated  $K_L^0$  much better than  $20\%$  for most observables reflecting energy response and topology of the showers.

In the main analysis part of this thesis, the successful adaptation and application of the Pandora particle flow algorithm (PandoraPFA) framework to AHCAL prototype data and simulation is presented and demonstrated: For more than  $99\%$  of the events the particle flow reconstruction works, while the remaining events mainly suffer from the absence of an ECAL prior to the AHCAL prototype. This allows to perform extensive studies on the limiting effects and the performance of the particle flow reconstruction for single charged pion events and two particle events, consisting of a pseudo-neutral hadron and a charged pion shower. Different energy and distance scenarios for both, AHCAL prototype data and two physics lists in GEANT4, are investigated.

Based on these studies, the reliability of the particle flow performance projections for a future lepton collider experiment have been further validated by two main results: First, the overall data to simulation agreement within  $10\%$  or better for most of the investigated particle flow observables and particle flow reconstructed energy spectra. This shows that the simulated sub-structure details of hadronic showers are accurately modelled and are exploited by PandoraPFA on the same level for simulation and data. Second, the validation of expected trends for the disentangled confusion types and the influence on the overall particle flow reconstruction performance. In the single charged pion study, the exclusively investigated doubled counted charged confusion energy shows an increasing trend for increasing charged pion energy agreeing with the expectations of more isolated topologies within the charged pion shower development for higher energies. For increasing charged pion energy this causes a slight degradation of the energy resolution, which is in general found to improve by a factor  $\sim 3$  in comparison to conventional calorimetric energy resolution. This is caused by the validated accurate charged hit clustering within PandoraPFA and the utilised sharp track momentum, which is as well effectively able to compensate for energy leakage, improving the reconstructed energy linearity. For the two particle studies, a decreasing recovery probability of the pseudo-neutral hadron energy is found for decreasing shower distances and increasing energies of the charged pion shower. A turning point at  $\sim 150$  mm shower separation is determined allowing a  $3\sigma$  recovery of higher than  $\sim 80\%$  ( $\sim 50\%$ ) of the pseudo-neutral hadron energy in the vicinity of a  $10$  GeV ( $30$  GeV) charged pion shower at equal or higher shower separations. Similar results are achieved in previous studies utilising an ECAL in addition, proving the excellent data quality of the

AHCAL prototype and the sufficiently adapted PandoraPFA interface framework. As expected, the hit and energy reconstruction efficiency and purity, calculated by the truth hit information, show decreasing performance for smaller shower distances. This is further verified by the detailed disentangled investigation of the two confusion types, double counted charged and lost neutral confusion energy: For decreasing shower distances a higher confusion level and an increasing imbalance is observed. The impact of these observations on the total reconstruction performance is reflected by an improving relative energy resolution with increasing shower distance, surpassing the conventional calorimetric approach for shower separations higher than 200 mm for both energy scenarios. Furthermore, it is found that additional longitudinal shower separation helps to improve the two particle separation at intermediate shower distances between 50 – 200 mm by up to  $\sim 10\%$ .

In the last part of this thesis, expected trends for confusion types and the impact on the jet energy resolution for simulated 20 – 250 GeV ILD jets are successfully validated for different PandoraPFA settings: Lost neutral (double counted charged) confusion energy becomes dominant for disabled re-clustering (fragment removal) algorithms. With increasing jet energies, the total confusion level and the type imbalance are found to increase, resulting in the observed degradation of the jet energy resolution up to 80% for the no re-clustering algorithm scenario. Furthermore, the impact of reduced shower sub-structure topology information, mimicking the consequences of an increased channel noise level caused e.g. by radiation damage, on the particle flow reconstruction performance is investigated. This scenario is simulated by increasing the hit energy thresholds, followed by a dedicated re-calibration recovering the average event energy mostly within 5%. The impact on the jet energy resolution is found to be negligible with thresholds higher by a factor 2. A degradation of  $\sim 60 - 80\%$  for thresholds higher by a factor 6 over all jet energies is observed. Based on the fact that most of the shower sub-structure topology information is lost with hit energy thresholds this high, the found jet energy resolution is better than anticipated. From this study it can be concluded that the lost topology information can be recovered to a large extent by PandoraPFA (by a high chance due to its internal forced clustering algorithms). This underlines the power of a highly optimised particle flow algorithm and potentially indicates that highly optimised detector effects, like low noise on channel level, might play a less significant role than expected for achieving highest precision. For both studies, similar trends for the individual confusion types and the reconstruction performance are observed for the same PandoraPFA settings applied to representative AHCAL two particle data events. The reproduced trends for those simplified scenarios based on prototype data further strengthen the reliability of the particle flow performance projections for future lepton collider experiments.

## 10.2 Outlook

For some of the results presented in the scope of this thesis, further investigations are required to determine the origin of the observed trends for the PandoraPFA performance. This includes a subsequent study of the data to simulation discrepancies found for the mean number of neutral PFOs and the mean double counted charged confusion energy for higher energies in the single particle reconstruction study. Those discrepancies could hint towards more isolated topologies in the shower development of the simulated charged pions. Studies of isolation criteria within those showers and comparison to MC truth shower information are currently carried out by the collaboration and might help to pinpoint discrepancies of the shower interaction model and real pion showers. Furthermore, the reasons for the achieved jet energy resolution for largely increased hit energy thresholds, which is better than expected, have to be investigated. PFA cheating algorithms,

allowing to disentangle the contributions from the intrinsic calorimetric energy resolution and the confusion term, and the explicit study of the impact of the forced-clustering algorithms within PandoraPFA will help to gain a deeper understanding.

Complementing the last part of the presented studies, a detailed re-investigation of the impact of different effective ECAL and HCAL granularities on the PandoraPFA performance is considered valuable. In the context of the ILD optimisation efforts, granularity vs. performance studies have been conducted, but not on the level of detail the methods presented in this thesis offer. Detailed studies of the level and balance of confusion types might reveal which PandoraPFA internal algorithms are most sensitive to which type of confusion for specific granularity assumptions. This could not only help to re-evaluate the optimised granularity levels of the calorimeter systems, but also to further improve the pattern recognition of the particle flow algorithms.

The adapted version of the PandoraPFA interface framework, which has been implemented for the AHCAL prototype data application in the context of this thesis, forms a powerful basis for subsequent studies. It could easily be adapted in order to study the particle flow performance for larger prototypes or prototype configurations closer to full collider detector systems. For 2022, the CALICE collaboration has planned common beam test campaigns of the SiW-ECAL and AHCAL prototypes. Combined beam test data is of high value, since the technical limitations by the absence of an ECAL, extensively investigated within this thesis, can be overcome. With the higher level of granularity provided by the ECAL an improved pattern recognition, track to cluster associations and re-clustering iterations are expected. This might result in reduced confusion levels and therefore an even better performance for the two particle separation, which is worth to be investigated. Furthermore, software compensation techniques are expected to improve the track momentum to cluster energy comparison in the particle flow reconstruction, as demonstrated by the implementation in the PandoraPFA default configuration for ILD jet simulations. An implementation in the calorimeter prototype application and a subsequent study of the impact on the reconstruction performance for single and two particle data events could help to further validate the reliability of those techniques in future lepton collider jet simulations.

Lastly, the implementation of calorimeter hit timing in the particle flow reconstruction might significantly improve the pattern recognition and help to separate showers within dense jet scenarios more efficiently based on their time information. The excellent timing capabilities of the AHCAL prototype could provide a sufficient testing ground with respect to timing implementations within PandoraPFA. Finally, due to the imaging capabilities of highly granular calorimeters, the implementation of multi-variate machine learning techniques in particle flow algorithms like PandoraPFA might be an option. These techniques are currently investigated for the application of PandoraPFA in LArTPCs, but might as well significantly improve the pattern recognition performance in the linear collider context. Both novel approaches could help to further reduce the confusion term and therefore even raise the performance projections for the jet energy resolution in a future lepton collider experiment.

# A Additional Plots: AHCAL Prototype Calibration

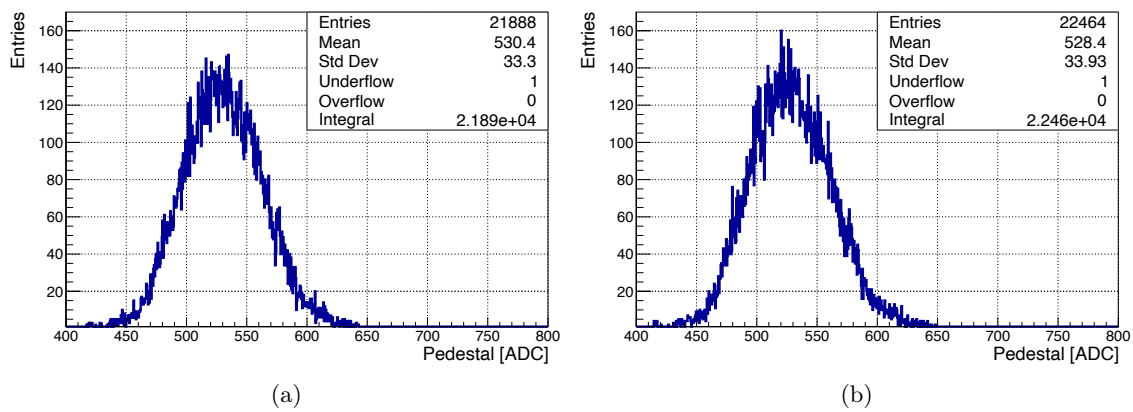


Figure A.1: Extracted pedestal values (mean of pedestal spectrum) on channel level. (a) May beam test (no power pulsing). (b) June beam test (power pulsing).

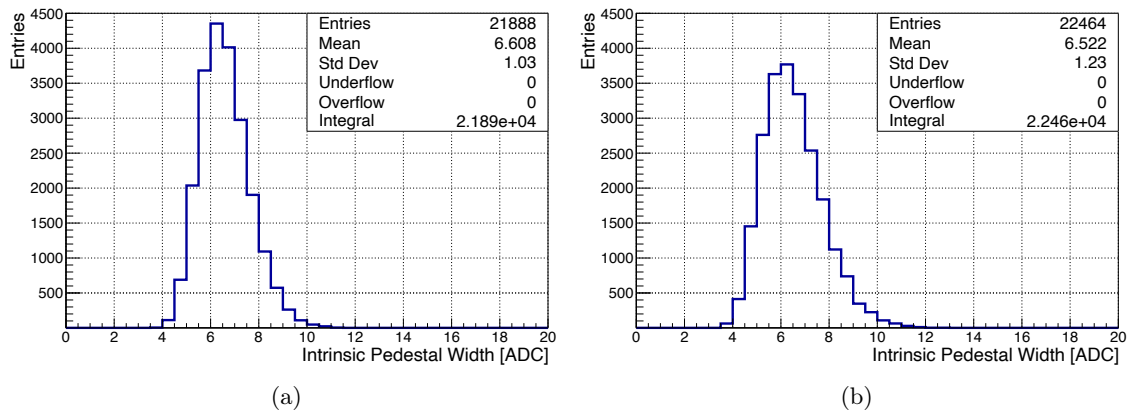


Figure A.2: Extracted intrinsic pedestal widths (RMS of pedestal spectrum) on channel level. (a) May beam test (no power pulsing). (b) June beam test (power pulsing).

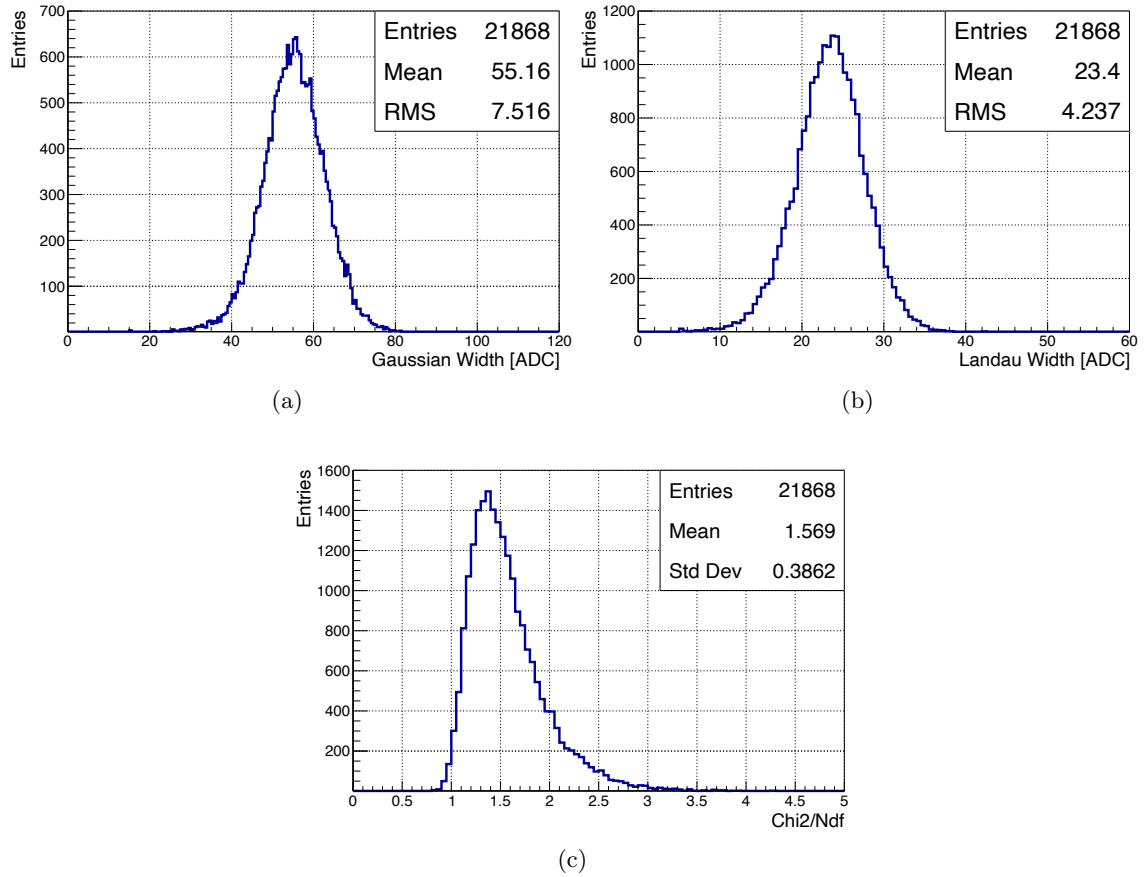


Figure A.3: Landau-Gaussian fit parameters and quality of 21888 AHCAL prototype channels for MIP calibration of May beam test 40 GeV muon data set. The missing 20 channels did not pass the requirements of at least 1000 hits per channel or  $\text{Chi}^2/\text{NDF} < 5$ : (a) Gaussian Width. (b) Landau Width. (c)  $\text{Chi}^2/\text{Ndf}$ .

# B Additional Plots: Simulation and Algorithm Validation

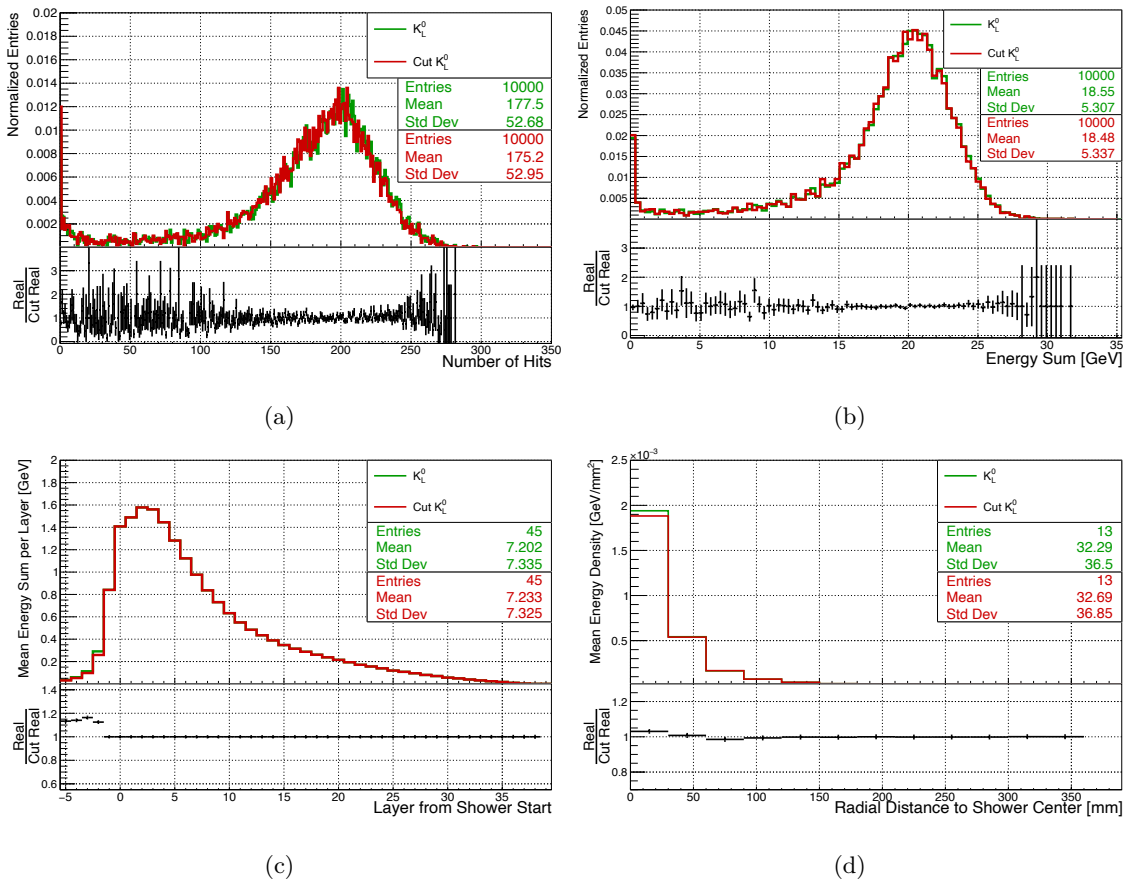


Figure B.1: Calorimetric observables for 20 GeV simulated samples of  $K_L^0$  and  $K_L^0$  with pseudo-neutral hadron generation algorithm applied (QGSP\_BERT\_HP): (a) Number of shower hits. (b) Hit energy sum. (c) Mean longitudinal energy profile. (d) Mean radial energy profile.



# C Sample Overview and Quality Validation for PandoraPFA Studies with AHCAL Prototype Data

Run	Particle	Energy [GeV]	$X_{DWC-AHCAL}$ [mm]	$Y_{DWC-AHCAL}$ [mm]
61260	$\pi^-$	60	14.79	7.97
61264	$\pi^-$	10	14.78	8.16
61270	$\pi^-$	20	14.26	8.21
61275	$\pi^-$	40	14.76	8.48
61280	$\pi^-$	80	14.71	8.25
61312	$\pi^-$	10	61.32	10.83
61314	$\pi^-$	10	112.81	10.75
61318	$\pi^-$	10	-84.79	10.97
61320	$\pi^-$	10	-84.21	10.97
61322	$\pi^-$	10	-133.99	10.75
61323	$\pi^-$	10	-133.99	10.87
61331	$\pi^-$	10	-33.16	-40.17
61333	$\pi^-$	10	15.71	-40.18
61334	$\pi^-$	10	15.77	-40.20
61342	$\pi^-$	10	163.74	-40.50
61368	$\pi^-$	30	181.53	-6.72
61373	$\pi^-$	30	81.11	-6.36
61381	$\pi^-$	30	-115.15	-5.47
61384	$\pi^-$	30	32.82	-6.29

Table C.1: Global DWC to AHCAL prototype alignment offsets for the studied data runs of the June 2018 beam test campaign at SPS CERN.

Run	Particle	Energy [GeV]	Type	$\langle x \rangle   \langle y \rangle$ [mm]	$\langle \sigma_x \rangle   \langle \sigma_y \rangle$ [mm]	$N_{raw}$	$\frac{N_{sel}}{N_{raw}}$ [%]
61264	$\pi^-$	10	D	5.2 -1.2	52.1 53.0	102,073	49.9
			Q	5.2 -1.2	52.1 53.0	100,000	67.4
			F	5.2 -1.2	52.1 53.0	100,000	67.6
61270	$\pi^-$	20	D	6.5 -1.7	46.6 44.0	97,802	62.4
			Q	6.5 -1.7	46.6 44.0	50,000	74.7
			F	6.5 -1.7	46.6 44.0	50,000	73.4
61384	$\pi^-$	30	D	30.0 -17.2	48.7 45.0	49,910	53.4
			Q	30.0 -17.2	48.7 45.0	50,000	76.6
			F	30.0 -17.2	48.7 45.0	60,000	83.2
61275	$\pi^-$	40	D	9.5 9.8	46.2 40.0	128,519	66.5
			Q	9.5 9.8	46.2 40.0	50,000	73.4
			F	9.5 9.8	46.2 40.0	50,000	72.0
61260	$\pi^-$	60	D	10.0 -3.2	47.1 39.3	133,646	67.3
			Q	10.0 -3.2	47.1 39.3	20,000	81.9
			F	10.0 -3.2	47.1 39.3	20,000	80.8
61280	$\pi^-$	80	D	9.2 3.7	44.4 39.0	99,009	69.1
			Q	9.2 3.7	44.4 39.0	10,000	82.2
			F	9.2 3.7	44.4 39.0	20,000	81.4

Table C.2: Summary of investigated charged pion samples for single particle PandoraPFA reconstruction study with centralised beam positions. D corresponds to data samples, Q (F) to simulation samples based on the QGSP\_BERT\_HP (FTFP\_BERT\_HP) physics list.  $\langle x \rangle$ ,  $\langle y \rangle$  and  $\langle \sigma_x \rangle$ ,  $\langle \sigma_y \rangle$  are the mean beam positions and beam position spreads.  $N_{raw}$  is the number of raw events and  $\frac{N_{sel}}{N_{raw}}$  corresponds to the event selection efficiency for the criteria introduced in Section [8.1.2](#).

Run	Particle	Energy [GeV]	Type	$\langle x \rangle   \langle y \rangle$ [mm]	$\langle \sigma_x \rangle   \langle \sigma_y \rangle$ [mm]	$N_{raw}$	$\frac{N_{sel}}{N_{raw}}$ [%]
61342	$\pi^-$	10	D	147.0 -46.5	54.2 53.0	96,905	51.5
			Q	147.0 -46.5	54.2 53.0	71,000	70.3
			F	147.0 -46.5	54.2 53.0	100,000	69.7
70000	$\pi^-$	20	Q	150.0 -18.0	50.0 50.0	50,000	78.5
			F	150.0 -18.0	50.0 50.0	50,000	77.7
61368	$\pi^-$	30	D	168.0 -18.0	52.1 43.3	63,267	69.1
			Q	168.0 -18.0	52.1 43.3	60,000	82.0
			F	168.0 -18.0	52.1 43.3	60,000	83.7
70001	$\pi^-$	40	Q	150.0 -18.0	50.0 50.0	50,000	73.4
			F	150.0 -18.0	50.0 50.0	50,000	77.5
70002	$\pi^-$	60	Q	150.0 -18.0	50.0 50.0	15,000	78.4
			F	150.0 -18.0	50.0 50.0	20,000	79.7
70003	$\pi^-$	80	Q	150.0 -18.0	50.0 50.0	20,000	85.9
			F	150.0 -18.0	50.0 50.0	20,000	84.8

Table C.3: Summary of investigated charged pion samples for single particle PandoraPFA reconstruction study with de-centralised beam positions. D corresponds to data samples, Q (F) to simulation samples based on the QGSP\_BERT\_HP (FTFP\_BERT\_HP) physics list.  $\langle x \rangle$ ,  $\langle y \rangle$  and  $\langle \sigma_x \rangle$ ,  $\langle \sigma_y \rangle$  are the mean beam positions and beam position spreads.  $N_{raw}$  is the number of raw events and  $\frac{N_{sel}}{N_{raw}}$  corresponds to the event selection efficiency for the criteria introduced in Section 8.1.2. Run number series 70000 corresponds to simulation samples with no available beam test data for the same de-centralised beam positions.

Appendix C Sample Overview and Quality Validation for PandoraPFA Studies with AHCAL Prototype Data

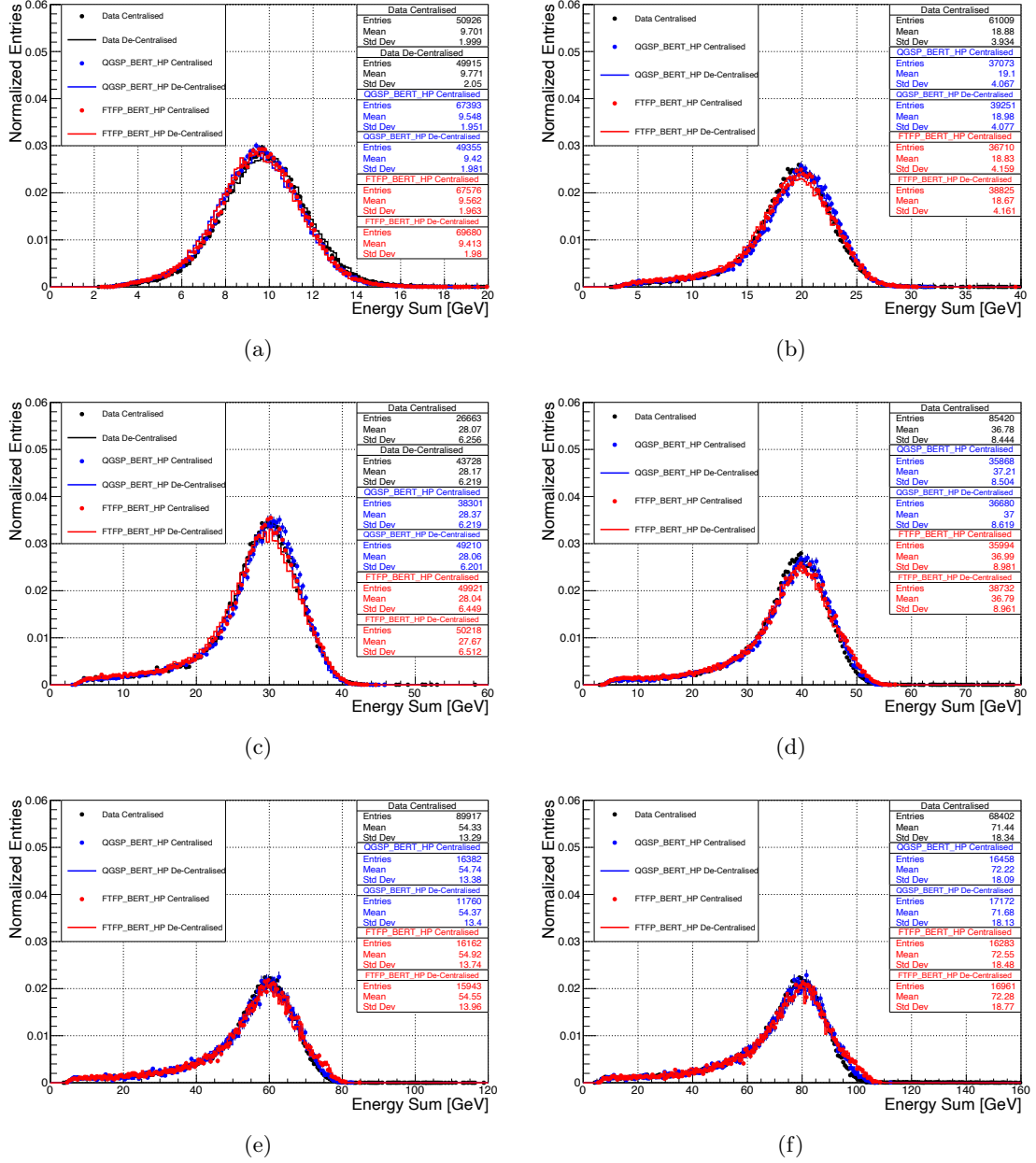


Figure C.1: Energy sum distributions for centralised and de-centralised selected data and simulation samples of (a) 10 GeV  $\pi^-$ . (b) 20 GeV  $\pi^-$ . (c) 30 GeV  $\pi^-$ . (d) 40 GeV  $\pi^-$ . (e) 60 GeV  $\pi^-$ . (f) 80 GeV  $\pi^-$ .

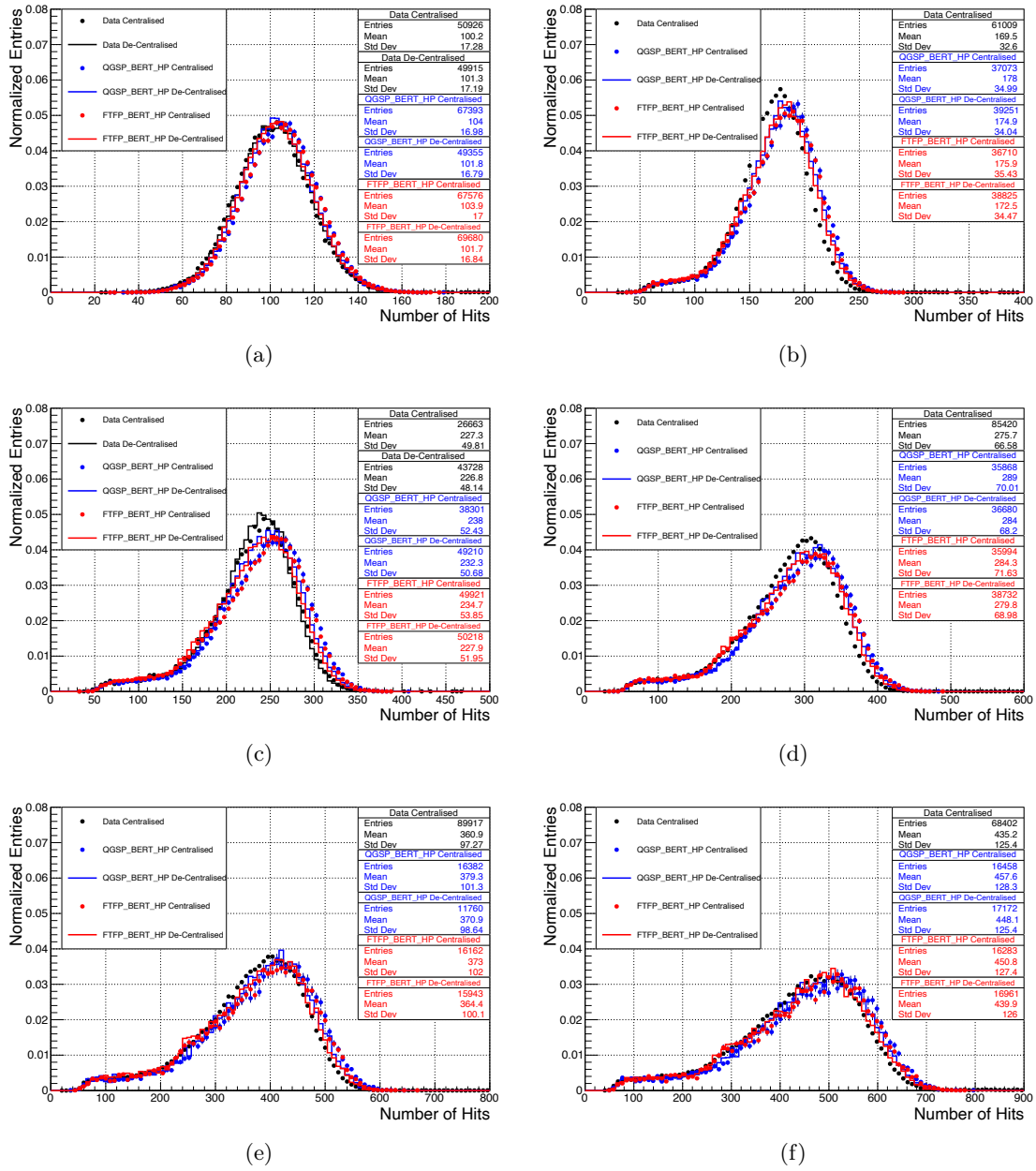


Figure C.2: Number of hits distributions for centralised and de-centralised selected data and simulation samples of (a) 10 GeV  $\pi^-$ . (b) 20 GeV  $\pi^-$ . (c) 30 GeV  $\pi^-$ . (d) 40 GeV  $\pi^-$ . (e) 60 GeV  $\pi^-$ . (f) 80 GeV  $\pi^-$ .

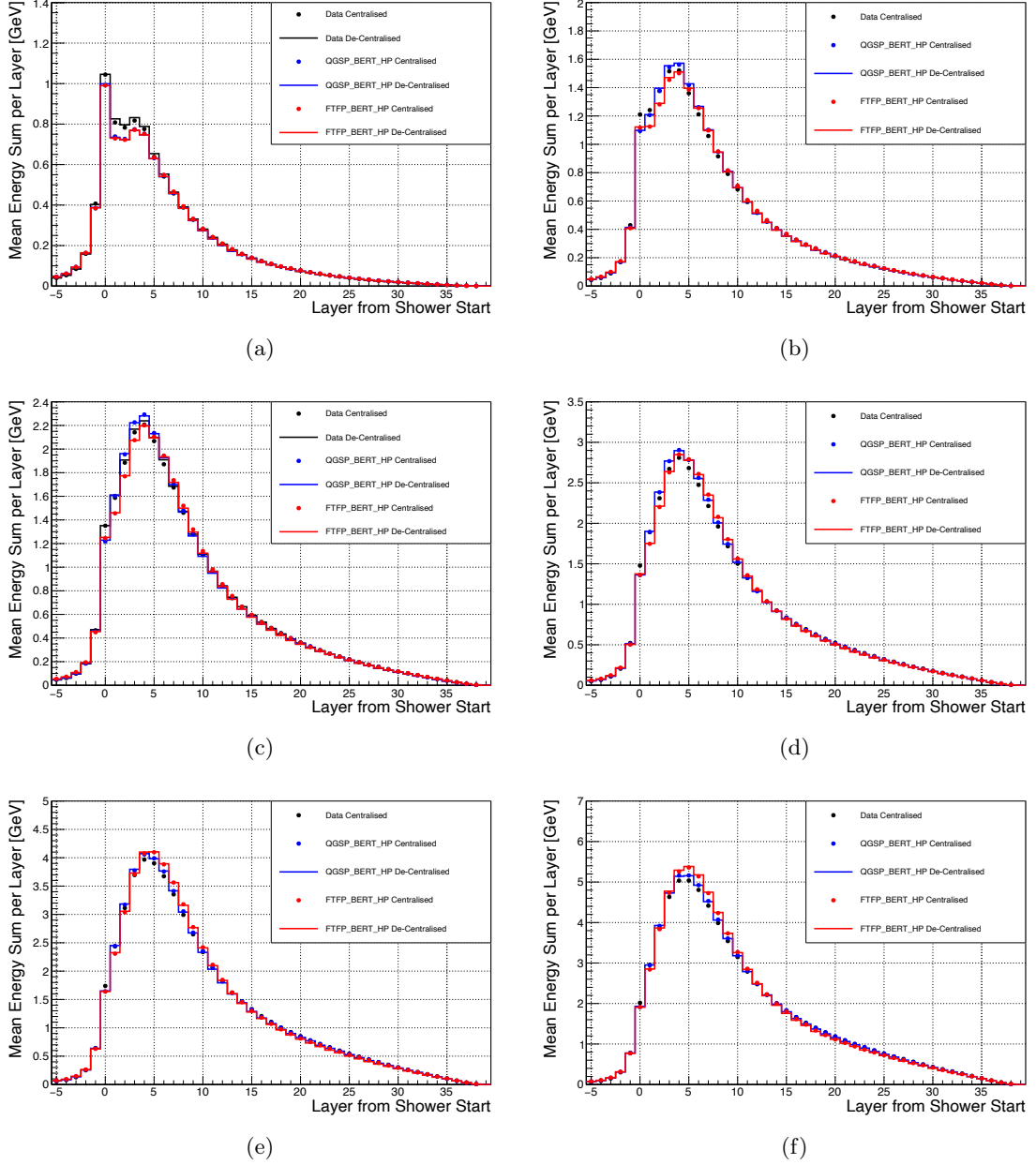


Figure C.3: Mean longitudinal shower energy profiles for selected centralised and de-centralised data and simulation samples of (a) 10 GeV  $\pi^-$ . (b) 20 GeV  $\pi^-$ . (c) 30 GeV  $\pi^-$ . (d) 40 GeV  $\pi^-$ . (e) 60 GeV  $\pi^-$ . (f) 80 GeV  $\pi^-$ .

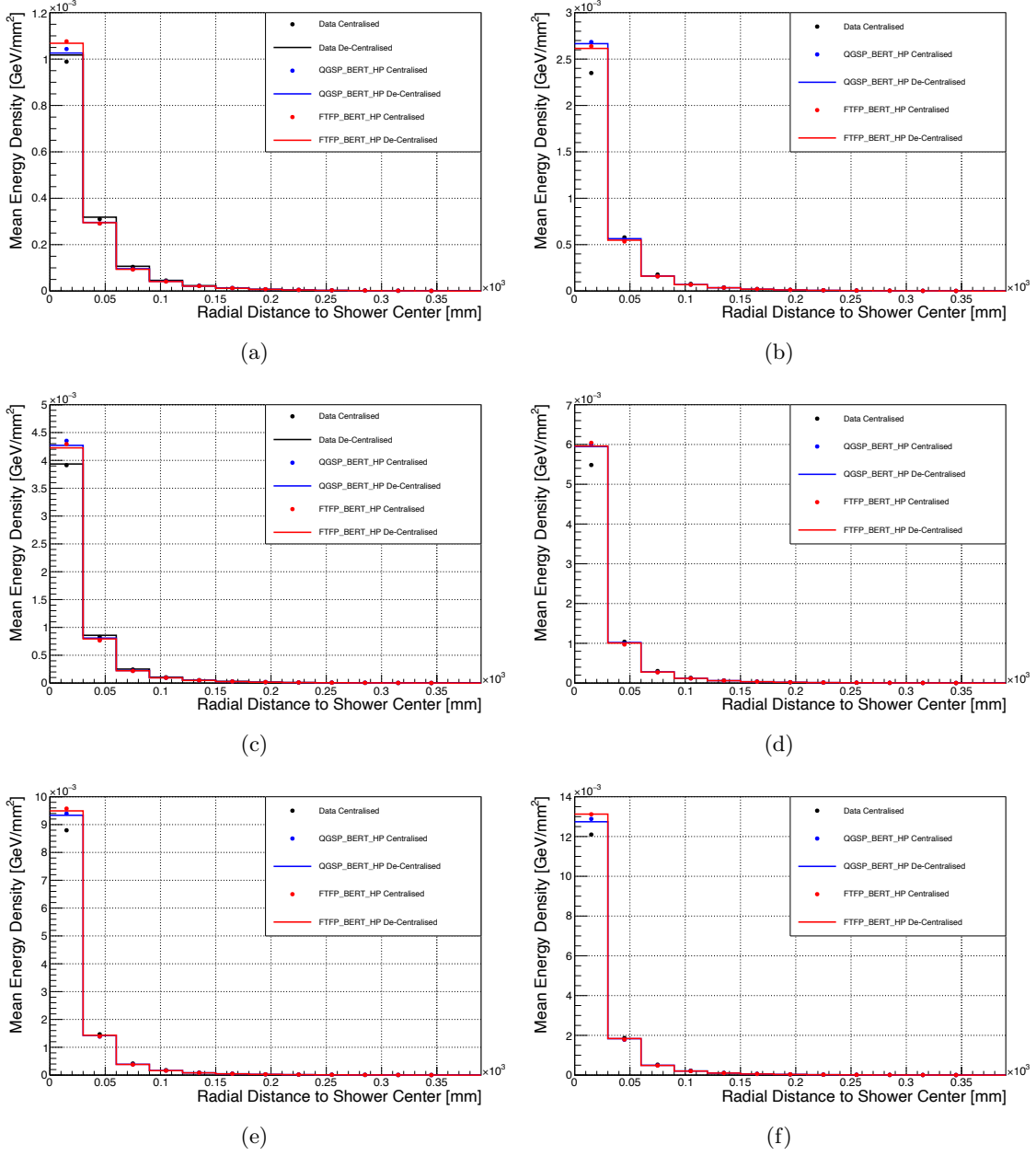


Figure C.4: Mean radial shower energy profiles for centralised and de-centralised selected data and simulation samples of (a) 10 GeV π<sup>-</sup>. (b) 20 GeV π<sup>-</sup>. (c) 30 GeV π<sup>-</sup>. (d) 40 GeV π<sup>-</sup>. (e) 60 GeV π<sup>-</sup>. (f) 80 GeV π<sup>-</sup>.

Run	Particle	Energy [GeV]	Type	$\langle x \rangle   \langle y \rangle$ [mm]	$\langle \sigma_x \rangle   \langle \sigma_y \rangle$ [mm]	$N_{raw}$	$\frac{N_{sel}}{N_{raw}}$ [%]
61312	$\pi^-$	10	D	51.22 1.7	53.0 52.8	95,620	53.0
			Q	51.22 1.7	53.0 52.8	100,000	69.4
			F	51.22 1.7	53.0 52.8	100,000	69.0
61314	$\pi^-$	10	D	99.5 1.4	53.5 52.9	191,622	53.8
			Q	99.5 1.4	53.5 52.9	100,000	70.5
			F	99.5 1.4	53.5 52.9	100,000	70.4
61318	$\pi^-$	10	D	-88.5 1.1	53.2 52.8	95,402	53.9
			Q	-88.5 1.1	53.2 52.8	100,000	70.4
			F	-88.5 1.1	53.2 52.8	100,000	68.9
61334	$\pi^-$	10	D	7.1 -46.2	53.1 54.0	95,267	50.8
			Q	7.1 -46.2	53.1 54.0	100,000	68.9
			F	7.1 -46.2	53.1 54.0	100,000	68.8
61342	$\pi^-$	10	D	147.0 -46.5	54.2 53.0	96,905	51.5
			Q	147.0 -46.5	54.2 53.0	71,000	70.3
			F	147.0 -46.5	54.2 53.0	100,000	69.7
61368	$\pi^-$	30	D	168.0 -18.0	52.1 43.3	63,267	69.1
			Q	168.0 -18.0	52.1 43.3	60,000	82.0
			F	168.0 -18.0	52.1 43.3	60,000	83.7
61373	$\pi^-$	30	D	75.0 -18.6	49.6 44.8	53,235	66.8
			Q	75.0 -18.6	49.6 44.8	15,000	74.7
			F	75.0 -18.6	49.6 44.8	55,000	76.4
61381	$\pi^-$	30	D	-111.5 -17.7	52.3 44.7	53,915	66.9
			Q	-111.5 -17.7	52.3 44.7	100,000	73.0
			F	-111.5 -17.7	52.3 44.7	100,000	77.3
61384	$\pi^-$	30	D	30.0 -17.2	48.7 45.0	49,910	53.4
			Q	30.0 -17.2	48.7 45.0	50,000	76.6
			F	30.0 -17.2	48.7 45.0	60,000	83.2
61260	$\pi^-$	60	D	10.0 -3.2	47.1 39.3	133,646	67.3
			Q	10.0 -3.2	47.1 39.3	20,000	81.9
			F	10.0 -3.2	47.1 39.3	20,000	80.8

Table C.4: Summary of investigated charged pion samples for two particle PandoraPFA reconstruction study. D corresponds to data samples, Q (F) to simulation samples based on the QGSP\_BERT\_HP (FTFP\_BERT\_HP) physics list.  $\langle x \rangle$ ,  $\langle y \rangle$  and  $\langle \sigma_x \rangle$ ,  $\langle \sigma_y \rangle$  are the mean beam positions and beam position spreads.  $N_{raw}$  are the number of raw events and  $\frac{N_{sel}}{N_{raw}}$  corresponds to the event selection efficiency for the criteria introduced in Section [8.1.2](#)

Run	Particle	Energy [GeV]	Type	$\langle x \rangle   \langle y \rangle$ [mm]	$\langle \sigma_x \rangle   \langle \sigma_y \rangle$ [mm]	$N_{raw}$	$\frac{N_{sel}}{N_{raw}}$ [%]
61264	pseudo-neutral	10	D	5.2 -1.2	52.1 53.0	102,073	49.9
			Q	5.2 -1.2	52.1 53.0	100,000	67.4
			F	5.2 -1.2	52.1 53.0	100,000	67.6
61312	pseudo-neutral	10	D	51.22 1.7	53.0 52.8	95,620	53.0
			Q	51.22 1.7	53.0 52.8	100,000	69.4
			F	51.22 1.7	53.0 52.8	100,000	69.0
61314	pseudo-neutral	10	D	99.5 1.4	53.5 52.9	191,622	53.8
			Q	99.5 1.4	53.5 52.9	100,000	70.5
			F	99.5 1.4	53.5 52.9	100,000	70.4
61318	pseudo-neutral	10	D	-88.5 1.1	53.2 52.8	95,402	53.9
			Q	-88.5 1.1	53.2 52.8	100,000	70.4
			F	-88.5 1.1	53.2 52.8	100,000	68.9
61320	pseudo-neutral	10	D	-88.3 1.1	53.1 52.9	94,715	74.2
			Q	-88.3 1.1	53.1 52.9	25,000	67.6
			F	-88.3 1.1	53.1 52.9	50,000	73.3
61322	pseudo-neutral	10	D	-135.1 1.7	53.8 52.6	64,832	73.9
			Q	-135.1 1.7	53.8 52.6	100,000	70.7
			F	-135.1 1.7	53.8 52.6	100,000	71.2
61331	pseudo-neutral	10	D	-40.2 46.5	53.0 53.4	109,343	74.4
			Q	40.2 46.5	53.0 53.4	100,000	72.9
			F	40.2 46.5	53.0 53.4	100,000	72.3
61333	pseudo-neutral	10	D	6.8 -46.4	52.8 53.6	97,582	74.7
			Q	6.8 -46.4	52.8 53.6	50,000	67.3
			F	6.8 -46.4	52.8 53.6	30,000	67.9
61334	pseudo-neutral	10	D	7.1 -46.2	53.1 54.0	95,267	50.8
			Q	7.1 -46.2	53.1 54.0	100,000	68.9
			F	7.1 -46.2	53.1 54.0	100,000	68.8
61342	pseudo-neutral	10	D	147.0 -46.5	54.2 53.0	96,905	51.5
			Q	147.0 -46.5	54.2 53.0	71,000	70.3
			F	147.0 -46.5	54.2 53.0	100,000	69.7

Table C.5: Summary of pseudo-neutral hadron samples generated from charged pions for two particle PandoraPFA reconstruction study. D corresponds to data samples, Q (F) to simulation samples based on the QGSP\_BERT\_HP (FTFP\_BERT\_HP) physics list.  $\langle x \rangle$ ,  $\langle y \rangle$  and  $\langle \sigma_x \rangle$ ,  $\langle \sigma_y \rangle$  are the mean beam positions and beam position spreads.  $N_{raw}$  are the number of raw events and  $\frac{N_{sel}}{N_{raw}}$  corresponds to the event selection efficiency for the criteria introduced in Section 8.1.2

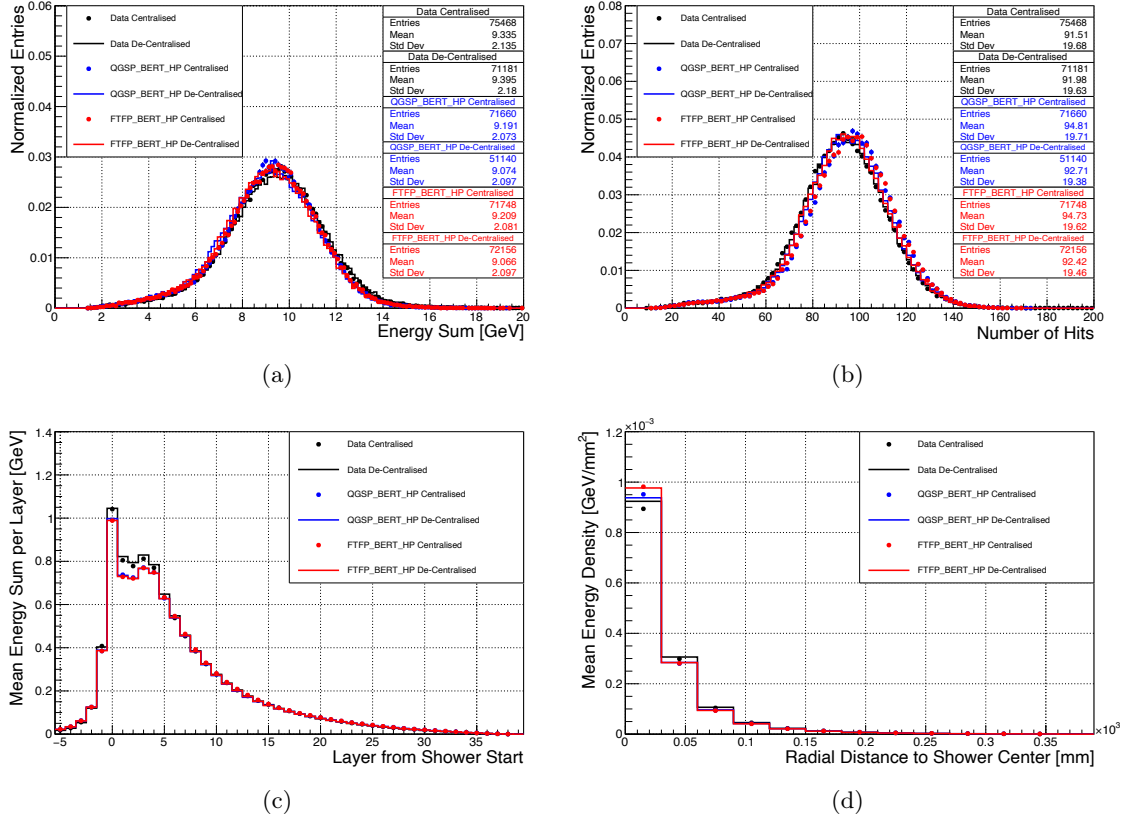


Figure C.5: Calorimetric observable distributions and mean energy profiles for centralised and de-centralised selected data and simulation samples of generated 10 GeV pseudo-neutral hadrons: (a) Energy sum. (b) Number of shower hits. (c) Longitudinal profile. (d) Radial profile.

---

Radial Distance Bin	Type	$N_{events}$ (10 GeV + 10 GeV)	$N_{events}$ (10 GeV + 30 GeV)
0 mm– 25 mm	D	13,632	43,334
	Q	9,253	67,639
	F	8,672	48,981
50 ± 25 mm	D	80,492	34,354
	Q	66,445	64,283
	F	62,491	67,435
100 ± 25 mm	D	81,746	39,936
	Q	101,716	93779
	F	96,748	101,792
150 ± 25 mm	D	67,912	54,730
	Q	102,732	91,882
	F	101,294	104,858
200 ± 25 mm	D	63,304	67,949
	Q	84,923	76,572
	F	86,152	91,326
250 ± 25 mm	D	60,925	53,766
	Q	62,947	53,812
	F	65,949	67,840
300 ± 25 mm	D	46,908	22,224
	Q	39,775	30,849
	F	43,804	40,208

Table C.6: Number of events in radial shower distance bins for investigated two particle event scenarios of overlaid pseudo-neutral (10 GeV) and charged pion showers (10 GeV or 30 GeV) for generated data (D) and simulation samples (Q and F for QGSP\_BERT\_HP and FTFP\_BERT\_HP physics lists).

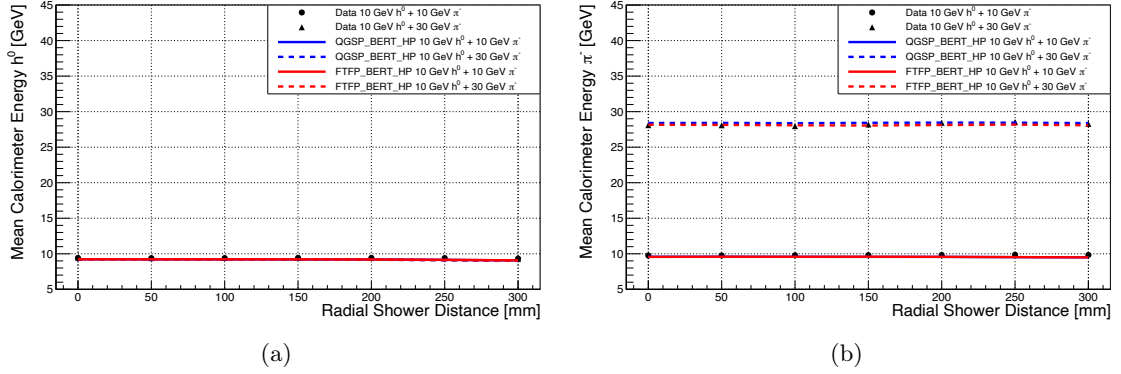


Figure C.6: Mean energy sum of overlaid particles sorted into respective radial shower distance bins for different overlay scenarios of AHCAL prototype data and simulation: (a) Pseudo-neutral hadrons (b) Charged pions.

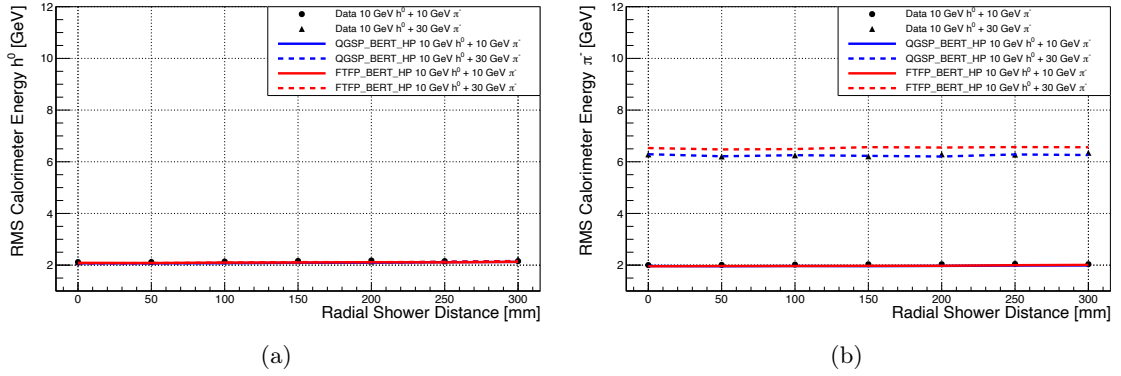


Figure C.7: RMS energy sum of overlaid particles sorted into respective radial shower distance bins for different overlay scenarios of AHCAL prototype data and simulation: (a) Pseudo-neutral hadrons (b) Charged pions.

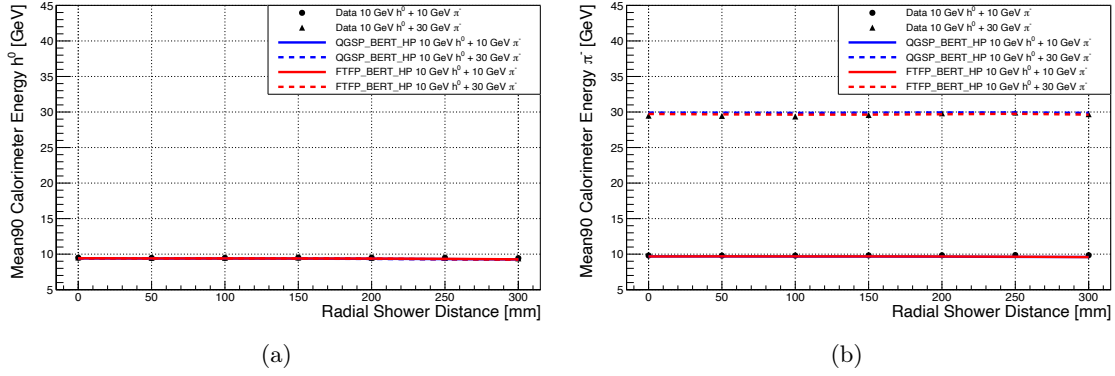


Figure C.8: Mean90 energy sum of overlaid particles sorted into respective radial shower distance bins for different overlay scenarios of AHCAL prototype data and simulation: (a) Pseudo-neutral hadrons (b) Charged pions.

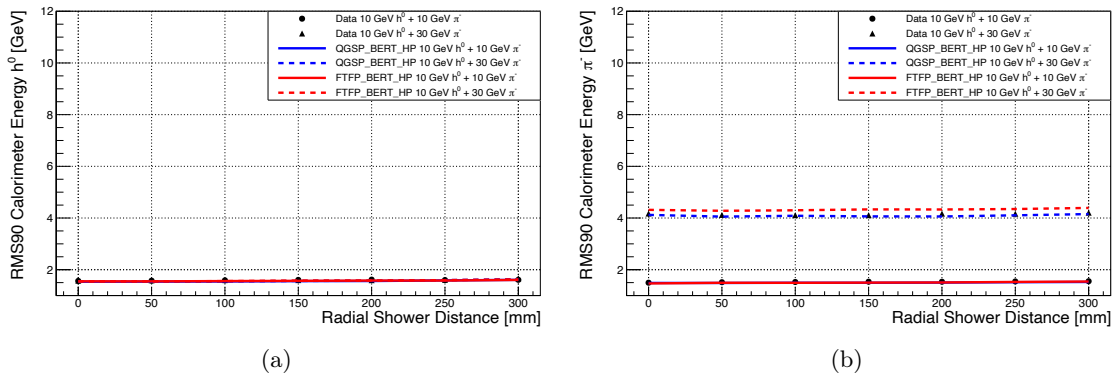


Figure C.9: RMS90 of energy sum of overlaid particles sorted into respective radial shower distance bins for different overlay scenarios of AHCAL prototype data and simulation: (a) Pseudo-neutral hadrons (b) Charged pions.

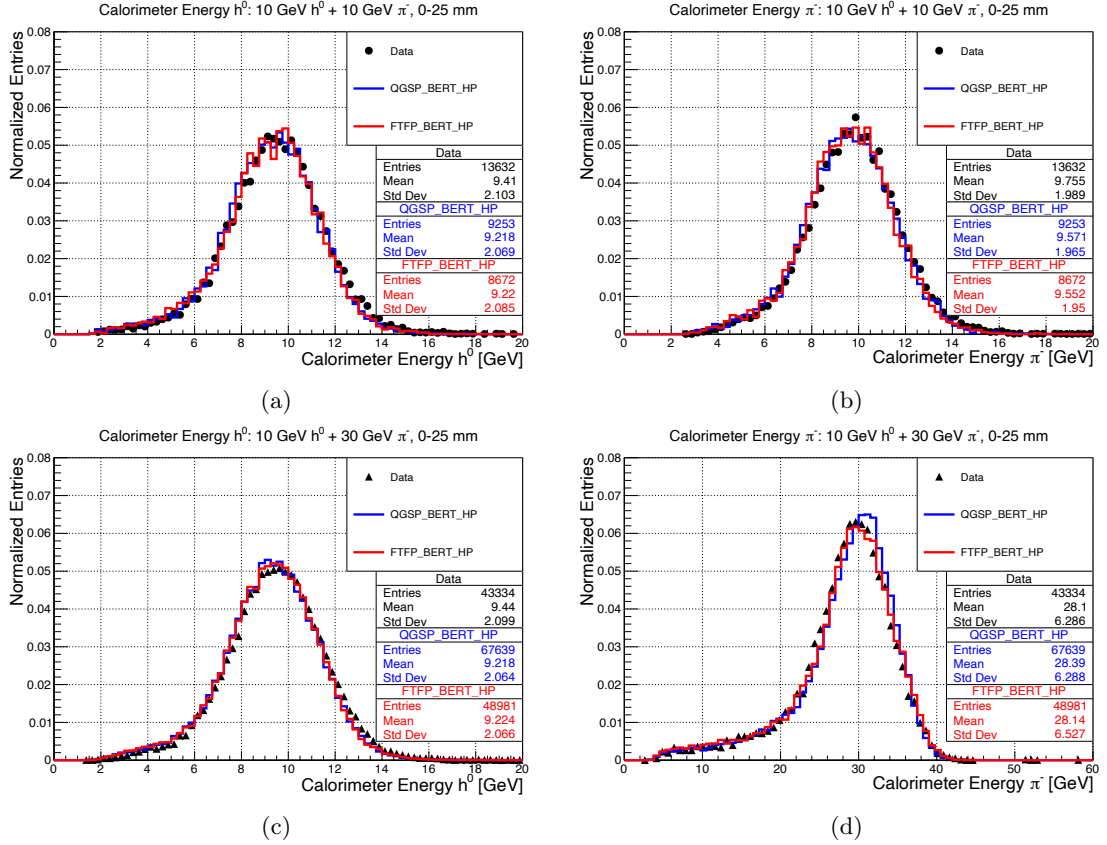


Figure C.10: Energy sum spectra of data and simulation events sorted into radial distance bin 0–25 mm for two particle event scenarios: (a) 10 GeV **pseudo-neutral hadron** + 10 GeV **charged pion**. (b) 10 GeV **pseudo-neutral hadron** + 10 GeV **charged pion**. (c) 10 GeV **pseudo-neutral hadron** + 30 GeV **charged pion**. (d) 10 GeV **pseudo-neutral hadron** + 30 GeV **charged pion**.

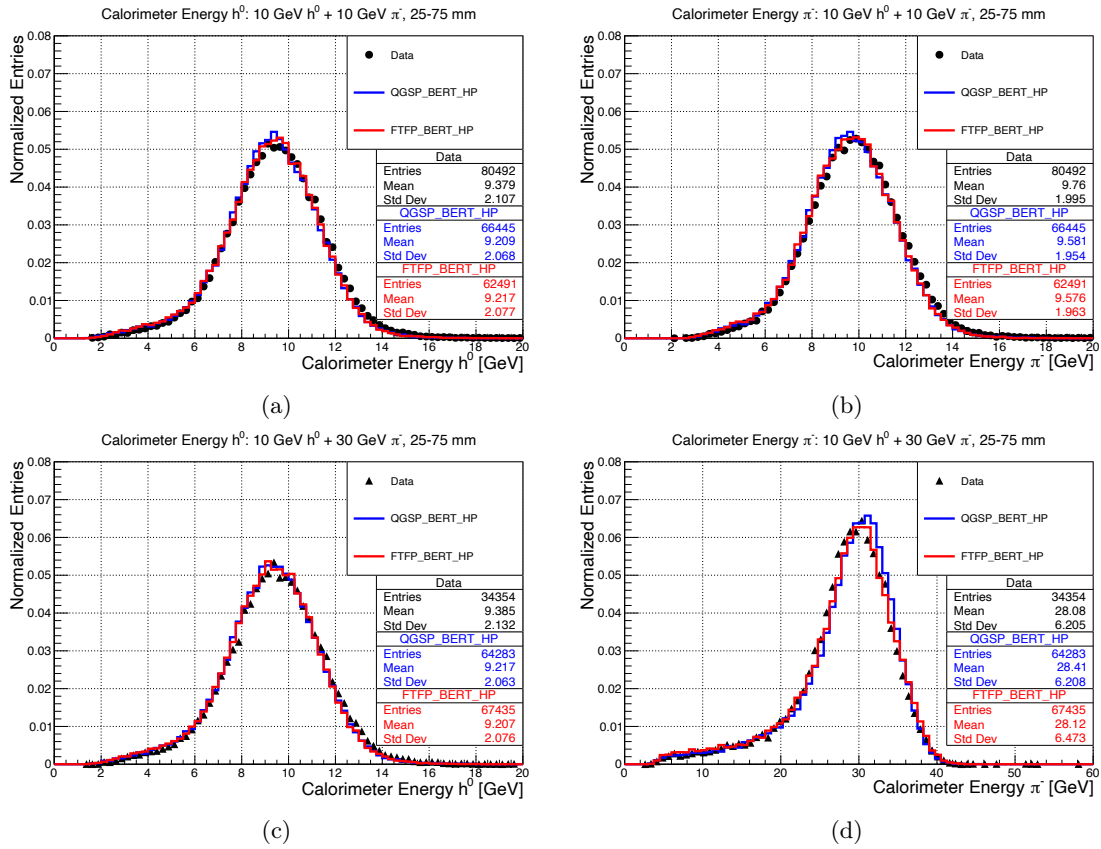


Figure C.11: Energy sum spectra of data and simulation events sorted into radial distance bin  $50 \pm 25$  mm for two particle event scenarios: (a) 10 GeV **pseudo-neutral hadron** + 10 GeV charged pion. (b) 10 GeV **pseudo-neutral hadron** + 10 GeV **charged pion**. (c) 10 GeV **pseudo-neutral hadron** + 30 GeV charged pion. (d) 10 GeV **pseudo-neutral hadron** + 30 GeV **charged pion**.

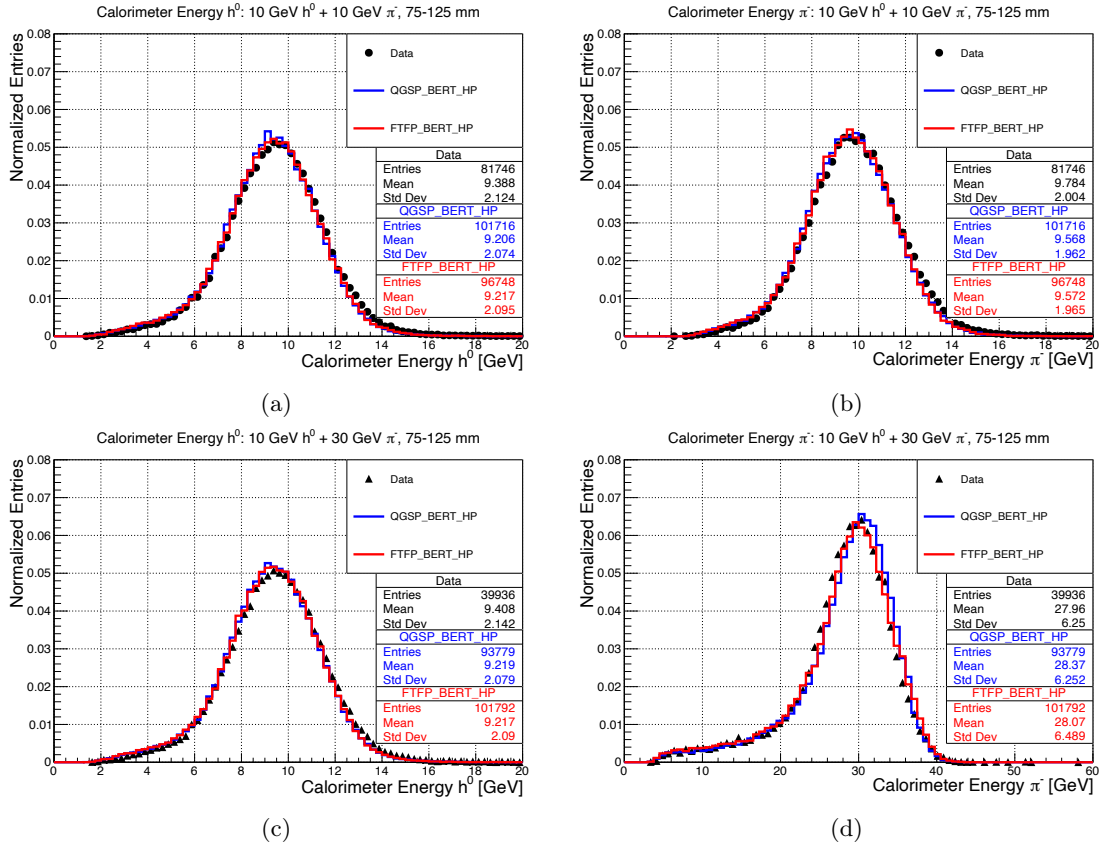


Figure C.12: Energy sum spectra of data and simulation events sorted into radial distance bin  $100 \pm 25$  mm for two particle event scenarios: (a) 10 GeV **pseudo-neutral hadron** + 10 GeV charged pion. (b) 10 GeV **pseudo-neutral hadron** + 10 GeV **charged pion**. (c) 10 GeV **pseudo-neutral hadron** + 30 GeV charged pion. (d) 10 GeV **pseudo-neutral hadron** + 30 GeV **charged pion**.

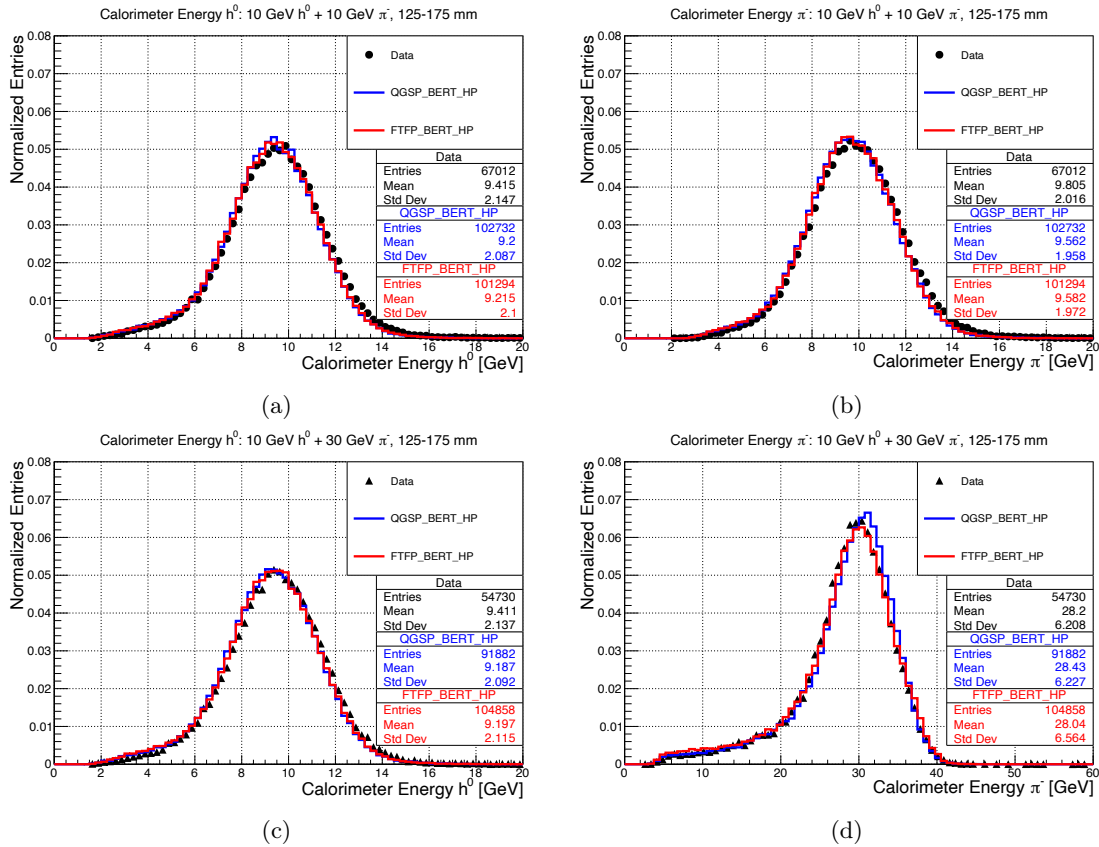


Figure C.13: Energy sum spectra of data and simulation events sorted into radial distance bin  $150 \pm 25$  mm for two particle event scenarios: (a) 10 GeV **pseudo-neutral hadron** + 10 GeV charged pion. (b) 10 GeV **pseudo-neutral hadron** + 10 GeV **charged pion**. (c) 10 GeV **pseudo-neutral hadron** + 30 GeV charged pion. (d) 10 GeV **pseudo-neutral hadron** + 30 GeV **charged pion**.

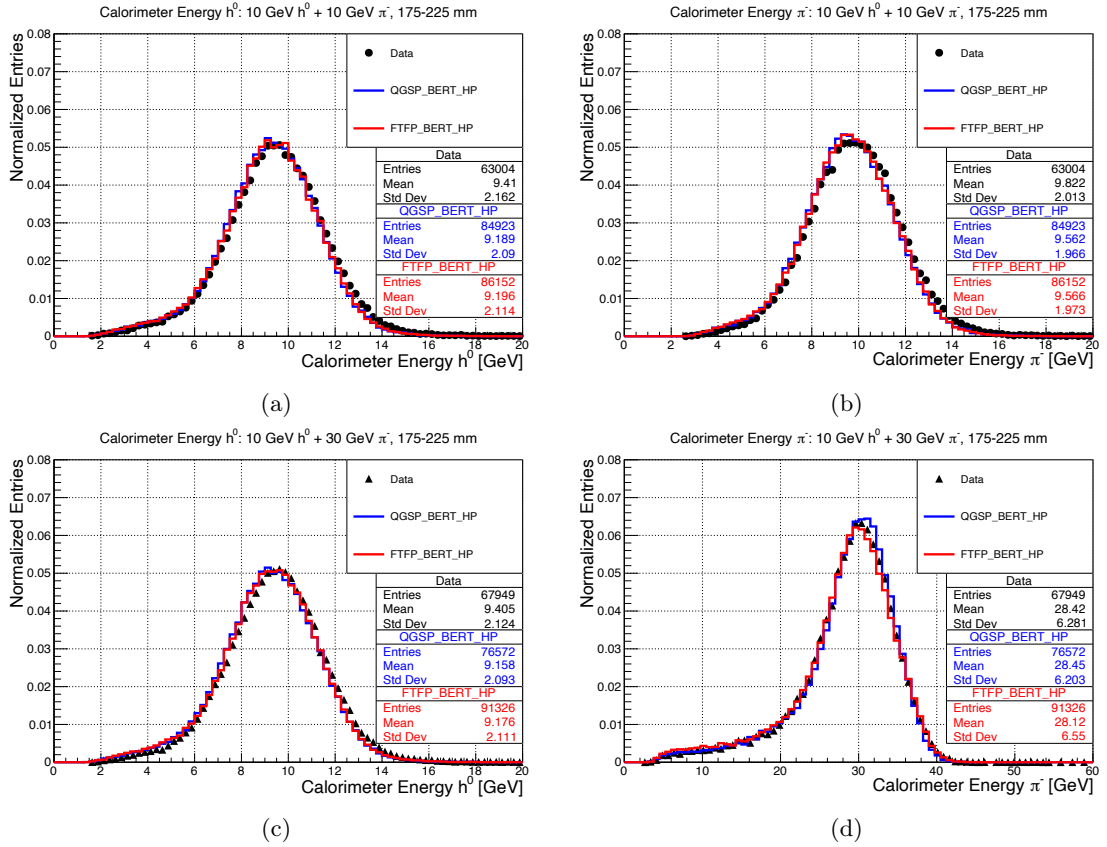


Figure C.14: Energy sum spectra of data and simulation events sorted into radial distance bin  $200 \pm 25$  mm for two particle event scenarios: (a) 10 GeV **pseudo-neutral hadron** + 10 GeV charged pion. (b) 10 GeV **pseudo-neutral hadron** + 10 GeV **charged pion**. (c) 10 GeV **pseudo-neutral hadron** + 30 GeV charged pion. (d) 10 GeV **pseudo-neutral hadron** + 30 GeV **charged pion**.

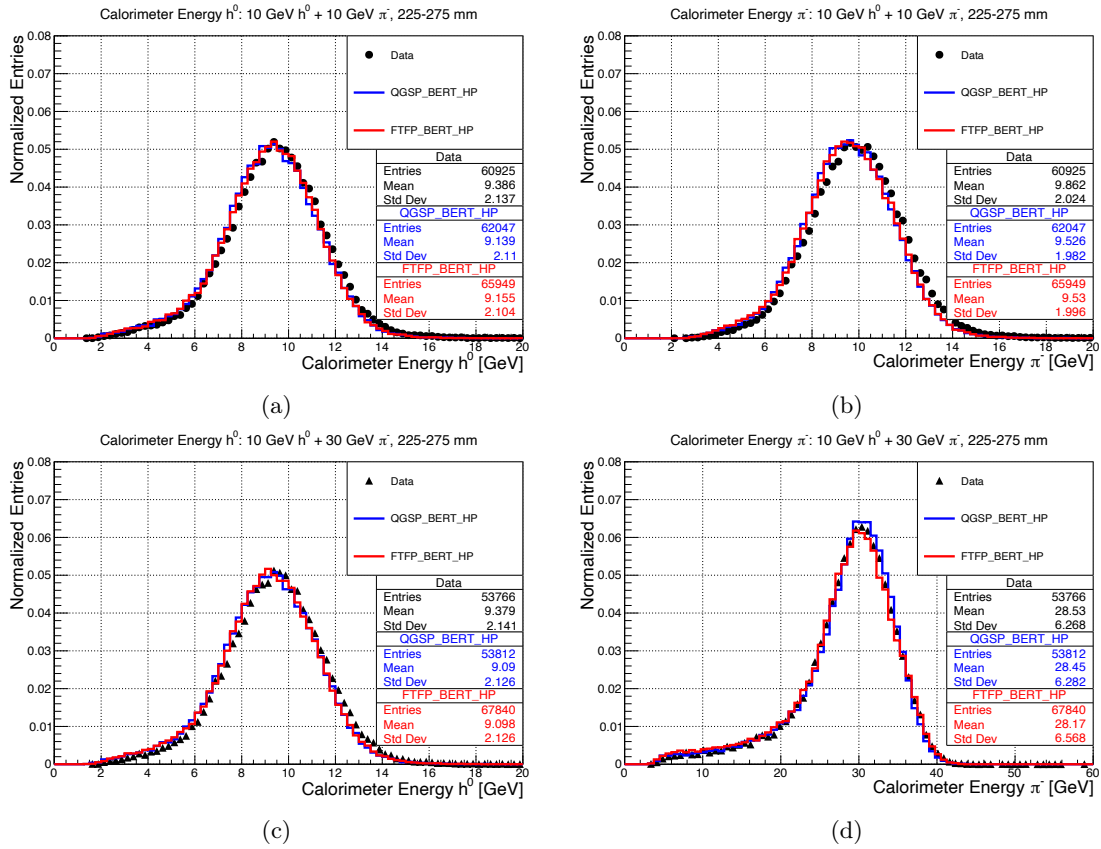


Figure C.15: Energy sum spectra of data and simulation events sorted into radial distance bin  $250 \pm 25$  mm for two particle event scenarios: (a) 10 GeV **pseudo-neutral hadron** + 10 GeV charged pion. (b) 10 GeV **pseudo-neutral hadron** + 10 GeV **charged pion**. (c) 10 GeV **pseudo-neutral hadron** + 30 GeV charged pion. (d) 10 GeV **pseudo-neutral hadron** + 30 GeV **charged pion**.

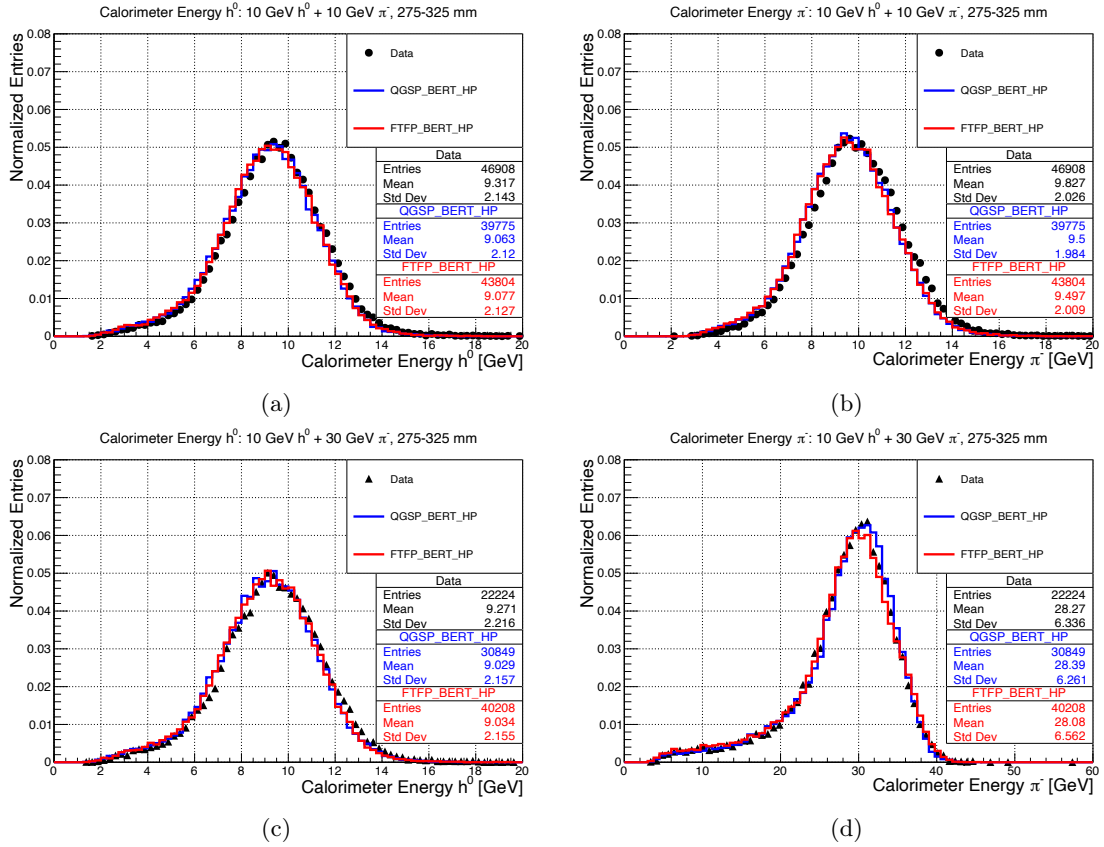


Figure C.16: Energy sum spectra of data and simulation events sorted into radial distance bin  $300 \pm 25$  mm for two particle event scenarios: (a) 10 GeV **pseudo-neutral hadron** + 10 GeV charged pion. (b) 10 GeV pseudo-neutral hadron + 10 GeV **charged pion**. (c) 10 GeV **pseudo-neutral hadron** + 30 GeV charged pion. (d) 10 GeV pseudo-neutral hadron + 30 GeV **charged pion**.

# D Additional Plots: Two Particle PandoraPFA Studies with AH-CAL Prototype Data

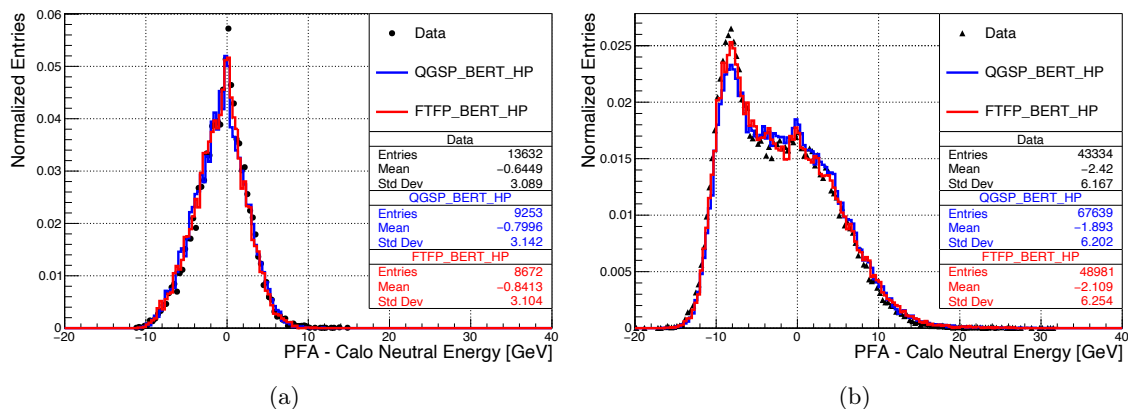


Figure D.1: Difference of neutral PFO energy sum and input neutral calorimetric energy sum for data and simulation samples of overlaid 0 – 25 mm radial distance: (a) 10 GeV pseudo-neutral hadron + 10 GeV charged pion. (b) 10 GeV pseudo-neutral hadron + 30 GeV charged pion.

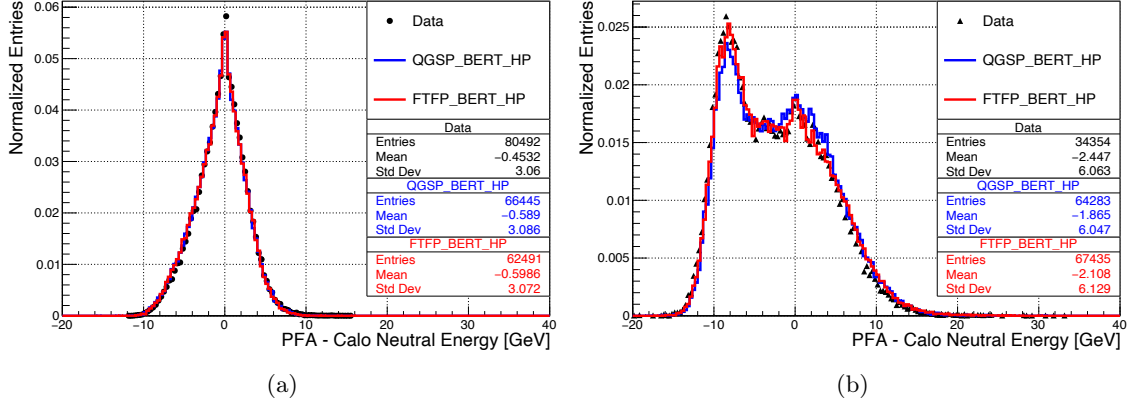


Figure D.2: Difference of neutral PFO energy sum and input neutral calorimetric energy sum for data and simulations samples of overlaid 25 – 75 mm radial distance: (a) 10 GeV pseudo-neutral hadron + 10 GeV charged pion. (b) 10 GeV pseudo-neutral hadron + 30 GeV charged pion.

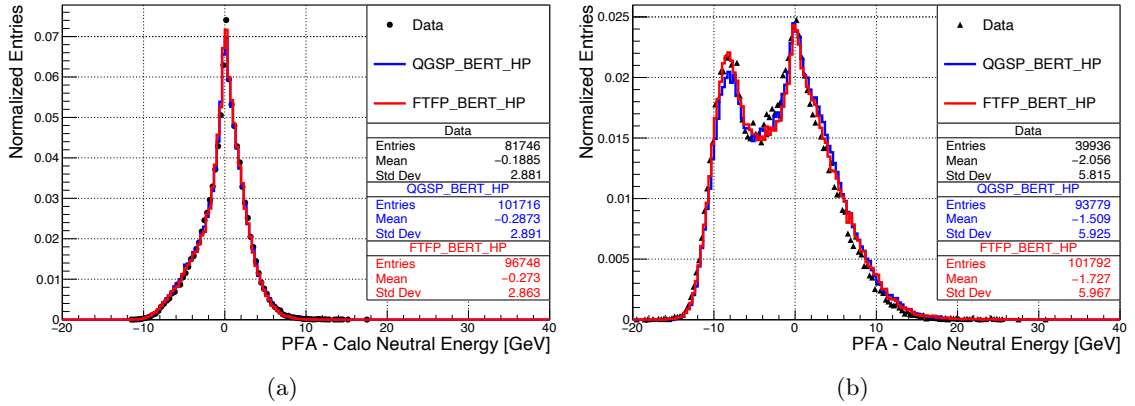


Figure D.3: Difference of neutral PFO energy sum and input neutral calorimetric energy sum for data and simulations samples of overlaid 75 – 125 mm radial distance: (a) 10 GeV pseudo-neutral hadron + 10 GeV charged pion. (b) 10 GeV pseudo-neutral hadron + 30 GeV charged pion.

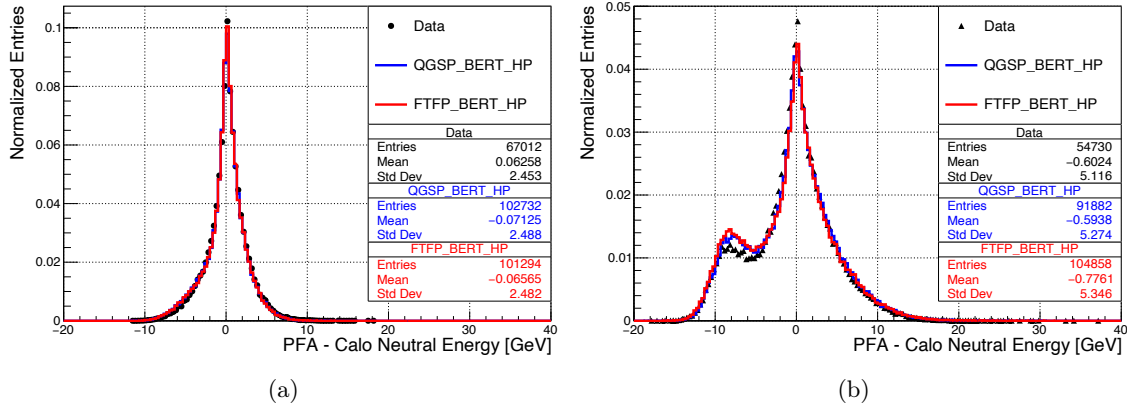


Figure D.4: Difference of neutral PFO energy sum and input neutral calorimetric energy sum for data and simulations samples of overlaid 125 – 175 mm radial distance: (a) 10 GeV pseudo-neutral hadron + 10 GeV charged pion. (b) 10 GeV pseudo-neutral hadron + 30 GeV charged pion.

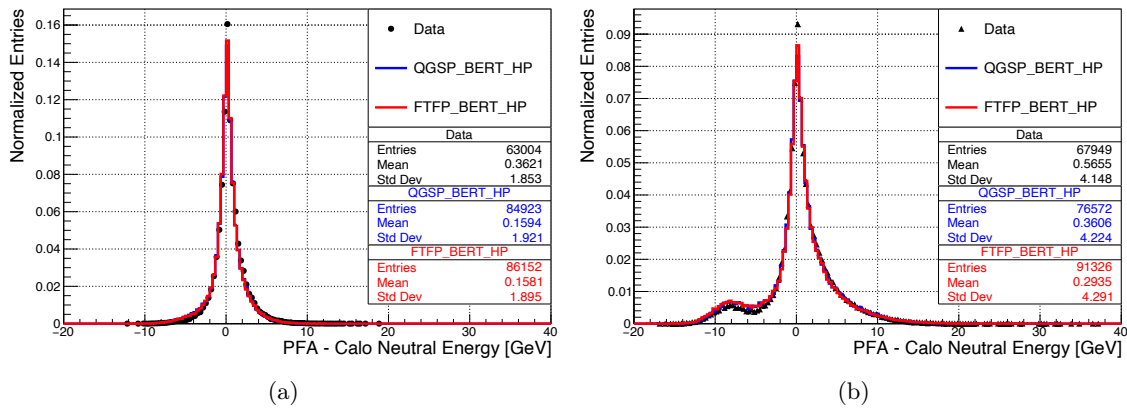


Figure D.5: Difference of neutral PFO energy sum and input neutral calorimetric energy sum for data and simulations samples of overlaid 175 – 225 mm radial distance: (a) 10 GeV pseudo-neutral hadron + 10 GeV charged pion. (b) 10 GeV pseudo-neutral hadron + 30 GeV charged pion.

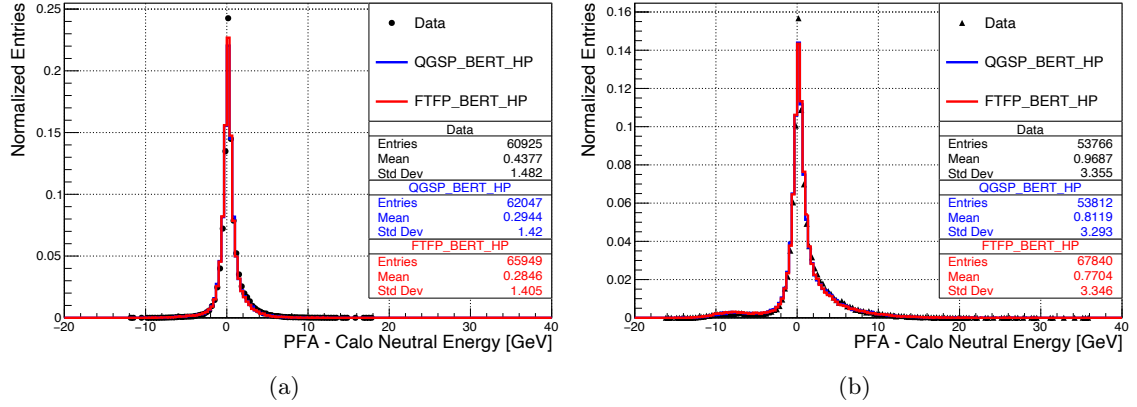


Figure D.6: Difference of neutral PFO energy sum and input neutral calorimetric energy sum for data and simulations samples of overlaid 225 – 275 mm radial distance: **(a)** 10 GeV pseudo-neutral hadron + 10 GeV charged pion. **(b)** 10 GeV pseudo-neutral hadron + 30 GeV charged pion.

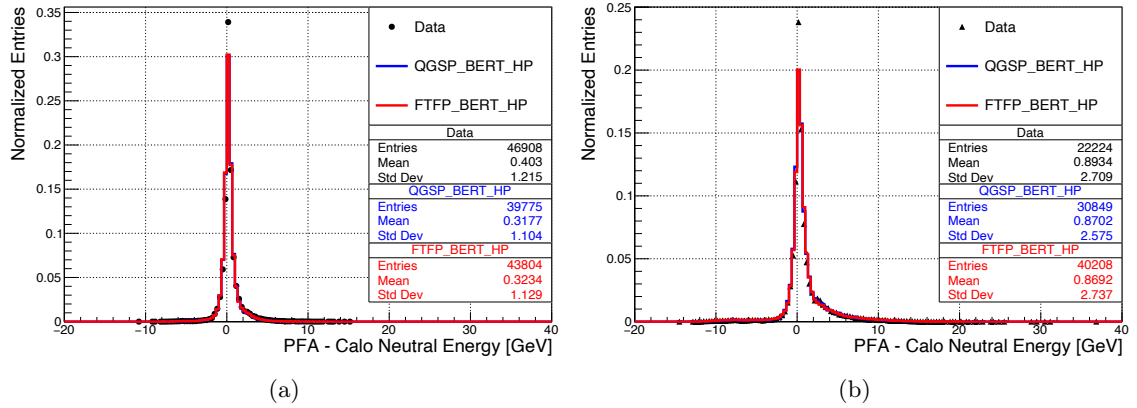


Figure D.7: Difference of neutral PFO energy sum and input neutral calorimetric energy sum for data and simulations samples of overlaid 275 – 325 mm radial distance: **(a)** 10 GeV pseudo-neutral hadron + 10 GeV charged pion. **(b)** 10 GeV pseudo-neutral hadron + 30 GeV charged pion.

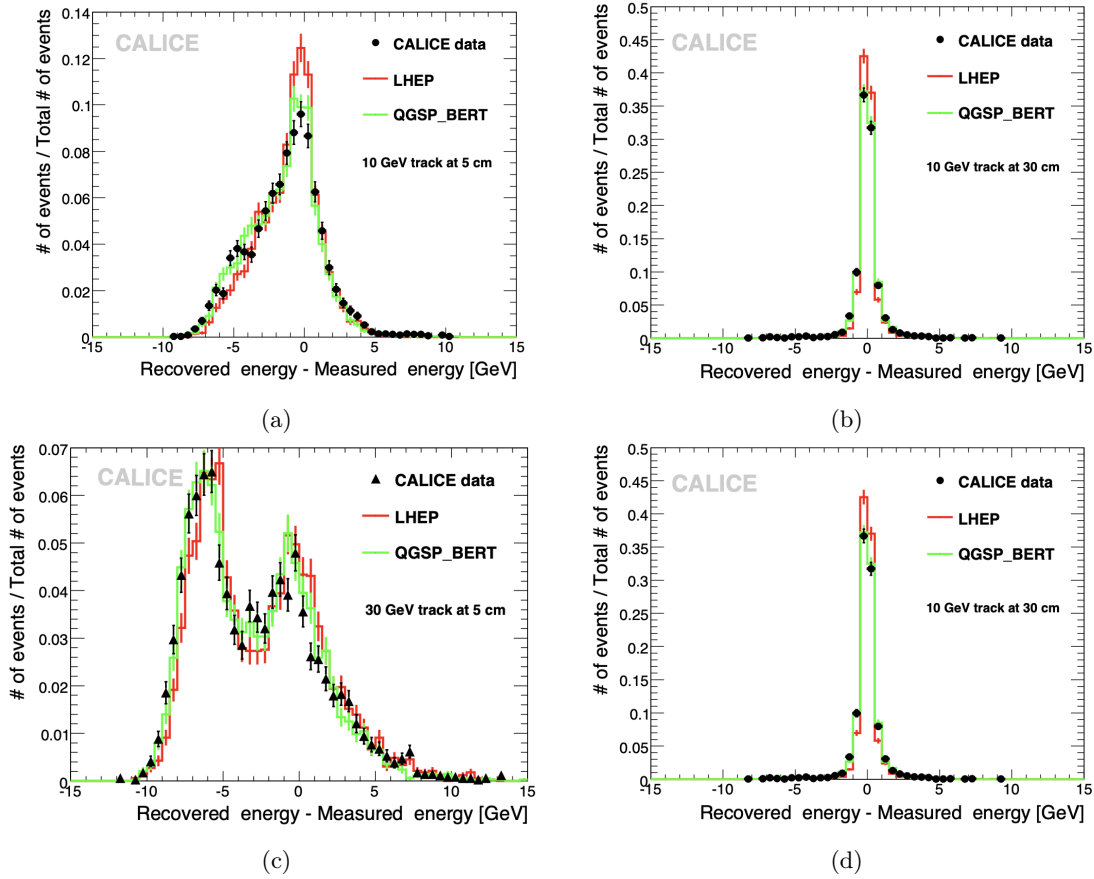


Figure D.8: Difference of neutral PFO energy sum and input neutral calorimetric energy sum for data and simulations samples of overlaid pseudo neutral hadron and charged pion shower at different distances: (a) 10 GeV + 10 GeV at 50 mm. (b) 10 GeV + 10 GeV at 300 mm distance. (c) 10 GeV + 30 GeV at 50 mm. (d) 10 GeV + 30 GeV at 300 mm for combined CALICE SiW-ECAL + AHCAL 2007 prototype studies [156].

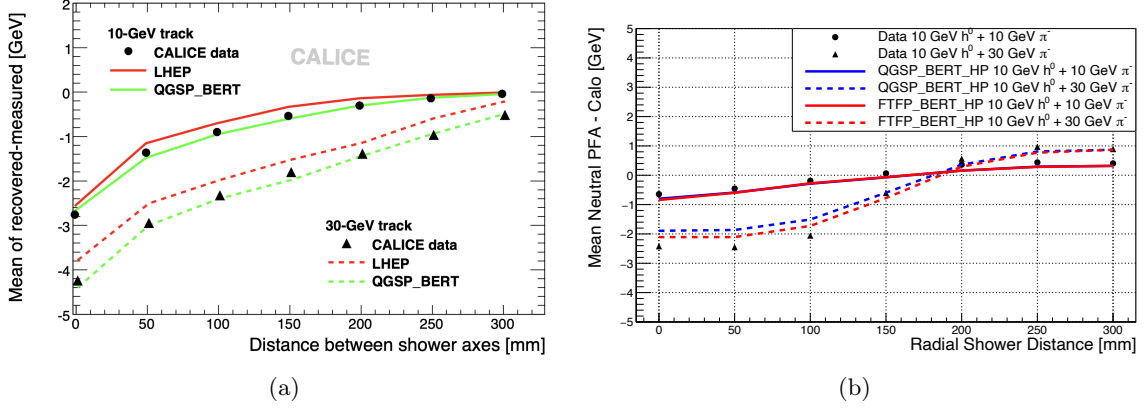


Figure D.9: Mean difference of neutral PFO energy sum and input neutral calorimetric energy sum over radial shower distance for data and simulation samples of (a) CALICE SiW-ECAL + AHCAL 2007 prototype studies [156]. (b) AHCAL prototype studies.

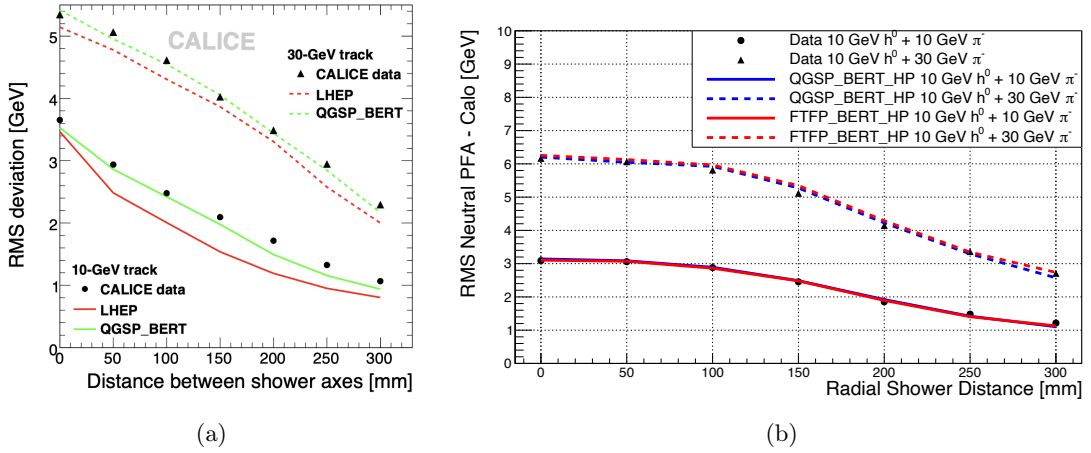


Figure D.10: RMS for difference of neutral PFO energy sum and input neutral calorimetric energy sum over radial shower distance for data and simulation samples of (a) CALICE SiW-ECAL + AHCAL 2007 prototype studies [156]. (b) AHCAL prototype studies.

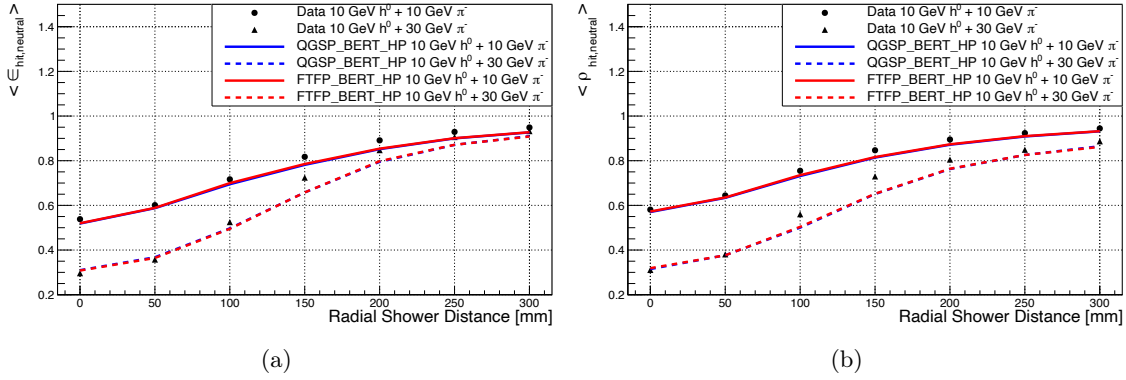


Figure D.11: Mean hit reconstruction efficiency (a) and purity (b) for 10 GeV pseudo-neutral hadrons in the vicinity of 10 GeV or 30 GeV charged pion showers over radial shower distance for investigated beam test and simulation samples.

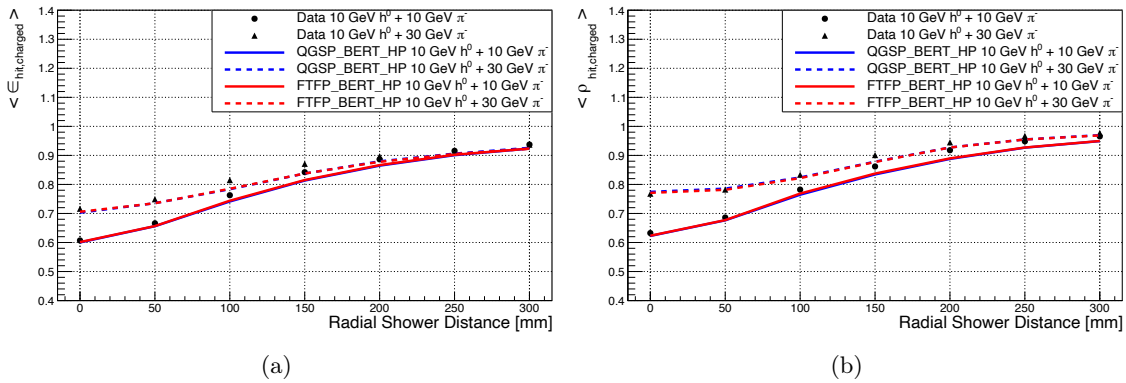
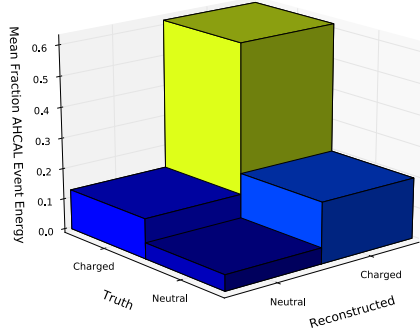


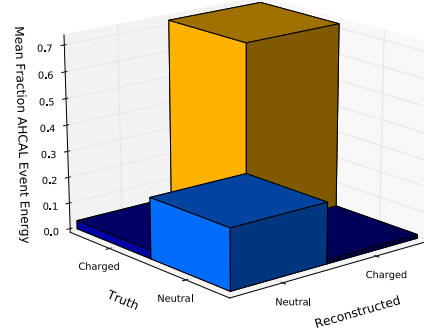
Figure D.12: Mean hit reconstruction efficiency (a) and purity (b) for 10 GeV or 30 GeV charged pion showers in the vicinity of 10 GeV pseudo-neutral hadrons over radial shower distance for investigated beam test and simulation samples.

10 GeV Neutral + 30 GeV Charged, 0mm, Confusion 3D, Data



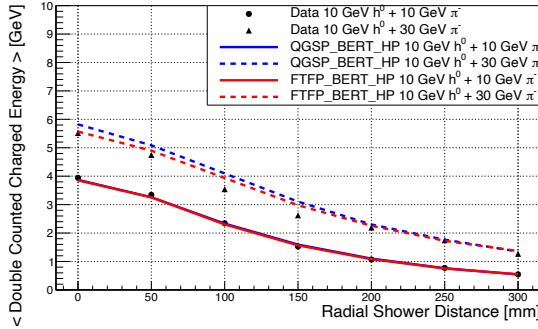
(a)

10 GeV Neutral + 30 GeV Charged, 300mm, Confusion 3D, Data

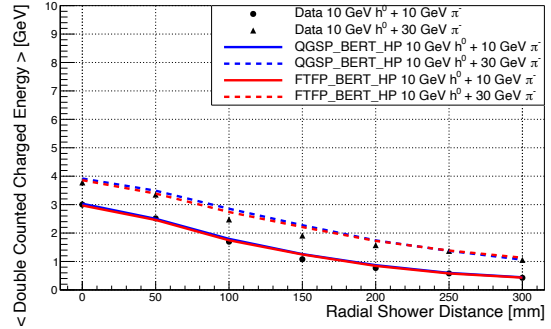


(b)

Figure D.13: Mean confusion matrices normalised to total two particle event energy for data samples of 10 GeV pseudo-neutral hadrons overlaid with 30 GeV charged pion showers at radial distance: (a) 0 – 25 mm (b) 275 – 325 mm



(a)



(b)

Figure D.14: Mean absolute double counted charged confusion energy over radial shower distance for data and simulation samples with shower start difference of pseudo-neutral hadron and charged pion (a)  $< 10$  layers. (b)  $\geq 10$  layers.

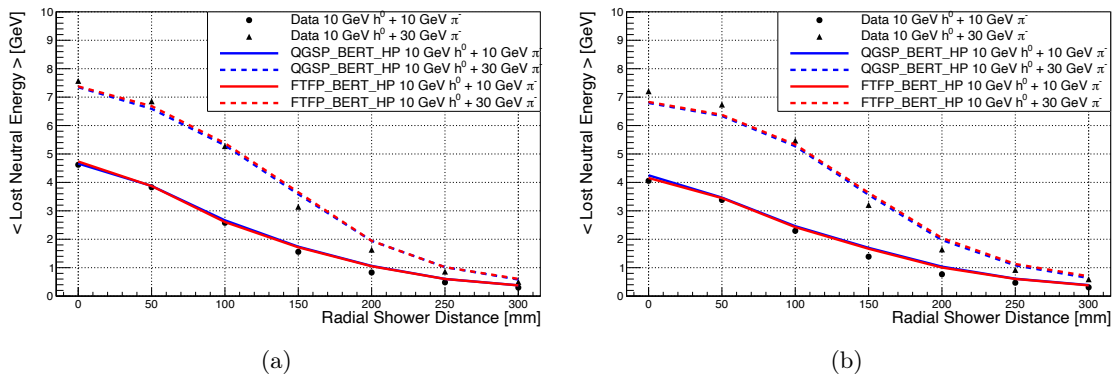
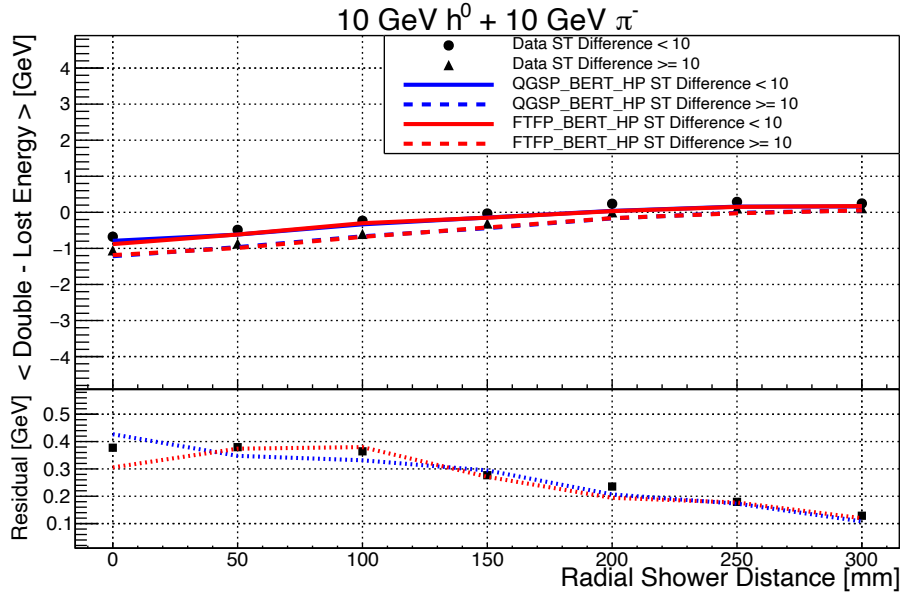
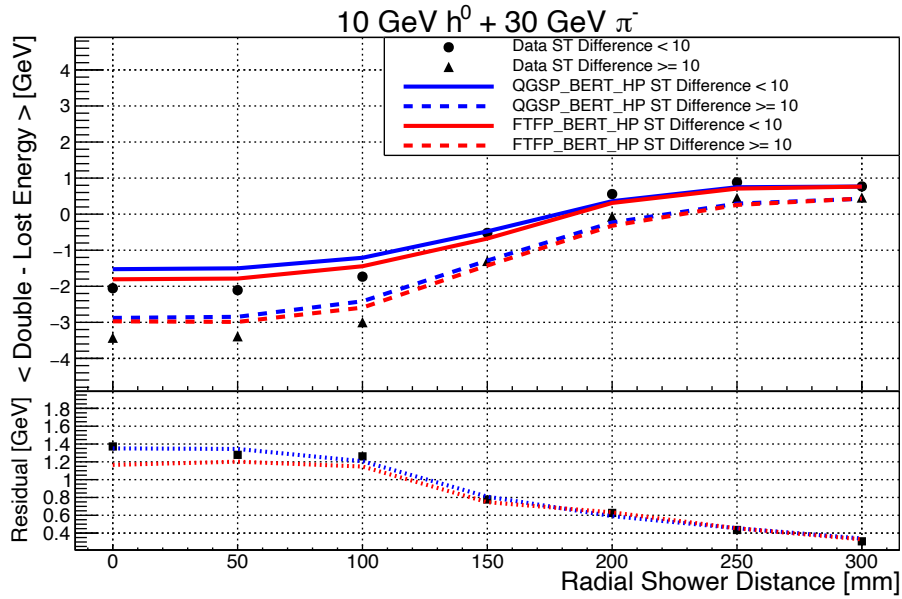


Figure D.15: Mean absolute lost neutral confusion energy over radial shower distance for data and simulation samples with shower start difference of pseudo-neutral hadron and charged pion (a)  $< 10$  layers. (b)  $\geq 10$  layers.

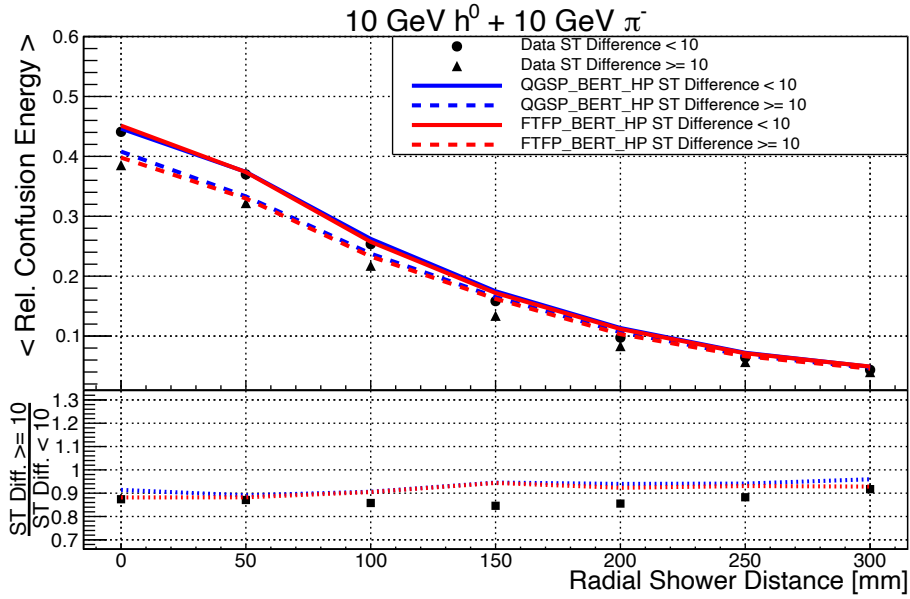


(a)

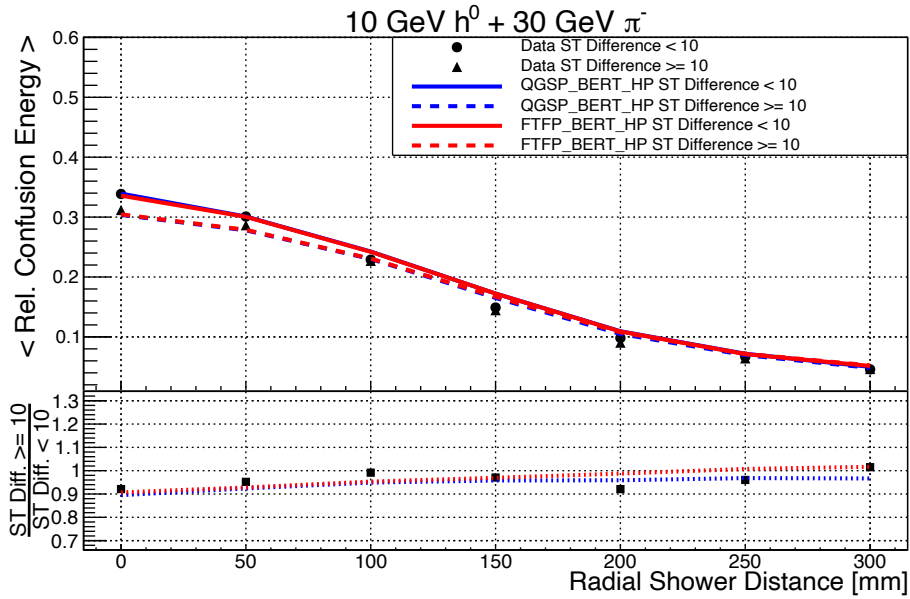


(b)

Figure D.16: Mean absolute confusion type difference of double counted charged and lost neutral confusion energy for 10 GeV pseudo-neutral hadrons in the vicinity of 10 GeV (a) or 30 GeV (b) charged pion showers over radial shower distance for data and simulation samples with shower start difference of pseudo-neutral hadron and charged pion < 10 layers (ST Difference < 10) and  $\geq 10$  layers (ST Difference  $\geq 10$ ).



(a)



(b)

Figure D.17: Mean fraction of confusion energy in two particle events for 10 GeV pseudo-neutral hadrons in the vicinity of 10 GeV (a) or 30 GeV (b) charged pion showers over radial shower distance for data and simulation samples with shower start difference of pseudo-neutral hadron and charged pion < 10 layers (ST Difference < 10) and  $\geq 10$  layers (ST Difference  $\geq 10$ ).



# E Additional Plots and Tables: Studies of Different PandoraPFA Settings and Hit Energy Thresholds

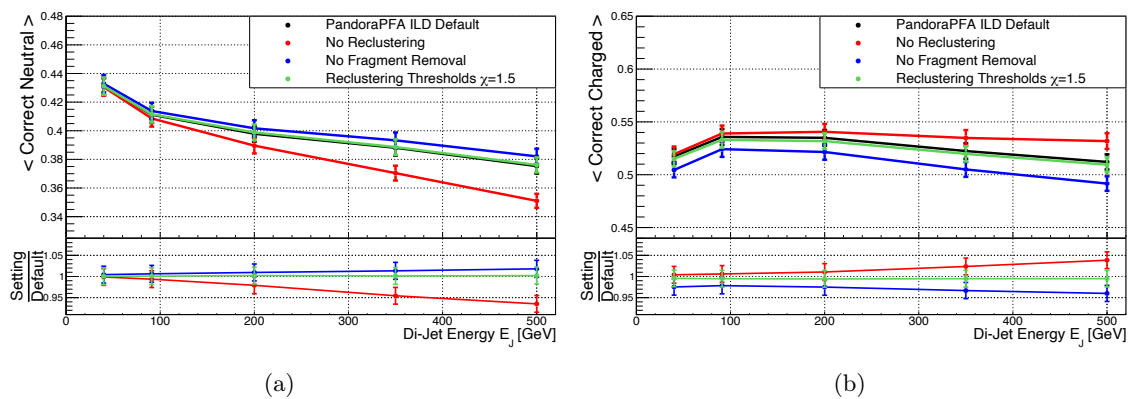


Figure E.1: Mean fraction of correct energy in event over di-jet energy of simulated  $uds$  ILD di-jet events for different PandoraPFA algorithm settings: (a) Neutral energy. (b) Charged energy.

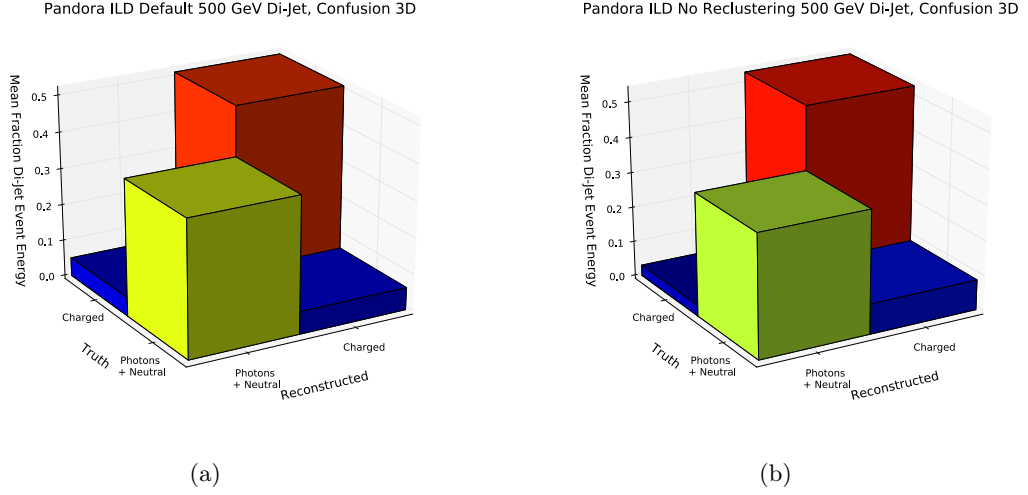


Figure E.2: Confusion matrices showing mean fraction of confused and correctly reconstructed event energy for simulated 500 GeV ILD di-jet events reconstructed with: (a) PandoraPFA default settings. (b) PandoraPFA no re-clustering settings. Labels correspond to type of hadron.

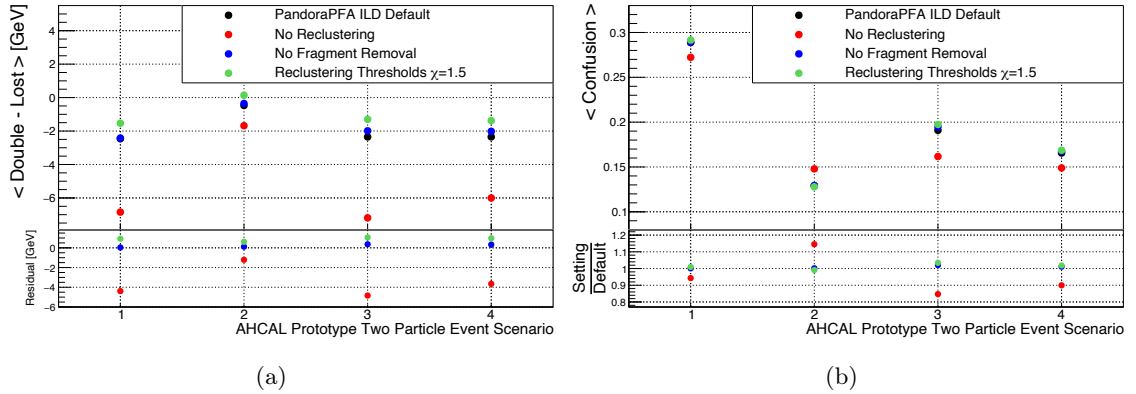


Figure E.3: Confusion parameters over AHCAL two particle data event scenarios for different PandoraPFA algorithm settings: (a) Mean absolute difference of double counted charged and lost neutral confusion energy. (b) Mean fraction of confusion energy in events.

1: 10 GeV  $h^0$  + 30 GeV  $\pi^-$ ,  $r = 0 - 50$  mm    2: 10 GeV  $h^0$  + 30 GeV  $\pi^-$ ,  $r = 125 - 175$  mm  
 3: 10 GeV  $h^0$  + 60 GeV  $\pi^-$ ,  $r = 0 - 50$  mm    4: 10 GeV  $h^0$  + 60 GeV  $\pi^-$ ,  $r = 125 - 175$  mm

Calibration Constant	Parameter
EcalBarrelMip	0.0001575
EcalEndcapMip	0.0001575
EcalRingMip	0.0001575
HcalBarrelMip	0.0004925
HcalEndcapMip	0.0004725
HcalRingMip	0.0004875
EcalBarrelEnergyFactors	0.006352 0.01290
EcalEndcapEnergyFactors	0.006722 0.01365
EcalRingEnergyFactors	0.006654 0.01352
HcalBarrelEnergyFactors	0.02878
HcalEndcapEnergyFactors	0.02858
HcalRingEnergyFactors	0.03499
MuonCalibration	56.7
PandoraEcalToMip	153.8460
PandoraHcalToMip	37.1747
PandoraMuonToMip	10.5263
PandoraSoftwareCompensationWeights	1.5912 -0.02819 0.0002506 -0.04242 0.0003351 -2.061e-05 0.1486 0.1996 -0.06972

Table E.1: ILD default constants for detector model ILD\_15\_o1\_v02 not affected by increased hit energy thresholds on PandoraPFA level. Given values are rounded for tabular listing.

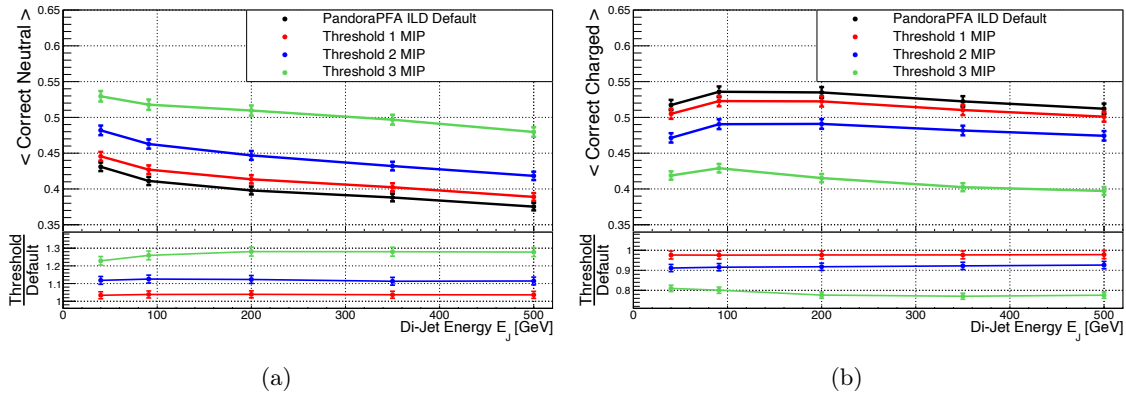


Figure E.4: Mean fraction of correct energy in event over di-jet energy of simulated ILD di-jet events for different hit energy thresholds: (a) Neutral energy. (b) Charged energy.



# Bibliography

- [1] The CALICE Collaboration. “Design, Construction and Commissioning of a Technological Prototype of a Highly Granular SiPM-on-tile Scintillator-Steel Hadronic Calorimeter”, in collaboration review, 2022.
- [2] O. Pinto. “Shower Shapes in a Highly Granular Analog Hadron Calorimeter”, PhD Thesis in progress, University of Hamburg, Hamburg, 2022.
- [3] A. Elkhali. “Analog Hadronic Calorimeter for a Future Linear Collider”, PhD Thesis, Wuppertal University, Wuppertal, 2020. DOI: 10.25926/2jx6-f298.
- [4] L. Emberger. “Time Calibration and Timing Studies with the CALICE AHCAL Technological Prototype” (preliminary title), PhD Thesis in progress, Technical University Munich, Munich, 2022.
- [5] V. Bocharnikov. “Studies on Single Shower Substructure with Graph Networks” (preliminary title), PhD Thesis in progress, NRNU MePhI, Moscow, 2022.
- [6] J. M. Mikhaeil. “Topological Shower Reconstruction in a Highly Granular Calorimeter with Optical Readout”, Bachelor Thesis, Universität Heidelberg, Heidelberg, 2019.
- [7] S. Huck. “Investigations of muon detection with the CALICE Analog Hadron Calorimeter”, Master Thesis, University of Hamburg, Hamburg, 2019. URL: [https://www.physik.uni-hamburg.de/en/iexp/gruppe-garutti/publikationen/bachelor-master-theses/\\_files/2019-master-huck-saiva.pdf](https://www.physik.uni-hamburg.de/en/iexp/gruppe-garutti/publikationen/bachelor-master-theses/_files/2019-master-huck-saiva.pdf).
- [8] L. Liu. “Beam Tracking in Test Beam Experiment on ILD AHCAL Large Prototype”, Contribution to CALICE Collaboration Meeting, Shanghai, China, 2018. URL: [https://agenda.linearcollider.org/event/7799/contributions/42265/attachments/33591/51486/caliceMeeting2018\\_liu.pdf](https://agenda.linearcollider.org/event/7799/contributions/42265/attachments/33591/51486/caliceMeeting2018_liu.pdf).
- [9] L. Liu. “Beam Tracking with Delay Wire Chambers”, Contribution to AHCAL Main Meeting, DESY, Hamburg, 2018. URL: [https://agenda.linearcollider.org/event/8082/contributions/43032/attachments/34070/52422/AHCALmain\\_liu.pdf](https://agenda.linearcollider.org/event/8082/contributions/43032/attachments/34070/52422/AHCALmain_liu.pdf).
- [10] H. Geiger and E. Marsden. “On a Diffuse Reflection of the alpha particles”, Proc. Royal Soc. 82, pp. 495-500, 1909. DOI: 10.1098/rspa.1909.0054.
- [11] A. Salam and J. C. Ward. “Weak and electromagnetic interactions”, Nuovo Cim 11, pp. 568-577, 1959. DOI: 10.1007/BF02726525.

- [12] S. L. Glashow. “Partial-symmetries of weak interactions”, Nucl. Phys. 22, pp. 579-588, 1961. DOI: 10.1016/0029-5582(61)90469-2.
- [13] A. Salam and J. C. Ward. “Electromagnetic and weak interactions”, Phys. Lett. B13.2, pp. 168-171, 1964. DOI: 10.1016/0031-9163(64)90711-5.
- [14] S. Weinberg. “A Model of Leptons”, Phys. Rev. Lett. 19, 1264, 1967. DOI: 10.1103/PhysRevLett.19.1264.
- [15] H. Fritzsch *et al.* “Advantages of the color octet gluon picture”, Phys. Lett. B47.4, pp. 365-368, 1973. DOI: 10.1016/0370-2693(73)90625-4.
- [16] ATLAS Collaboration. “Observation of a new particle in the search for the Standard Model Higgs boson with the ATLAS detector at the LHC”, Phys. Lett. B716.1, pp. 1-29, 2012. DOI: 10.1016/j.physletb.2012.08.020.
- [17] CMS Collaboration. “Observation of a new boson at a mass of 125GeV with the CMS experiment at the LHC”, Phys. Lett. B716.1, pp. 30-61, 2012. DOI: 10.1016/j.physletb.2012.08.021.
- [18] MissMJ, Nasfarley88, *et al.* “Standard Model of Elementary Particles”, Licensed under CC BY 3.0, 2014. URL: [https://commons.wikimedia.org/wiki/File:Standard\\_Model\\_of\\_Elementary\\_Particles.svg#/media/File:Standard\\_Model\\_of\\_Elementary\\_Particles\\_modified\\_version.svg](https://commons.wikimedia.org/wiki/File:Standard_Model_of_Elementary_Particles.svg#/media/File:Standard_Model_of_Elementary_Particles_modified_version.svg).
- [19] J. Christman. “The Weak Interaction”, Scientific American, 1959. URL: [http://www.physnet.org/modules/pdf\\_modules/m281.pdf](http://www.physnet.org/modules/pdf_modules/m281.pdf).
- [20] H. Yukawa. “On the Interaction of Elementary Particles I”, Proc. Phys. Math. Soc. Jap. 17, pp. 48-57, 1935. DOI: 10.1143/PTPS.1.1.
- [21] H. D. Politzer. “Reliable Perturbative Results for Strong Interactions?”, Phys. Rev. Lett. 30, 1346, 1973. DOI: 10.1103/PhysRevLett.30.1346.
- [22] G. Hanson *et al.* “Evidence of Jet Structure in Hadron Production by  $e^+e^-$  Annihilation”, Phys. Rev. Lett. 35, 1609, 1975. DOI: 10.1103/PhysRevLett.35.1609.
- [23] David Griffiths. “Introduction to Elementary Particles”, John Wiley & Sons, 2020. ISBN: 9783527834631.
- [24] P. W. Higgs. “Broken Symmetries and the Masses of Gauge Bosons”, Phys. Rev. Lett. 13.16, pp. 508-509, 1964. DOI: 10.1103/PhysRevLett.13.508.
- [25] F. Englert and R. Brout. “Broken Symmetry and the Mass of Gauge Vector Mesons”, Phys. Rev. Lett. 13.9, pp. 321-323, 1964. DOI: 10.1103/PhysRevLett.13.321.
- [26] G. S. Guralnik *et al.* “Global Conservation Laws and Massless Particles”, Phys. Rev. Lett. 13, 585, 1964. DOI: 10.1103/PhysRevLett.13.585.
- [27] K. G. Begeman *et al.* “Extended rotation curves of spiral galaxies: dark haloes and modified dynamics”, Monthly Notices of the Royal Astronomical Society 249.3, pp. 523-537, 1991. DOI: 10.1093/mnras/249.3.523.

- [28] G. Giesen *et al.* “CMB photons shedding light on dark matter”, *Journal of Cosmology and Astroparticle Physics* 12, 008, 2012. DOI: 10.1088/1475-7516/2012/12/008.
- [29] U. Dore and D. Orestano. “Experimental results on neutrino oscillations”, *Rep. Prog. Phys.* 71, 106201, 2008. DOI: 10.1088/0034-4885/71/10/106201.
- [30] A. D. Sakharov. “Violation of CP Invariance, C asymmetry, and baryon asymmetry of the universe”, *Pisma Zh. Eksp. Teor. Fiz.* 5, pp. 32-35, 1967. DOI: 10.1070/PU1991v034n05ABEH002497.
- [31] G. Apollinari *et al.* “High Luminosity Large Hadron Collider HL-LHC”, arXiv:1705.08830 [physics.acc-ph], 2017. DOI: 10.5170/CERN-2015-005.1.
- [32] L. Evans and P. Bryant. “LHC Machine”, *JINST* 3, S08001, 2008. DOI: 10.1088/1748-0221/3/08/s08001.
- [33] S. Myers. “The LEP Collider, from design to approval and commissioning”, *CERN Yellow Reports: Monographs*, 1991. DOI: 10.5170/CERN-1991-008.
- [34] M. Benedikt *et al.* “FCC-ee: The Lepton Collider: Future Circular Collider Conceptual Design Report Volume 2”, *Eur. Phys. J. Spec. Top.* 228, pp. 261-623, 2019. DOI: 10.1140/epjst/e2019-900045-4.
- [35] CEPC Study Group. “CEPC Conceptual Design Report: Volume 1 - Accelerator”, arXiv:1809.00285 [physics.acc-ph], 2018. URL: <https://arxiv.org/abs/1809.00285>.
- [36] H. Baer, T. Barklow, K. Fujii, *et al.* “The International Linear Collider Technical Design Report - Volume 2: Physics”, 2013. URL: <https://linearcollider.org/files/images/pdf/Physics.pdf>.
- [37] K. A. Olive *et al.* (Particle Data Group). “Review of Particle Physics”, *Chinese Physics C* Vol. 38, No. 9, 2014. DOI: 10.1088/1674-1137/38/9/090001.
- [38] J. Yan *et al.* “Measurement of the Higgs boson mass and  $e^+e^- \rightarrow ZH$  cross section using  $Z \rightarrow \mu^+\mu^-$  and  $Z \rightarrow e^+e^-$  at the ILC”, *Phys. Rev. D* 94, 113002, 2016. DOI: 10.1103/PhysRevD.94.113002.
- [39] K. Fujii *et al.* “Physics Case for the International Linear Collider”, arXiv:1506.05992 [physics.ins-det], 2015. URL: <https://arxiv.org/abs/1506.05992>.
- [40] M. A. Thomson. “Model-independent measurement of the  $e^+e^- \rightarrow HZ$  cross section at a future  $e^+e^-$  linear collider using hadronic Z decays”, *Eur. Phys. J. C* 76, 72, 2016. DOI: 10.1140/epjc/s10052-016-3911-5.
- [41] M. Farina *et al.* “Higgs couplings and naturalness”, *Phys. Rev. D* 90, 015014, 2014. DOI: 10.1103/PhysRevD.90.015014.
- [42] C. F. Dürig. “Measuring the Higgs Self-coupling at the International Linear Collider”, PhD Thesis, University of Hamburg, Hamburg, 2016. DOI: 10.3204/PUBDB-2016-04283.
- [43] R. Covarelli *et al.* “Vector-Boson Scattering at the LHC: unravelling the Electroweak sector”, *International Journal of Modern Physics A*, 36, 2130009, 2021. DOI: 10.1142/S0217751X2130009X.

- [44] The ATLAS, CDF, CMS, D0 Collaborations. “First combination of Tevatron and LHC measurements of the top-quark mass”, arXiv:1403.4427 [hep-ex], 2014. URL: <https://arxiv.org/abs/1403.4427>.
- [45] F. Bezrukov *et al.* “The Standard Model Higgs boson as the inflaton”, Phys. Lett. B 659, pp. 703-706, 2008. DOI: 10.1016/j.physletb.2007.11.072.
- [46] A. De Simone *et al.* “Running Inflation in the Standard Model”, Phys. Lett. B 678, pp. 1-8, 2009. DOI: 10.1016/j.physletb.2009.05.054.
- [47] M. Habermehl. “Dark Matter at the International Linear Collider”, PhD Thesis, University of Hamburg, Hamburg, 2018. DOI: 10.3204/PUBDB-2018-05723.
- [48] M.T. Nunez Pardo de Vera. “ILC as a SUSY discovery and precision instrument”, arXiv:2012.10155 [hep-ex], 2020. URL: <https://arxiv.org/abs/2012.10155>.
- [49] T. Behnke, J. E. Brau, B. Foster, *et al.* “The International Linear Collider Technical Design Report - Volume 1: Executive Summary”, arXiv:1306.6327 [physics.ins-det], 2013. URL: <https://arxiv.org/abs/1306.6327>.
- [50] L. Evans and S. Michizone. “The International Linear Collider Machine Staging Report 2017”, Addendum to the International Linear Collider Technical Design Report published in 2013, arXiv:1711.00568 [physics.ins-det], 2017. URL: <https://arxiv.org/abs/1711.00568>.
- [51] K. Fujii *et al.* “Physics Case for the 250 GeV Stage of the International Linear Collider”, arXiv:1710.07621 [hep-ex], 2018. URL: <https://arxiv.org/abs/1710.07621>.
- [52] C. Adolphsen *et al.* “The International Linear Collider Technical Design Report - Volume 3.1: Accelerator R&D in the Technical Design Phase”, arXiv:1306.6353 [physics.acc-ph], 2013. URL: <https://arxiv.org/abs/1306.6353>.
- [53] T. Hellert *et al.* “Analysis of multibunch free electron laser operation”, Phys. Rev. Accel. Beams, Vol. 20, Issue 9, 090702, 2017. DOI: 10.1103/PhysRevAccelBeams.20.090702.
- [54] M. Altarelli *et al.* “XFEL: The European X-Ray Free-Electron Laser. Technical design report”, 2006. DOI: 10.3204/DESY\_06-097.
- [55] International Linear Collider International Development Team. “Proposal for the ILC Preparatory Laboratory (Pre-lab)”, arXiv:2106.00602 [physics.acc-ph], 2021. DOI: 10.5281/zenodo.4742043.
- [56] T. Behnke, J. E. Brau, P. N. Burrows, *et al.* “The International Linear Collider Technical Design Report - Volume 4: Detectors”, arXiv:1306.6329 [physics.ins-det], 2013. URL: <https://arxiv.org/abs/1306.6329>.
- [57] Y. Li *et al.* “CMOS sensors for the vertex detector of the future international linear collider”, Nucl. Instrum. Meth. A572, pp. 300-304, 2007. DOI: 10.1016/j.nima.2006.10.324.
- [58] M. Boronat. “DEPFET pixel detector for future e+e- experiments”, Nuclear and Particle Physics Proceedings Vol. 273-275, pp. 982-987, 2006. DOI: 10.1016/j.nuclphysbps.2015.09.154.

- [59] F. Sauli. “GEM: A new concept for electron amplification in gas detectors”, Nucl. Instrum. Meth. A386, pp. 531-534, 1997. DOI: 10.1016/S0168-9002(96)01172-2.
- [60] Y. Giomataris *et al.* “MICROMEAS: a high-granularity position-sensitive gaseous detector for high particle-flux environments”, Nucl. Instrum. Meth. A376, pp. 29-35, 1996. DOI: 10.1016/0168-9002(96)00175-1.
- [61] M. Breidenbach *et al.* “Updating the SiD Detector concept”, arXiv:2110.09965 [physics.ins-det], 2021. URL: <https://arxiv.org/abs/2110.09965>.
- [62] M. Aicheler, P. Burrows, M. Draper, *et al.* “A Multi-TeV Linear Collider Based on CLIC Technology : CLIC Conceptual Design Report”, CERN Yellow Reports: Monographs, 2012. DOI: 10.5170/CERN-2012-007.
- [63] L. Linssen *et al.* “Physics and Detectors at CLIC: CLIC Conceptual Design Report”, arXiv:1202.5940 [physics.ins-det], 2012. URL: <https://arxiv.org/abs/1202.5940>.
- [64] F. Pitters. “The CLIC Detector Concept”, CERN-Proceedings-2017-001, arXiv:1802.06008, 2017. DOI: 10.23727/CERN-Proceedings-2017-001.
- [65] R. Wigmans. “Calorimetry: Energy Measurement in Particle Physics”, Second Edition, International Series of Monographs on Physics Book 168, Oxford University Press, 2017. DOI: 10.1093/oso/9780198786351.001.0001.
- [66] B. L. Berman and S.C. Fultz. “Measurements of the giant dipole resonance with monoenergetic photons”, Rev. Mod. Phys., Volume 47, pp. 713-761, 1975. DOI: 10.1103/RevModPhys.47.713.
- [67] C. Patrignani *et al* (Particle Data Group). “Review of Particle Physics”, Chinese Physics C, Vol. 40, Nr. 10, 2016. DOI: 10.1088/1674-1137/40/10/100001.
- [68] E. Brianne. “Time development of hadronic showers in a Highly Granular Analog Hadron Calorimeter”, PhD Thesis, University of Hamburg, Hamburg, 2018. DOI: 10.3204/PUBDB-2018-02769.
- [69] L. Cerrito. “Radiation and Detectors: Introduction to the Physics of Radiation and Detection Devices”, Springer, 2017. DOI: 10.1007/978-3-319-53181-6.
- [70] P. S. Auchincloss *et al.* “A study of the energy dependence of the mean, truncated mean, and most probable energy deposition of high-energy muons in sampling calorimeters”, Nucl. Instrum. Meth. A343, pp. 463-469, 1994. DOI: 10.1016/0168-9002(94)90225-9.
- [71] Y. Israeli. “Energy Reconstruction in Highly Granular Calorimeters for Future Electron-Positron Colliders”, PhD Thesis, Technical University Munich, Munich, 2019. URL: <http://nbn-resolving.de/urn/resolver.pl?urn:nbn:de:bvb:91-diss-20190131-1459326-1-7>.
- [72] I. C. Brock and T. Schörner-Sadenius. “Physics at the Terascale”, Wiley-VCH, 2011. DOI: 10.1002/978-3-527-63496-5.
- [73] S. Agostinelli *et al.* “GEANT4 - a simulation toolkit”, Nucl. Instrum. Meth. A506, pp. 250-303, 2003. DOI: 10.1016/S0168-9002(03)01368-8.

- [74] J. Allison *et al.* “Recent developments in GEANT4”, Nucl. Instrum. Meth. A835, pp. 186-225, 2016. DOI: 10.1016/j.nima.2016.06.125.
- [75] J. Allison *et al.* “GEANT4 developments and applications”, IEEE Transactions on Nuclear Science 53, pp. 270-278, 2006. DOI: 10.1109/TNS.2006.869826.
- [76] J. Apostolakis *et al.* “Progress in Geant4 Electromagnetic Physics Modelling and Validation”, Journal of Physics: Conference Series 664(7), 072021, 2015. DOI: 10.1088/1742-6596/664/7/072021.
- [77] The CALICE Collaboration. “DHCAL with minimal absorber: measurements with positrons”, Journal of Physics: Conference Series 928(1), 012037, 2015. DOI: 10.1088/1742-6596/928/1/012037.
- [78] The CALICE Collaboration. “Validation of GEANT4 Monte Carlo Models with a Highly Granular Scintillator-Steel Hadron Calorimeter”, JINST 8 P07005, 2013. DOI: 10.1088/1748-0221/8/07/P07005.
- [79] GEANT4 Collaboration. “Physics Reference Manual Release 10.7”, December 2020. URL: <https://geant4-userdoc.web.cern.ch/UsersGuides/PhysicsReferenceManual/fo/PhysicsReferenceManual.pdf>.
- [80] N. Feege. “Low-energetic Hadron Interactions in a Highly Granular Calorimeter”, Ph.D. Thesis, University of Hamburg, Hamburg, 2011. URL: <https://bib-pubdb1.desy.de/record/94643/>.
- [81] A. Heikkinen *et al.* “Bertini intra-nuclear cascade implementation in Geant4”, Proceedings for 13th International Conference on Computing in High-Energy and Nuclear Physics (CHEP 2003), eConf C0303241 MOMT008, 2003. URL: <https://arxiv.org/abs/nucl-th/0306008>.
- [82] G. Folger *et al.* “String parton models in Geant4”, Proceedings for 13th International Conference on Computing in High-Energy and Nuclear Physics (CHEP 2003), eConf C0303241 MOMT007, 2003. URL: <https://arxiv.org/abs/nucl-th/0306007>.
- [83] B. Anderssons *et al.* “A model for low-pT hadronic reactions with generalizations to hadron-nucleus and nucleus-nucleus collisions”, Nuclear Physics B 281, pp. 289-309, 1987. DOI: 10.1016/0550-3213(87)90257-4.
- [84] N. S. Amelin *et al.* “Semihard collisions in Monte Carlo quark gluon string model”, Phys. Rev. D 46, pp. 4873-4881, 1992. DOI: 10.1103/PhysRevD.46.4873.
- [85] J. M. Quesada *et al.* “Recent Developments in Pre-Equilibrium and De-Excitation Models in Geant4”, Progress in Nuclear Science and Technology 2, pp. 936-941, 2011. DOI: 10.15669/pnst.2.936.
- [86] J. Apostolakis *et al.* “GEANT4 Physics lists for HEP”, IEEE Nuclear Science Symposium Conference Record, pp. 833-836, 2008. DOI: 10.1109/NSSMIC.2008.4774655.
- [87] J. Yarba. “Recent Developments and Validation of Geant4 Hadronic Physics”, Journal of Physics: Conference Series 396, 022060, 2012. DOI: 10.1088/1742-6596/396/2/022060.

- 
- [88] O. Hartbrich. “Scintillator Calorimeters for a Future Linear Collider Experiment”, PhD Thesis, Bergische Universität Wuppertal, Wuppertal, 2016. DOI: 10.3204/PUBDB-2016-02800.
- [89] C. W. Fabjan and F. Gianotti. “Calorimetry for particle physics”, *Rev. Mod. Phys.* 75, pp. 1243-1286, 2003. DOI: 10.1103/RevModPhys.75.1243.
- [90] C. Biino. “The CMS Electromagnetic Calorimeter: overview, lessons learned during Run 1 and future projections”, *Journal of Physics: Conference Series* 587(1), 012001, 2015. DOI: 10.1088/1742-6596/587/1/01200.
- [91] The ATLAS Collaboration *et al.* “The ATLAS Experiment at the CERN Large Hadron Collider”, *JINST* 3 S08003, 2007. DOI: 10.1088/1748-0221/3/08/s08003.
- [92] The CMS Collaboration. “Performance of the CMS Hadron Calorimeter with Cosmic Ray Muons and LHC Beam Data”, *JINST* 5 T03012, 2010. DOI: 10.1088/1748-0221/5/03/T03012.
- [93] S. N. Karpov on behalf of the ATLAS Collaboration. “Simulation and validation of the ATLAS Tile Calorimeter response”, *JINST* 9 C09018, 2014. DOI: 10.1088/1748-0221/9/09/C09018.
- [94] A. Bernstein *et al.* “Beam tests of the ZEUS barrel calorimeter”, *Nucl. Instrum. Meth.* A336, pp. 23-52, 1993. DOI: 10.1016/0168-9002(88)91072-8.
- [95] W. Braunschweig *et al.* “Results from a test of a PbCu liquid argon calorimeter”, *Nucl. Instrum. Meth.* A265, pp. 419-434, 1988. DOI: 10.1016/S0168-9002(98)90008-0.
- [96] The CALICE Collaboration. “Hadronic energy resolution of a highly granular scintillator-steel hadron calorimeter using software compensation techniques”, *JINST* 7 P09017, 2012. DOI: 10.1088/1748-0221/7/09/P09017.
- [97] R. Wigmans. “The dual-readout approach to calorimetry”, *Nucl. Instrum. Meth.* A732, pp. 475-479, 2013. DOI: 10.1016/j.nima.2013.04.005.
- [98] R. Wigmans. “The DREAM project - Towards the ultimate in calorimetry”, *Nucl. Instrum. Meth.* A617, pp. 129-133, 2010. DOI: 10.1016/j.nima.2009.09.118.
- [99] J. S. Marshall, A. Münnich and M. A. Thomson. “Performance of Particle Flow Calorimetry at CLIC”, *Nucl. Instrum. Meth.* A700, pp. 153-162, 2013. DOI: 10.1016/j.nima.2012.10.038.
- [100] M. A. Thomson. “Particle Flow Calorimetry and the PandoraPFA Algorithm”, *Nucl. Instrum. Meth.* A611, pp. 25-40, 2009. DOI: 10.1016/j.nima.2009.09.009.
- [101] A. Ebrahimi. “Jet Energy Measurements at ILC: Calorimeter DAQ Requirements and Application in Higgs Boson Mass Measurements”, PhD Thesis, University of Hamburg, Hamburg, 2017. DOI: 10.3204/PUBDB-2017-11891.
- [102] J. S. Marshall *et al.* “Pandora - LC Reconstruction Documentation”, December 2021. URL: [https://github.com/PandoraPFA/Documentation/blob/master/Pandora\\_LC\\_Reconstruction.pdf](https://github.com/PandoraPFA/Documentation/blob/master/Pandora_LC_Reconstruction.pdf).

- [103] J. S. Marshall and M. A. Thomson. “The Pandora Particle Flow Algorithm”, Proceedings of CHEF2013 - Calorimetry for the High Energy Frontier, 2013. URL: <https://arxiv.org/abs/1308.4537>.
- [104] R. Acciarri *et al.* “The Pandora multi-algorithm approach to automated pattern recognition of cosmic-ray muon and neutrino events in the MicroBooNE detector”, Eur. Phys. J. C78, 82, 2018. DOI: 10.1140/epjc/s10052-017-5481-6.
- [105] I. Abt *et al.* “Energy flow and charged particle spectra in deep inelastic scattering at HERA”, Zeitschrift fuer Physik 63, pp. 377-389, 1994. DOI: 10.1007/BF01580319.
- [106] CMS Collaboration. “Particle-flow reconstruction and global event description with the CMS detector”, JINST 12, P10003, 2017. DOI: 10.1088/1748-0221/12/10/P10003.
- [107] S. Green. “Calorimetry at a Future Linear Collider”, PhD Thesis, University of Cambridge, Cambridge, 2017. DOI: 10.17863/CAM.15859.
- [108] H. L. Tran *et al.* “Software compensation in Particle Flow reconstruction”, Eur. Phys. J. C77, 698, 2017. DOI: 10.1140/epjc/s10052-017-5298-3.
- [109] F. Gaede. “Marlin and LCCD: Software tools for the ILC”, Nucl. Instrum. Meth. A559, pp. 177-180, 2006. DOI: 10.1016/j.nima.2005.11.138.
- [110] B. Li *et al.* “April: A novel Algorithm for Particle Reconstruction at ILC”, Proceeding of third conference on Calorimetry for the High Energy Frontier (CHEF), Fukuoka, Japan, 2019. DOI: 10.1088/1748-0221/15/05/C05016.
- [111] CALICE Collaboration. CALICE Collaboration Webpage, August 2021. URL: <https://twiki.cern.ch/twiki/bin/view/CALICE/CaliceCollaboration>.
- [112] The CMS Collaboration. “The Phase-2 Upgrade of the CMS endcap calorimeter: Technical Design Report”, CERN-LHCC-2017-023, CMS-TDR-019, April 2018. URL: <https://cds.cern.ch/record/2293646/files/CMS-TDR-019.pdf>.
- [113] The CALICE Collaboration. “Design and Electronics Commissioning of the Physics Prototype of a Si-W Electromagnetic Calorimeter for the International Linear Collider”, JINST 3 P08001, 2008. DOI: 10.1088/1748-0221/3/08/P08001.
- [114] The CALICE Collaboration. “Performance of the first prototype of the CALICE scintillator strip electromagnetic calorimeter”, Nucl. Instrum. Meth. A763, pp. 278-289, 2014. DOI: 10.1016/j.nima.2014.06.039.
- [115] The CALICE Collaboration. “First results of the CALICE SDHCAL technological prototype”, Nucl. Instrum. Meth. A608, pp. 372-383, 2009. DOI: <https://doi.org/10.1016/j.nima.2009.07.026>.
- [116] K. Kotera, *et al.* “A novel strip energy splitting algorithm for the fine granular readout of a scintillator strip electromagnetic calorimeter”, Nucl. Instrum. Meth. A789, pp. 158-164, 2015. DOI: 10.1016/j.nima.2015.04.001.
- [117] The CALICE Collaboration. “Construction and Response of a Highly Granular Scintillator-based Electromagnetic Calorimeter”, Nucl. Instrum. Meth. A887, pp. 150-168, 2018. DOI: 10.1016/j.nima.2018.01.016.

- [118] G. Drake, *et al.* “Resistive Plate Chambers for hadron calorimetry: Tests with analog readout”, Nucl. Instrum. Meth. A578, pp. 88-97, 2007. DOI: 10.1016/j.nima.2007.04.160.
- [119] B. Bilki for the CALICE Collaboration. “Construction and Testing of the CALICE Digital Hadron Calorimeter”, Proceedings of International Conference on Calorimetry for the High Energy Frontier (CHEF 2013), pp. 168-174, Paris, France, 2013. URL: <https://inspire.hep.net/files/d236d6ca330058eed08c7fb99f4db9fc>.
- [120] B. Bilki for the CALICE Collaboration. “CALICE Digital Hadron Calorimeter: Calibration and Response to Hadrons”, Journal of Physics Conference Series, Vol. 587 No. 1, pp. 012038, 2015. DOI: 10.1088/1742-6596/587/1/012038.
- [121] The CALICE Collaboration. “Analysis of Testbeam Data of the Highly Granular RPC-Steel CALICE Digital Hadron Calorimeter and Validation of Geant4 Monte Carlo Models”, Nucl. Instrum. Meth. A939, pp. 89-106, 2019. DOI: 10.1016/j.nima.2019.05.013.
- [122] The CALICE Collaboration. “Construction and commissioning of a technological prototype of a high-granularity semi-digital hadronic calorimeter”, JINST 10 P10039, 2015. DOI: 10.1088/1748-0221/10/10/p10039.
- [123] The CALICE Collaboration. “First results of the CALICE SDHCAL technological prototype”, JINST 11 P04001, 2016. DOI: 10.1088/1748-0221/11/04/p04001.
- [124] C. Neubueser. “Comparison of Two Highly Granular Hadronic Calorimeter Concepts”, PhD Thesis, University of Hamburg, Hamburg, 2016. DOI: 10.3204/PUBDB-2016-05499.
- [125] The CALICE Collaboration. “Construction and Commissioning of the CALICE Analog Hadron Calorimeter Prototype”, JINST 5 P05004, 2010. DOI: 10.1088/1748-0221/5/05/P05004.
- [126] F. Sefkow and F. Simon for the CALICE Collaboration. “A highly granular SiPM-on-tile calorimeter prototype”, Proceedings of CALOR 2018, Eugene, OR, USA, 2018. DOI: 10.1088/1742-6596/1162/1/012012.
- [127] CALICE Collaboration. “A high granularity scintillator hadronic-calorimeter with SiPM readout for a linear collider detector”, Nucl. Instrum. Meth. A540, pp. 368-380, 2005. DOI: 10.1016/j.nima.2004.12.002.
- [128] F. Simon and C. Soldner. “Uniformity Studies of Scintillator Tiles directly coupled to SiPMs for Imaging Calorimetry”, Nucl. Instrum. Meth. A620, pp. 196-201, 2010. DOI: 10.1016/j.nima.2010.03.142.
- [129] Y. Liu, *et al.* “A Design of Scintillator Tiles Read Out by Surface-Mounted SiPMs for a Future Hadron Calorimeter”, Proceedings for IEEE Nuclear Science Symposium, Talk N17-8, arXiv:1512.05900.2014, 2014.
- [130] C. Soldner. “The Time Development of Hadronic Showers and the T3B Experiment”, PhD Thesis, Ludwigs-Maximilians-Universität München, München, 2013. URL: <https://cds.cern.ch/record/2069127>.
- [131] E. Garutti. “Silicon Photomultipliers for High Energy Physics Detectors”, Preprint submitted to Nucl. Instrum. Meth. A, 2018. DOI: 10.1088/1748-0221/6/10/C10003.

- [132] HAMAMATSU PHOTONICS K.K., Solid State Division. “MPPC - Technical Note”, April 2021. URL: [https://www.hamamatsu.com/resources/pdf/ssd/mppc\\_kapd9008e.pdf](https://www.hamamatsu.com/resources/pdf/ssd/mppc_kapd9008e.pdf).
- [133] S. Krause. “Studies of the Response of Silicon Photomultipliers and Testbeam Data Analysis of a Highly Granular Analog Hadron Calorimeter Prototype”, PhD Thesis, Johannes Gutenberg Universität Mainz, Mainz, 2020. DOI: 10.25358/openscience-1642.
- [134] A. Vásquez-Ramírez, *et al.* “Simulated Response of MuTe, a Hybrid Muon Telescope”, To be published in JINST, preprint arXiv:1912.10081, 2020, DOI: 10.1088/1748-0221/15/08/P08004.
- [135] S. Piatek, Hamamatsu Corporation and New Jersey Institute of Technology. “How does temperature affect the performance of an SiPM?”, 2017. URL: <https://hub.hamamatsu.com/us/en/technical-note/sipm-temperature-performance/index.html>.
- [136] Hamamatsu Photonics. “MPPC Series 13360 Datasheet”, 2016. URL: [https://www.hamamatsu.com/resources/pdf/ssd/s13360\\_series\\_kapd1052e.pdf](https://www.hamamatsu.com/resources/pdf/ssd/s13360_series_kapd1052e.pdf).
- [137] S. Piatek, Hamamatsu Corporation and New Jersey Institute of Technology. “Physics and operation of the MPPC silicon photomultiplier”, 2014. URL: <https://hub.hamamatsu.com/jp/en/technical-note/sipm-physics-operation/index.html>.
- [138] 3M. “3M Enhanced Specular Reflector (ESR) - Application Guidelines”, 2021. URL: [http://www.3m.com/3M/en\\_US/p/d/eebgdar000006/](http://www.3m.com/3M/en_US/p/d/eebgdar000006/).
- [139] Y. Liu *et al.* “A Design of Scintillator Tiles Read Out by Surface-Mounted SiPMs for a Future Hadron Calorimeter”, 2014 IEEE Nuclear Science Symposium Proceeding, December 2015. URL: <https://arxiv.org/abs/1512.05900>.
- [140] L. M. S. de Silva and F. Simon. “Effects of misalignment on response uniformity of SiPM-on-tile technology for highly granular calorimeters”, JINST 15 P06030, 2020. DOI: 10.1088/1748-0221/15/06/P06030.
- [141] M. Bouchel *et al.* “SPIROC (SiPM Integrated Read-Out Chip): dedicated very front-end electronics for an ILC prototype hadronic calorimeter with SiPM read-out”, JINST 6 C01098, 2011. DOI: 10.1088/1748-0221/6/01/C01098.
- [142] Omega, LAL/IN2P3. “SPIROC2 User Guide”, 2009. URL: [https://indico.cern.ch/event/232082/contributions/493652/attachments/385835/536707/Spiroc2\\_userGuide2009\\_datasheet.pdf](https://indico.cern.ch/event/232082/contributions/493652/attachments/385835/536707/Spiroc2_userGuide2009_datasheet.pdf).
- [143] T. Christian. “Power Pulsing Studies of an Extended Analogue Hadron Calorimeter Layer”, Bachelor Thesis, Universität Heidelberg, Heidelberg, 2019. URL: <http://www.kip.uni-heidelberg.de/Veroeffentlichungen/details.php?id=4081>.
- [144] J. Kvasnicka and I. Polak. “LED Calibration Systems for CALICE Hadron Calorimeter”, Proceedings of the 2nd International Conference on Technology and Instrumentation in Particle Physics (TIPP 2011), 2012. DOI: <https://doi.org/10.1016/j.phpro.2012.02.379>.
- [145] A. Steen for the CMS Collaboration. “Beam-tests of prototype modules for the CMS High Granularity Calorimeter at CERN”, JINST 14, 04, C04008, 2019. DOI: 10.1088/1748-0221/14/04/C04008.

- [146] Y. Sudo. “Temperature Compensation and HG/LG Inter-Calibration”, Contribution to CALICE Collaboration Meeting, Shanghai, China, 2018. URL: [https://agenda.linearcollider.org/event/7799/contributions/42262/attachments/33592/51488/TempComp\\_HGLGIC\\_201809\\_calice.pdf](https://agenda.linearcollider.org/event/7799/contributions/42262/attachments/33592/51488/TempComp_HGLGIC_201809_calice.pdf).
- [147] A. Provenza. “Calibration and Analysis of Data taken with the Technological Prototype of the Analog Hadron Calorimeter (AHCAL) for a Detector at the International Linear Collider”, PhD Thesis, University of Hamburg, Hamburg, 2018. DOI: 10.3204/PUBDB-2019-00522.
- [148] S. Schröder. “Commissioning of a prototype hadronic calorimeter”, Master Thesis, University of Hamburg, Hamburg, 2015. URL: [https://www.physik.uni-hamburg.de/en/iexp/gruppe-garutti/publikationen/bachelor-master-thesen/\\_files/2015-master-schroeder-sarah.pdf](https://www.physik.uni-hamburg.de/en/iexp/gruppe-garutti/publikationen/bachelor-master-thesen/_files/2015-master-schroeder-sarah.pdf).
- [149] F. Lenzen. “Channel by Channel MIP-Calibration of the Analogue Hadronic Calice-Calorimeter”, Bachelor Thesis, Bergische Universität Wuppertal, Wuppertal, 2014.
- [150] O. Pinto. “Operation and Calibration of a Highly Granular Hadron Calorimeter with SiPM-on-Tile Read-out”, Proceedings for IEEE Nuclear Science Symposium, arXiv:2004.00370, 2020. URL: <https://arxiv.org/abs/2004.00370>.
- [151] Y. Sudo. “HG/LG Inter-Calibration and Gain Stability”, Contribution to AHCAL Main Meeting, DESY, Hamburg, 2018. URL: [https://agenda.linearcollider.org/event/8082/contributions/43029/attachments/34071/52425/HGLGIC\\_main\\_meeting.pdf](https://agenda.linearcollider.org/event/8082/contributions/43029/attachments/34071/52425/HGLGIC_main_meeting.pdf).
- [152] L. Emberger. “Analysis of Testbeam Data Recorded with the Large CALICE AHCAL Technological Prototype”, Proceedings for International Workshop on Future Linear Colliders (LCWS2021), arXiv:2105.08497, 2021. URL: <https://arxiv.org/abs/2105.08497>.
- [153] F. Gaede *et al.* “LCIO - A persistency framework for linear collider simulation studies”, arXiv:physics/0306114 [physics.data-an], 2003. URL: <https://arxiv.org/abs/physics/0306114>.
- [154] M. Frank *et al.* “DD4hep: A Detector Description Toolkit for High Energy Physics Experiments”, Journal of Physics: Conference Series 513(2), 022010, 2014. DOI: 10.1088/1742-6596/513/2/022010.
- [155] CALICE Collaboration. “Pion and proton showers in the CALICE scintillator-steel analogue hadron calorimeter”, JINST 10, P04014, 2015. DOI: 10.1088/1748-0221/10/04/P04014.
- [156] The CALICE Collaboration. “Tests of a Particle Flow Algorithm with CALICE Test Beam Data”, JINST 6 P07005, 2011. DOI: 10.1088/1748-0221/6/07/P07005.
- [157] V. Bocharnikov. “Particle ID in the AHCAL + Single Shower Substructure”, Contribution to CALICE Collaboration Meeting, Virtual, 2020. URL: [https://agenda.linearcollider.org/event/8608/contributions/46466/attachments/35887/55715/VB\\_AHCAL\\_PID\\_CALICE\\_collab.pdf](https://agenda.linearcollider.org/event/8608/contributions/46466/attachments/35887/55715/VB_AHCAL_PID_CALICE_collab.pdf).
- [158] O. Lobban *et al.* “On the energy measurement of hadron jets”, Nucl. Instrum. Meth. A495, pp. 107-120, 2002. DOI: 10.1016/S0168-9002(02)01615-7.

- [159] The ILD Collaboration. “International Large Detector: Interim Design Report”, arXiv:2003.01116 [physics.ins-det], 2020. URL: <https://arxiv.org/abs/2003.01116>.
- [160] R. Ete on behalf of the ILD concept group. “The ILD Software Tools and Detector Performance”, Proceedings for 40th International Conference on High Energy physics (ICHEP2020), Prague, 2020. URL: <https://pos.sissa.it/390/909/pdf>.
- [161] R. Frühwirth. “Application of Kalman filtering to track and vertex fitting”, Nucl. Instrum. Meth. A262, pp. 444-450, 1987. DOI: [https://doi.org/10.1016/0168-9002\(87\)90887-4](https://doi.org/10.1016/0168-9002(87)90887-4).
- [162] E. Garutti and Y. Musienko. “Radiation damage of SiPMs”, Preprint submitted to Nucl. Instrum. Meth. A, arXiv:1809.06361, 2018. DOI: [10.1016/j.nima.2018.10.191](https://doi.org/10.1016/j.nima.2018.10.191).
- [163] R. Ete. “Toward and automated calibration procedure”, Talk at the Linear Collider Workshop 2017 (LCWS2017), Strasbourg, France, 2017. URL: [https://agenda.linearcollider.org/event/7645/contributions/39963/attachments/32198/48827/LCWS2017\\_LCCalibration.pdf](https://agenda.linearcollider.org/event/7645/contributions/39963/attachments/32198/48827/LCWS2017_LCCalibration.pdf).

# List of Figures

2.1	Standard Model of Particle Physics	6
3.1	Higgs Production at a Future $e^+e^-$ Collider	13
3.2	Higgs Boson Branching Ratios	14
3.3	Higgs Recoil Mass Measurement: $Z \rightarrow \mu\mu$	15
3.4	Relative Precision Projections of Higgs Couplings	17
3.5	International Linear Collider (ILC)	19
3.6	International Large Detector (ILD)	21
3.7	Silicon Detector (SiD)	22
3.8	Compact Linear Collider (CLIC)	23
3.9	CLIC Detector Concept	24
4.1	Electromagnetic Interactions	26
4.2	Electromagnetic Shower	27
4.3	Mass Stopping Power: Muons in Copper	29
4.4	Landau-Vavilov Energy Loss Distribution	29
4.5	Hadronic Shower	30
4.6	Intra Nuclear Cascade	33
4.7	Parton String Model	33
4.8	Geant4 Physics Lists	34
4.9	Particle Flow Reconstruction Concept	39
4.10	Particle Flow Reconstruction Confusion Types	40
4.11	PandoraPFA Algorithm Classes	42
4.12	ILD Di-Jet Simulations and Relative Single Jet Energy Resolution	45
5.1	Working Principle Silicon Photomultiplier (SiPM)	51
5.2	SiPM Saturation and Breakdown Voltage Temperature Dependence	52
5.3	Hamamatsu SiPM MPPC S13360-1325PE	53
5.4	SiPM-on-Tile Design	54
5.5	SiPM-on-Tile Response Uniformity	55
5.6	SPIROC2E Readout Chip	56
5.7	AHCAL HBU and AHCAL Prototype Layer	57
5.8	Power Pulsing Operation Mode	58
5.9	AHCAL Prototype at SPS CERN 2018	58
5.10	AHCAL Prototype Data Event Displays Particle Types	59
5.11	Delay Wire Chambers SPS CERN 2018	60
5.12	SiPM Bias Voltage Adjustment Temperature	61

5.13	Examples Pedestal Spectra	63
5.14	Extracted Pedestals Memory Cell Level	64
5.15	Extracted Intrinsic Pedestal Widths Memory Cell Level	64
5.16	Cell-to-Cell and Channel-to-Channel Variation Pedestals	65
5.17	Pedestal Map Layer 12	66
5.18	Pedestal Stability Time and Detector Mode	66
5.19	Example Fitted MIP Spectrum	67
5.20	Extracted MIP Constants May and June Beam Test	68
5.21	MIP Constants Variation	68
5.22	MIP Constant Stability Time and Detector Mode	69
5.23	MIP Calibration Validation Global Level	70
5.24	MIP Calibration Validation Channel Level and Systematics	71
5.25	Example Single Photon Spectrum	72
5.26	Extracted Gain Constants	72
5.27	Gain Constant Map Layer 12	73
5.28	Gain Stability June Beam Test	74
5.29	Light Yield Channel Level	74
5.30	Illustration High Gain Low Gain Intercalibration	75
5.31	Intercalibration Spectrum and Extracted Constants	76
5.32	Low Gain Pedestals Channel Level	76
5.33	Intercalibration and Low Gain Pedestal Validation	77
5.34	MPPC S13360-1325PE Saturation Measurement	78
6.1	DD4hep Simulation Geometry AHCAL Prototype	83
6.2	Digitisation Chain AHCAL Prototype Event Simulation	84
6.3	Charged Pion Event Display Shower Start Layer	86
6.4	Shower Start Finding Algorithm Threshold Illustration	87
6.5	Event Displays: Soft and Hard Primary Interaction Simulation	88
6.6	Hardness Cut Illustration	88
6.7	Determined Shower Start vs. MC Truth Shower Start Layer	89
6.8	Shower Start Finding Efficiencies Simulated Charged Pions	90
6.9	Example Shower Start Layer Distribution Charged Pions	91
6.10	Shower Start Finding Algorithm Results $K_L^0$	92
6.11	Shower Start Finding Algorithm Results Muons and Electrons	92
6.12	Illustration Pseudo-Neutral Hadron Generation Algorithm	94
6.13	Number Cut Hits vs. Shower Start Layer	94
6.14	$K_L^0$ vs. Pseudo-Neutral Hadron Calorimetric Observables	95
6.15	Illustration of Two Particle Event Overlay	96
6.16	Beam Contamination 10 GeV Charged Pion Data	98
6.17	Performance Gradient Boosted Decision Tree Event Classification	99
7.1	AHCAL Prototype Beam Profile Examples Charged Pion Data and Simulation	102
7.2	AHCAL Prototype Muon Response Data and Simulation	103
7.3	AHCAL Prototype Electron Response Data and Simulation	104
7.4	AHCAL Prototype Pion Response Data and Simulation	105
8.1	Overview Event Selection and Preparation	108
8.2	Visualisation Track Implementation and Calorimeter Front Face Projection	109

8.3	Inter-DWC Calibration Example Hit to Fit Position Residuals	109
8.4	Example Track Reconstruction in X Plane	110
8.5	DWC Track Slopes Example Charged Pion Sample	111
8.6	Correlation DWC and AHCAL X Position Example Muon Run	111
8.7	Track Quality Validation 10 GeV Charged Pion Samples	113
8.8	Distribution Radial Shower Distances Two Particle Samples	116
8.9	PandoraPFA Interface Framework AHCAL Prototype Studies	117
8.10	Hadronic MIP to GeV Scale Conversion $K_s^0$ Simulations	119
8.11	<i>PandoraHcalToHadScale</i> Calibration AHCAL Prototype	120
8.12	PandoraPFA Visual Monitoring Event Display Example	121
8.13	Event Display Visualisation Adaption Track to Cluster Association Algorithm	122
8.14	Event Display Visualisation Impact Track Driven Merging Algorithm Threshold	123
8.15	Event Display Visualisation Impact Outer Sampling Layer Definition	124
8.16	Event Display Visualisation Isolated Hit Merging Algorithm	125
8.17	Single Particle Studies: Reconstructed Event Classes Data	126
8.18	Single Particle Studies: Event Displays Reconstructed Event Classes	127
8.19	Single Particle Studies: Number Confusion Events	128
8.20	Single Particle Studies: Example Neutral PFO Multiplicity Distributions Data	129
8.21	Single Particle Studies: Neutral PFO Multiplicity and Neutral PFO Energy Sum	130
8.22	Single Particle Studies: Charged Hit and Energy Clustering Efficiency	131
8.23	Single Particle Studies: Example PFO Energy Sum Distributions	132
8.24	Single Particle Studies: Energy Linearity	133
8.25	Single Particle Studies: Relative Energy Resolution	133
8.26	Single Particle Studies: Energy Sum Neutral PFOs Leakage Study	134
8.27	Two Particle Studies: Reconstructed Event Classes Data	136
8.28	Two Particle Studies: Event Displays Reconstructed Event Classes	137
8.29	Two Particle Studies: Example Spectra Neutral Energy Difference	138
8.30	Two Particle Studies: Example Sigma Determination	139
8.31	Two Particle Studies: $3\sigma$ Recovery Probability Pseudo-Neutral Hadron Energy	140
8.32	Two Particle Studies: $2\sigma$ Recovery Probability Pseudo-Neutral Hadron Energy	141
8.33	Two Particle Studies: Neutral Energy Reconstruction Efficiency and Purity	143
8.34	Two Particle Studies: Charged Energy Reconstruction Efficiency and Purity	143
8.35	Two Particle Studies: Double Counted Charged and Lost Neutral Confusion Energy	144
8.36	Two Particle Studies: Confusion Type Balance and Total Confusion Energy	145
8.37	Two Particle Studies: Example PFO Energy Sum Distributions	146
8.38	Two Particle Studies: Reconstructed Total Event Energy	147
8.39	Two Particle Studies: Relative Energy Resolution	148
8.40	Example Event Display Longitudinal Shower Separation	148
8.41	Two Particle Studies: $3\sigma$ Recovery Probability Longitudinal Shower Separation	150
9.1	Example Event Displays ILD Di-Jet Events	153
9.2	PandoraPFA Default Settings: Jet Energy Linearity and Relative Energy Resolution	154
9.3	PandoraPFA Settings: Confusion Energy	156
9.4	PandoraPFA Settings: Confusion Type Difference and Total Confusion Fraction	157
9.5	PandoraPFA Settings: Jet Energy Linearity and Relative Energy Resolution	157
9.6	PandoraPFA Settings AHCAL: Confusion Energy	158
9.7	Example Event Displays ILD Di-Jet Event Different Hit Energy Thresholds	160

9.8	Hit Energy Thresholds: Re-Calibration PandoraPFA ILD	162
9.9	Hit Energy Thresholds: Confusion Energy	163
9.10	Hit Energy Thresholds: Confusion Type Difference and Total Confusion Fraction	163
9.11	Hit Energy Thresholds: Jet Energy Linearity and Relative Energy Resolution	164
9.12	Example Event Displays AHCAL Data Different Hit Energy Thresholds	165
9.13	Hit Energy Thresholds: Re-Calibration PandoraPFA AHCAL Prototype	166
9.14	Hit Energy Thresholds: $3\sigma$ Recovery Probability AHCAL Data	167
A.1	Extracted Pedestals Channel Level	173
A.2	Extracted Intrinsic Pedestal Widths Channel Level	173
A.3	MIP Calibration Fit Parameters and Quality	174
B.1	$K_L^0$ vs. $K_L^0$ Cut Calorimetric Observables	175
C.1	Energy Sum Distributions Single $\pi^-$ Samples	180
C.2	Number of Hits Distributions Single $\pi^-$ Samples	181
C.3	Mean Longitudinal Shower Energy Profiles Single $\pi^-$ Samples	182
C.4	Mean Radial Shower Energy Profiles Single $\pi^-$ Samples	183
C.5	Calorimetric Observables Pseudo-Neutral Hadron Samples	186
C.6	Mean Energy Sum Two Particle Samples	188
C.7	RMS Energy Sum Two Particle Samples	188
C.8	Mean90 Energy Sum Two Particle Samples	189
C.9	RMS90 Energy Sum Two Particle Samples	189
C.10	Energy Sum Distributions Individual Particles: Distance Bin 0-25mm	190
C.11	Energy Sum Distributions Individual Particles: Distance Bin $50 \pm 25$ mm	191
C.12	Energy Sum Distributions Individual Particles: Distance Bin $100 \pm 25$ mm	192
C.13	Energy Sum Distributions Individual Particles: Distance Bin $150 \pm 25$ mm	193
C.14	Energy Sum Distributions Individual Particles: Distance Bin $200 \pm 25$ mm	194
C.15	Energy Sum Distributions Individual Particles: Distance Bin $250 \pm 25$ mm	195
C.16	Energy Sum Distributions Individual Particles: Distance Bin $300 \pm 25$ mm	196
D.1	Two Particle Studies: Neutral Energy Difference Spectra 0 – 25 mm	197
D.2	Two Particle Studies: Neutral Energy Difference Spectra 25 – 75 mm	198
D.3	Two Particle Studies: Neutral Energy Difference Spectra 75 – 125 mm	198
D.4	Two Particle Studies: Neutral Energy Difference Spectra 125 – 175 mm	199
D.5	Two Particle Studies: Neutral Energy Difference Spectra 175 – 225 mm	199
D.6	Two Particle Studies: Neutral Energy Difference Spectra 225 – 275 mm	200
D.7	Two Particle Studies: Neutral Energy Difference Spectra 275 – 325 mm	200
D.8	Previous Two Particle Studies: Example Neutral Energy Difference Spectra	201
D.9	Two Particle Studies: Mean Neutral Energy Difference	202
D.10	Two Particle Studies: RMS Neutral Energy Difference	202
D.11	Two Particle Studies: Neutral Hit Reconstruction Efficiency and Purity	203
D.12	Two Particle Studies: Charged Hit Reconstruction Efficiency and Purity	203
D.13	Two Particle Studies: Example Confusion Matrices Data	204
D.14	Longitudinal Shower Separation Study: Double Counted Charged Confusion Energy	204
D.15	Longitudinal Shower Separation Study: Lost Neutral Confusion Energy	205
D.16	Longitudinal Shower Separation Study: Confusion Type Difference	206

D.17	Longitudinal Shower Separation Study: Fractional Confusion Event Energy . . . .	207
E.1	PandoraPFA Settings: Correct Energy . . . . .	209
E.2	PandoraPFA Settings: Example Confusion Matrices . . . . .	210
E.3	PandoraPFA Settings AHCAL: Confusion Type Difference and Confusion Fraction	210
E.4	Hit Energy Thresholds: Correct Energy . . . . .	211

# List of Tables

5.1 Main Specifications Hamamatsu MPPC-S13360-1325PE SiPM . . . . .	53
5.2 Summary AHCAL Calibration Results and Uniformity/Stability Studies . . . . .	80
6.1 Event Overlay: Low Energy and Overlaid Hits Summary . . . . .	97
9.1 Calibration Constants ILD_l5_o1_v02 Hit Energy Thresholds . . . . .	162
9.2 Calibration Constants AHCAL Prototype Hit Energy Thresholds . . . . .	166
C.1 Global DWC to AHCAL Prototype Alignment Offsets . . . . .	177
C.2 Centralised Single Charged Pion Samples Single Particle Studies . . . . .	178
C.3 De-centralised Single Charged Pion Samples Single Particle Studies . . . . .	179
C.4 Single Charged Pions Samples Two Particle Studies . . . . .	184
C.5 Single Pseudo-Neutral Hadron Samples Two Particle Studies . . . . .	185
C.6 Events Radial Shower Distance Bins Two Particle Studies . . . . .	187
E.1 ILD Default Calibration Constants Detector Model ILD_l5_o1_v02 . . . . .	211

# Acknowledgements

The last page of this thesis I dedicate to the numerous people who have supported and accompanied me on my long way through my studies and this doctoral thesis.

First of all, I would like to thank my supervisor Felix Sefkow for his excellent supervision and for the possibility of this doctoral study. Thank you for having your door always open, for your guidance and continuous advice over the last four years, even under pandemic circumstances. I profited a lot from your immense knowledge about physics, calorimetry and politics, of course, shaping me as a young scientist. I would like to thank Norbert Herrmann for his friendly willingness to act as the second referee of this thesis.

Next, I would like to give special thanks to my second supervisor Katja Krüger. Thank you for the guidance over the last years, all of your questions, ideas, proofreading of abstracts and presentations and for all the fruitful discussions. Your massive knowledge about physics and your huge experimental experience had a significant impact on all of my work over the last years. A special thank you goes as well to Marcel Stanitzki for being my DESY mentor continuously supporting me, for all the discussions and your inspiring and cheerful character.

In general, I would like to thank all current and former members of the FTX group at DESY for all of their advice, help and discussions. Special thanks go to Andrea for all of her help with respect to administrative tasks and all the nice conversations, which I enjoyed very much.

Of course, I have to thank all the current and former members of the AHCAL group at DESY and beyond: Jiri, Yuji, Ambra, Eldwan, Remi, Lan, Oskar, Matthias, Ole, Jonas, Timo, Malinda, Merijn, Jack, Saiva, Erik, Antoine, Anna, Sebastian, Amine, Lorenz, Christian G., Christian W., Konrad, Wataru, Linghui, etc. Thank you for the fantastic collaborative atmosphere, the wonderful and unforgettable test beam experiences at DESY and SPS CERN and the entertaining and sometimes crazy nights in Tokyo. Special thanks go to my dear DESY PhD student colleagues, and friends, Olin and Vladimir for all the memorable times in particular the containership experience.

I would like to thank all members of the CALICE collaboration, which actively supported me and for all the fruitful discussions during many collaboration and analysis meetings. With regard to this I want to thank in particular Frank, Marina, Lucia, Roman and Francois.

In addition, I would like to thank Hans-Christian and all members of his Heidelberg KIP group for their regular warm welcome, friendly help and the nice times whenever I was staying in Heidelberg. Furthermore, I would like to thank John Marshall for his continuous support and advice about PandoraPFA. These extensive discussions have been of tremendous help.

Special thanks also go to the colleagues and friends who proofread sections of this thesis: Matthew, Konrad, Peter, Jakob, Anna and Tolga. Thank you for your time and feedback.

Zum Abschluss möchte ich mich natürlich bei meiner Familie und meinen Freunden bedanken. Vielen lieben Dank für die jahrelange Unterstützung, euer offenes Ohr für mich und meine Probleme und das gelegentliche Zurückholen in die reale Welt. Besonderer Dank gilt hier meiner Mutter Grit, meiner Schwester Laura und meinem Onkel Björn. Zu guter Letzt möchte ich mich natürlich bei dir bedanken, Verena, für deine dauerhafte, grenzenlose Unterstützung, deine Liebe über all die Jahre und die große Stärke, die du mir gibst. Danke dir für alles!